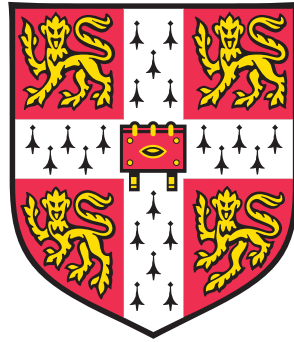


Understanding Membrane Curvature Sensing



Adeline Colussi

MRC Laboratory of Molecular Biology

University of Cambridge

This dissertation is submitted for the degree of

Doctor of Philosophy

Understanding Membrane Curvature Sensing

Eukaryotic cells are characterised by membranes with varied and dynamic compositions and shapes. Consequently, membrane-binding proteins are tuned to recognise and modify these membrane states to perform their functions. To study the curvature sensitivity of proteins, I have developed a single-particle assay using NanoSight technology that tracks the Brownian motion of particles to measure their size. I optimised this system to track fluorescently labelled lipid-binding domains bound to liposomes of different sizes moving freely in solution. The comparison of the size distribution of the total liposomes with the fluorescently labelled population allowed me to determine their curvature preferences. To validate the method I tested proteins from the Bin/Amphiphysin/Rvs (BAR) superfamily, which are inherently curved and have known curvature preferences. My method was capable of recapitulating the behaviour of BAR domains with different curvature preferences. I then expanded the range of targets and showed that this assay is also capable of detecting curvature preferences for a variety of other lipid-binding domain families. As such, I identified AKT PH domain as a new curvature-sensing domain. Finally, using the ENTH domain of Epsin1 that causes vesicle budding, I demonstrated that this method can also be used to study membrane remodelling.

Trafficking involves generation and sensing of membrane curvature combined with recognition of specific cargo. Endophilin consists of a curvature-sensitive BAR domain followed by an SH3 (Src-homology 3) domain and has recently been identified in a clathrin-independent endocytosis pathway, FEME (fast endophilin-mediated endocytosis), involved in the uptake of cell surface receptors. Endophilin recognises ligands *via* its SH3 domain, binding G-protein coupled receptors (GPCRs) directly in their intracellular loop 3 and receptor tyrosine kinase (RTKs) via adaptor proteins. However, a specific recognition motif has not been identified yet. Here, using a combination of biophysical approaches and NMR spectroscopy, I characterised the Endophilin binding motif of ALIX (ALG-2-interacting protein X) adaptor protein and of the GPCR α 2A adrenergic receptor. Comparison of SH3-peptide models resulted in a putative Endophilin recognition site.

Declarations

This dissertation is submitted for the degree of Doctor of Philosophy. The contents are the result of my own work and include nothing which is the outcome of work done in collaboration except as declared below and specified in the text. Other contributors are identified by their initials (TR – Trevor Rutherford, HMM – Harvey McMahon). It is not the same as any work that I have submitted or that is being submitted for a degree or diploma or other qualification at the University of Cambridge or any other University or similar institution. I further state that no substantial part of my dissertation has already been submitted, or, is being concurrently submitted for any such degree, diploma or other qualification at the University of Cambridge or any other University or similar institution. It does not exceed 60'000 words in length.

All the Nuclear Magnetic Resonance work was carried out in collaboration with Trevor Rutherford (MRC LMB). He set up the NMR experiments, processed the spectra and carried out the modelling.

Harvey McMahon helped with the cloning of some of the constructs used in this study and performed the preliminary mutagenesis work on Endophilin binding.

Acknowledgements

First, I would like to thank my supervisor, Harvey McMahon, for giving me the opportunity of working in his lab and introducing me to the wonderful world of membrane curvature. Throughout my PhD, he has always been open to discussions, bringing innovative ideas and a long-term vision to my projects. Thanks to him I am also finally able to do PCR mutagenesis (most of the time).

Without Leonardo Almeida-Souza and his continuous support, new ideas and deep scientific discussions, this thesis would not have come to be. He always had an open ear and a pragmatic solution to every problem, big or small. When the project was stalled and nothing else would help, he was also there with offers for cake and tea.

Trevor Rutherford was the driving force behind the NMR part of this thesis. He spent many night hours and week-ends collecting data, changing samples in the magnet or setting up modelling calculations. Yvonne Vallis took over the cell biology part of the thesis, trying every trick in the book to establish a working protocol.

Thanks also go to all the members of the McMahon lab, past and present, in particular Vladan Martinović and Wai-Ching Hon who taught me protein purification and biophysics, Rohit Mittal and his vast scientific knowledge and everybody for making this lab a unique working environment.

Several core LMB facilities greatly facilitated my work. Special thanks go to Chris Johnson and Stephen McLaughlin for their help with the biophysics, Sew Peak Chew for the mass spectrometry and the media kitchen and glass wash for being very accommodating with my media and buffer requirements.

I am grateful to Harvey McMahon, Leonardo Almeida-Souza, Rohit Mittal, Trevor Rutherford and Homa Majd for their proof-reading.

Finally, I wish to thank my family for their continuous support despite the geographical distance.

Contents

List of Figures	iii
List of Tables	vi
List of Abbreviations	vii
1 Introduction	1
1.1 Membrane curvature	1
1.1.1 Membrane shape	1
1.1.2 Generation of high membrane curvature	2
1.1.3 Sensing membrane curvature	6
1.2 Lipid-binding domains	9
1.2.1 BAR domains as curvature sensors and generators	9
1.2.2 Non-BAR lipid-binding domains	13
1.3 Endocytosis and Endophilin	18
1.4 Aims of this thesis	23
2 Measuring curvature sensitivity of proteins in a single-particle solution assay	25
2.1 Introduction	25
2.2 Results	30
2.2.1 Nanoparticle tracking analysis using NanoSight technology	30
2.2.2 NTA validation	34
2.2.3 BAR domain curvature sensitivity	36
2.2.4 Curvature sensitivity of other lipid-binding domains	43
2.2.5 Vesiculation by ENTH	53
2.3 Discussion	56

3	Endophilin binding motif in Endophilin-mediated endocytosis	65
3.1	Introduction	65
3.2	Results	68
3.2.1	<i>In vitro</i> interaction of adrenergic receptors ICL3 and adaptor proteins with Endophilin	68
3.2.2	Endophilin A1 SH3 – Alix PRD interaction: NMR model	71
3.2.3	Endophilin A1 SH3 - ADRA2A ICL3 interaction	85
3.3	Discussion	91
4	Final thoughts	97
5	Material and methods	99
5.1	Reagents	99
5.1.1	Buffer recipes	99
5.1.2	Liposome preparation	101
5.2	Molecular Biology	102
5.2.1	cDNA library generation	107
5.2.2	Fragment Exchange (FX) Cloning	107
5.2.3	Mutagenesis (HMM and AC)	107
5.3	Recombinant protein expression and purification	108
5.3.1	Recombinant protein expression in <i>E. coli</i>	108
5.3.2	Small-scale protein purification	108
5.3.3	Large-scale protein purification	109
5.3.4	Protein labelling	109
5.4	Biochemical assays	110
5.4.1	Liposome flotation	110
5.4.2	GST pull-down	110
5.4.3	Isothermal Titration Calorimetry	111
5.5	NanoSight measurements	111
5.6	NMR	112
5.6.1	Recombinant protein expression	112
5.6.2	Protein labelling for Paramagnetic Relaxation Enhancement PRE	112
5.6.3	Data collection (TR) and analysis (TR and AC)	113
6	Bibliography	115

List of Figures

1.1	Membrane curvature in cellular structures	2
1.2	Curvature topology on an endocytic vesicle	2
1.3	Mechanisms of cellular curvature generation	3
1.4	Mechanisms of cellular curvature sensing	7
1.5	BAR domains overview	10
1.6	Structure of phospholipids	13
1.7	Overview of non-BAR lipid binding domains	15
1.8	Clathrin-mediated endocytosis stages	19
1.9	Structure of Endophilin N-BAR and SH3	20
2.1	Working principle of NanoSight LM10	31
2.2	Detection of particle centres	32
2.3	Tracking of particles	32
2.4	NTA data representation	33
2.5	Size distribution of 100 nm and 216 nm calibration beads based on NTA	34
2.6	Size distribution of 100 nm and 216 nm calibration beads based on DLS	35
2.7	Size distribution of 50 nm fluorescent liposomes alone or after mixing with unlabelled 200 nm liposomes	35
2.8	Size distribution of 200 nm fluorescent liposomes alone or after mixing with unlabelled 100 nm liposomes	36
2.9	Curvature preference of Endo NBAR-488	38
2.10	Comparison of Alexa488 and sfGFP for NTA curvature sensitivity measure- ments	38
2.11	Curvature sensitivity of Endo NBAR-sfGFP	39
2.12	Curvature sensitivity of Endo NBAR-sfGFP by liposome flotation assay	40
2.13	Influence of PI(4,5)P ₂ content on curvature sensitivity of Endophilin	41

2.14	Comparison of BAR domain curvatures from Endophilin, FCHo2 and IRSp53	41
2.15	Curvature sensitivity of FCHo2 BARX-sfGFP	42
2.16	Curvature sensitivity of IRSp53 BAR-sfGFP	43
2.17	Effect of salt additives on aggregates of IRSp53 BAR-sfGFP	45
2.18	Effect of salt additives on binding of IRSp53 BAR-sfGFP to liposomes	46
2.19	Effect of addition of His-SUMO on PKC β 2 C1BC2-sfGFP aggregation and binding to liposomes	46
2.20	Binding of ANTH-sfGFP, Annexin A7-sfGFP and CYTH3 PH-sfGFP on FolchSA liposomes	47
2.21	Binding of lipid-binding domains on FolchSA spiked with 2% PI(3)P, PI(4,5)P ₂ , PI(3,4,5)P ₃ or 5% PS	48
2.22	Binding of FAK1 and Talin1 FERM-sfGFP on FolchS-50% PS liposomes	49
2.23	Binding of PKC β 2 C1B-sfGFP and C1BC2-sfGFP on FolchS-50% PS+3% PMA liposomes	49
2.24	Effects of CaCl ₂ and EDTA on binding of PKC β 2 C1B-C2 domain on FolchS-50% PS+3% PMA liposomes	50
2.25	Curvature sensitivity of HRS FYVE-sfGFP binding to FolchS+2% PI(3)P liposomes	51
2.26	Curvature sensitivity of PKC β 2 C1B-sfGFP binding to FolchS-50% PS+3% PMA liposomes	52
2.27	Curvature sensitivity of FAK1 FERM-sfGFP binding to FolchS-50% PS liposomes	52
2.28	Curvature sensitivity of Talin1 FERM-sfGFP binding to FolchS-50% PS liposomes	53
2.29	Curvature sensitivity of AKT PH-sfGFP binding to FolchS-2% PI(3,4,5)P ₃ liposomes	54
2.30	Size reduction of liposomes after incubation with ENTH wild-type (wt) or L6W	55
2.31	Dose-response of vesiculation with ENTH wild-type (wt) or L6W	55
2.32	Dose-response curve of vesiculation with ENTH wild-type (wt) or L6W	55
2.33	Time-course of ENTH vesiculation after addition of 2 μ M ENTH wild-type	56
2.34	Crystal structures of AKT PH in absence and presence of IP4	62
3.1	SH3 binding to polyproline II helix	66

3.2	Endophilin pull-down by adrenergic GPCRs ICL3 and adaptor proteins PRD	69
3.3	ITC measurements of affinity between Endophilin SH3 and Alix PRD or ADRA2A ICL3 fragments	71
3.4	^1H - ^{15}N HSQC overlay of Endophilin SH3 free or with increasing amounts of Alix	73
3.5	Magnetisation transfer in CBCA(CO)NH and HNCACB spectra and assignment of a fragment of Endophilin SH3	74
3.6	Assigned ^1H - ^{15}N HSQC of Endophilin SH3 free or with increasing amounts of Alix	75
3.7	Endophilin SH3 CSP upon Alix titration	77
3.8	Titration of Endophilin SH3 on Alix, effects on ^1H - ^{15}N	78
3.9	Titration of Endophilin SH3 on Alix, effects on ^1H - ^{13}C	79
3.10	Nitroxide radical probe 4-maleimido-TEMPO (2,2,6,6-Tetramethyl-1-piperidinyloxy)	81
3.11	Shift maps and heatmaps of Endophilin SH3 PRE induced by TEMPO-labelled Alix at positions T7, P17 and A25	81
3.12	Models of SH3-Alix complex with KPQPPARPPP or RPPPPVLPA binding motifs	84
3.13	Pull-down of Endophilin full-length or SH3 with GST-Alix mutants	85
3.14	Endophilin SH3 CSP upon ADRA2A titration	86
3.15	CSP and PRE of ADRA2A with Endophilin SH3	87
3.16	Position of E304 on Endophilin SH3 for TEMPO labelling	88
3.17	Shift maps and heatmaps of Endophilin SH3 PRE induced by TEMPO-labelled ADRA2A at positions D12 or E24	89
3.18	Models of SH3-ADRA2A complex with HAERPPGPRR or RPPGPRRPER binding motif	90
3.19	Effect of ADRA2A phosphomimetics on Endophilin binding	91
3.20	Alignment of Endophilin binding motifs in Alix, ADRA2A, Itch and synaptojanin and resulting consensus sequence	95
5.1	Schematic drawing of vector backbones used	102

List of Tables

2.1	Comparison of existing methods to measure curvature sensitivity of proteins	28
2.2	Lipid-binding domains planned for this study	44
2.3	Purified lipid-binding domains	44
2.4	Soluble lipid-binding domains	47
2.5	Lipid-binding domains with corresponding lipid composition for NTA assays	51
2.6	Dose-response curve of ENTH vesiculation	54
3.1	GPCR ICL3 and adaptor protein PRD sequences tested by mutagenesis experiments	70
3.2	Summary of HADDOCK results for the two best SH3-Alix models	83
3.3	Summary of HADDOCK results for the two best SH3-ADRA2A models	88
5.1	Buffer recipes used in this thesis	99
5.2	Lipids used in this thesis	101
5.3	Constructs used in this thesis	103

List of Abbreviations

Abbreviation	Description
β -PIX	PAK-interacting exchange factor beta
Abl	Abelson tyrosine-protein kinase
ACF1	ATP-utilizing chromatin assembly and remodeling factor 1
ADP	adenosine diphosphate
ADRA2A	alpha-2A adrenergic receptor
ADRB1	beta-1 adrenergic receptor
ADRB2	beta-2 adrenergic receptor
AIR	ambiguous interaction restraints
AKT/PKB	protein kinase B
ALIX	ALG-2-interacting protein X
ALPS	amphipathic lipid packing sensor
ANTH	AP180 N-terminal homology
AP180	clathrin coat-associated protein AP180
AP2	adaptor protein complex 2
APPL1	adapter protein containing PH domain, PTB domain and leucine zipper motif 1
Arf1	ADP-ribosylation factor 1
ArfGAP1	ADP-ribosylation factor GTPase-activating protein 1
Arp2/3	actin-related protein 2/3
Atg14	autophagy-related protein 14
Atg3	autophagy-related protein 3
Atg8	autophagy-related protein 8
BAIAP2	brain-specific angiogenesis inhibitor 1-associated protein 2

BAR	Bin/Amphiphysin/Rvs
BAR-PH	Bin/Amphiphysin/Rvs pleckstrin homology
BARX	extended BAR
BATS	Barkor/Atg14(L) autophagosome targeting sequence
BAX	Bcl2-associated X protein
Bcl2	B-cell lymphoma 2
Bif-1	Bax-interacting factor 1
BTK	Bruton's tyrosine kinase
CAH	central amphipathic helix
CALM	clathrin assembly lymphoid myeloid leukemia
Cbl	casitas B-lineage lymphoma
CCP	clathrin-coated pit
CCV	clathrin-coated vesicle
CIE	clathrin-independent endocytosis
CIN85	Cbl-interacting protein of 85kDa
Cip4	Cdc42-interacting protein 4
CLIC/GEEK	clathrin-independent carriers and GPI-enriched endocytic compartments
CME	clathrin-mediated endocytosis
CMOS	complementary metal-oxide semiconductor
COPI/II	coat protein I/II
cPLA2	cytosolic phospholipases A2
Crk	cancer/testis antigen 10 regulator of kinase
cryo-EM	cryo-electron microscopy
CSP	chemical shift perturbation
CYTH3	cytohesin 3
Dab2	Disabled homolog 2
DAG	diacylglycerol
DivIVA	septum site-determining protein DivIVA
DLS	dynamic light scattering
DMSO	dimethyl sulfoxide
DOPS	1,2-dioleoyl-sn-glycero-3-phospho-L-serine

EDTA	ethylenediaminetetraacetic acid
EEA1	endosome antigen 1
EGF	epidermal growth factor
EGFP	enhanced green fluorescent protein
EGFR	EGF receptor
ENTH	epsin N-terminal homology domain
ER	endoplasmic reticulum
ESCRT	endosomal sorting complex required for transport
F-BAR	Fes/Cip4 homology Bin/Amphiphysin/Rvs
FAK	focal adhesion kinase
FBP17	formin-binding protein 17
FCHo2	F-BAR domain only protein 2
FEME	fast endophilin-mediated endocytosis
FERM	4.1, ezrin/radixin/moesin
Fes	feline sarcoma
FTLA	finite track length adjusted
FX	fragment exchange
FYVE	Fab1, YOTB, Vac1, EEA1
GAK	G-associated kinase
GAP	GTPase-activating protein
GFP	green fluorescent protein
Gla	γ -carboxyglutamate-rich
GMAP-120	galanin message-associated peptide
GPCR	G-protein coupled receptor
GPI	glycosylphosphatidylinositol
GRAF1	GTPase regulator associated with focal adhesion kinase 1
GRAM	glucosyltransferase, rab-like GTPase activators and myotubularins
Grb2	signal transducing adapter molecule 2
GRK3	G protein-coupled receptor kinase 3
GRP1	general receptor for phosphoinositides
GST	glutathione S-transferase

GUV	giant unilamellar vesicle
H0	helix zero
HADDOCK	high ambiguity driven protein-protein docking
HEPES	N-(2-Hydroxyethyl)piperazine-N'-(2-ethanesulfonic acid)
HGF	hepatocyte growth factor
HRS	hepatocyte growth factor-regulated tyrosine kinase substrate
Hsc70	heat shock cognate 70
HSQC	heteronuclear single quantum coherence
I-BAR	inverted Bin/Amphiphysin/Rvs
ICL3	intracellular loop 3
IF-BAR	inverse F-BAR
IMAC	immobilized metal ion affinity chromatography
IMD	IRSp53-MIM homology domain
ING2	inhibitor of growth protein 2
IPTG	isopropyl β -D-1-thiogalactopyranoside
IRS1	insulin receptor substrate 1
IRSp53	insulin receptor substrate protein of 53 kDa
ITC	isothermal titration calorimetry
Itch	E3 ubiquitin-protein ligase Itchy homolog
Kes1p	KrE11-1 Suppressor/Oxysterol-binding protein homolog 4
KRIT1	Krev interaction trapped protein 1
LPA	lysophosphatidic acid
LRRK2	leucine-rich repeat kinase 2
MARCKS-ED	effector domain of myristoylated alanine-rich C-kinase substrate
Met	hepatocyte growth factor receptor
MICALL1	molecule interacting with CasL protein like 1
MIM/MTSS1	missing in metastasis/metastasis suppressor protein 1
MTMR2	myotubularin-related protein 2
MTSSL1	metastasis suppressor 1 like
N-BAR	N-terminal helix and Bin/Amphiphysin/Rvs

NADPH	nicotinamide adenine dinucleotide phosphate
NCF4	neutrophil cytosol factor 4
Nck	non-catalytic region of tyrosine kinase adaptor protein 1
NECAP1	adaptin ear-binding coat-associated protein 1
Ni-NTA-DOGS	1,2-dioleoyl-sn-glycero-3-[(N-(5-amino-1-carboxypentyl)iminodiacetic acid)succinyl] (nickel salt)
NMR	nuclear magnetic resonance
NOE	nuclear Overhauser effect
NOESY	nuclear Overhauser effect spectroscopy
NTA	nanoparticle tracking analysis
Nup133	133 kDa nucleoporin
OXR1	oxidation resistance protein 1
PA	phosphatidic acid
PAK	p21-activated kinase
PC	phosphatidylcholine
PDZ	postsynaptic density protein 95, Drosophila discs large tumor suppressor and zonula occludens-1
PE	phosphatidylethanolamine
PE	phosphatidylethanolamine
PH	pleckstrin homology
PHD	plant homeodomain
PI	phosphatidylinositol
PI4P5KI γ	phosphatidylinositol-4-phosphate 5-kinase
PICK1	protein interacting with C kinase 1
PIK3C3	phosphatidylinositol 3-kinase catalytic subunit type 3
PIP	phosphatidylinositol
PKC	protein kinase C
PLC δ	1-phosphatidylinositol 4,5-bisphosphate phosphodiesterase delta-1
PMA	phorbol-12-myristate-13-acetate
PPII	polyproline helix type II

PRD	prolin-rich domain
PRE	paramagnetic relaxation enhancement
PROPPIN	β -propellers that bind polyphosphoinositides
PS	phosphatidylserine
PTB	phosphotyrosine binding
PX	phox homology
PX-BAR	phox homology Bin/Amphiphysin/Rvs
Rab5	Ras related protein
RF	radio frequency
RTK	receptor tyrosine-kinase
sfGFP	superfolder GFP
SGK3	serum/glucocorticoid-regulated kinase 3
SH3	SRC Homology 3
SH3GL1/2/3	SH3 domain-containing GRB2-like protein 1/2/3
SKAP55	Src kinase associated protein of 55kDa
SLiC	single liposome curvature
SNX1	sorting nexin 1
SpoVM	stage V sporulation protein M
Src	Rous sarcoma oncogene cellular homolog
SUMO	small ubiquitin-like modifier
SUV	small unilamellar vesicle
SV	synaptic vesicle
TCEP	tris(2-carboxyethyl)phosphine
TEMPO	2,2,6,6-tetramethyl-1-piperidinyloxy
TM	transmembrane
Tris	tris(hydroxymethyl)aminomethane
Ubl	ubiquitin-like
UVRAG	ultraviolet radiation resistance-associated gene protein
Vps15	vacuolar protein sorting-associated protein 15
Vps30	vacuolar protein sorting-associated protein 30
Vps34	vacuolar protein sorting-associated protein 34

Vps38	vacuolar protein sorting-associated protein 38
WDFY3	WD repeat and FYVE domain-containing protein 3
WDR45B	WD repeat-containing protein 45B
WIPI1	WD repeat domain phosphoinositide-interacting protein 1
WRP/srGAP3	WAVE-associated Rac GAP/slit-robo GAP3
wt	wild-type
Y2R	neuropeptide Y receptor Y2

Chapter 1

Introduction

1.1 Membrane curvature

1.1.1 Membrane shape

Eukaryotic cells are characterized by membranes with varied and dynamic compositions and topologies. Specialised cells like neurons or enterocytes (intestinal epithelial cells) have a highly defined and regulated shape in form of dendritic trees or microvilli. More generally, even in less specialised cells, the plasma membrane can harbour particular highly curved structures such as filopodia. In all eukaryotic cells, intracellular membrane compartments have a shape adapted to their function. Although some organelles, like lysosomes and peroxisomes can be spherical, other organelles display different shapes (Fig. 1.1A). The endoplasmic reticulum (ER) forms a network of interconnected tubes and sheets (Fig. 1.1B), the Golgi consists of stacks of perforated membranes (Fig. 1.1C) while mitochondria form a tubular system (Fig. 1.1D). Even within organelles, membranes can take a specialised shape, for example cristae of the inner mitochondrial membrane (Fig. 1.1E) or interconnected thylakoid stacks in chloroplasts.

Although some of those structures are stable over time, most are highly dynamic, being remodelled not only during cell division, growth or migration but also at steady state, as in trafficking. Changes can occur locally, by bending or extending a tube from a flat membrane (Fig. 1.1F). Alternatively, more profound changes can modify the topology of membranes. Topological remodelling occurs through membrane fusion and fission, for example fusion between ER tubules creating three-way junctions.

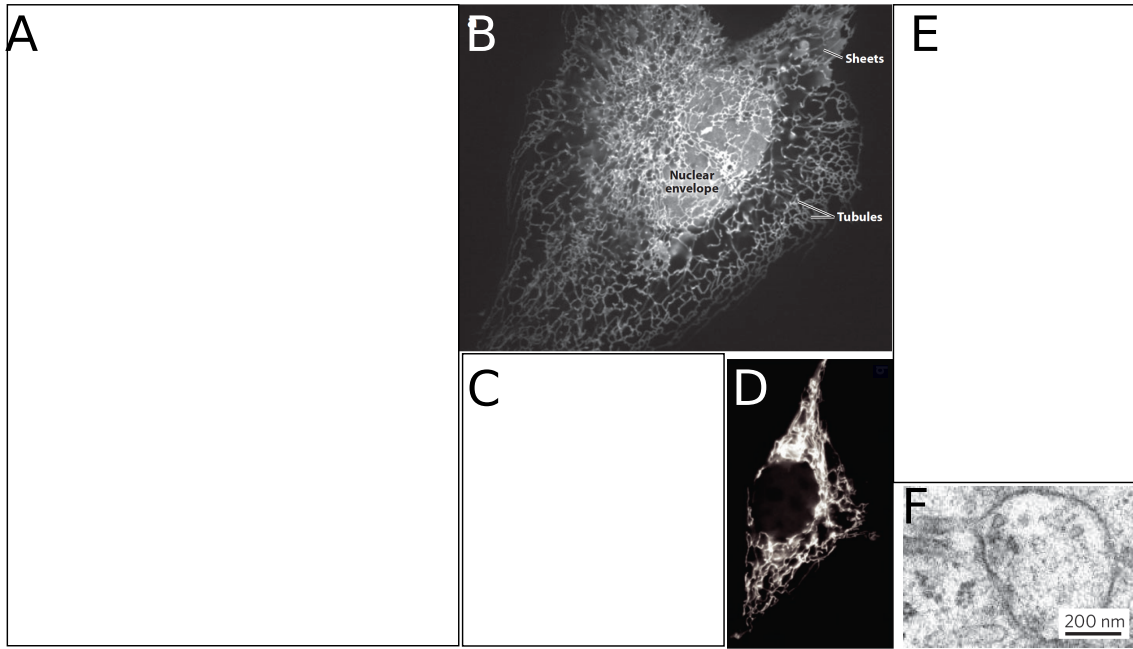


Figure 1.1: Membrane curvature in cellular structures. A. Cell. B. ER tubes and sheets. C. Perforated Golgi membranes. D. Mitochondrial tubular network. E. Mitochondria inner structure. F. Tube extending from endosome. A, C, E were taken from [1], B from [2], D from [3], F from [4] and were reproduced with permission.

1.1.2 Generation of high membrane curvature

Formation and remodelling of membrane structures requires changes in membrane curvature. Positive curvature corresponds to convex structures and negative curvature to concave structures (Fig. 1.2).

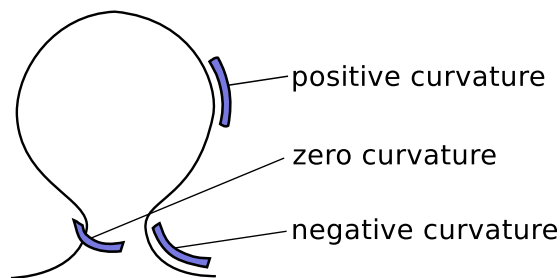


Figure 1.2: Curvature topology on an endocytic vesicle.

Several mechanisms have been described for generation of high membrane curvature (Fig. 1.3) [4, 2, 5]. Curvature can either be generated by processes intrinsic to the membrane and be mediated by lipids or integral or peripheral membrane proteins or curvature can be applied by cytosolic proteins binding transiently to membranes without insertion.

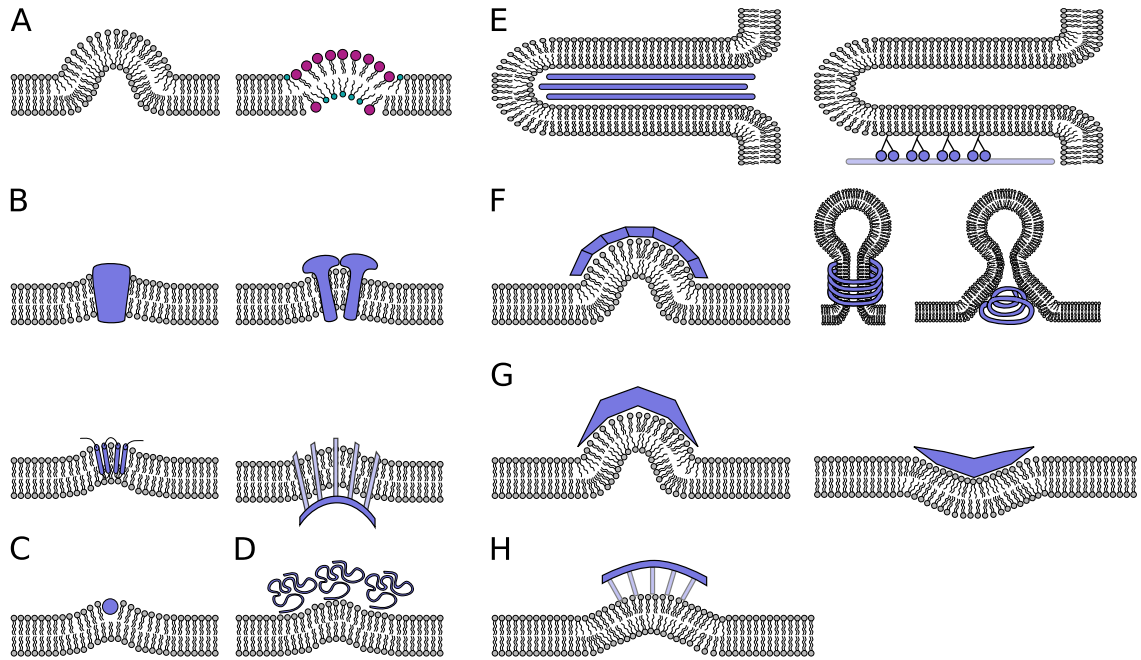


Figure 1.3: Mechanisms of cellular curvature generation.

A. Lipid asymmetry: lipid accumulation on one leaflet (left) or non-cylindrical lipids (right). B. Conical transmembrane proteins (top left), transmembrane proteins with large non-membrane domains (top right), hairpin membrane insertion (bottom left), clustering of transmembrane proteins (bottom right). C. Shallow insertion in one leaflet. D. Protein crowding. E. Cytoskeleton pushing (left) or pulling *via* molecular motors (right). F. Oligomerisation of flat monomers (left) into helical structures around (middle) or inside (right) the constriction. G. Crescent-shape protein dimers with positive (left) or negative (right) curvature. H. Indirect scaffolding. Adapted from [4, 6, 7]

Membrane-intrinsic mechanisms

The first mechanism is driven by asymmetry between the two membrane leaflets (Fig. 1.3A). One possible source of lipid asymmetry comes from the action of flippases that transport lipids between leaflets [8, 9]. Accumulating lipids in one leaflet over the other can drive membrane bending (Fig. 1.3A, left). For example, given a 5 nm membrane thickness, a 50 nm vesicle would contain 56 % more lipids on the outer than the inner leaflet [4].

The relative volumes of headgroup and acyl chain of each lipid also influence their curvature generating properties. Cylindrical lipids with similar sizes of headgroups and acyl chains like phosphatidylcholine (PC) can form stable planar bilayers [10]. On the other hand, lipids with headgroups smaller than their acyl chains like phosphatidylethanolamine (PE) or phosphatidic acid (PA) favour negative curvature while lipids with opposite properties, larger headgroup than acyl chain like lysophosphatidic acid (LPA), prefer positive curvature. An alteration of membrane curvature can therefore occur by changing lipid properties,

modifying the size of the lipid headgroup using enzymes [11], like interconverting LPA and PA using phospholipase A₂ or lysophosphatidic acid acyl transferase [12, 13, 14] (Fig. 1.3A, right).

Besides the distribution and composition of lipids, curvature can also be achieved by full or partial insertion of protein into the membrane. Curvature can be imposed by conical-shaped integral membrane proteins or transmembrane proteins with large non-membrane domains (Fig. 1.3B, top left and right). For example, the transmembrane region of nicotinic acetylcholine receptors or voltage dependent K⁺ channels is conical [15, 16] and these receptors accumulate in areas of higher membrane curvature [17, 18]. To efficiently generate high local curvature (30-50 nm diameter) at physiological concentrations, integral membrane proteins would need to have a highly conical shape, seldom achieved except in rare cases for proteins with hairpin insertions in the membrane like caveolins [19] (Fig. 1.3B, bottom left). Alternatively, clustering of transmembrane receptors *via* attachment proteins would also further increase local membrane curvature [20, 21] (Fig. 1.3B, bottom right).

Shallow protein insertions in only one leaflet, down to the interface between headgroup and acyl chain, will push headgroups apart and consequently wedge the surrounding acyl chains apart (Fig. 1.3C) [22]. An accumulation of such insertions in close proximity will generate membrane curvature. This has been calculated and experimentally measured for several amphipathic helix-containing proteins such as α -synuclein [23], ENTH (Epsin N-terminal homology domain) [24, 25] or N-BAR (N-terminal helix and Bin/Amphiphysin/Rvs) domain proteins like Endophilin [26, 27]. Insertion of hydrophobic loops or segments can also generate membrane curvature, as seen with the tandem C2 domains of Synaptotagmin1 [28, 29] or with reticulons and DP1/Yop1 family proteins [30]

More recently, a new mechanism has been proposed, where collisions between membrane-tethered proteins generates sufficient lateral pressure to bend the membrane [31] (Fig. 1.3D). In this case, close proximity of membrane-tethered proteins is necessary and sufficient to induce membrane curvature, without need of insertion into membranes. The authors showed that in their *in vitro* system, a protein coverage above 20 % was sufficient to bend membranes and targeting to the membrane could be achieved either by insertion of a helix into the membrane or by binding specific lipid headgroups. For example, targeting enough His-GFP to giant unilamellar vesicles (GUV) containing Ni-bound lipids (Ni-NTA-DOGS) was sufficient to generate tubules. Pushing this hypothesis further, the same group showed that intrinsically disordered proteins, when targeted to membranes, were powerful curva-

ture generators, as they occupy a larger hydrodynamic volume than a globular protein of similar molecular weight, as shown for the C-terminal domains of Epsin and AP180 [32].

Membrane-extrinsic mechanisms

Membrane curvature can also be generated by forces imposed by the cytoskeleton and molecular motors or by the interaction, without insertion, of cytosolic proteins with the membrane. Polymerisation of the cytoskeleton itself can generate membrane curvature (Fig. 1.3E, left), for example, actin filaments are involved in the formation of filopodia, pseudopodia, phagocytic cups and axonal growth cones [33, 34, 35, 36]. Moreover, the cytoskeleton can also generate stable curved membrane regions through motor proteins (Fig. 1.3E, right). During the cytokinesis step of cell division, actin rings form at the membrane between the two future daughter cells. Contraction of the rings by the action of myosin II forms a furrow where later on, membrane fusion will occur to separate the two daughter cells [37]. Pulling membranes along microtubules, connected through proteins of the kinesin and dynein family [38] can extend tubules. This has been implicated in formation of the ER tubular network [39, 40].

Peripheral membrane proteins can deform membranes by forming a curved scaffold around them. This can take several forms. Polymerisation of straight monomers into helical oligomers can drive membrane curvature generation (Fig. 1.3F, left). Oligomerisation can occur around the necks of the membrane being constricted, as is the case for dynamin at the neck of endocytic vesicles [41, 42, 43] (Fig. 1.3F, middle). Alternatively, proteins oligomerising inside the constriction, as is the case for ESCRTs (endosomal sorting complexes required for transport) [44], mediate budding away from the cytoplasm, inside multivesicular bodies [45, 46, 47] or towards the extracellular space for virus budding [48, 49, 50] as well as cytokinesis [51, 52, 53] (Fig. 1.3F, right).

Crescent-shape protein dimers can also provide scaffolding sufficient to bend membranes (Fig. 1.3G). Bin/Amphiphysin/Rvs (BAR) domains are typical examples for this category of protein and define a superfamily of proteins [54]. BAR domains are elongated helical domains with various inherent curvatures, ranging from very positive (BAR and N-BAR like Arfaptin, Endophilin, Amphiphysin) (Fig. 1.3G, left), shallow positive (F-BAR like FCHo2) to negative or inverted (I-BAR like IRSp53) [55, 56, 57] (Fig. 1.3G, right). Addi-

tion of those proteins onto artificial membranes generates tubules, as seen for example with Arfaptin2 [58] and FCHo2 [56], or tubules with inverted geometry with IRSp53 [59, 60].

In the two previous examples of scaffolding generating membrane curvature, the curved protein oligomers or dimers bound directly to the membrane. However, curved coats can also generate membrane curvature by binding indirectly, *via* adaptor proteins, to the membrane (Fig. 1.3H). This is the case for clathrin, COPI and COPII protein coats [61, 62]. Clathrin itself has no affinity for membranes, however other proteins like Epsin, CALM (clathrin assembly lymphoid myeloid leukemia) or amphiphysin bridge it to the membrane.

It is worth noting, that in a majority of cases, more than one mechanism is involved in generating curvature. For example N-BAR domains like the one of Endophilin or Amphiphysin consist of both an amphipathic helix and a BAR domain [26, 58]. Both the H0 amphipathic helix of Endophilin as well as the BAR domain were shown to be involved in generating membrane curvature [63, 27], although the importance of H0 for curvature generation has been contested [64]. In addition, Endophilin and other BAR-domain proteins have also been shown to form striations on membrane tubules [65], so oligomerisation might be an additional force for curvature generation. Epsin was shown to curve membranes both through insertion of its N-terminal amphipathic helix [24] and a crowding effect enhanced by its intrinsically disordered C-terminal region [32], although H0 insertion was shown to contribute more than crowding [5].

1.1.3 Sensing membrane curvature

To maintain cellular homeostasis, biochemical reactions need to happen at the right place at the right time. The diverse shapes of membranes present in a cell offer, in addition to lipid composition, an additional mechanism to spatiotemporally control reactions happening at cellular membranes. For example, during clathrin-mediated endocytosis, as formation of the bud into a vesicle progresses, different curvatures are generated and are indicative of how far clathrin-mediated endocytosis has progressed. This could fine-tune the timing of protein recruitment for curvature-sensitive proteins.

Two main mechanisms by which proteins can sense membrane curvature have been described (Fig. 1.4) [58, 66, 67, 68, 6]. One of the mechanisms relies on scaffolding. There, a curved, positively charged, protein surface will preferentially bind a negatively charged membrane surface of corresponding curvature, as this would maximise interaction energy.

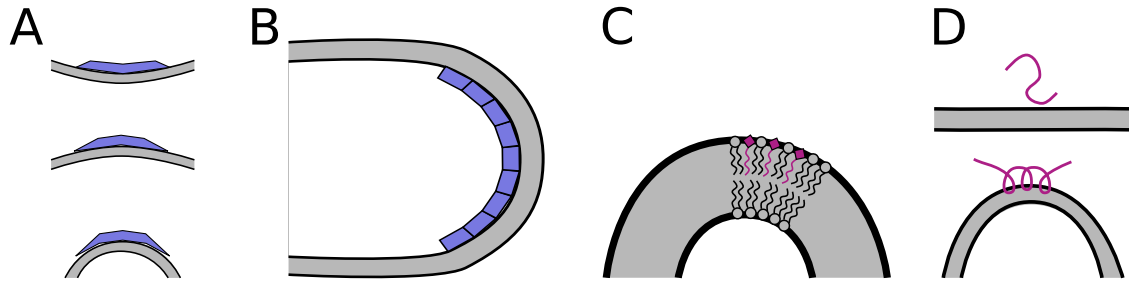


Figure 1.4: Mechanisms of cellular curvature sensing.

A. Scaffolding by crescent-shape proteins. B. Scaffolding by oligomers of flat monomers. C. Hydrophobic insertions in lipid packing defects. D. Folding of amphipathic helix onto curved membrane. Adapted from [66]

Crescent-shaped BAR domains, in addition to their curvature generation activities described above, can also preferentially bind membranes of similar curvature as has been shown for Endophilin BAR binding on highly curved liposomes [26] or MTSSL1 (metastasis suppressor 1 like) I-BAR on negatively curved membranes [69] (Fig. 1.4A).

Curvature sensing by scaffolds can also happen for proteins forming curved oligomers (Fig. 1.4B). For example, at low concentrations, Dynamin helices assemble on the neck of vesicles, an area of high curvature [70, 71]. In the gram-positive bacteria *B. subtilis*, DivIVA oligomers specifically localise to areas of the cell with negative curvature, cell poles and polar septum during cell division [72, 73, 74].

Curved protein scaffolds can sense various curvatures ranging from very high positive curvatures to negative curvatures. An alternative mechanism, specific for highly curved membrane surfaces, consists of asymmetric hydrophobic insertions (Fig. 1.4C). Curved membranes formed of cylindrical lipids or substantial amounts of conical lipids or lipids with mono-unsaturated acyl chains in flat membranes generate lipid packing defects [75, 76]. Lipid packing defects result from a geometrical mismatch between lipid and membrane shape [75] and correspond to areas of lower lipid density.

Typical motifs for curvature sensing using hydrophobic insertions are amphipathic helices. Amphipathic helices are disordered in solution but fold into a helix when in contact with membranes (Fig. 1.4D) [24, 77, 26]. They lie flat, parallel to the membrane at the depth of the phosphate-glycerol backbone [26, 78, 79, 80]. A well studied example of curvature-sensing amphipathic helices are ALPS (amphipathic lipid packing sensors) found in several proteins of the early secretory pathway, for example the nucleoporin Nup133, the sterol-binding protein Kes1p, the golgin GMAP-120 [81] or ArfGAP1 (ADP-ribosylation factor

GTPase-activating protein 1) [82]. ArfGAP1 activation of GTP hydrolysis by Arf1 is essential for COPI coat disassembly [83, 84, 85]. This process should however only happen once the vesicle is fully formed and mature. A good indicator of vesicle maturation is its shape and therefore curvature. ArfGAP1 affinity for membranes [86] and resulting activity increase dramatically for small vesicles (smaller than 100 nm diameter) [82], a size similar to that of typical coated vesicles. During coat assembly and vesicle maturation, Arf1-GTP is protected from hydrolysis as the affinity of ArfGAP1 for flat membranes is weak. Once the vesicle reaches a critical size, ArfGAP1 is recruited *via* its ALPS motif, triggering GTP hydrolysis and coat disassembly. This is an elegant way to spatiotemporally control a biochemical process.

The amphipathic helix formed by ALPS has a hydrophilic face with few charged residues, mostly serines and threonines [77, 81, 87, 88] and a hydrophobic face with large hydrophobic residues [86]. Other curvature sensing amphipathic helices with different properties have been described. The N-terminus amphipathic helix of α -Synuclein has large, charged residues like lysines on its hydrophilic face and small hydrophobic amino acids as well as threonines on its hydrophobic face [89, 90]. The *B. subtilis* protein SpoVM that binds to the positively curved forespore has a central proline residue that introduces a kink in the helix [91].

A common feature of curvature-sensing amphipathic helices is their unusual properties compared with other amphipathic helices [67]. The absence of charged residues on the hydrophilic face of ALPS and its insensitivity to the presence of charged lipids suggest that binding is driven by hydrophobic interactions. Interestingly, introducing charged amino acids on the hydrophilic face of ALPS increases its affinity but decreases its curvature sensing ability by increasing its affinity for flat membranes [81]. Introducing hydrophobic residues on the hydrophobic face of α -Synuclein increases its affinity but reduces its curvature sensitivity [92]. This suggests a mechanism by which hydrophobic insertions contribution to curvature sensing must exceed affinity for flat membranes provided by electrostatics [92].

Hydrophobic insertions not related to amphipathic helices can also provide curvature sensitivity. Synaptotagmin1 C2 domains [28] or a cyclic peptide derived from loop 3 of Synaptotagmin1 C2B domain [93] preferentially bind small liposomes. Alkyl chains attached to proteins as in the geranylgeranylated G β 1 γ 2 or a C16-chain covalently attached to ovalbumin can also act as curvature sensors [94]. Curvature sensing can also be observed in the

accumulation of conical transmembrane proteins like cytochrome *b5* [95] or GPCRs [96] in regions of higher membrane curvature.

More than one curvature sensing module can be present as is the case for N-BAR domains [68, 97, 60] although one study argues that only the amphipathic helix is responsible for curvature sensing [98] as N-BAR, F-BAR and I-BAR proteins tested all preferentially bound to small liposomes. N-BAR contain a typical amphipathic helix, but presence of amphipathic helices has also been reported in other BAR and I-BAR proteins [97, 60, 98]. A different way of combining curvature sensing modules was found in the lipid kinase Vps34/PIK3C3 (Phosphatidylinositol 3-kinase catalytic subunit type 3). This protein can form multiple complexes with a three-dimensional Y-shaped structure [99]. Complex I formed of Vps34, Vps15, Vps30 and Atg14 is active in autophagy and complex II, where Atg14 is replaced by Vps38, is important in endocytic sorting. Whereas complex II was active both on Giant Unilamellar Vesicles (GUVs), and Small Unilamellar Vesicles (SUVs), complex I activity was restricted to SUVs. Both complexes bind lipids through the Vps34 kinase located at the tip of one of the arms of the Y, however complex I also has an ALPS-like amphipathic helix in the BATS domain of Atg14 (absent in complex II, replaced by Vps38) situated at the tip of the other arm of the Y. This shape might accommodate smaller liposomes better than flat membranes. A combination of ALPS and three-dimensional structure of a protein complex might explain the specific activity for complex I on SUVs only.

Finally, it is worth noting that several proteins can act both to sense curvature as well as generate tubules or vesicles (Endophilin N-BAR [26], FCHo2 F-BAR [58], I-BAR [59, 100]). Dynamin is both a curvature sensor at low concentration [70, 71] and a generator at high concentration [101]. Curvature sensing and generation might be two faces of the same principle where protein concentration, affinity for membranes and protein/lipid ratio dictate which phenomenon dominates.

1.2 Lipid-binding domains

1.2.1 BAR domains as curvature sensors and generators

BAR domains were first identified as a conserved domain in Bin/Amphiphysin/Rvs [102, 65, 58] and are involved in membrane binding, curvature sensing or generation. Crystal

structures for several BAR domains have been solved and show a conserved architecture of three kinked helices forming a coiled coil. BAR domains exist as weak dimers in solution [58, 26, 56], although subnanomolar affinity for Endophilin dimers has also been reported [103]. Upon dimerisation, BAR domains form a six-helix bundle with a curved positively charged surface (Fig. 1.5). This crescent-shaped surface binds negatively charged membranes. Several classes of BAR domains were identified based on the curvature or the dimer, ranging from very concave (classical BAR), shallow concave (F-BAR) to convex (I-BAR) (Fig. 1.5, top). Additional features like amphipathic helices (N-BAR) or additional lipid-binding domains (Pleckstrin homology PH in BAR-PH or Phox homology PX in PX-BAR) were also identified in some members of the BAR domain superfamily (Fig. 1.5, bottom).

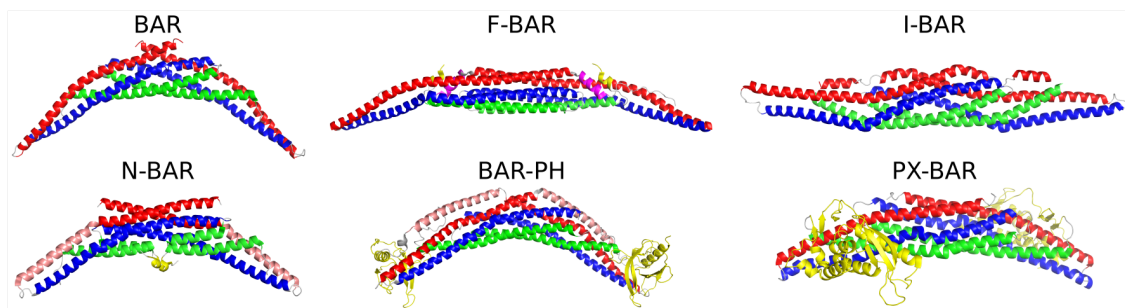


Figure 1.5: BAR domains overview.

BAR domains can sense membrane curvature by preferentially binding to liposomes of a specific diameter range [58, 26, 69]. They have also been shown to induce tubulation or vesiculation [58, 26]. The rigidity of the BAR domain is essential for curvature generation as no tubulation was observed in an Endophilin mutant with increased flexibility in the arms of the BAR domain [104]. N-BAR domains present an unstructured N-terminus that folds into an amphipathic helix, called H0, upon membrane binding [26]. Presence of an additional amphipathic helix with a large positively-charged hydrophilic face and a large hydrophobic face in N-BAR domains confers additional affinity for membranes [58, 65, 105] by lowering the k_{off} [65] in membrane binding. *In vitro*, the H0 helix is not necessary for vesiculation by Endophilin or Amphiphysin [58, 64] and tubulation was still present in H0 deletion mutants albeit at higher protein concentrations. However, increasing the number of amphipathic helices per BAR domain was shown to favour vesiculation over tubulation and to generate vesicles of smaller sizes [106]. After deletion of H0, BAR curvature sensitivity increased as seen for Endophilin [26] and Amphiphysin [58], although

a different assay shows that curvature sensitivity is entirely mediated by the amphipathic helix [98].

F-BAR domains are characterised by a shallower concave membrane-interaction surface (Fig. 1.5). Addition of F-BAR on liposomes induced tubulation. The size of tubules varied from 20 to 70 nm diameter for FCHo2 depending on the protein concentration [107]. In the case of Cip4, tubules were larger and with a more homogeneous diameter of 60-80 nm [108]. Tubules induced by overexpression of F-BAR in mammalian cells had a larger diameter than tubules resulting from overexpression of N-BAR proteins [108]. This supports a mechanism of curvature generation based on scaffolding. Ordered protein arrays on lipid tubules have been observed for several F-BAR proteins [107, 109, 110] and cryo-EM studies on FBP17 (Formin-binding protein 17) showed the importance of both tip-to-tip interactions as well as lateral contacts for formation and stabilisation of a helical structure [108].

Unlike other BAR domains, I-BAR form a convex surface and have been shown to bind [100, 69] and stabilise negative membrane curvature *in vitro* as well as *in vivo* [59]. Overexpression of IRSp53 I-BAR induced extracellular instead of intracellular tubules (as observed for N- and F-BAR) [111] and addition of the same construct on lipid vesicles induced invaginations towards the inside of the liposome [59].

Several BAR domain proteins also contain an additional lipid-binding domain, Pleckstrin homology (PH) or Phox homology (PX), both specific for phosphoinositides. Combining a curvature-sensing module (BAR) with a phosphoinositide-specific one (PH or PX) would provide coincidence detection not only for a membrane compartment of given lipid composition but also for particular microdomains with a specific curvature [112]. Sortin Nexin 1 (SNX1) is formed of a PI(3)P/PI(3,5)P₂ specific PX domain followed by a high curvature specific BAR domain. Functionality of both domains was required for correct targeting of SNX1 to tubular structures of the early endosome and for working endosome to *trans*-Golgi network trafficking [112]. Coincidence detection might also occur for BAR-PH domain although this is less understood: in APPL1, the PH residues usually involved in phosphoinositide binding are not conserved [113] although the PH domain still binds phosphoinositides [114].

With their functions of membrane curvature sensing and generation, BAR domains are especially useful in trafficking processes. During clathrin-mediated endocytosis, shallow

curved FCHo1/2 proteins are recruited at early stages and were proposed to sculpt the initial bud site [107, 115]. At later stages, N-BAR domains with higher curvatures, Endophilin and Amphiphysin, are recruited to clathrin-coated pits with Dynamin [116] and cooperate with Dynamin in vesicle scission [116, 117]. BAR domain proteins have also been involved in clathrin-independent endocytosis. The BAR-PH containing protein GRAF1 (GTPase Regulator Associated with Focal Adhesion Kinase 1) remodels membrane in the tubulovesicular CLathrin-Independent Carriers and GPI-Enriched Endocytic Compartments (CLIC/GEEC) endocytosis pathway [118] involved in internalisation of bacterial toxins, GPI-anchored proteins and extracellular fluid. Endophilin is also involved in uptake of Shiga and Cholera toxins in a clathrin-independent pathway [119]. Recently, our group described a novel Endophilin dependent endocytic pathway called Fast Endophilin Mediated Endocytosis (FEME). This pathway is responsible for ligand-triggered uptake of G-Protein Coupled Receptors (GPCRs) and Receptor Tyrosine Kinase (RTKs) at the leading edge [120] and the uptake of Cholera and Shiga toxins [119]. In this pathway, Endophilin can bind cargo receptors through its C-terminal SH3 domain, induce membrane curvature through its BAR domain and facilitate membrane fission with its multiple amphipathic helices [106] in collaboration with Dynamin [116].

Other processes also make use of the BAR domains properties on membranes. Transverse tubules (T-tubules) are narrow tubes extended from the plasma membrane in skeletal and cardiac muscles [121] involved in muscle contraction. Their formation is dependent on BAR domain proteins. In *Drosophila melanogaster* with mutations in Amphiphysin, the T-tubule network is severely disorganized and the flies are flightless [122]. In mammals, missense mutations in the BAR domain of Amphiphysin2 disrupting tubulation in cells cause autosomal recessive centronuclear myopathy [123]. Similarly, initiation of the formation of dendritic spines, post-synaptic protrusions of excitatory synapses, is reliant on the I-BAR protein MIM/MTSS1 (Missing In Metastasis/Metastasis Suppressor protein 1) [124]. MIM binds PIPs-rich membranes [59] and deforms the membrane into proto-protrusions prior to Arp2/3-complex actin polymerisation [124]. A similar phenomenon was observed for WAVE-associated Rac GAP/slit-robo GAP 3 (WRP/srGAP3), an inverse F-BAR (IF-BAR) domain protein (F-BAR with properties similar to I-BAR in terms of convex shape and induction of "inverse" tubules). srGAP3 forms on dendrites a bud where spine precursors emerge and deletion of srGAP3 resulted in impaired long-term memory in mice [125].

1.2.2 Non-BAR lipid-binding domains

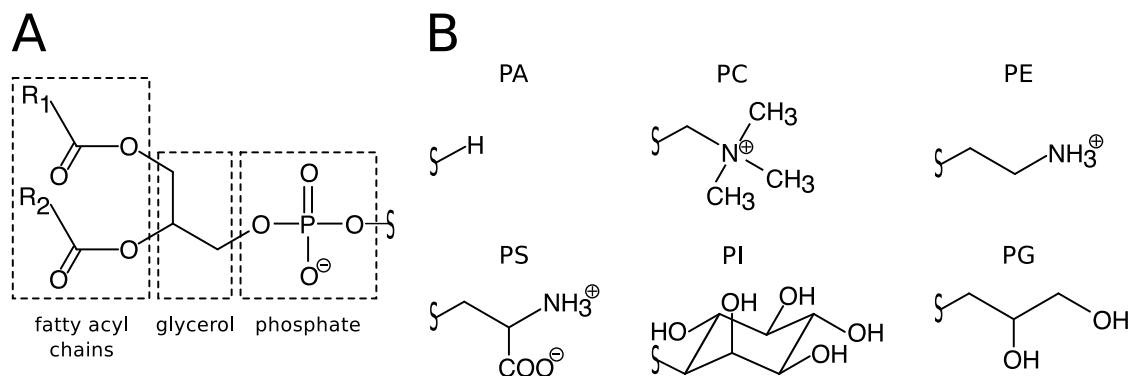


Figure 1.6: Structure of phospholipids. A. General structure. B. Common lipid head-groups.

Recruitment of proteins on membranes is essential for processes as diverse as maintaining cell and organelle shape, trafficking or signalling. Cellular membranes are composed of several thousands different phospholipids and other lipids. The main phospholipid head-groups are phosphatidylcholine (PC), phosphatidylethanolamine (PE), phosphatidylserine (PS), phosphatidic acid (PA) and phosphatidylinositol (PI) (Fig. 1.6) [126]. In addition, lipids with different backbones (non phospholipids), sterols or sphingolipids, are also present. The lipid composition varies between membranes of different organelles and presence of specific lipid headgroups, especially differentially phosphorylated PI (PIPs) marks specific membrane compartments [127]. Recognition of specific lipid headgroups or of membrane properties (like charge) is essential for correct targeting and function of peripheral membrane proteins. Several lipid binding domains with varied lipid specificity have evolved (Fig. 1.7). Phosphoinositides can be specifically recognised by domains like PH [128, 129], PTB [130, 131], GRAM [132], FERM [133, 134], PX [135, 136, 137, 138], FYVE [139, 140, 141], PHD [142, 143], PROPPIN [144], PDZ [145], ENTH [24, 146], ANTH [147, 148], whereas some are specific for DAG (C1 [149]) or PS and negatively charged membranes (C2 [150], annexin [151], Gla [152], Discoidin C2 [153]).

Pleckstrin Homology (PH) domain was first identified in the N-terminus of pleckstrin and was shown to bind PI(4,5)P₂ [128]. A crystal structure of PLC δ -PH in complex with IP(3,4,5)P₃, the headgroup of PI(4,5)P₂, identified the phosphoinositide binding site [154] as a pocket formed by the β 1- β 2 loop with sequence motif KXn (K/R)XR (Fig. 1.7A) [155]. Some PH domains, (Bruton's tyrosine kinase BTK [156, 157], General Receptor for Phosphoinositides 1 GRP1 [158], Protein Kinase B PKB/AKT [159]) are very spe-

cific for the second messengers PI(3,4,5)P₃ or PI(3,4)P₂ produced after activation of cell surface receptors and PI3K [160]. The high selectivity and affinity of these PH domains allows specific targeting to membranes containing PI(3,4,5)P₃ or PI(3,4)P₂, despite the higher concentration of PI(4,5)P₂ [161]. Although some PH domains have high affinity for phosphoinositides, genome-wide studies in yeast showed that most do not bind phosphoinositides strongly [162].

Phosphotyrosine binding (PTB) domains specifically bind peptides with phosphorylated tyrosines [130]. Though uncommon, some PTB domains interact with PIPs [163, 164, 165]. PTB are structurally similar to PH domains, the main difference being the presence of a helix between β 1 and β 2 strands, a feature of PTB domains. One side of this helix forms the PIPs binding site [163] (Fig. 1.7B). GRAM (Glucosyltransferases, Rab-like GTPase activators and Myotubularins) domains also share a similar three-dimensional structure with PH domains [166] and are specific for PI(3)P and PI(3,5)P₂ [132] (Fig. 1.7C). FERM (4.1, ezrin/radixin/moesin) domains are found at the N-terminus of proteins that link the actin cytoskeleton to the plasma membrane. FERM domain consists of three subdomains and its subdomain C also has a PH/PTB fold [167] and binds PIPs. The PIPs binding site is however not in the PH/PTB fold but in a cleft between the additional C-terminal α -helix of subdomain C and subdomain A [167] (Fig. 1.7D). FAK (Focal Adhesion Kinase) is kept in an autoinhibited state by the FERM domains binding its catalytic domain [168, 169]. In a model of FAK activation by lipids, after formation of focal adhesions and activation of PI4P5KI γ lipid kinase, high local concentrations of PI(4,5)P₂ are synthesized and bind in the FERM domain, releasing autoinhibition [170].

Phox Homology PX domains were first identified in p40^{phox} and p47^{phox} subunits of NADPH oxidase complex [180]. Most PX domains are specific for PI(3)P [181] although some have preferences for other PIPs [182, 183, 184] but only few bind with high affinity [181]. The PX domain structure consists of three β -strands followed by four α -helices [182, 172]. The PIPs binding pocket is formed by β 1- β 2 loop and one of the helices (Fig. 1.7E). p47^{phox} has an additional binding pocket for phosphatidic acid that contributes to membrane binding [182].

FYVE (Fab1, YOTB, Vac1, EEA1) domains are zinc-finger domains specific for PI(3)P and are thus mostly found in endosomal, multivesicular body and phagosomal proteins [185]. A shallow PI(3)P binding pocket is formed by conserved basic residues on β 1 and provides almost all hydrogen bonds to PI(3)P (Fig. 1.7F) [185, 173]. In addition, hydrophobic

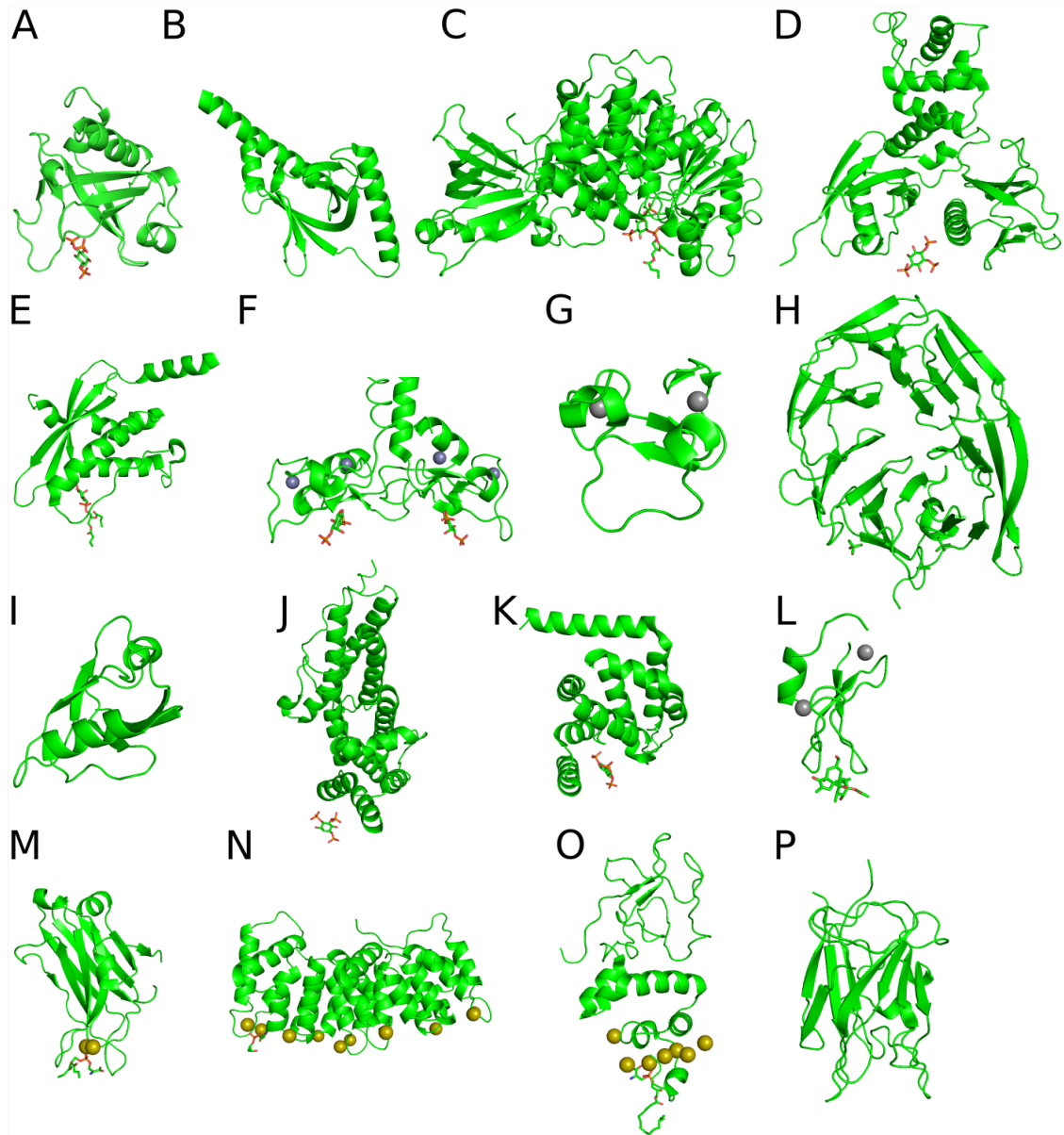


Figure 1.7: Overview of non-BAR lipid binding domains.

A. PH (1MAI) [154]. B. PTB (1M7E) [164]. C. GRAM (1ZVR) [171]. D. FERM (1GC6) [167]. E. PX (1H6H) [172]. F. FYVE (1JOC) [173]. G. PHD (2G6Q) [174]. H. PROPPIN (4AV9) [175]. I. PDZ (2PKU) [176]. J. ANTH (1HFA) [148]. K. ENTH (1H0A) [24]. L. C1 (1PTR) [177]. M. C2 (1DSY) [178]. N. Annexin (1A8A) [179]. O. Gl α (1NL2) [152]. P. Discoidin C2 (1CZS) [153]. The membrane-binding sites face down. Co-crystallised lipids or lipid headgroups are shown in sticks. Grey spheres represent Zn $^{2+}$ ions and yellow spheres Ca $^{2+}$ ions.

Adapted from [159]

residues in a loop penetrate in the bilayer [140]. FYVE domains are only efficiently targeted to endosomes as dimers, increasing the avidity by binding two PI(3)P molecules [186, 173] and EEA1 (Endosome Antigen 1) indeed includes a coiled-coil that allows dimerisation of the FYVE domain (Fig. 1.7F) [173]. A structurally related zinc-finger domain, Plant

Homeodomain PHD, present in several chromatin regulatory factors, has also been shown to bind PIPs in the nucleus and regulate activity of ING2 (inhibitor of growth protein 2) tumor suppressor (Fig. 1.7G) [142]. This has however been contested in a study showing that a polybasic region C-terminal of the PHD domain and not the PHD domain itself is responsible for PIPs binding and specificity [143].

PROPPIN (β -propellers that bind polyphosphoinositides) form a family of proteins involved in autophagy that bind PI(3)P and PI(3,5)P₂ with high affinity and selectivity [175, 187, 188]. PROPPIN form a seven-bladed β -propeller with two PIPs binding sites formed by charged and polar residues as well as each one of the arginines of the conserved FRRG loop (Fig. 1.7H), that was previously shown to be essential for membrane binding [144, 189]. Further affinity for membranes is provided by insertion of a hydrophobic loop [187, 190]. Phosphorylation of this loop following environmental stress abolishes membrane binding and promotes vacuole fusion in *P. pastoris* yeast [191].

PDZ (Postsynaptic density protein 95, *Drosophila* discs large tumor suppressor and zonula occludens-1) domains are commonly found in multi-domain scaffolding proteins and generally bind to the C-terminus of binding partners by augmentation of one β -sheet [192]. Several PDZ domains, up to 20% according to large-scale studies [193], have been found to bind PIPs and membranes through a cationic patch opposite the PDZ binding groove and a cysteine-rich loop in the case of PICK1 (Protein Interacting with C Kinase 1) (Fig. 1.7I) [176].

The N-terminal domains of several clathrin adaptor proteins, AP2 α -subunit [194], AP180 [147], CALM [148] (both have an AP180 N-terminal homology domain ANTH) and Epsin (Epsin N-terminal homology domain ENTH) [24] share a superhelical solenoid fold (Fig. 1.7J, K) and bind PIPs, mostly PI(4,5)P₂. ANTH interacts with PI(4,5)P₂ headgroup *via* a basic patch with low affinity (Fig. 1.7J) [194, 148], whereas the binding site on ENTH lies in a pocket formed in part by H0, the unstructured N-terminus that folds into an amphipathic helix upon membrane binding (Fig. 1.7K) and inserts into it, generating high curvature and inducing vesiculation [24, 25]. Although ENTH of Epsin, a protein active on the plasma membrane, preferentially binds PI(4,5)P₂, ENTH domains found in other proteins can have different lipid specificities. The ENTH domain of EpsinR, active at the trans-Golgi network, is specific for PI(4)P instead [195, 196].

C1 and C2 domains were named after the first and second conserved regions of protein kinase C (PKC). The C1 domain binds diacylglycerol (DAG) and thus is responsible for PKC activation [149], whereas the C2 domain provides calcium-dependent binding to PS [150]. C1 domain is a cysteine-rich zinc-finger domain formed of two β -sheets followed by an α -helix (Fig. 1.7L). C1 domains affinity for membranes comes from several mechanisms. DAG or its analogue phorbol ester bind in a cavity between the β -sheets [177] forming a hydrophobic surface that inserts into membranes [197, 198]. This brings a positively charged surface in contact with acidic lipid headgroups [199], providing additional non-specific electrostatic interaction.

C2 domains consist of eight β -strands organised in two four-stranded β -sheets (Fig. 1.7M) [200]. Calcium ions bind in loops through acidic residues, inverting the electrostatics of this region, thereby allowing binding to negatively charged lipid headgroups [201, 202]. Although C2 domains of conventional PKCs and Synaptotagmin bind PS, variations in the calcium-binding loops generate diversity of phospholipid selectivity. For example the C2 domain of cPLA2 binds zwitterionic PC instead [203, 204].

Conventional PKC isozymes (α , β I, β II, γ) contain both C1 and C2 domains and both are necessary for high-affinity membrane binding and release of autoinhibition of PKC [205]. This suggests a model where cytosolic PKC C2 domain binds Ca^{2+} , targeting PKC to the membrane with low-affinity [206]. PKC then diffuses on the membrane until the C1 domain binds DAG, providing high-affinity binding and activation of PKC [205]. In novel PKC (δ , ϵ , η , ϕ), the C2 domain does not bind calcium. Recruitment to membranes is then mediated by the C1 domain only, which has a two orders of magnitude higher affinity for membranes than conventional PKC C1 [207].

Several protein domains recognise PS *via* different mechanisms. Annexin core consists of generally four α -helical annexin repeats that can each bind up to three calcium ions through the loops linking the helices (Fig. 1.7N) [179]. Ca^{2+} ions are coordinated both by protein residues and phospholipids, bridging annexin to the membrane. With the calcium-dependence of membrane binding of most annexins, they have roles in diverse processes involving calcium, including vesicle trafficking, intracellular signalling, membrane repair and even display calcium-channel activities [208]. Gla (γ -carboxyglutamate-rich) domain is found in extracellular proteins involved in blood coagulation [209]. Similar to annexin, calcium ions are coordinated both by protein residues, in this case γ -carboxyglutamate, and phosphatidylserine (Fig. 1.7O) [152]. Unlike annexins and Gla, discoidin C2 domains,

structurally similar but unrelated to PKC C2 and found in coagulation proteins, bind PS in the absence of calcium (Fig. 1.7P) [153]. Affinity for membranes and specificity for PS are provided by a combination of insertion of hydrophobic loops, electrostatic interaction between positively charged residues and phosphate groups as well as specific contacts to the PS headgroup [153].

Spatiotemporal control of the recruitment of lipid-binding proteins to membranes is crucial for cellular homeostasis. Correct localisation to a cellular compartment can be easily achieved for lipid-binding domains with a strict requirement for the presence of a particular lipid headgroup, for example FYVE domains are targeted to PI(3)P-containing endosomes [185, 173]. Temporal control can be ensured in cases where synthesis of the preferred headgroup is regulated as is the case for PI(3,4,5)P₃-binding PH domains. Alternatively, for calcium-dependent lipid-binding domains, recruitment to the membrane is controlled by calcium influx into the cell. Since the discovery of lipid-binding domains, headgroup specificity and calcium-dependency have been extensively studied [210, 159, 211], however, except in a few isolated cases [28, 93, 212], little is known about curvature sensitivity of non-BAR lipid-binding domains and how it contributes to subcellular targeting and protein regulation.

1.3 Endocytosis and Endophilin

The plasma membrane delimits the boundary of the cell and organelles allow compartmentalisation of cellular processes, however regulated transport needs to occur across these membranes and between intracellular compartments. Ions and small molecules can cross membranes through proteic channels or transporters, but larger molecules, proteins and lipids require transport *via* transient vesicles. Endocytosis is a process by which cells take up essential nutrients, regulate cell-surface receptors and cell membrane area. It is also an entry pathway for bacterial toxins and viruses. The best characterised pathway is clathrin-mediated endocytosis (CME). During initiation of CME (Fig. 1.8A), localised membrane curvature is created, cargo is concentrated and scaffolding proteins are recruited by the action of F-BAR domain containing proteins and adaptor proteins [107, 213, 214, 215]. Clathrin is then recruited and assembles into a coat, while curvature of the CCP (clathrin-coated pit) increases (Fig. 1.8B). After formation of a clathrin-coated vesicle (CCV) (Fig. 1.8C), dynamin-induced scission releases the vesicle inside the cell

(Fig. 1.8D) [216]. The vesicle is then uncoated, whereby clathrin is disassembled through the action of heat shock cognate 70 (Hsc70) and either auxilin or cyclin G-associated kinase (GAK) [217] and adaptor proteins are removed after hydrolysis of PI(4,5)P₂ by synaptojanin [218, 219].

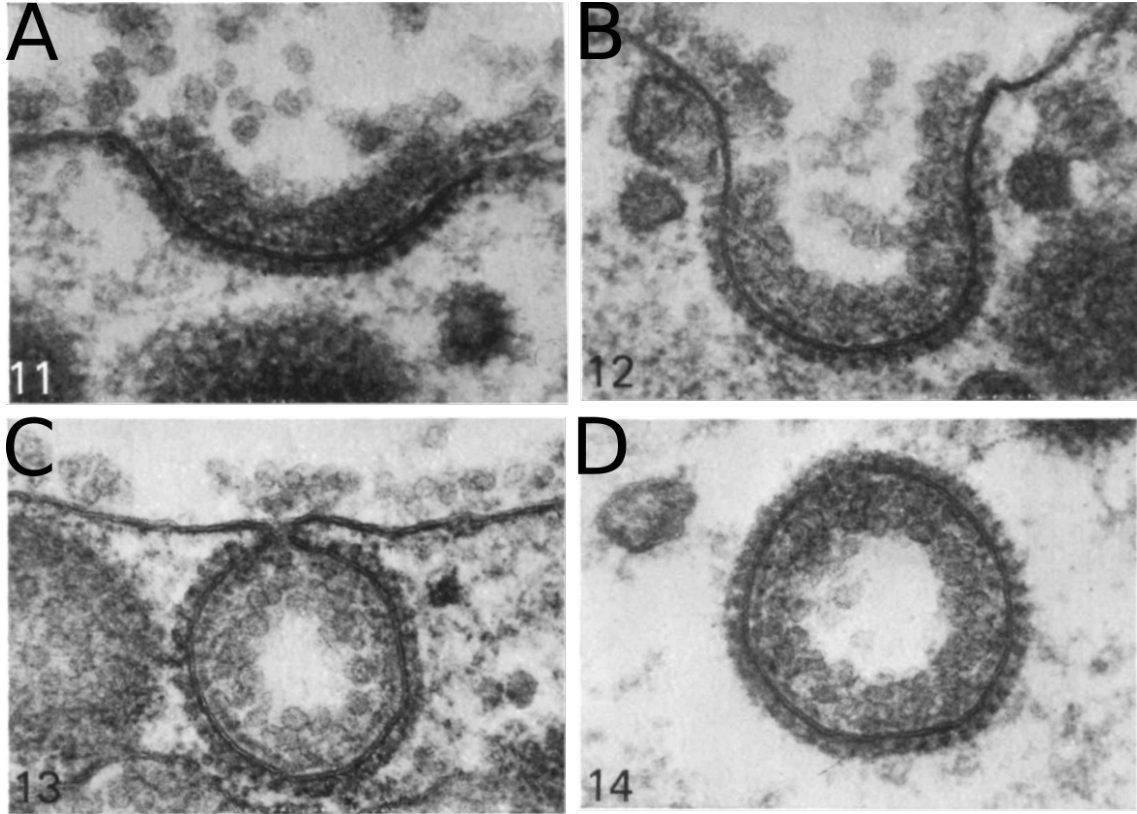


Figure 1.8: Clathrin-mediated endocytosis stages.

A. Initiation of clathrin-coated pit (CCP). B. Maturation of CCP. C. Membrane tethered clathrin-coated vesicle (CCV). D. Free CCV. (taken from [220] and reproduced with permission)

Membrane curvature generation and sensing are essential for endocytosis. BAR domains and amphipathic helices are two structural entities responsible for induction and recognition of membrane curvature and N-BAR domain proteins possessing both are involved in a variety of processes requiring membrane remodelling, one of these being endocytosis. Endophilin contains, in addition to its N-BAR domain, an additional central amphipathic helix (CAH), formed by a section of helix 1 (H1I) of the BAR domain (Fig. 1.9A). The N-BAR domain is followed by a variable region containing several phosphorylation sites [221, 222] and an SH3 (Src homology 3) domain mediating protein-protein interaction by binding proline-rich sequences (Fig. 1.9B). Endophilin proteins form two subfamilies, A and B, with similar overall structures, although H0 and the loop between helix 2 and 3 are longer in Endophilin B than A [223]. Endophilin A1, A2 and A3 are associated with

processes on the plasma membrane whereas Endophilin B1 and B2 mostly act on intracellular organelles [224, 225, 226]. Endophilin A2, B1 and B2 are expressed in most organs whereas Endophilin A1 is the brain-specific isoform and Endophilin A3 is expressed both in brain and testes [227, 228].

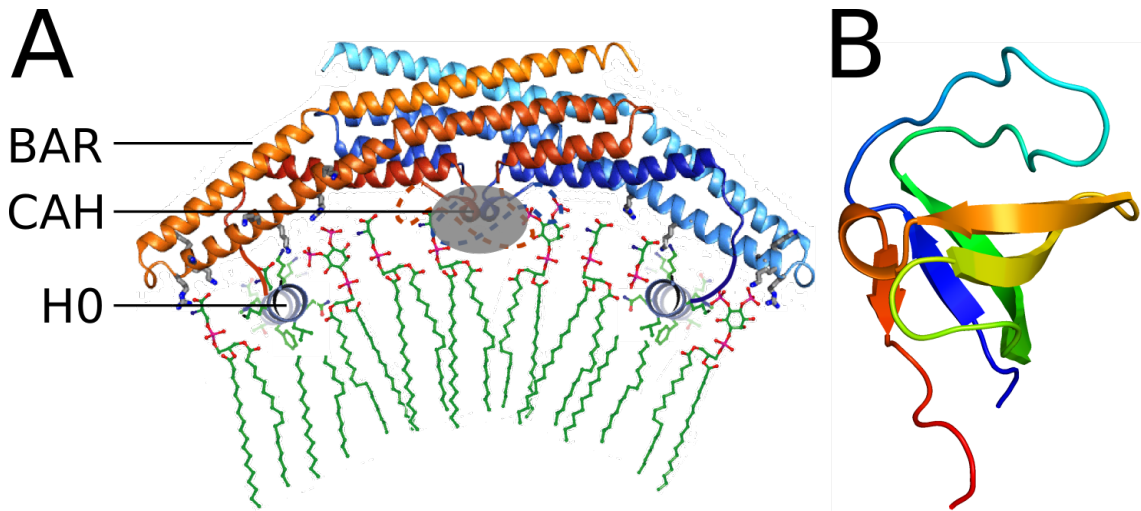


Figure 1.9: Structure of Endophilin N-BAR (A) and SH3 (B). A was modified from [26] with permission, B is pdb 3IQL from [229]

CME is an important pathway for recycling of synaptic vesicles (SV) [230]. In neurons, Endophilin A is localised at presynaptic nerve terminals and is recruited to presynaptic membrane following synaptic stimulation [231, 232, 228, 233, 234, 235]. In the lamprey giant synapse, interfering with the binding of Endophilin N-BAR to the membrane resulted in accumulation of shallow CCPs at stimulated synapses, suggesting a role of Endophilin N-BAR in CCP maturation [236]. Deletion of Endophilin A in flies and nematodes impaired SV endocytosis and caused an increase of both early and late-stage clathrin-coated intermediates as well as free CCVs [237, 234, 232, 238], suggesting a role for Endophilin at several stages of CME. Endophilin A also binds the PRD of both dynamin and synaptojanin *via* its SH3 domain [228] and forms a complex with dynamin on the narrow neck of CCVs, which also promotes binding of dynamin to lipids *in vitro* [239]. Injection of a peptide blocking Endophilin SH3 (PP19) [240] or antibodies against synaptojanin PRD in the lamprey giant synapse both led to an accumulation of free CCVs [241] and Endophilin was shown to be responsible for the correct recruitment and localisation of synaptojanin during CME [218, 242] and therefore of vesicle uncoating [243]. Endophilin is also involved in vesicle scission, as injection of Endophilin SH3 or PP19 peptide in the lamprey synapse resulted in an accumulation of late-stage CCVs with a narrow neck [241].

Although Endophilin plays an important role at different stages of SV recycling by CME, increasing evidence shows its role in a clathrin-independent endocytosis (CIE) pathway. In several synapses as diverse as inner hair cells [244], calyx of Held [245], hippocampal boutons [246, 247] or ribbon synapse of retinal bipolar cells [248], different modes of endocytosis differing by their speed were observed. At the goldfish retina ribbon synapse, after a short stimulus, membrane retrieval occurred with a time constant of 1 s [249], whereas after longer stimuli, excess membrane was retrieved in two phases, where the fast mode was followed by a slower endocytosis process (time constant 10 s). Disrupting amphiphysin-dynamin interactions or clathrin binding to accessory proteins significantly reduced the slow phase of endocytosis, whereas the fast phase was unaffected [248, 250] suggesting that slow endocytosis relies on CME whereas fast endocytosis is clathrin-independent. Blocking the fast phase could be achieved by introducing a dominant-negative Endophilin construct lacking its SH3 domain resulting in a fraction of SV to be endocytosed by the slow instead of the fast pathway [250, 251]. This indicated a role for Endophilin in fast, clathrin-independent SV endocytosis.

In addition to its role in CME and CIE of synaptic vesicles, Endophilin is also involved in internalisation of activated receptors tyrosine kinase (RTKs) and G-protein coupled receptors (GPCRs) using tubulovesicular carriers [120]. This clathrin-independent endocytic pathway was named FEME (fast Endophilin-mediated endocytosis) [120]. After activation by EGF (epidermal growth factor), EGF receptor (EGFR) is ubiquitinated by Cbl (Casitas B-lineage lymphoma) [252], which recruits CIN85 adaptor (Cbl-interacting protein of 85 kDa) [253]. CIN85 is constitutively bound to Endophilin through a PRD-SH3 interaction, linking Cbl and Endophilin after EGF stimulation [254]. Using dominant-negative constructs to interfere with CIN85 PRD – Endophilin SH3 complex formation reduced internalisation and down-regulation of EGFR [254, 120], although the importance of Cbl-CIN85-Endophilin for EGFR internalisation has been contested [255]. Cbl-CIN85-Endophilin was also important for internalisation of another RTK, the hepatocyte growth factor (HGF) receptor Met [256, 120]. Alix (ALG-2 interacting protein X) is another adaptor protein that binds Endophilin by PRD-SH3 contacts and is involved in Endophilin-dependent endocytosis of EGFR [257]. Deletion of Alix delays EGFR degradation by lowering degradation rate in the first hour after EGF stimulation, but the difference in degradation rate between wild-type and knock-out cell lines disappeared in the following hours [257].

Unlike FEME uptake of RTK that proceeds through adaptor proteins linking RTKs to Endophilin, Endophilin can bind GPCRs directly. In contrast to arrestin-mediated, CME uptake of GPCRs where after receptor activation and phosphorylation, arrestin binds to the C-terminal tail of the GPCR and interacts with AP2 and clathrin [258], Endophilin binds proline-rich sequences in the intracellular loop 3 (ICL3) of some GPCRs with its SH3 domain [259, 120] mediating their uptake following ligand activation [120]. The structure of Endophilin is well suited to its essential function in FEME. Its SH3 domain binds to cargo and cargo adaptors and its N-BAR domain facilitates both formation of a vesicle through scaffolding by the BAR domain and scission by inserting amphipathic helices in the membrane [106]. In addition, Endophilin SH3 recruits dynamin [116], an essential component for vesicle scission in FEME [120]. Endophilin has also recently been shown to directly participate in scission of elongating tubules by imposing friction on the membrane tube [260]. The FEME pathway can be hijacked by bacterial toxins [119]. Shiga toxin induces tubular membrane invaginations as a first step for its uptake into cells [261], which are recognised by Endophilin A2 [119]. Endophilin collaborates with dynamin and actin for scission of vesicles from these tubular invaginations [119]. FEME was also reported in axon growth cones, where Endophilin A3-mediated endocytosis of vesicles happens at the apical side of the leading edge of the cone in a dynamin- and actin-dependent manner [262].

The two members of the Endophilin B subfamily have been less studied than Endophilin A, but show roles non-related to endocytosis. They mostly act on intracellular membranes. The difference in localisation between Endophilin A and B is not well understood. H1I plays a role as a chimeric Endophilin B1 construct with H1I from Endophilin A1 partly redistributes to the plasma membrane [104]. However, localisation is more complex. Other regions are also important as Endophilin A1 Δ H1I still localises to the plasma membrane [104] and different lipid specificities, protein binding partners and potentially curvature preferences probably contribute as well. Endophilin B2-deficient mice showed impaired endosomal function and trafficking of vesicles to late endosomes and lysosomes [263]. Endophilin B2 also plays a role in mitophagy, in particular inner mitochondrial membrane degradation together with Endophilin B1/Bif-1 [225]. Endophilin B1 was first identified as a binding partner of BAX (Bcl2-associated X protein) [227, 264]. Bif-1 promotes the conformational change of BAX [264, 265] necessary for its activation and subsequent permeabilisation of the mitochondrial outer membrane [266], which triggers caspase activation

and apoptosis. Endophilin B1 is required to maintain the morphology of mitochondria [267] and also plays a role in the generation of autophagosomes from Golgi membranes by promoting formation of a Beclin1-UVRAG-PI3KC3 complex [268].

In addition to its roles in CME and CIE, Endophilin A is also involved in autophagy. The Parkinson's disease associated kinase LRRK2 (Leucine-rich repeat kinase 2) phosphorylates Endophilin at position S75 (situated in H1I) [269]. Phosphorylated Endophilin favours vesiculation over tubule formation when added on liposomes by preventing CAH to insert deeply in the membrane [27]. The current model suggests a role for Endophilin in autophagosome formation and maturation [270]. Endophilin, present on phagophore membranes, generates high curvature, which helps recruit Atg3 [271], leading to lipidation of Atg8 [272] and progression of autophagosome formation. In Endophilin A-deficient mice, fewer autophagosomes, which could not be compensated by overexpression of Endophilin B, were observed [273]. This reduced autophagic flux resulted in neurodegeneration [273].

1.4 Aims of this thesis

Membranes of eukaryotic cells occur in various shapes, flat areas, elongated tubules or vesicles. Formation and sensing of membrane curvature by proteins is essential for cellular homeostasis. Two mechanisms by which proteins can sense membrane curvature have been previously described [66]. The first relies on curved scaffolds that preferentially bind to membranes of similar curvature [58], the second on amphipathic helices or hydrophobic loops as sensors of lipid packing defects [77], a hallmark of highly curved membranes. However, several questions remain open. First, are there additional ways to sense membrane curvature? To answer this, other lipid-binding domains should be screened for curvature sensitivity and the mechanism by which they sense curvature studied. Second, there is discrepancy over the relative contributions of BAR domains and amphipathic helices in curvature sensing for proteins that contain both. Although initial experiments with BAR domain proteins showed that the preferred vesicle size correlated with the shape of the BAR domain, both *in vitro* and *in vivo* [26, 69, 59], newer data suggest that the amphipathic helix only drives curvature sensing [94] and that flat F-BAR and negatively curved I-BAR domains also preferentially bind to highly curved membranes. Using Endophilin as a model, studying curvature sensitivity of constructs containing either only BAR or H0 as well as mutants might shed light on this debate.

To target both of these questions, an assay based on single particle should be used in order to ensure accurate and precise sizing of the liposomes, to allow better discrimination power than bulk assays. In addition, liposomes should be freely floating in solution to avoid potential artefacts from surface tethering. As no current assay fulfils both requirements, in this thesis I established a new method, NTA, based on sizing of freely diffusing particles by their Brownian motion. After validating its sizing ability using calibration beads, I could reproduce known curvature preferences of selected BAR domains. A screen of non-BAR lipid-binding domains identified a new curvature sensor, the PH domain of AKT. I also showed that NTA can be used to follow membrane remodelling, using vesiculation by ENTH as a model system, opening the way to characterise other membrane remodelling effectors.

Endophilin has been implicated at several steps of clathrin-mediated endocytosis [236, 237, 240, 243]. More recently, it has also been described as an essential component of a clathrin-independent pathway, FEME, involved in uptake of activated GPCRs, RTKs [120] as well as bacterial toxins [119]. Consisting of an N-BAR domain able to sense and generate curvature as well as an SH3 domain recognising cargo and recruiting dynamin, Endophilin could be involved in every step of the endocytosis process. However, apart from the receptors identified by Boucrot *et al.* [120], little is known about the scope of FEME, which other receptors transit through FEME or when FEME is used. Understanding cargo selection by Endophilin SH3 would contribute to understanding of FEME, however existing data based on peptide libraries and modelling were not enough to define a consensus Endophilin binding motif. In this thesis, I characterised by NMR the binding of a cargo receptor and an adaptor protein to Endophilin SH3 and generated models of the binding site. This resulted in a putative consensus sequence that can be used to identify more FEME target receptors.

Chapter 2

Measuring curvature sensitivity of proteins in a single-particle solution assay

2.1 Introduction

Eukaryotic cells are characterised by membranes with varied and dynamic compositions and topologies, ranging from elongated tubules and flat membrane areas to small vesicles. These shapes are characterised by different local curvatures that have to be generated, maintained and recognised by proteins. Shape of membranes is essential for their function, be it trafficking, signalling, division or migration to cite only a few examples, and is necessary to maintain cellular homeostasis.

Several methods have been developed to study curvature sensitivity of proteins. The earliest developed assays are based on centrifugation [58]. There, the candidate protein is incubated with liposomes of different sizes. Free protein and protein bound to liposomes are then separated by centrifugation based on the different pelleting efficiency of liposomes and proteins. Alternatively, presence of a fluorescently-tagged protein on a lipid surface, either liposomes of different sizes, lipid tubes of variable diameter or a curved lipid film, can be observed using microscopy [94, 274, 96, 275].

Two variations of the curvature sensitivity assay based on centrifugation have been developed. Both use liposomes extruded to different radii by passing through filters of set

pore size [276]. In liposome co-sedimentation assays, the candidate protein is incubated with liposomes that are then pelleted by ultracentrifugation. The ratio of protein in pellets (with liposomes) or free in the supernatant for different sizes of liposomes indicates curvature preference [58]. Alternatively, in a flotation assay, liposomes and proteins are mixed at the bottom of a centrifuge tube and layered with a density gradient. During ultracentrifugation, liposomes will rise to the surface due to their lower density. The ratio of free protein at the bottom of the tube to protein bound to liposomes in the supernatant indicates curvature preference [77].

Several methods relying on microscopy exist. In a single liposome curvature (SLiC) assay [94], fluorescent liposomes containing biotinylated lipids are tethered to a streptavidin-coated glass surface and their size is calculated from the fluorescent intensity after imaging under a microscope. Imaging is repeated after addition of fluorescent protein to detect liposomes to which protein bound. Another group used NTA (Nanoparticle Tracking Analysis) to characterise curvature sensitivity of MARCKS-ED (the effector domain of myristoylated alanine-rich C-kinase substrate) [277] and a cyclic peptide derived from Synaptotagmin1 [93]. NTA sizes freely diffusing particles by measuring their Brownian motion. Curvature preference data can be obtained by comparing the size distribution of liposomes alone to that of protein-bound liposomes.

An alternative way of generating curvature is by pulling a nanotube from a Giant Unilamellar Vesicle (GUV) using a bead trapped in optical tweezers [274]. The GUV is aspirated in a micropipette, whose suction force sets the membrane tension of the GUV. The radius of the nanotube is determined by the aspiration force and the membrane bending rigidity and can be adjusted by varying the suction force in the micropipette. Fluorescent protein localisation on the tube and on the GUV can then be detected under a confocal microscope.

The study of proteins binding to negative curvatures is difficult using liposomes which display only positive curvatures. Solid-supported membranes are a useful tool [275]. In this technique, a hard surface is engraved with a pattern, then a membrane bilayer, which is expected to follow the patterning, is formed on top of the surface. Localisation of protein on the crests or troughs of the wavy patterning can be observed under a microscope. A similar assay has recently been used to study the effect of membrane curvature on clathrin-mediated endocytosis [278].

All methods described above measure curvature sensitivity *in vitro* using purified, fluorescently labelled proteins. Curvature-driven protein localisation could also be observed *in vivo* in the special case of *B. subtilis* [91, 73]. Bacteria generally lack intracellular structures and cytosolic proteins only see mild negative membrane curvature. During formation of the spore however, areas of positive curvature are generated around the spore and some proteins like SpoVM have been shown to specifically localise to those regions [91]. Preference for high negative curvature could also be observed for the protein DivIVA that accumulates at poles and at the edge of the division septum in dividing *B. subtilis* [72, 73]. *In vivo* curvature-dependent sorting of GPCRs (G-protein coupled receptors) could also be assessed by measuring the distribution of GPCRs along filopodia or tubes pulled from cell membrane [96]. Preference for high positive curvature was driven by the conical shape of the transmembrane (TM) region of GPCRs. Redistribution of the GPCR Y2R (neuropeptide Y receptor Y2) along filopodia also occurred after ligand activation, which induces conformational changes in the TM domain [279].

All the existing methods have advantages and drawbacks (Tab. 2.1). Despite extrusion, liposomes size distributions remain polydisperse [280] and even when using different filter pore sizes, liposome size distributions are overlapping [98]. This results in lower discrimination power for bulk techniques like liposome co-sedimentation or flotation assays. In addition, in liposome co-sedimentation assays, artefacts due to protein pelleting, a result of protein aggregation, multimerisation or simply use of large proteins, are common.

SLiC was developed to circumvent drawbacks arising from the polydispersity of sizes of extruded liposomes by sizing particles individually. However, the tethering process might introduce artefacts. As liposomes are tethered to a surface by a biotin-streptavidin link, but are still in solution and therefore subject to Brownian motion, this may affect membrane tension and increase hydrophobic defects, explaining why all domains tested with this method tend to bind preferentially to higher curvatures, [94, 98] even those for which dramatically different curvature preferences have been reported by other assays like for I-BAR domain containing proteins [100].

Nanotubes pulled from GUVs can have various diameters, allowing the study of several different curvatures sequentially [281, 282]. However, as the membrane is pulled into a tube, the applied lateral tension affects lipid packing density and lipid diffusion [283]. This might affect sorting of proteins on the membrane. Although solid-supported membranes are especially useful to study negative curvature, the major drawback of this technique

is that it relies on the assumption that the membrane closely follows the patterning of the underlying surface. Confirming this or determination of the exact curvature is experimentally hard. Studying curvature sensitivity *in vivo* may provide more physiologically relevant information. It is however, for now, restricted to particular cases, like sporulation or division in *B. subtilis* or sorting of integral membrane proteins [96].

Table 2.1: Comparison of existing methods to measure curvature sensitivity of proteins

Method	Principle	Advantages	Disadvantages
Liposome co-sedimentation [58]	different pelleting efficiencies of free <i>versus</i> liposome-bound protein	easy	bulk, polydisperse liposome sizes, artefacts from protein aggregation
Flotation assay [77]	different densities of protein and liposomes separated by a gradient	easy	bulk, polydisperse liposome sizes
SLiC [94]	localisation of fluorescent protein on liposomes tethered to a surface	single-particle sizing	artefacts from liposome tethering
Tubule from GUV [274]	localisation of fluorescent protein along tubules pulled from a GUV	set curvature can be adjusted	application of lateral tension
Solid-supported membrane [275]	localisation of fluorescent protein on membrane layered on a curvy surface	study of negative curvature preference	hard to determine precise membrane curvature
<i>In vivo</i> [91, 96]	localisation of fluorescent protein on specialised subcellular structures	physiologically relevant	limited to special cases

In order to test membrane curvature sensing of proteins, I wanted a technique that combines advantages of liposome co-sedimentation/flotation and SLiC assays while avoiding their drawbacks. For this, a single-particle, solution technique would be ideal. There, liposomes would be freely floating in solution avoiding potential artefacts from tethering to a surface. In addition, a large population of liposomes would be sized individually, allowing better size determination than in bulk assays. For these reasons, I turned to NanoSight Nanoparticle Tracking Analysis (NTA) developed by Malvern. NTA is a microscopy-based technique where freely diffusing liposomes can be individually sized based on their Brownian motion. Experimental design to measure curvature sensitivity of proteins using NTA would involve sizing all liposomes or protein-bound liposomes only. Comparing both size distributions would indicate curvature preference of the protein tested.

NTA uses light diffraction to image particles moving freely in solution by Brownian motion. Position in the x and y dimension of each particle is tracked over time and mean squared displacement $\overline{(x,y)^2}$ is calculated. For diffusion in two dimensions, generally $\overline{(x,y)^2} = 4Dt$. Although Brownian motion occurs in three dimensions, NTA records motion in two dimensions, as a two-dimensional projection of a three-dimensional trajectory.

The Stokes-Einstein equation (Eq. 2.1.1) describes how the diffusion coefficient D correlates with the diameter d of a particle, temperature T and solvent viscosity η (t represents time and K_B Boltzmann constant).

$$Dt = \frac{TK_B}{3\pi\eta d} \quad (2.1.1)$$

By combining those two equations, the size d of a particle can be calculated with Eq. 2.1.2.

$$\frac{\overline{(x, y)^2}}{4} = Dt = \frac{TK_B}{3\pi\eta d} \rightarrow d = \frac{Tk_B}{3\pi\eta D} = \frac{4Tk_B}{3\pi\eta \overline{(x, y)^2}} \quad (2.1.2)$$

NTA can detect particles by recording diffracted light. Alternatively, insertion of a long-pass filter blocks diffracted light and allows detection of fluorescent particles only. In order to measure the curvature sensitivity of protein binding to membranes, unlabelled liposomes can be detected by diffraction. After addition of fluorescently-labelled protein, only liposomes with bound protein will appear fluorescent and those can be detected in fluorescence mode. Alternatively, different dyes with different excitation/emission wavelengths could be used to label liposomes and proteins.

In this thesis, I demonstrate the use of NTA to study curvature sensing and vesiculation. I first validated NTA's sizing capability with calibration beads of known sizes. Where curvature sensitivity of proteins was previously known, this was reproduced by NTA. Next, other lipid-binding domains were screened for curvature sensitivity. Finally, curvature generation was also monitored by NTA.

2.2 Results

2.2.1 Nanoparticle tracking analysis using NanoSight technology

The instrument, NanoSight LM10 (Malvern), used in this study is based on a conventional upright microscope (Fig. 2.1A). The sample is imaged in a specially-designed glass chamber where the bottom surface, called optical flat, is coated with a metallised surface to reduce background (Fig. 2.1B). The sample can be made to flow using a syringe pump to reduce photobleaching and increase the number of particles tracked (Fig. 2.1C). Laser light is used for illumination of the sample. As laser light reaches the layer of liquid sample after passing through the glass optical flat, the light is refracted and forms a beam through the sample (Fig. 2.1D). Particles present in the sample will diffract light that is then collected by a long working distance 20x objective (Fig. 2.1E). In order to collect red-shifted light emitted by fluorophores, a long-pass filter is introduced to block diffracted light (Fig. 2.1F). Imaging acquisition and single particle tracking and analysis is performed using Nanosight NTA software (Malvern).

The typical procedure I followed for data collection using NTA goes as follows. The samples are prepared and diluted in NTA buffer as described in Material & Methods (chapter 5) and then introduced into the imaging chamber using the syringe pump. 60-120 s movies are recorded using a high-sensitivity CMOS camera operating at 25 frames per second. After background subtraction, the centre of particles is determined (Fig. 2.2, red crosses). The threshold for detection of particles can be adjusted depending on the intensity of the particles present in the sample. Particles are then automatically tracked (Fig. 2.3A). The top number next to each particle indicates the estimated size of that particle for the last frame, while the bottom number indicates the number of frames that particle has been tracked for. Three parameters are automatically set for each movie but can also be adjusted manually [284]. "Blur" allows smoothing of pixel intensities around a particle to reduce noise, e.g. from diffraction rings, thus reducing the number of false particle centres. "Max jump distance" indicates the maximal distance from a particle in a given frame in which it will look for this particle in the next frame. In order to prevent accidentally merging tracks from different particles, if another particle enters the zone defined by the max jump distance, tracks from both particles will be discarded from further analysis. "Min track length" sets the minimum number of consecutive frames a particle has to be tracked for, in order for it to be included in the analysis. Tracking over a larger number

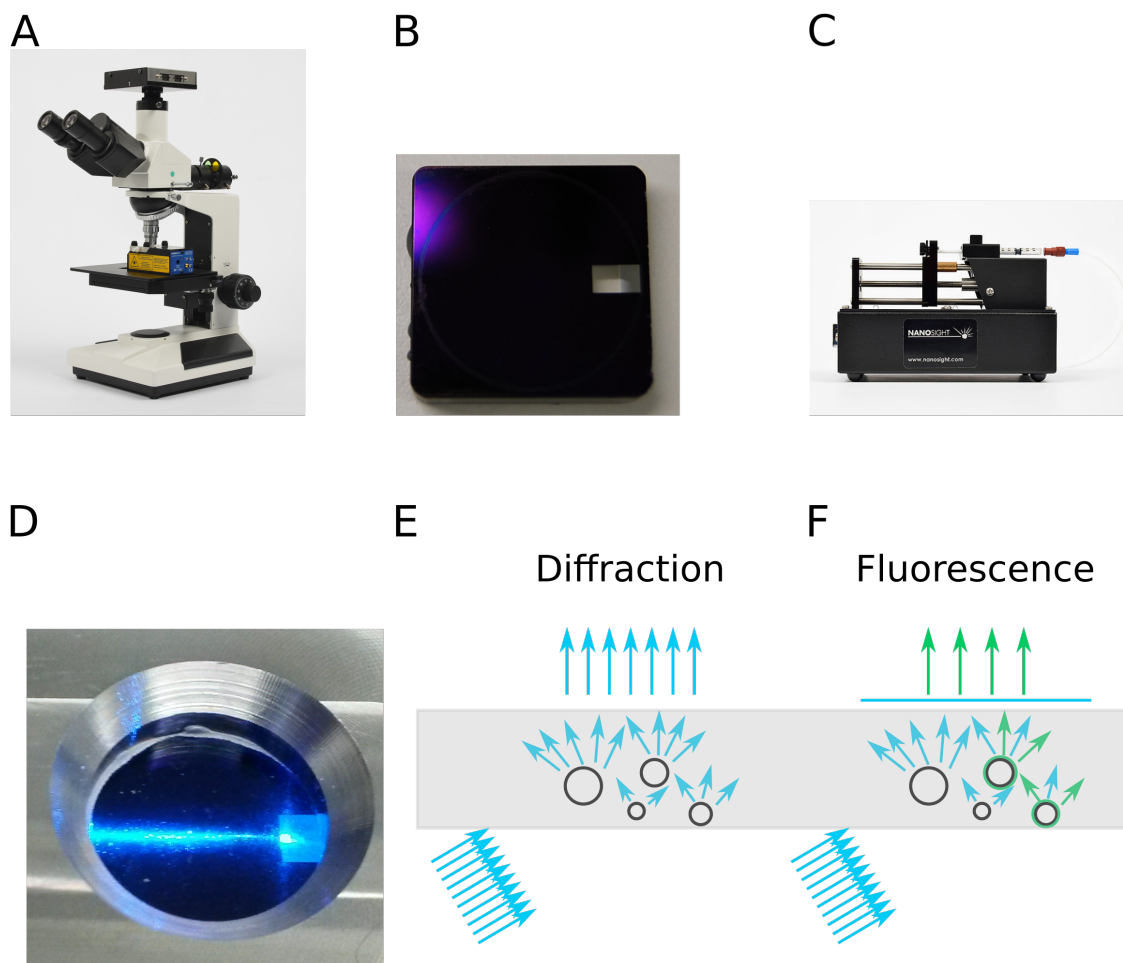


Figure 2.1: Working principle of NanoSight LM10.

A. Microscope. **B.** Glass optical flat with metallised surface. **C.** Syringe pump. **D.** Laser beam going through sample. **E** Particles diffracting light. **F** Long-pass filter blocking diffracted light and letting only fluorescence emitted light through. (A, C were reproduced with permission from Malvern)

of frames increases the accuracy of size determination. It however reduces the number of fast diffusing, small particles tracked as they might move out of the small observation volume and biases the data towards larger, slower diffusing particles. While the data are processed, plots of concentration (Fig. 2.3A) and intensity as a function of size (Fig. 2.3B) as well as a three-dimensional plot combining the two previous plots (Fig. 2.3C) appear.

At the end of the tracking, for monodisperse samples like calibration beads, the data can be further corrected by FTLA (finite track length adjusted). As the depth of scattering volume is small, particles, especially small ones, are tracked for only a few frames, resulting in artificial line broadening without affecting the mean. This can be mathematically modelled and compensated for [285]. After application of FTLA correction, the true distribution can be recovered. Further corrections for vibration and drift are then applied using a Malvern

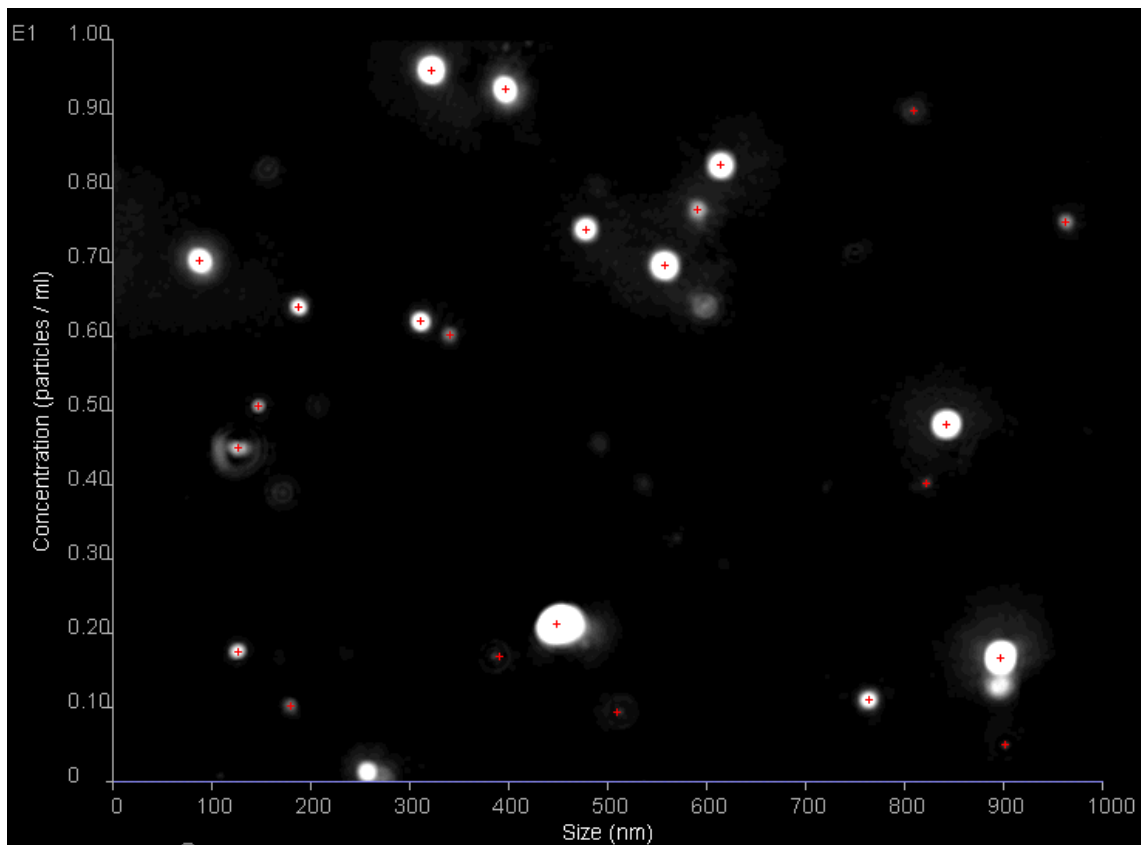


Figure 2.2: Detection of particle centres

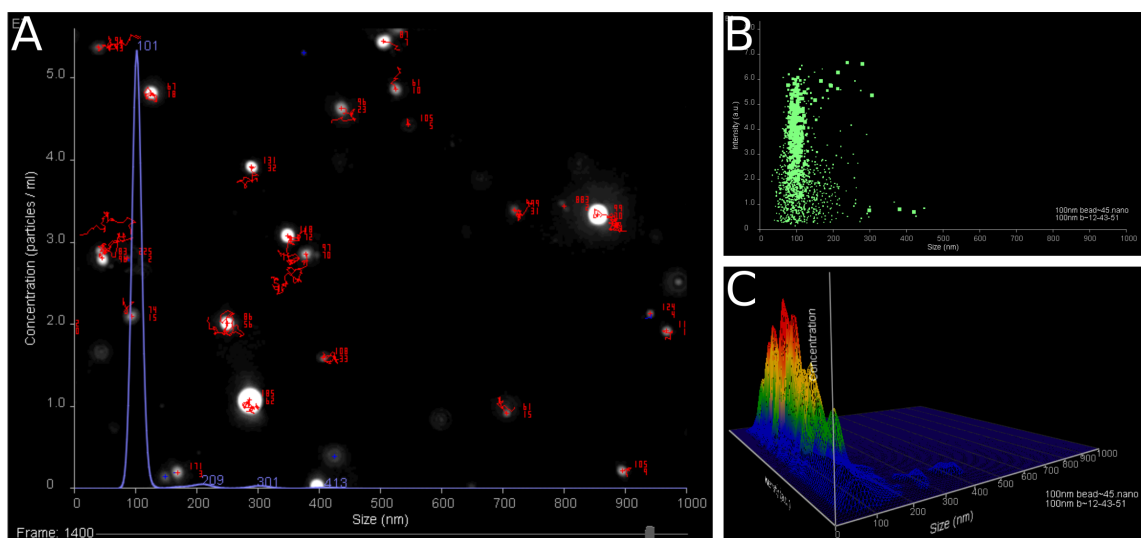


Figure 2.3: Tracking of particles.

A. Tracking of single particles with individual sizes overlaid with plot of concentration as a function of size. B. Intensity as a function of size. C. Concentration and intensity as a function of size.

proprietary algorithm, resulting in the final data. Drift originating from pump flow is subtracted by calculating the total drift of all particles (which should be zero in a static sample as Brownian motion is random) and subtracting it from each particle's trajectory.

The number of particles per size are binned in 5 nm bins. The concentration of particles in each bin is calculated using the estimated dimensions of the observation volume ($100\ \mu\text{m}$ by $80\ \mu\text{m}$ field of view by $10\ \mu\text{m}$ beam depth [286]). Data with the concentration of particles in each bin can then be exported and used with a plotting software.

Data can be presented as plots of concentration as a function of size (Fig. 2.4A) like in the direct output of the NTA software. Alternatively, data can be displayed as box plots with the box containing 25-75 % of the data and the middle line indicating the median. Whiskers on each side show where 10-90 % of the data is situated (Fig. 2.4B).

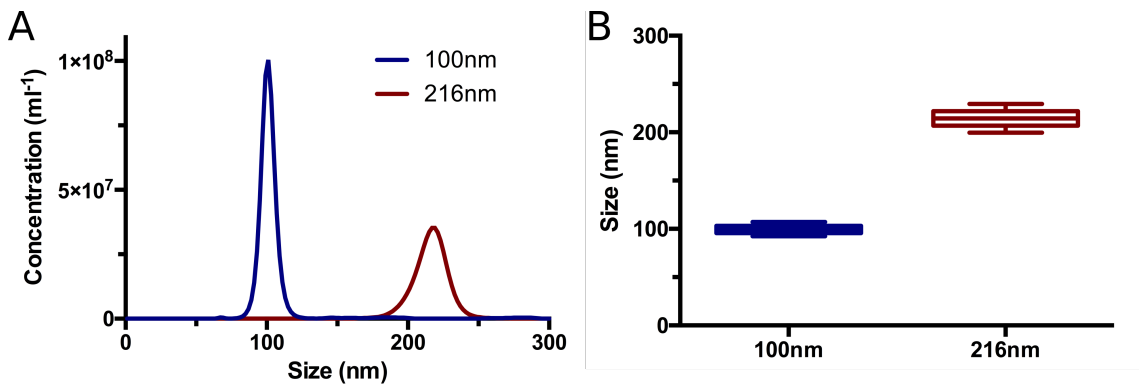


Figure 2.4: NTA data representation. A. Concentration *versus* size. B. Corresponding box plot

The experimental design to measure curvature sensitivity of protein binding to membrane consists of fluorescent lipid-binding domains being added to non-fluorescent liposomes. Measurements using diffraction detect all liposomes and provide a size distribution for the entire liposome population, whereas after introduction of the fluorescent filter, only fluorescent liposomes are visualised, *i.e.* only liposomes which have fluorescent protein bound. Comparison between size distributions obtained by diffraction and fluorescence indicate the curvature preference for a given protein.

Concentrations of detected particles should be kept to 10^8 - 10^9 /ml (corresponding to pM) [284]. This corresponds to 10-100nM lipids, assuming a liposome contains 10'000 to 100'000 lipid molecules. Using lower concentrations of sample reduces the statistical accuracy of the size measurement. On the other hand, if the sample concentration is higher than 10^9 /ml, particles tend not to get resolved from each other, as they are in too close proximity. In addition, the probability of particles crossing path, resulting in both particles' tracks being discarded, increases. Regarding fluorescent proteins, concentrations have to be kept below

5 nM, otherwise background of unbound protein becomes too high. Measurements were therefore generally conducted at 1-2 nM.

2.2.2 NTA validation

The first step undertaken was to check the precision and accuracy of NTA to size particles and compare it to the established Dynamic Light Scattering (DLS) method. For this, calibration beads were used. The sizes were chosen to be similar to typical liposomes, hence 100 nm and 216 nm. NTA sized these beads at 100 ± 5 nm and 217 ± 11 nm respectively (Fig. 2.5). As liposome size distributions are broader than calibration beads, I then wanted to test how NTA would size calibration beads when they were mixed. As shown in Figure 2.5 (green curve), NTA was able to differentiate both populations of beads. I then repeated the experiment using DLS. Size distributions obtained for individual beads were broader than NTA, 110 ± 10 nm and 214 ± 22 nm (Fig. 2.6). In addition, DLS was not able to distinguish both populations after both sizes of beads were mixed. Instead, the size obtained, 180 ± 60 nm, was intermediate between both populations. 100 and 216 nm beads were too close in size to be discriminated by DLS. Therefore, NTA was more precise and accurate than DLS and was also better at differentiating two populations of beads of different sizes in a biologically relevant size range.

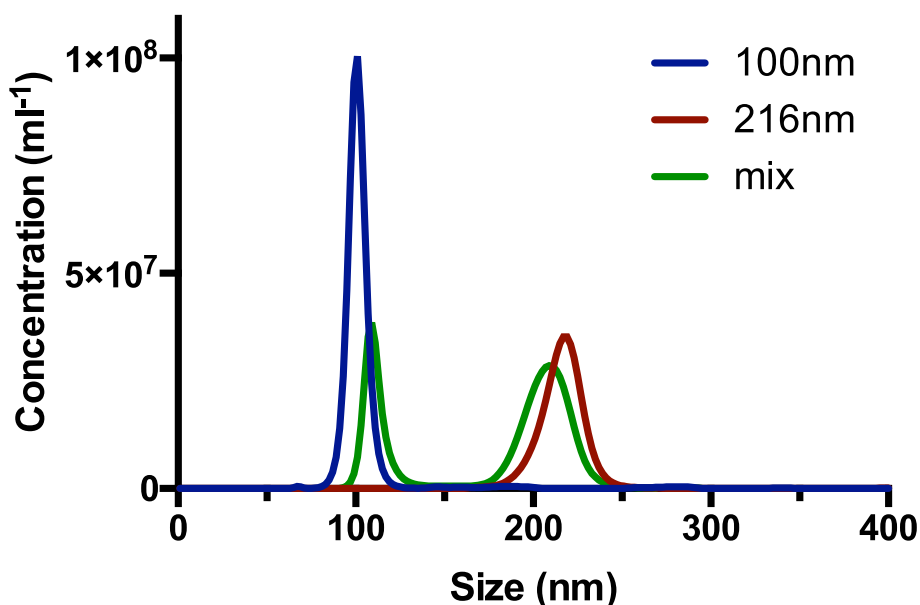


Figure 2.5: Size distribution of 100 nm and 216 nm calibration beads based on NTA

During measurements of curvature sensitivity, I would expect fluorescent proteins to bind to only a sub-population of unlabelled liposomes, so the next control was to check NTA's

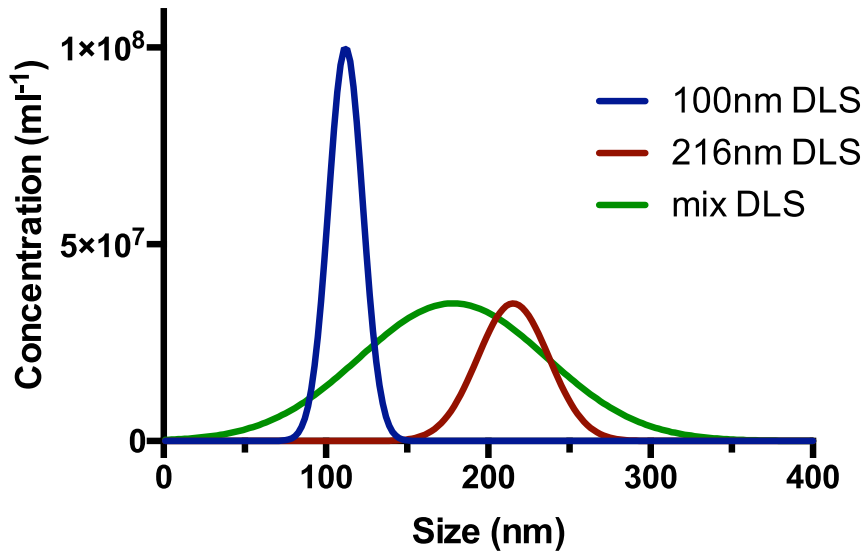


Figure 2.6: Size distribution of 100 nm and 216 nm calibration beads based on DLS

ability to size fluorescent particles when mixed with unlabelled particles of a different size. For that, I sized separately fluorescent liposomes extruded at 50 nm (Fig. 2.7, blue curve) and 200 nm unlabelled liposomes (Fig. 2.7, black curve) using diffraction. Both populations were then mixed and the size of fluorescent particles determined (Fig. 2.7, red curve). Size distributions of fluorescent 50 nm liposomes measured on their own or in a mix of large, unlabelled liposomes were overlapping, highlighting the ability of NTA to size fluorescent particles even when in the presence of unlabelled particles of different size.

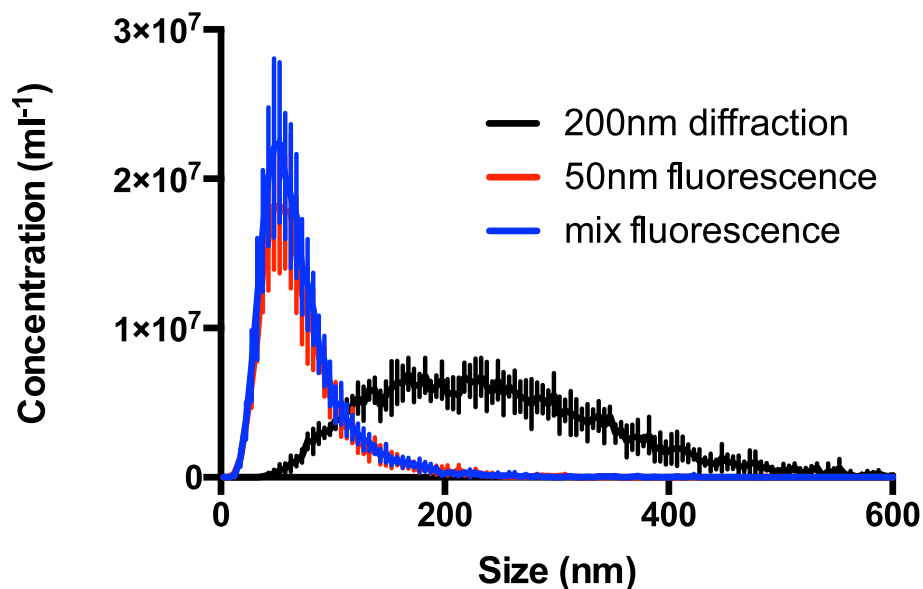


Figure 2.7: Size distribution of 50 nm fluorescent liposomes alone (red) or after mixing (blue) with unlabelled 200 nm (black) liposomes. "diffraction" and "fluorescence" indicate the absence or presence of a fluorescence filter for particle detection

The experiment was repeated with 200 nm fluorescent liposomes to confirm that the sizing of larger fluorescent liposomes (Fig. 2.8, blue curve) was also accurate when mixed (Fig. 2.8, red curve) with small, unlabelled liposomes (Fig. 2.8, black curve). This experiment yielded similar results to the previous one, confirming that NTA can size both small or large sub-populations of fluorescent liposomes in the presence or absence of unlabelled liposomes of a different size.

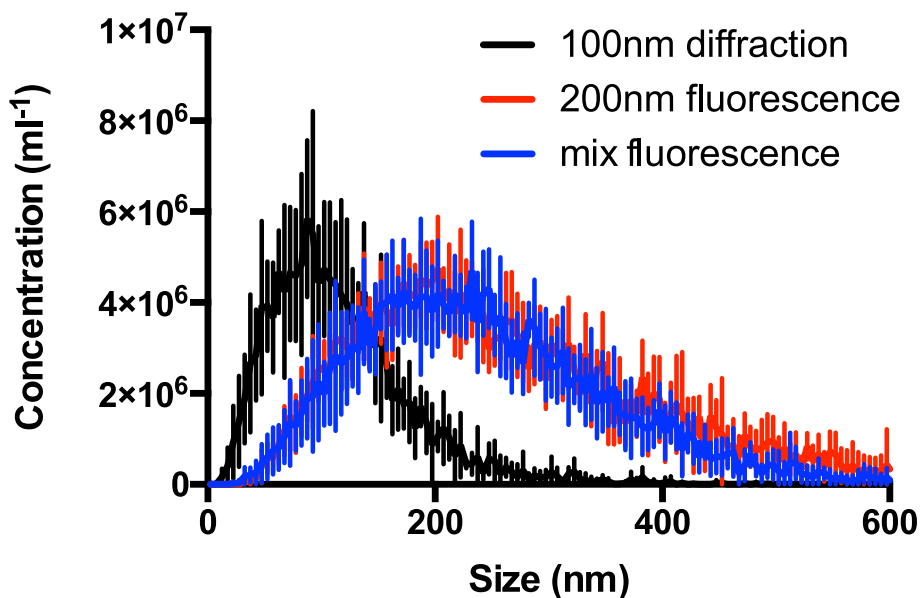


Figure 2.8: Size distribution of 200 nm fluorescent liposomes alone (red) or after mixing (blue) with unlabelled 100 nm (black) liposomes. "diffraction" and "fluorescence" indicate the absence or presence of a fluorescence filter for particle detection

These experiments demonstrated several advantages of NTA compared to other available sizing techniques. NTA is a single-particle method that can size large populations. NTA was also able to accurately and precisely size calibration beads in a biologically relevant size range and was better at distinguishing two populations of similar sizes present in a mixed population. Finally, NTA was able to specifically detect and size a subset of liposomes within a population. These properties of NTA confirm its usability as a tool to measure curvature sensitivity of proteins.

2.2.3 BAR domain curvature sensitivity

After having confirmed NTA sizing abilities, I then needed a proof of principle that NTA could be used to measure curvature sensitivity of proteins. Thus I started by using lipid-binding domains with known curvature preferences. Bin/Amphiphysin/Rvs (BAR) do-

mains are elongated dimers forming six-helix bundles with different curvatures [287, 55, 58]. Curvature preferences for several BAR domains have been determined using liposome co-sedimentation or flotation assays and correlate with their three-dimensional structures. The flatter the domain is, the larger are the liposomes it preferentially binds to. Endophilin A (SH3GL1/2/3) forms highly curved banana-shaped dimers [288] and was previously shown to preferentially bind small liposomes [26]. Endophilin however also contains an N-terminal amphipathic helix and has been shown to generate curvature, producing smaller vesicles or tubules [26, 65, 289]. I nevertheless chose Endophilin A2 as my first test protein, considering that under the low protein concentrations needed to work in NTA (1-5 nM), vesiculation and tubulation might be negligible. This assumption was tested below before proceeding with further experiments on curvature sensitivity.

Rat Endophilin A2 N-BAR labelled on the only available cysteine at Q228C with Alexa488[®]-maleimide, a kind gift from Emma Evergren who purified and labelled it, was used in this study [290]. Size distribution of liposomes alone under diffraction was recorded (Fig. 2.9, black curve). After addition of protein, the size distribution was measured under fluorescence (Fig. 2.9, red curve) to check curvature sensitivity of Endo NBAR-488 on liposomes of defined composition (for details see Material & Methods (chapter 5)). In this measurement, all fluorescent liposomes (*i.e.* Endophilin-bound liposomes) are detected and sized. The measurement is then repeated in diffraction mode (Fig. 2.9, blue curve) to check for vesiculation by Endophilin. Given the similar size distributions of liposomes in the absence (Fig. 2.9, black curve) or presence (Fig. 2.9, blue curve) of Endo NBAR-488, at the low protein concentrations used for NTA, I concluded that Endo NBAR-488 did not vesiculate liposomes and could therefore be used as a candidate for curvature sensitivity. As expected from its three-dimensional structure and published data [26, 288], Endo NBAR-488 preferentially bound small liposomes (Fig. 2.9, red curve).

Using protein labelled at a single site with a small fluorophore provided a clean system to work with. However, Alexa488 photobleached quickly under the strong laser beam used for NTA, so other fluorophores were tested for high fluorescent intensity and slow photobleaching under NTA conditions. The best candidate was found to be superfolder Green Fluorescent Protein (sfGFP) [291]. In addition to its brightness and slower photobleaching, it allows for higher throughput in protein production, as candidate proteins can be directly purified as fusion proteins with sfGFP, thereby reducing the number of purification steps required. Before using sfGFP routinely as a fluorophore for NTA, I checked that a 27kDa

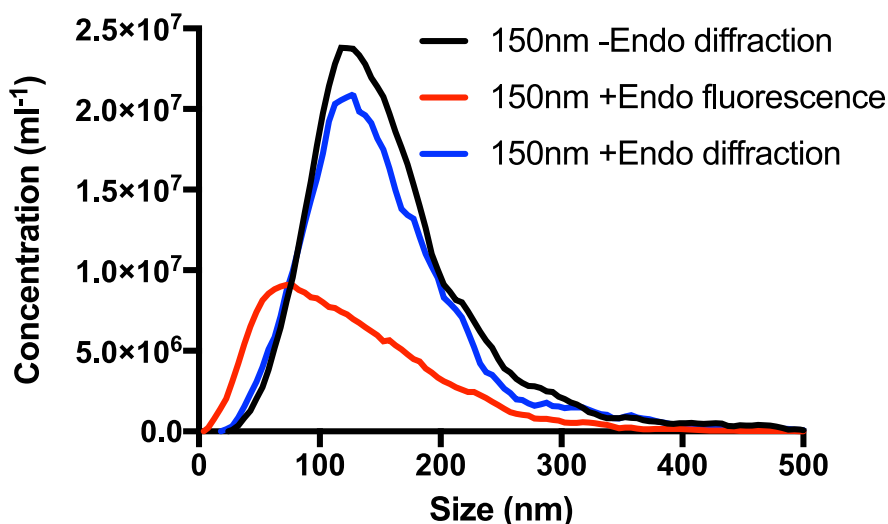


Figure 2.9: Curvature preference of Endo NBAR-488. Size distributions of liposomes alone (black), fluorescent (red) or all (blue) particles after addition of Endo NBAR-A488 "diffraction" and "fluorescence" indicate the absence or presence of a fluorescence filter for particle detection

tag, which is of similar or larger size than most lipid-binding domains used, did not change curvature sensitivity of protein binding. I therefore compared Endo NBAR-488 and Endo NBAR-sfGFP curvature preferences (Fig. 2.10, blue and red curves). Both fluorophores resulted in very similar curvature preferences, validating the use of sfGFP for NTA.

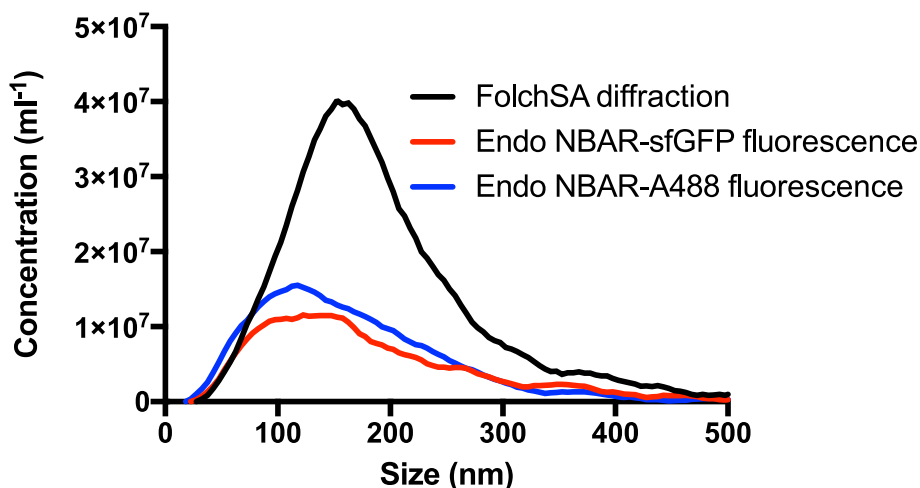


Figure 2.10: Comparison of Alexa488 and sfGFP for NTA curvature sensitivity measurements. Size distributions of all liposomes (black), Endo NBAR-sfGFP (red) or Endo NBAR-Alexa488 (blue) bound liposomes. "diffraction" and "fluorescence" indicate the absence or presence of a fluorescence filter for particle detection

To confirm Endophilin preference for small liposomes, the experiment was repeated using liposomes extruded to 250 nm diameter (Fig. 2.11, blue), 150 nm (red) or 80 nm (green) as

inputs. Data representations as size distributions (Fig. 2.11A) or box plots (Fig. 2.11B) clearly show that Endophilin preferentially binds to the smallest available liposomes.

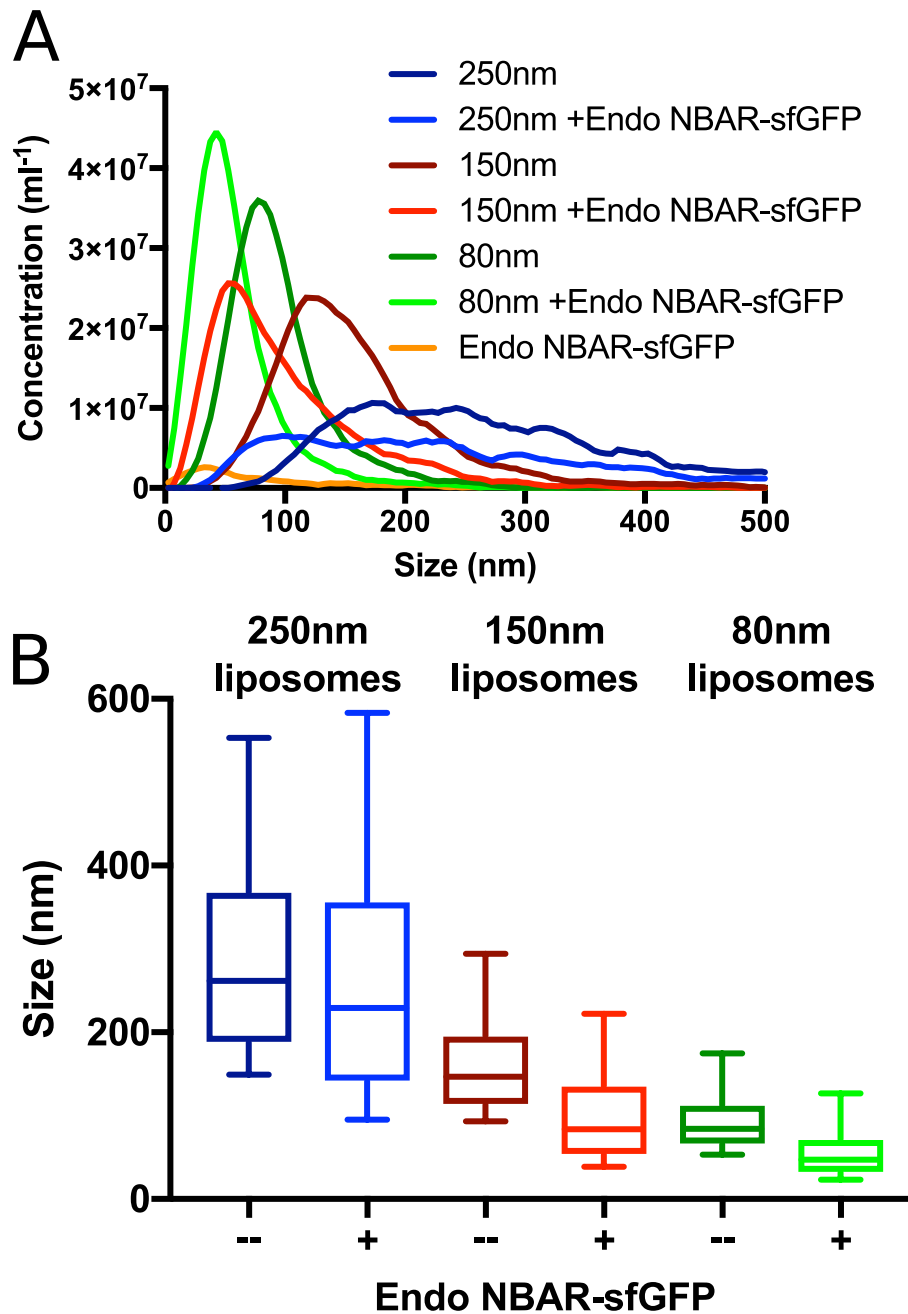


Figure 2.11: Curvature sensitivity of Endo NBAR-sfGFP. A. Size distributions of all liposomes (darker colours) or Endo N-BAR-sfGFP bound liposomes only (lighter colours) or 250 nm (blue), 150 nm (red) or 80 nm liposomes. B. Box plot representation of the same data

These results were also validated by using the published method of liposome flotation assay [77, 292]. Endo NBAR-sfGFP was incubated with 250 nm or 80 nm or without (–) liposomes, then samples were mixed with a gradient medium and layered with a density gradient as described in Material & Methods (chapter 5). During ultracentrifugation,

proteins stayed at the bottom of the tube, while liposomes rose to the surface, carrying bound proteins if any. With 250 nm liposomes, as in the absence of liposomes (Fig. 2.12, 250 nm, -), Endo NBAR-sfGFP was primarily found in the bottom two fractions, whereas when using 80 nm liposomes, Endophilin could also be detected in the top fraction. This experiment also confirmed Endophilin’s preferential binding to smaller liposomes.

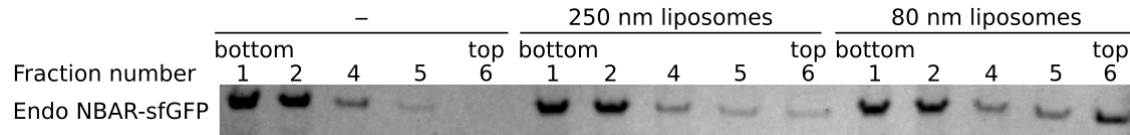


Figure 2.12: Curvature sensitivity of Endo NBAR-sfGFP by liposome flotation assay in the absence (-) or presence of 250 nm or 80 nm liposomes.

Endophilin binding to membranes is increased by negatively charged lipids (like phosphatidylserine PS) and PI(4,5)P₂ [293]. I wanted to test the effect of lipid composition, in particular PI(4,5)P₂ concentration on curvature sensitivity of Endophilin. Liposomes used routinely for experiments with Endophilin contain 2% PI(4,5)P₂, and I also measured its curvature preference in the absence (0%) or in the presence of 5% PI(4,5)P₂ (Fig. 2.13). With increasing concentrations of PI(4,5)P₂, Endophilin preference for small liposomes, although still present, became less stringent and increasingly larger liposomes could also be bound.

Having confirmed that Endophilin preferentially bound to smaller liposomes, I tested other BAR domain proteins with different curvature preferences, FCHo2 (Fes and Cip4 Homology domain Only 2) and Insulin receptor substrate p53 IRSp53 (BAIAP2 Brain-specific angiogenesis inhibitor 1-associated protein 2). FCHo2 has an F-BAR domain which is less curved than Endophilin NBAR (Fig. 2.14 middle *versus* left) and has been shown to be curvature insensitive and bind all sizes of liposomes equally [56]. On the other hand, IRSp53 is an I-BAR protein (inverted BAR, also called IMD for IRSp53-MIM homology domain) [294] and is relatively flat (Fig. 2.14 right) [57]. IRSp53 is enriched on and stabilises negative membrane curvature [100].

For FCHo2, an extended construct comprising the BAR domain and part of the unstructured region at its C-terminal was used to increase lipid-binding properties (as suggested in [107]). This construct containing residues 1-324 is hence called BARX for extended BAR. As for Endophilin, a fusion construct with sfGFP was used. Despite using the extended construct, binding affinity was lower than observed for Endophilin, especially to 200 nm liposomes (Fig. 2.15, blue). As it was hard to judge the exact curvature preference on 120

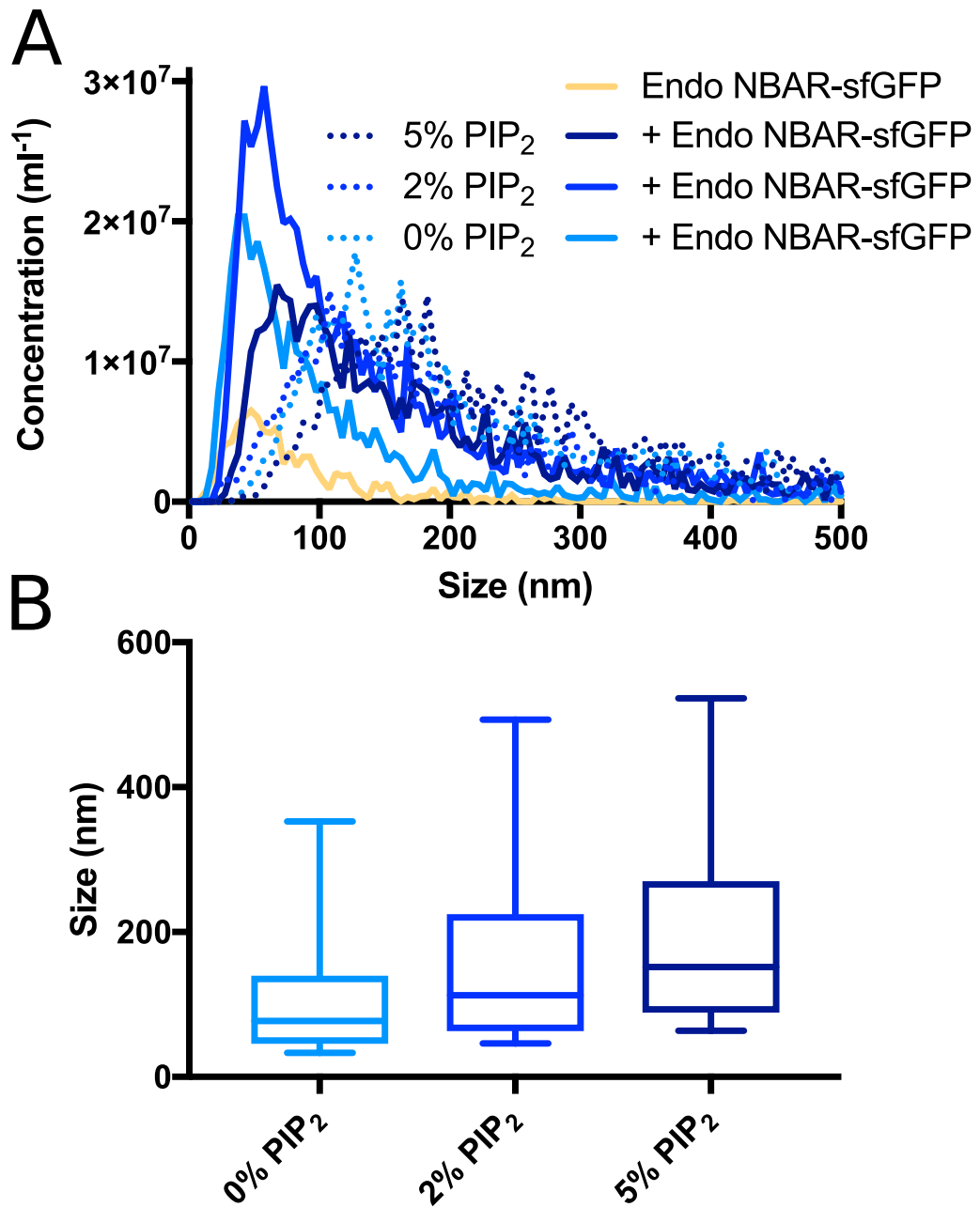


Figure 2.13: Influence of $\text{PI}(4,5)\text{P}_2$ content on curvature sensitivity of Endophilin. A. Size distribution of liposomes input (dotted lines) and Endophilin-bound liposomes only (solid lines) at different concentrations of $\text{PI}(4,5)\text{P}_2$. B. Box plot representation of the same data.



Figure 2.14: Comparison of BAR domain curvatures from Endophilin [295], FCHo2 [56] and IRSp53 [57]

and 80 nm liposomes (Fig. 2.15, red and green), data were normalised (Fig. 2.15B) and showed that FCHo2 indeed bound liposomes equally irrespective of their sizes.

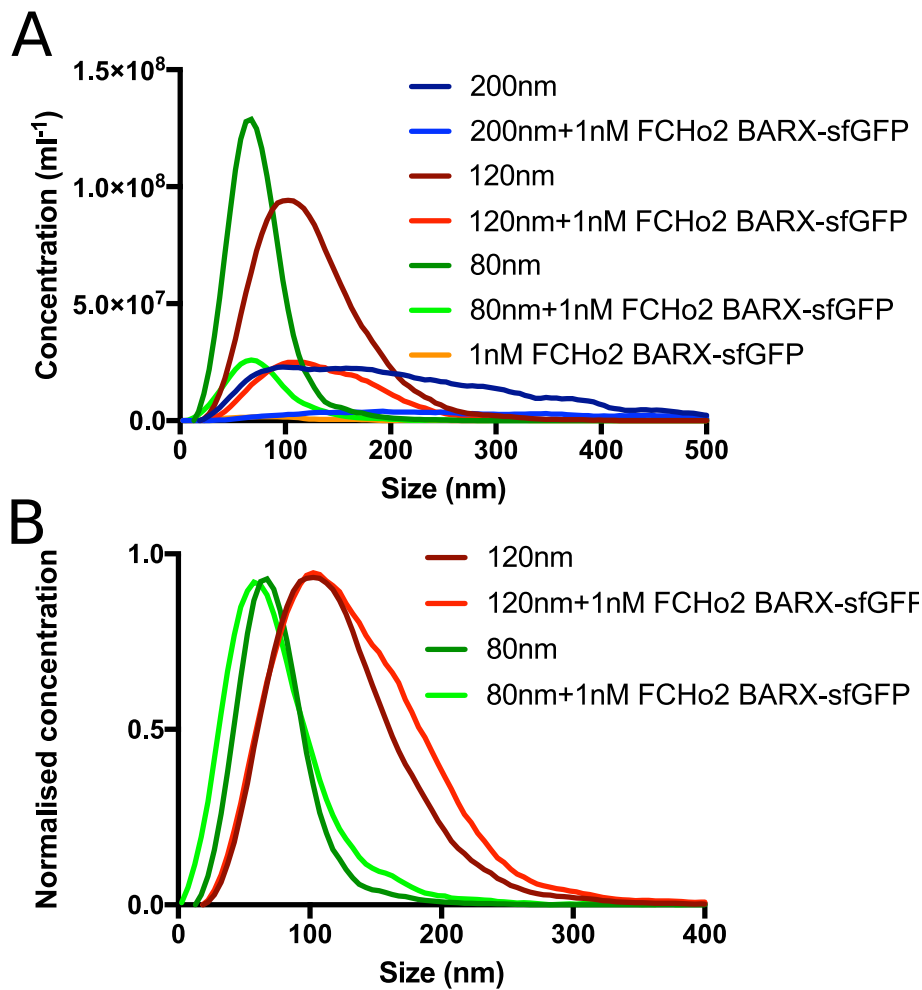


Figure 2.15: A. Curvature sensitivity of FCHo2 BARX-sfGFP. B. Normalised data for 120 and 80 nm liposomes.

As IRSp53 binds to negative membrane curvature, I expected it to preferentially bind to larger liposomes with less positive curvatures. In a similar experiment as the one used with Endophilin and FCHo2, I tested IRSp53 BAR-sfGFP binding to liposomes of different sizes (Fig. 2.16). IRSp53 BAR-sfGFP bound to the largest possible fraction of the 200 nm liposomes with a peak around 350 nm. No binding was observed for 120 and 80 nm. This could be explained by the absence of large enough liposomes for binding. The small peaks observed around 50 nm with IRSp53 BAR-sfGFP in the presence of 120 or 80 nm is of similar intensity as the one without addition of liposomes, therefore corresponding to a small fraction of aggregated protein.

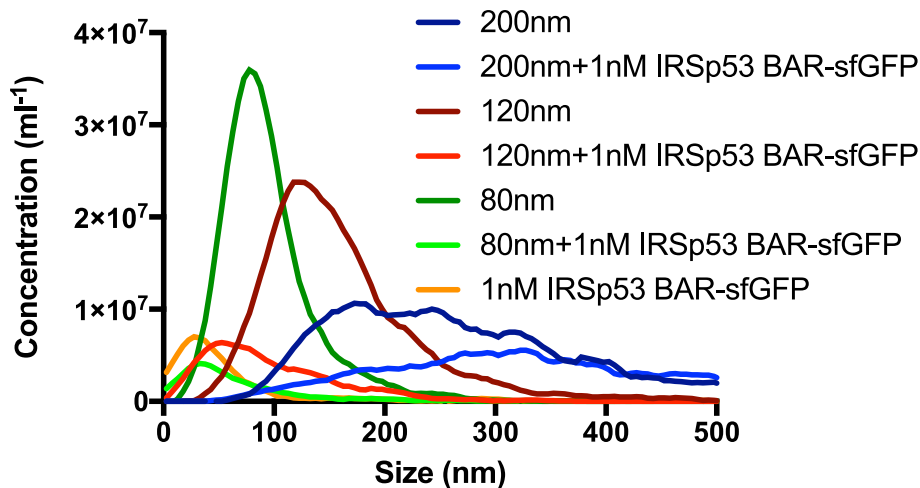


Figure 2.16: Curvature sensitivity of IRSp53 BAR-sfGFP

The experiments with BAR domains of known curvature sensitivity of Endophilin, FCHo2 and IRSp53 confirmed that NTA is a valid technology to measure curvature sensitivity of lipid-binding domains.

2.2.4 Curvature sensitivity of other lipid-binding domains

Having demonstrated that NTA can be used to measure curvature sensitivity of protein binding to membranes, the next step was to expand the range of curvature sensitive domains to non-BAR lipid-binding domain families. The initial plan was to test proteins from all known lipid-binding families. Discoidin C2 and γ -carboxyglutamate rich (Gla) domains were excluded from the screen as they are extracellular proteins carrying post-translational modifications (disulfide bonds for discoidin C2 [296] and vitamin K dependent γ -carboxyglutamate for Gla domains [297]) that would make protein production in *E. coli* impractical. The resulting list of candidate domains I started with is found in table 2.2.

For some of these constructs, cloning failed due to low concentration of the corresponding cDNA in the libraries used. For others, expression in *E. coli* was very low or the resulting purified protein was unstable. This resulted in the following list of purified soluble sfGFP fusion proteins (Tab. 2.3).

As for every experiment using NTA, I started by checking signal from protein alone (in the absence of lipids). Some of the domains showed high concentrations of aggregates. This was surprising as construct boundaries were chosen whenever possible based on domains for which a crystal structure had been obtained. Furthermore, proteins were purified using

Table 2.2: Lipid-binding domains planned for this study

BAR Endophilin A2 Amphiphysin1 FCHo2 IRSp53	PHD ING2 ACF1	C1 PKC δ PKC β 2	FYVE HRS EEA1 WDFY3	GRAM MTMR2 OXR1
BAR-PX SNX9	PTB Dab2 IRS1	C1-C2 PKC β 2	FERM FAK1 Talin1 KRIT1	PROPPIN WIPI1 WDR45B
PH AKT PLC δ 1 CYTH3	PX NCF4 SGK3	C2 PLC δ 1 cPLA2 Synaptotagmin1	ENTH/ANTH AP180 Epsin1	Annexin AnnexinA1 AnnexinA4 AnnexinA7
	PDZ PICK1	C2-Gaq PLC β 1b		Others MICALL1 NECAP1 PHear

Table 2.3: Purified lipid-binding domains

BAR Endophilin A2 Amphiphysin1 FCHo2 IRSp53	PH AKT PLC δ 1 CYTH3	C1 PKC δ PKC β 2	FYVE HRS EEA1 WDFY3	Annexin AnnexinA7
BAR-PX SNX9	PTB Dab2 IRS1	C1-C2 PKC β 2	FERM FAK1 Talin1	ENTH/ANTH AP180 Epsin1
GRAM OXR1	PX SGK3	C2 cPLA2 Synaptotagmin1		Others MICALL1 NECAP1 PHear

size exclusion chromatography which in all cases eluted after the void volume, indicating a soluble state.

Several methods were tried to remove the aggregates, with varying levels of success. The easiest way was to increase salt concentration (the buffer used for NTA, NS, contained 100 mM NaCl) or to use buffer additives as described in [298]. I tried different concentrations of kosmotropes and chaotropes using IRSp53 BAR-sfGFP as a test candidate. Increasing NaCl concentration to 150 mM (Fig. 2.17, dark blue) decreased the number of IRSp53 BAR-sfGFP aggregates, while 500mM mM NaCl (Fig. 2.17, blue) abolished aggregates. Addition of 100 mM LiCl or KCl (Fig. 2.17, green, khaki) decreased the number of aggregates to similar levels as 150 mM NaCl while salts containing divalent ions like CaCl₂ (Fig. 2.17, dark red), MgSO₄ (Fig. 2.17, purple) and (NH₄)₂SO₄ (Fig. 2.17, pink)

suppressed aggregates already at 100 mM. To test how efficient CaCl_2 was to reduce aggregates, lower concentrations were also tested. 50 (Fig. 2.17, red) and even 10 mM CaCl_2 (Fig. 2.17, orange) were sufficient to completely abolish aggregates.

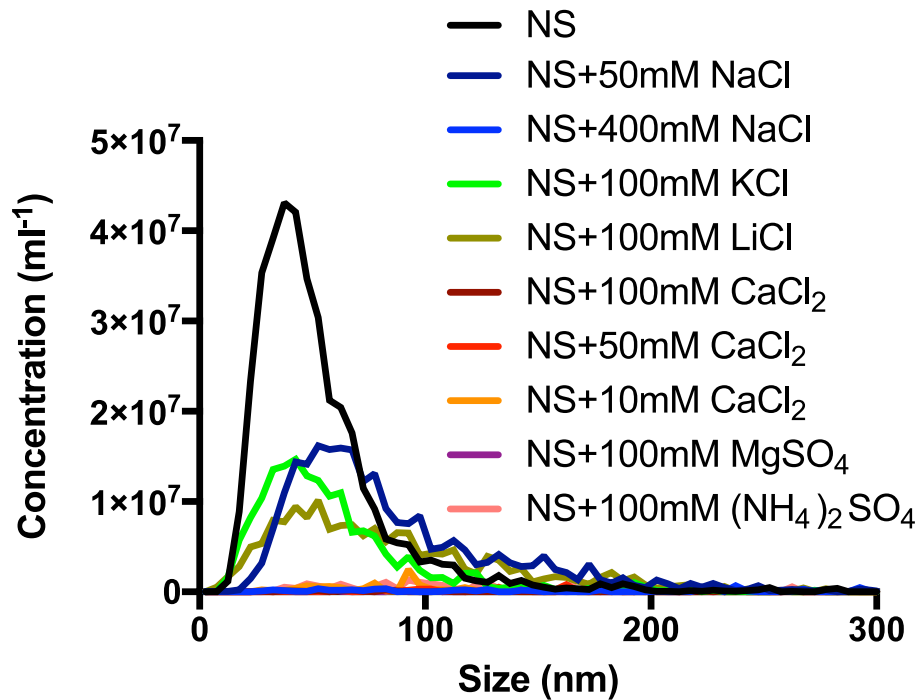


Figure 2.17: Effect of salt additives on aggregates of IRSp53 BAR-sfGFP

I then tested if those buffer conditions were suitable for measurements of curvature preference of membrane binding on NTA. I chose 200 mM NaCl (NS+100 mM NaCl, Fig. 2.18, green) and 10 mM CaCl_2 (Fig. 2.18, red) as additives. Although both reduced aggregates (Fig. 2.18, dark red and dark green), they both also interfered with binding of IRSp53 BAR-sfGFP to liposomes (Fig. 2.18, light red and light green), as no binding could be observed any more. In addition, high salt and calcium ions promote liposome aggregation and fusion [299], making this strategy unsuitable for measurements with liposomes.

I then tried another way to reduce unspecific protein-protein interaction resulting in aggregates by adding an inert carrier protein, in this case His-SUMO. For this experiment I used C1BC2 domain of $\text{PKC}\beta 2$ fused to sfGFP, $\text{PKC}\beta 2$ C1BC2-sfGFP (Fig. 2.19). 1.1 μM His-SUMO was enough to suppress aggregates (Fig. 2.19, dark red), whereas 0.11 μM His-SUMO increased the size of observed aggregates (Fig. 2.19, dark blue). As 1 nM $\text{PKC}\beta 2$ was used in this experiment, a 1000-fold excess of His-SUMO was necessary to abolish aggregates. However, addition of 1.1 μM His-SUMO also impaired binding to liposomes (Fig. 2.19, light red).

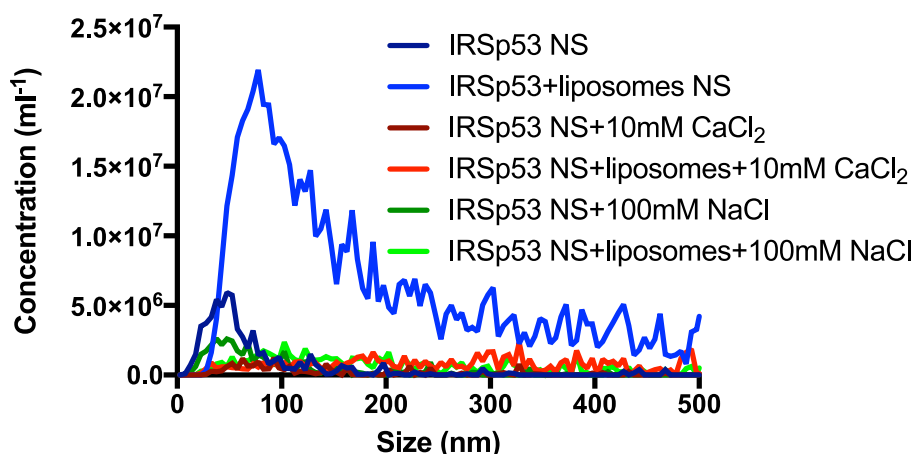


Figure 2.18: Effect of salt additives on binding of IRSp53 BAR-sfGFP to liposomes

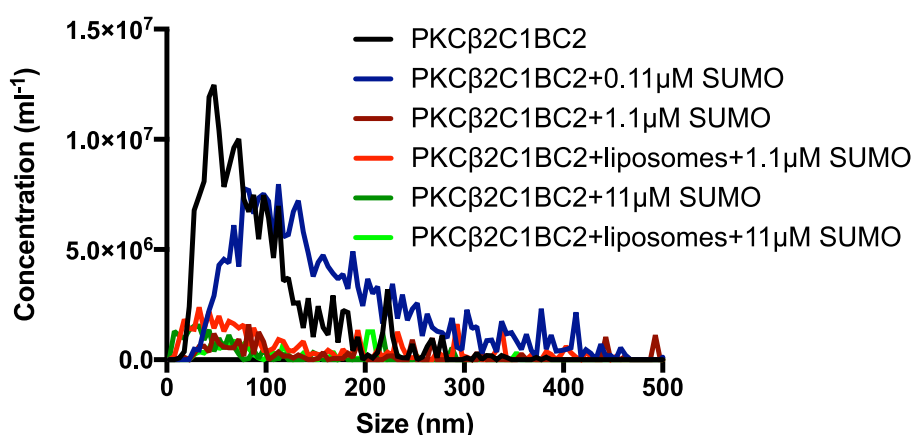


Figure 2.19: Effect of addition of His-SUMO on PKC β 2 C1BC2-sfGFP aggregation and binding to liposomes

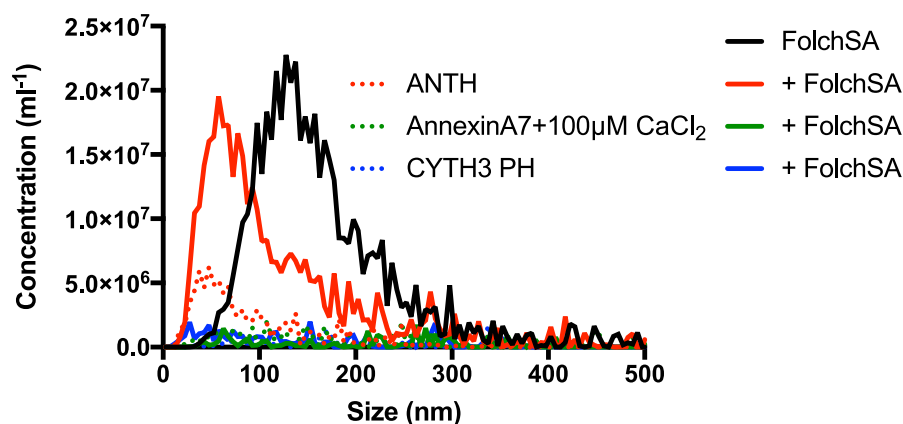
As a last resort, I tried to filter protein using spin concentrators with 100 or 300 kDa molecular weight cut-off. In some cases it reduced aggregates, in other cases, no protein came through as either the whole protein formed aggregates or the protein stuck to the filter. Ultimately, for proteins showing heavy aggregation, the easiest and safest way was to purify them again by nickel affinity chromatography followed by size exclusion.

Out of the 27 expressed sfGFP-lipid-binding domains, 19 were soluble and could be assayed for their curvature sensitivity (Tab. 2.4). Three (PLC δ 1 PH, SGK3 PX and MICALL1) showed high aggregation that I could not suppress by any of the above strategies. Those were excluded from further analysis. Seven other domains (FAK1 FERM, Talin1 FERM, Dab2 PTB, Synaptotagmin1 C2, AP180 ANTH, Epsin1 ENTH and OXR1 GRAM) that still had significant levels of aggregates were nonetheless kept with caution (Tab. 2.4 italicised).

Table 2.4: Soluble lipid-binding domains

BAR Endophilin A2 Amphiphysin1 FCHo2 IRSp53	PH AKT CYTH3	C1 PKC δ PKC β 2	FYVE HRS EEA1 WDFY3	Annexin AnnexinA7
BAR-PX SNX9	PTB <i>Dab2</i> IRS1	C1-C2 PKC β 2	FERM <i>FAK1</i> <i>Talin1</i>	ENTH/ANTH <i>AP180</i> <i>Epsin1</i>
	GRAM <i>OXR1</i>	C2 cPLA2 <i>Synaptotagmin1</i>		Others NECAP1 Phear

After sorting out the aggregation problems, I started measuring curvature sensitivity for these lipid binding domains, using a 1:1 mixture of Sigma Folch and Avanti polar brain lipids (FolchSA) as an initial lipid composition. Although I could observe significant binding for some protein domains like ANTH-sfGFP (Fig. 2.20, red), no binding was observed for other proteins like Annexin A7-sfGFP or CYTH3 PH-sfGFP (Fig. 2.20, blue, green). Interestingly, in this preliminary experiment ANTH-sfGFP showed preference for high curvatures as it was preferentially binding smaller liposomes (Fig. 2.20, red).

**Figure 2.20:** Binding of ANTH-sfGFP, Annexin A7-sfGFP and CYTH3 PH-sfGFP on FolchSA liposomes

As only a few domains bound tightly enough to FolchSA under NTA conditions, I looked in the literature for specific interactions or preferences of lipid-binding domains for headgroups as a way to increase binding affinity. FYVE domains have a preference for PI(3)P [140, 185] and FERM domains for acidic phospholipids or PI(4,5)P₂ [170]. Annexins also prefer acidic phospholipids [179]. C1 domains specifically bind DAG (diacylglycerol) or, with stronger affinity, its analogue PMA (phorbol 12-myristate 13-acetate) [300], whereas C2 domains have more diverse preferences: cPLA2 binds PC [301], Synaptotagmin1 C2 prefers

PI(4,5)P₂ and negatively charged lipids [302, 28]. PH and PTB domains generally bind to phosphoinositides; AKT was reported to bind to PI(3,4)P₂ or PI(3,4,5)P₃ [303, 304], CYTH3 binds to PI(3,4,5)P₃ [305], Dab2 PTB binds PI(4,5)P₂ [164, 163], whereas IRS1 PTB binds either PI(4,5)P₂ or PI(3,4,5)P₃ [306].

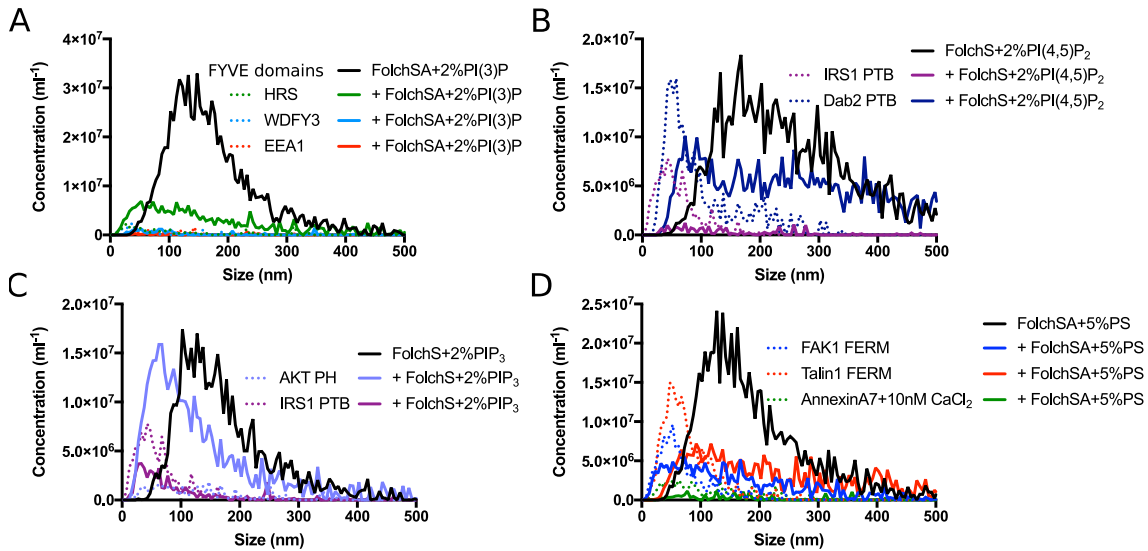


Figure 2.21: Binding of lipid-binding domains on FolchSA spiked with 2% PI(3)P (A), PI(4,5)P₂ (B), PI(3,4,5)P₃ (C) or 5% PS (D)

In order to increase the binding of domains to liposomes, I decided to spike the current liposome composition, FolchSA, with the appropriate headgroup for each domain. I therefore used 2% PI(3)P (Fig. 2.21A), PI(4,5)P₂ (Fig. 2.21B) or PI(3,4,5)P₃ (Fig. 2.21C) or 5% PS (Fig. 2.21D). HRS FYVE-sfGFP displayed binding, albeit low, to FolchSA+2% PI(3)P liposomes (Fig. 2.21A, green), but neither EEA1 nor WDFY3 FYVE-sfGFP (Fig. 2.21A, red, blue) bound to those liposomes. On FolchSA+2% PI(4,5)P₂ liposomes, Dab2 PTB-sfGFP showed binding (Fig. 2.21B, dark blue) despite a lot of aggregates, however IRS1 PTB-sfGFP (Fig. 2.21B, purple) did not. IRS1 PTB-sfGFP did not significantly bind to FolchSA+2% PI(3,4,5)P₃ either (Fig. 2.21C, purple), however AKT PH-sfGFP did (Fig. 2.21C, light blue). Finally, on FolchSA+5% PS, both FAK1 and Talin1 FERM, despite some aggregates, showed some binding (Fig. 2.21D, blue and red). On the other hand, Annexin A7-sfGFP did not bind to FolchSA+5% PS in the presence of a five-fold excess of CaCl₂ (Fig. 2.21D, green). In these preliminary experiments, several lipid-binding domains showed signs of curvature preference. HRS FYVE-sfGFP peak was slightly shifted towards smaller liposomes compared to the input distribution (Fig. 2.21A, green). AKT PH-sfGFP displayed tighter binding to smaller liposomes as well (Fig. 2.21C, light blue). FAK1 and Talin1 FERM-sfGFP-bound liposomes, on the other hand, were slightly larger

than the input distribution, indicating a preference for less positively curved membranes (Fig. 2.21D, blue and red).

Although FAK1 and Talin1 FERM showed some binding to FolchSA+5% PS (Fig. 2.21D, blue and red), this could potentially be increased with higher amounts of PS. Therefore, I tried very high concentration of PS, 50% in Sigma Folch (FolchS), to check if any strong binding occurred with 2 nM protein. Binding could indeed be observed both for FAK1 (Fig. 2.22, blue) and Talin1 (Fig. 2.22, red) FERM-sfGFP.

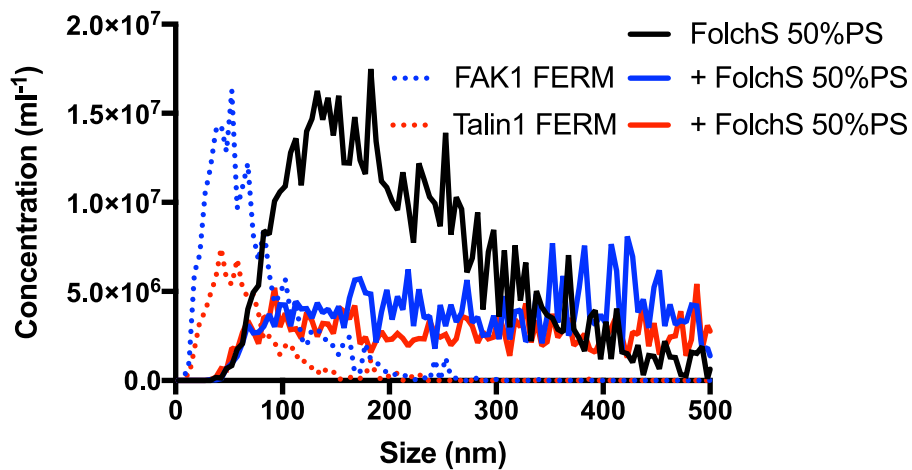


Figure 2.22: Binding of FAK1 and Talin1 FERM-sfGFP on FolchS-50% PS liposomes

I finally tested binding of PKC β 2 C1B-sfGFP and C1BC2-sfGFP. To improve binding, 50% PS and 3% PMA (a diacylglycerol analogue to which C1 domains bind with higher affinity) in FolchS was used (Fig. 2.23). Both constructs displayed similar binding to this liposome composition.

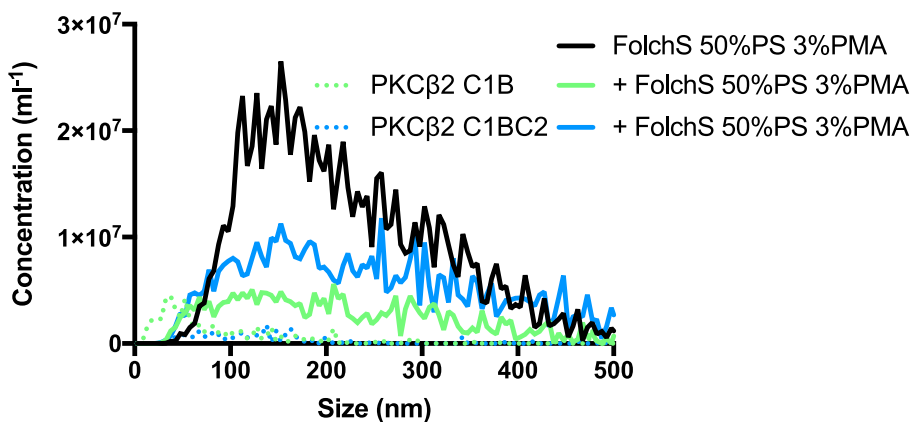


Figure 2.23: Binding of PKC β 2 C1B-sfGFP and C1BC2-sfGFP on FolchS-50% PS+3% PMA liposomes

In order to differentiate binding by C1B domain only from coordinated binding from both C1B and C2 domains, I first wanted to ensure that binding of PKC β 2 C1BC2-sfGFP indeed occurred through both domains, despite high concentrations of PS and PMA used. As C2 domain binding to lipids is calcium dependent, I investigated the binding in the presence of CaCl₂ *versus* EDTA (Fig. 2.24). Binding was similar in the presence of a five-fold excess of calcium (blue) or of EDTA (purple). Even in the presence of a 1000-fold excess of EDTA (pink), it was only marginally reduced, indicating that binding occurs primarily through C1B and that C2 does not contribute significantly. In order to check binding of C1B *versus* C1BC2, a different lipid composition with lower PS and PMA should therefore be used.

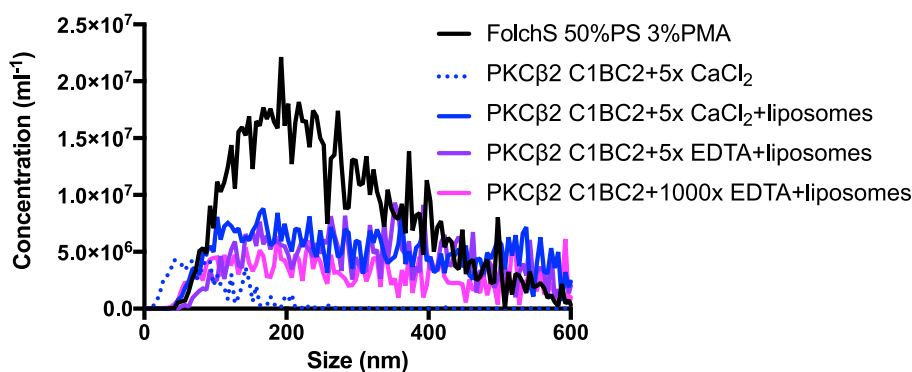


Figure 2.24: Effects of CaCl₂ and EDTA on binding of PKC β 2 C1B-C2 domain on FolchS-50% PS+3% PMA liposomes

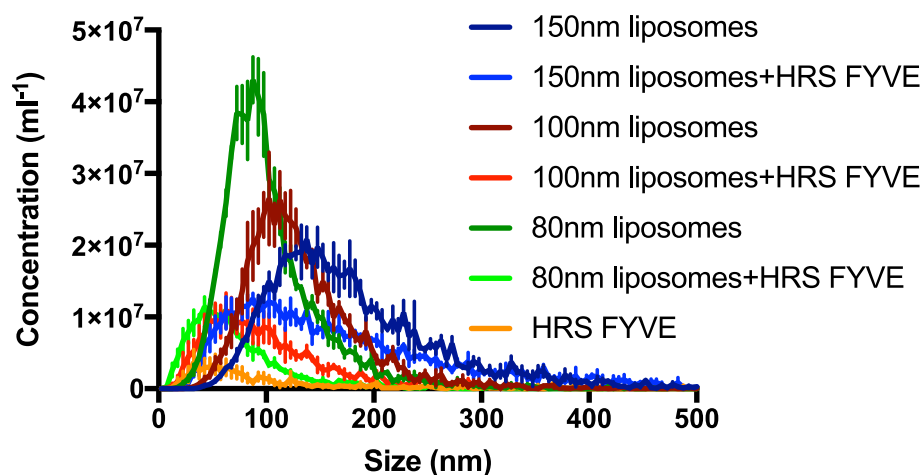
Based on those preliminary experiments, for some lipid-binding domains, I could determine appropriate lipid compositions for which binding could be observed in NTA (Tab. 2.5). I then started investigating their curvature preferences. For this, I used liposomes of composition identified above, extruded at three different sizes, resulting in 200 nm, 120 nm and 80 nm particles. This allowed me to check the consistency of the curvature preferences between different sizes. It also made identification of curvature insensitive domains easier as they would bind equally to every size distribution of input liposomes.

I thus checked curvature sensitivity of HRS FYVE-sfGFP binding to FolchS+2% PI(3)P (Fig. 2.25). Unlike BAR domains, HRS FYVE-sfGFP did not display any striking curvature preference and was found to bind all sizes of liposomes. However, for all three sizes of liposomes, the peak of HRS binding was to slightly smaller sizes than the input distribution, possibly indicating a slight preference for higher curvatures.

The next candidate domain was PKC β 2 C1B-sfGFP. Its curvature preference was measured on FolchS-50% PS+3% PMA liposomes (Fig. 2.26). PKC β 2 C1B-sfGFP was found on all

Table 2.5: Lipid-binding domains with corresponding lipid composition for NTA assays

Construct	Lipid composition
Endophilin A2 BAR	FolchSA
Amphiphysin1 BAR	FolchSA
FCHo2 BARX	FolchSA
IRSp53 BAR	FolchSA
AP180 ANTH	FolchSA
Epsin1 ENTH	FolchSA
AKT PH	FolchS+5% PI(3,4,5)P ₃
Dab2 PTB	FolchS+2% PI(4,5)P ₂
HRS FYVE	FolchS+2% PI(3)P
FAK1 FERM	FolchS-50% PS
Talin1 FERM	FolchS-50% PS
PKC β 2 C1B	FolchS-50% PS+3% PMA

**Figure 2.25:** Curvature sensitivity of HRS FYVE-sfGFP binding to FolchS+2% PI(3)P liposomes. Mean \pm SEM, n=3

sizes of liposomes when using 150 nm liposomes (blue). On the other hand, when using 120 nm liposomes (red), PKC β 2 C1B-sfGFP showed a peak binding closer to 80 nm.

I then assessed FAK1 and Talin1 FERM-sfGFP curvature sensitivity on FolchS-50% PS liposomes (Fig. 2.27, 2.28). When using 200 nm liposomes (blue) both FERM domains bound to all sizes. In the case of Talin1 FERM-sfGFP, the concentration of fluorescent liposomes in the presence of Talin1 FERM-sfGFP was similar to the input concentration of liposomes, indicating that all liposomes present had Talin1 FERM-sfGFP bound, whereas for FAK1 FERM-sfGFP, the concentration of fluorescent liposomes was lower than the total input. This might indicate that Talin1 FERM had a higher affinity for FolchS-50% PS liposomes.

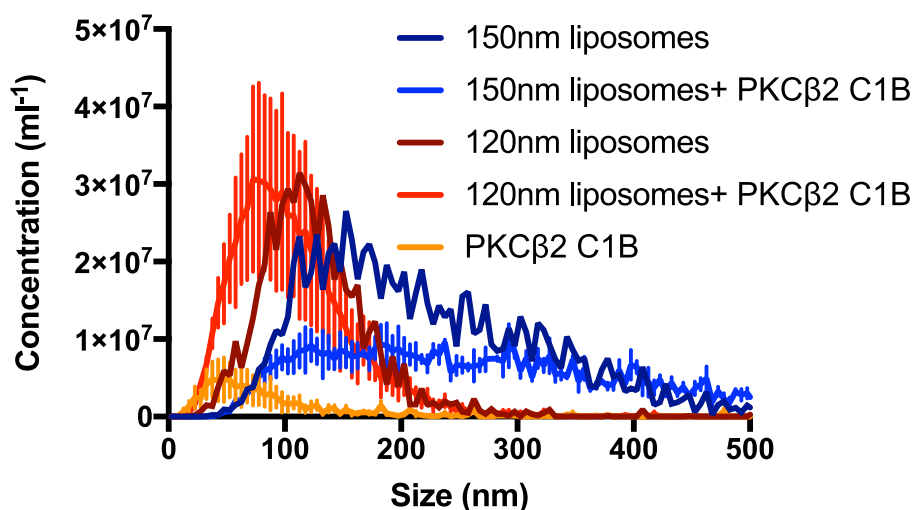


Figure 2.26: Curvature sensitivity of PKC β 2 C1B-sfGFP binding to FolchS-50% PS+3% PMA liposomes. Mean \pm SEM, n=3

Both constructs behaved similarly when added to 120 nm liposomes (Fig. 2.27, 2.28 red); they bound preferentially the smaller end of the size distribution with a maximum binding efficiency close to 100 nm. On 90 nm liposomes (Fig. 2.27, 2.28, green), both FAK1 and Talin1 preferentially bound smaller liposomes with a peak around 80 nm.

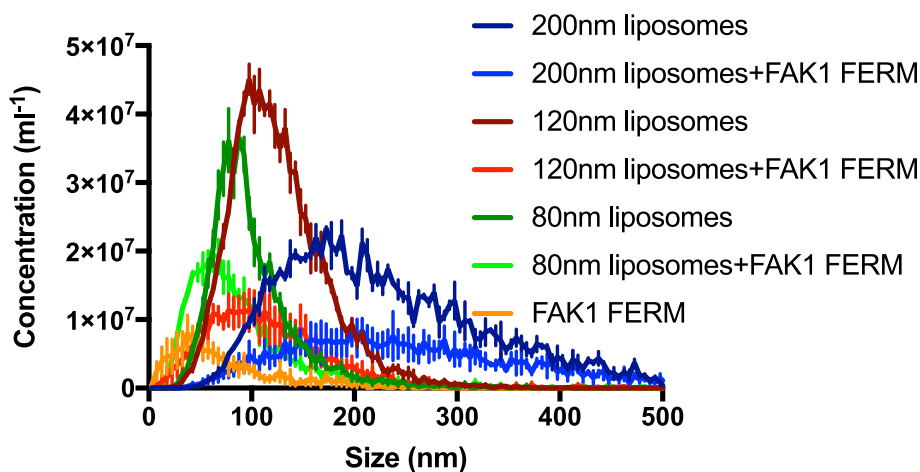


Figure 2.27: Curvature sensitivity of FAK1 FERM-sfGFP binding to FolchS-50% PS liposomes. Mean \pm SEM, n=3

The last domain I checked was the PH domain of AKT. I used Sigma Folch liposomes supplemented with 2 % PI(3,4,5)P₃ (Fig. 2.29). AKT PH-sfGFP consistently preferentially bound to smaller liposomes than the input distribution, indicating preference for higher curvature, a fact that has not been reported to date.

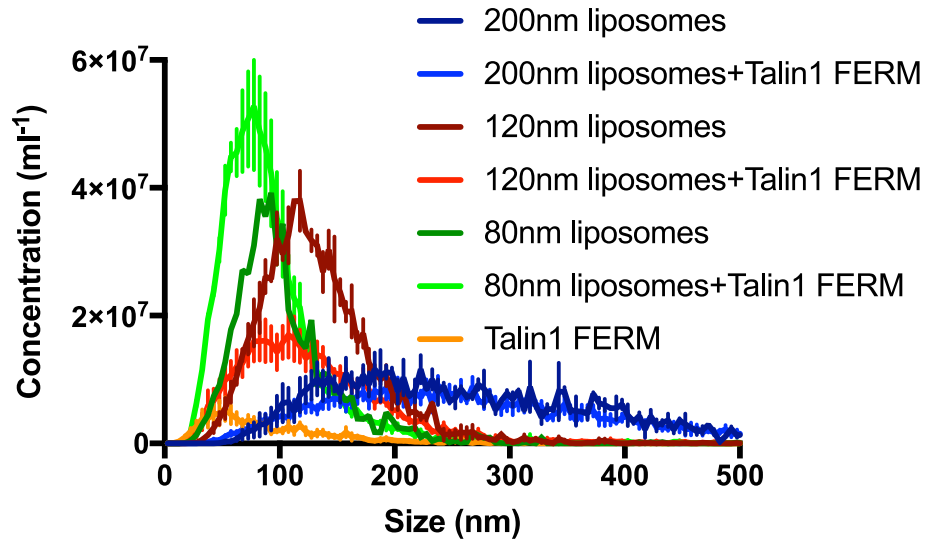


Figure 2.28: Curvature sensitivity of Talin1 FERM-sfGFP binding to FolchS-50% PS liposomes. Mean \pm SEM, n=3

2.2.5 Vesiculation by ENTH

Having shown how NTA could be used to measure curvature sensitivity of protein binding, I was curious to test if it could also be used to test aspects of membrane remodelling. For this I chose the ENTH domain of Epsin1 as a model candidate. ENTH can form tubules (tubulation) or smaller vesicles (vesiculation) after addition to liposomes [24]. In addition, Ford *et al.* identified a mutant in the amphipathic helix, L6W, that increased vesiculation over tubulation.

The first test was to check if I could observe a reduction in size of liposomes after incubation with ENTH (Fig. 2.30). Both ENTH wild-type (wt) and L6W mutant induced a reduction in size of liposomes after incubation. In addition, L6W mutant generated a higher number of small vesicles than the wild-type.

As NTA could detect vesiculation, the next step was to test the effect of ENTH dose on vesiculation. For this, liposomes were incubated with different concentrations of ENTH, either wild-type or L6W mutant, then sized (Fig. 2.31). Increase in concentration of small liposomes was dependent on the concentration of ENTH added for both ENTH wild-type (Fig. 2.31A) or L6W mutant (Fig. 2.31B).

In order to quantify the dose-response of ENTH vesiculation, the concentration of liposomes in the bin with the maximum concentration (here 5 nm bin with centre around 82.5 nm indicated by the dotted black line) was extracted from the data and plotted as function of

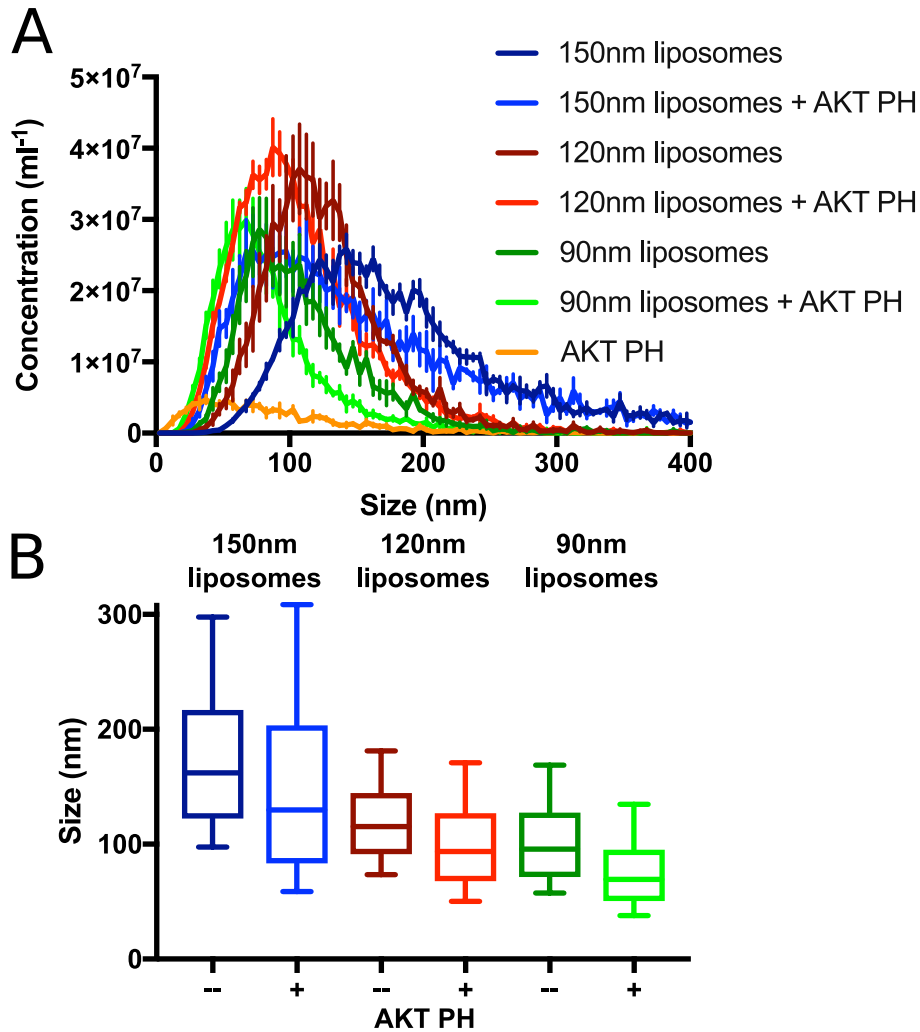


Figure 2.29: Curvature sensitivity of AKT PH-sfGFP binding to FolchS-2 % PI(3,4,5)P₃ liposomes. A. Size distributions of liposomes input (darker curves) and AKT PH-sfGFP bound liposomes only (lighter curves). Mean \pm SEM, n=3. B. Box plot representation of the same .

ENTH concentration (Fig. 2.32). The curve followed a typical dose-response and maximal response (top), inflection point and Hill coefficient were read (Tab. 2.6). ENTH wild-type and L6W showed a similar inflection point ($5 \mu\text{M}$ for wild-type and $4 \mu\text{M}$ for L6W) but mostly differed in their maximum response, which was higher for L6W ($3.2 \cdot 10^7/\text{ml}$) than wild-type ($2.6 \cdot 10^7/\text{ml}$), confirming the higher vesiculation efficiency of ENTH L6W mutant over wild-type.

Table 2.6: Dose-response curve of ENTH vesiculation

	ENTH wt	ENTH L6W
Top ($10^7/\text{ml}$)	2.6(2)	3.20(13)
Inflection (μM)	4(1)	5(1)
Hill coefficient	3.4(1.4)	3.7(8)

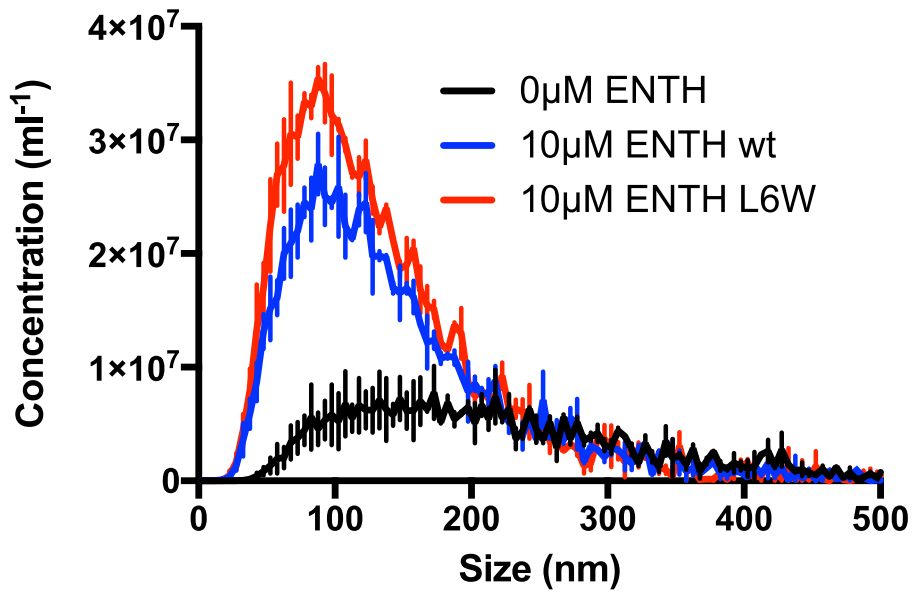


Figure 2.30: Size reduction of liposomes after incubation with ENTH wild-type (wt) or L6W

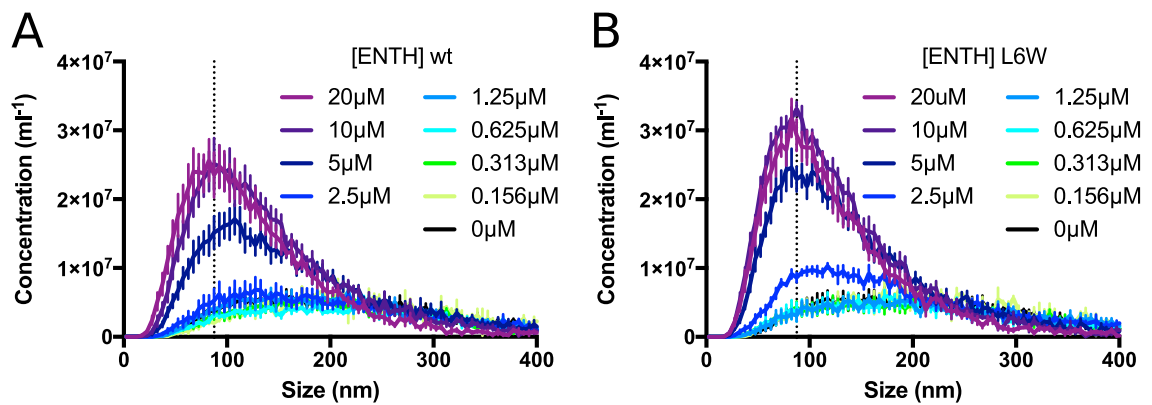


Figure 2.31: Dose-response of vesiculation with ENTH wt (A) or L6W (B)

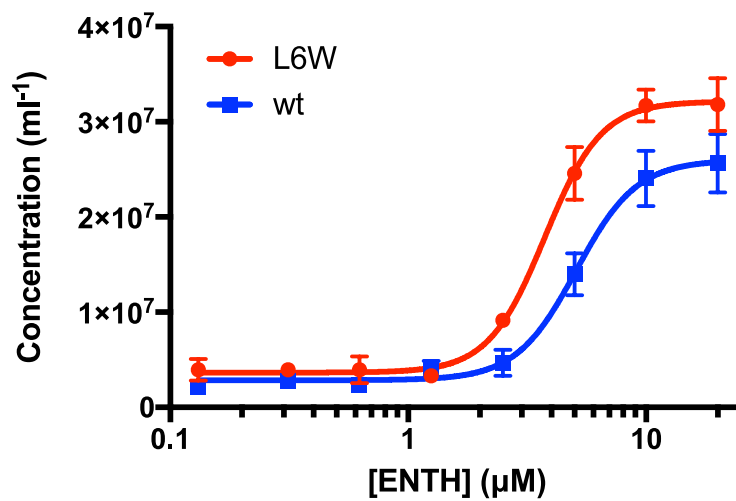


Figure 2.32: Dose-response curve of vesiculation with ENTH wild-type (wt) or L6W

As the dose-response of ENTH vesiculation could be studied by NTA, I then tried if kinetics of vesiculation could also be followed by NTA. For this, I incubated liposomes with ENTH and took aliquots at different time points for analysis. These aliquots were diluted 500-fold in NS buffer, the dilution required to reach the required total particle concentration for analysis by NTA, then sized by NTA (Fig. 2.33). At the 10 seconds time point, the reaction was still in progress. After 20 seconds, the reaction was already over as there was no increase in the concentration of small liposomes after longer incubations. Accurately measuring kinetics of reactions happening within tens of seconds using NTA is difficult due to time needed for manual mixing of samples and should be left for faster methods.

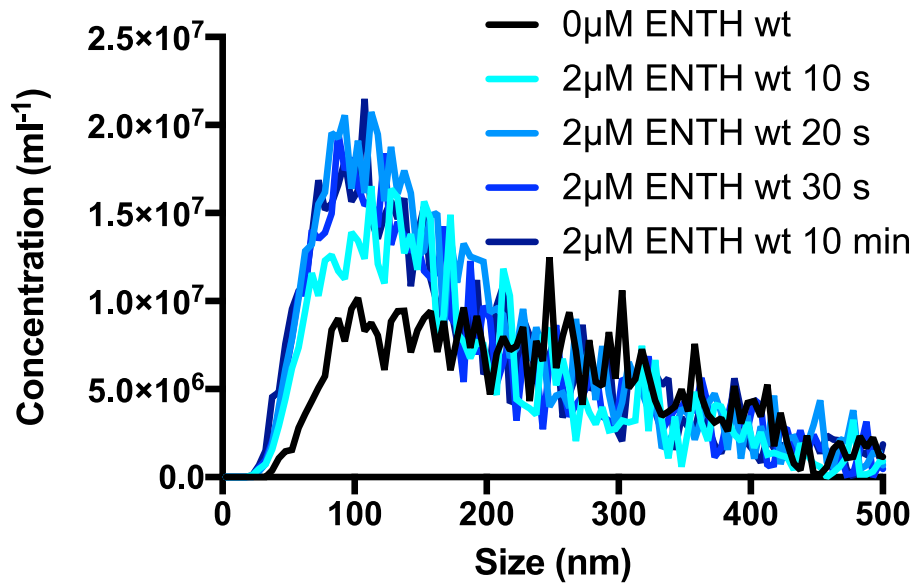


Figure 2.33: Time-course of ENTH vesiculation after addition of 2 μ M ENTH wild-type

2.3 Discussion

Membrane shape of subcellular structures is important for their function. Increasing evidence supports the role of membrane curvature for protein localisation and regulation [307, 308]. Here I have described the development of a new method to test the curvature sensitivity of protein binding to membranes. I showed that Nanoparticle Tracking Analysis (NTA) could reproduce both published curvature preferences for several BAR domain proteins as well as results obtained from liposome flotation assay with Endophilin. Among the non-BAR lipid-binding domains tested, most bound all sizes of liposomes non-selectively and did not show a strong preference for any particular curvature. The PH do-

main of RAC- α serine/threonine-protein kinase (AKT), however, preferentially bound to smaller liposomes, a previously unreported observation.

NTA tracks single particles and calculates their size based on Brownian motion equation. Compared to Dynamic Light Scattering (DLS), NTA was both more precise and more accurate (Fig. 2.5 *versus* 2.6). In addition, NTA was better at sizing a mixed population. This probably derives from the fact that DLS produces a bulk measurement, whereas NTA is a single-particle method. In addition, NTA measurements did not suffer as much as DLS from bias introduced by contaminations by a small fraction of larger, highly diffracting, particles.

Nevertheless, some aspects of NTA equipment and software could be improved. During analysis of the NTA videos, three parameters are set automatically. "Blur" sets smoothing of pixels around a particle to reduce noise. "Max jump distance" sets the maximal radius around a particle where it should be found in the following frame. "Min track length" sets the minimal number of frames a particle has to be tracked in order to be included in the analysis. Although automatically chosen values for each parameter are generally good, they might be different for each movie, especially in recordings with protein alone (which mostly contains residual small aggregates) *versus* protein-liposome mix. In order to unify processing of the data within an experiment, it would be good to keep those parameters consistent, *i.e.* to manually set for movies with protein alone the values automatically chosen for movies with protein-liposome mix. However only values for max jump distance are indicated on the results. It is then not possible for the user to manually input values for blur and min track length as those are only reported as "auto". Although this would prevent the bias towards smaller particles when measuring protein alone, it does not affect the results from measurements of protein-liposome mixes.

In the current setup, the size of all liposomes is measured by diffraction and, following mixing with fluorescent protein, the size of fluorescent, protein-bound, liposomes only is measured under fluorescence mode. Comparison of both size distributions indicates curvature preference. Further analysis could be performed using the fluorescent intensity of each particle, which is proportional to the number of protein molecules bound to a liposome. These data would allow determination of the surface density of proteins as a function of liposome size and curvature. Although fluorescent intensity of each particle is measured for each frame, it is not straightforward to use this information. As particles are flown through the sample chamber and the observation volume, they move not only in x and

y dimensions but also in z, in and out of focus, resulting in a variable recorded fluorescence intensity. In addition, photobleaching occurs due to the high power laser, despite the use of a pump to continuously flow sample. Between z movement and photobleaching, extracting the actual fluorescence intensity of a particle is difficult but could be attempted. During an NTA experiment, several parameters are recorded for each particle, namely diffusion coefficient and fluorescence intensity for each frame. The current analysis relies on the NTA software that provides the number of particles per bin size only. Further developments will be done to improve the analysis performed to better fit our questions.

Measurements of curvature sensitivity of protein binding to membranes using NTA were heavily influenced by protein-specific characteristics. NTA can detect particles as small as 10 nm [286] and will pick up signal from any diffracting or fluorescent particle, depending on the insertion of a fluorescence filter. As such, presence of protein aggregates will interfere with accurate measurements. A surprisingly high proportion of sfGFP-fusion lipid-binding domains purified here (about a third of the domains from the initial purification round) showed presence of aggregates. Causes can range from rough treatment during purification, concentration, freezing or thawing of the protein, choice of construct boundaries (although they were chosen whenever possible to match those used for structure determination by crystallisation) or interference of the GFP fusion with protein stability. Increasing salt concentration helped reduce the concentration of aggregates (Fig. 2.17), hinting at aggregation resulting from electrostatic interactions, but in turn also significantly reduced binding to liposomes (Fig. 2.18), making this of little use for routine measurements of curvature sensitivity with NTA. No general solution against aggregates has been found yet, although careful procedures during concentration and thawing of protein seemed the most helpful. This nevertheless raises a caution with NTA results where a protein preferentially binds to high curvatures, as NTA is unable to distinguish between protein aggregates and protein bound to small liposomes. NTA results should therefore be further validated with a different method.

Another important decision to make while using NTA for measuring curvature sensitivity is the choice of fluorophore for lipid-binding domains. Here, superfolder Green Fluorescent Protein (sfGFP) [291] was chosen to streamline purification by eliminating the need of additional steps for labelling with an organic fluorophore. Despite its large size, 27kDa, similar or larger than most lipid-binding domains used in this thesis, sfGFP fusion Endophilin NBAR had similar curvature preference as the Alexa488-labelled protein

(Fig. 2.10). sfGFP or Alexa488 turned out to be good choices as two studies showed that some organic dyes display unspecific binding to membranes [309, 310]. Those studies used eggPC or eggPC:DOPS 9:1 [310] or cell membranes [309] and showed that Alexa488 has little unspecific binding to membranes unlike for example atto647N. They however pointed out that unspecific dye binding to membranes is highly dependent on the lipid composition used, especially its overall charge, as well as the charge and hydrophobicity of the fluorophore tested. The affinity of sfGFP alone for Folch liposomes was assessed in NTA; no detectable signal of fluorescent liposomes could be recorded after incubation of Folch liposomes with sfGFP (data not shown), indicating the suitability of sfGFP under these conditions.

Lipid composition is the next factor that influences NTA measurements, both in terms of binding affinity as well as curvature sensitivity. Folch lipids, extracted from brain, contain a complex mixture of lipids which should reflect natural membrane composition. However, most non-BAR lipid-binding domains tested here did not bind strongly enough on Folch liposomes for their curvature preference to be assessed (Fig. 2.20). In order to detect enough fluorescent liposomes after addition of a lipid-binding domain, the specific lipid headgroup those domains interact with had to be added, such as 2% PI(3)P for FYVE domains (Fig. 2.21A), 2% PI(4,5)P₂ for PTB domains (Fig. 2.21B), 3% PMA for C1 domains (Fig. 2.23) or 2% PI(3,4,5)P₃ for AKT PH (Fig. 2.21C). For some domains such as HRS FYVE, Dab2 PTB, PKC β 2C1B or AKT PH, this was efficient and curvature sensitivity data could be collected, whereas for some other proteins of the same domain families like EEA1 or WDFY3 FYVE (Fig. 2.21A) or IRS1 PTB (Fig. 2.21B,C), this was not sufficient and little to no binding was observed.

In NTA assays, fluorescent protein concentrations must be kept low (1-5 nM) to reduce background fluorescence. This is low compared to binding affinities of small lipid-binding domains for lipids. For example, yeast PH domains were found to bind to lipids with an affinity in the range of 1-20 μ M [162, 311], indicating that the concentrations of protein used in NTA measurements are around a thousand fold lower than the K_D . Similarly, dissociation constants for BAR domain dimers in solution have been measured in the range of 5-10 μ M range [58, 26], although others reported subnanomolar affinity for Endophilin dimers [103]. Using 1-5 nM protein in NTA assays would correspond to a concentration about a thousand fold lower than the dimerisation K_D , nevertheless binding to liposomes was observed. This would suggest that BAR domains would bind membranes as monomers

and then dimerise on the membrane, as has been previously postulated [66]. This discrepancy between protein concentration and affinity to lipids might explain why for most small lipid-binding domains lipid composition had to be carefully adjusted in order to push the equilibrium towards binding. In addition, liposome concentration has to be in the range of 10^8 - 10^9 particles/ml, corresponding to picomolar concentrations of particles or 10-100 nM lipids for NTA. For comparison, bulk assays generally use 0.1-1 mM lipids and 1 μ M protein. Therefore, the protein-to-lipid ratio in NTA experiments is about ten times higher than in bulk assays. This can reduce the apparent curvature sensitivity by allowing protein to bind to less ideally curved liposomes. The higher protein-to-lipid ratio would also favour curvature generation by protein crowding, further decreasing apparent curvature sensitivity.

Lipid composition also played a role in curvature sensitivity of protein binding. This was particularly noticeable in the reduction of stringency of curvature preference of Endo NBAR-sfGFP to liposomes with increasing PI(4,5)P₂ (Fig. 2.13). This could be explained by an increase in binding sites and therefore affinity, which could compensate for the slightly less ideal curvature of larger liposomes. As this has for now been only tested for Endophilin NBAR domain, an alternative explanation could be that increasing PI(4,5)P₂ facilitates local remodelling by Endophilin, allowing it to comfortably bind on larger liposomes by locally generating its preferred, higher, curvature. To distinguish between these explanations, this experiment should be repeated with a different protein domain which is not capable of generating membrane curvature. This however hints at a potential concern for domains that are detected as being curvature insensitive. It could be possible that they are able to locally remodel membrane, a phenomenon that would remain unseen by NTA and most other techniques for measuring curvature sensitivity.

In the case of the FERM domains of Talin1 and FAK1 (Fig. 2.27, 2.28), liposomes containing 50 % PS were used in order to obtain high affinity binding. However, this high, unphysiological, concentration of negatively charged lipid headgroups might mask a curvature preference by providing excess binding sites. Those experiments should be repeated with lower concentrations of PS, that would still ensure sufficient binding without introducing artefactual binding sites. Alternatively, curvature sensitivity of those FERM domains could be tested on liposomes containing 2 % PI(4,5)P₂ [170].

In practical terms of using NTA as a method to measure curvature sensitivity, it means that lipid composition should be carefully adjusted for each lipid-binding domain family,

and potentially even for each domain within a family. This will obviously result in a lower throughput of screening.

From those preliminary results as well as the literature, it seems that there are two main ways of sensing curvature for individual proteins [66, 67, 68, 6]. Proteins can have dedicated domains, BAR domains, that can recognise any curvature given their elongated shape and mode of lipid binding *via* several positively charged residues spread along a 20Å-long rod [26, 69]. Alternatively, if proteins only have to be targeted to highly curved membranes, a small, economical, amphipathic helix or hydrophobic insertions might suffice [82, 81]. Protein complexes can also become curvature sensitive, either as oligomers, in the case of dynamin for example [70], or as heteromeric protein complexes like the class III phosphatidylinositol-3-kinase PI3KC3 (Vps34) complex I [99].

Some indications of curvature sensitivity were observed in preliminary experiments for ANTH, HRS FYVE, FAK1 and Talin1 FERM domains and confirmed for AKT PH domain. However, most small, non-BAR lipid-binding domains studied here showed little to no curvature preference. Although the screen is still ongoing and will help identify other curvature-sensitive domains, it seems that for most of those protein domains, curvature is not the main mode of targeting. Considering their high specificity for lipid headgroups that are synthesised at very defined locations within a cell (like PI(3)P for FYVE domains on early endosomes [312]), curvature sensing might be redundant with efficient targeting mediated by lipid headgroup specificity only.

NTA identified AKT PH domain as a lipid-binding domain that preferentially binds to highly curved membranes. I therefore looked at AKT PH domain structures to try to understand how this small lipid-binding domain could sense high curvature. The two known mechanisms of curvature sensing would be scaffolding through oligomerisation of the PH domain - considering it does not contain a BAR domain - or by insertion of an amphipathic helix in hydrophobic defects. The PH domain from AKT has been shown to interact and form complexes [313], so this mechanism of high curvature sensing could be possible if after oligomerisation, AKT PH formed a curved scaffold. Comparing crystal structures of apo-AKT PH (Fig. 2.34A,B orange) with the structure in complex with inositol 1,3,4,5-tetrakisphosphate (IP4), the water-soluble headgroup of PI(3,4,5)P₃ (Fig. 2.34A,B blue) [314] shows that upon binding to IP4, a previously flexible loop forms an α -helix. However, this helix, consisting of residues DVDQREA, is not amphipathic. Curvature sensing could instead be mediated by insertion of hydrophobic amino acids. Indeed, Trp22 and most

especially Tyr18, located in a loop, could sense lipid packing defects (Fig. 2.34C, cyan). All these potential mechanisms of curvature sensing by AKT PH should be further investigated.

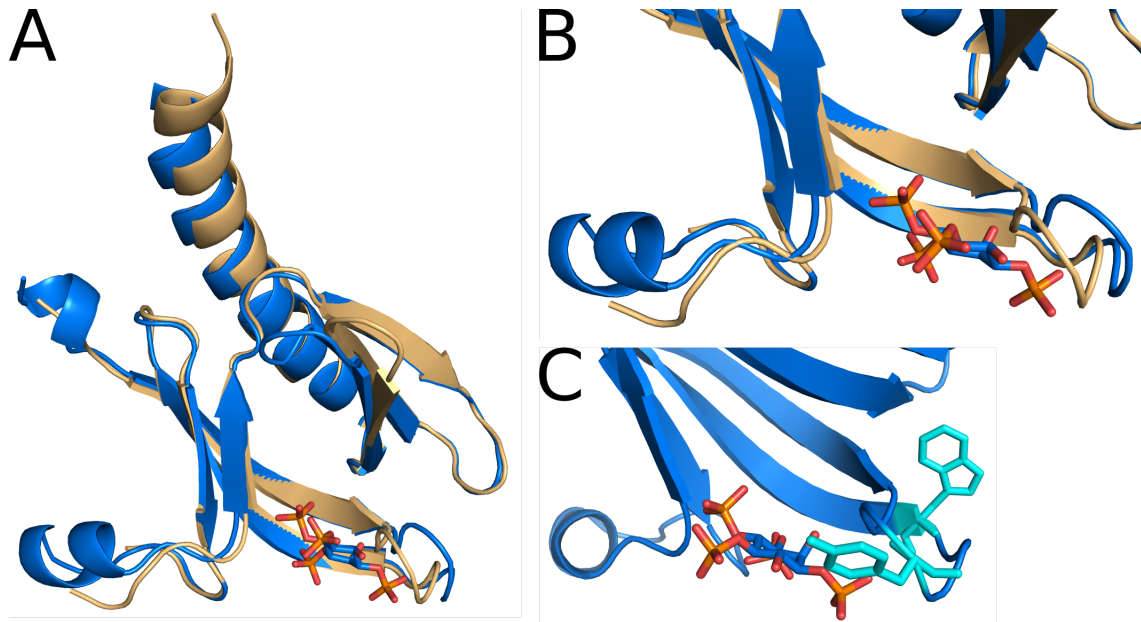


Figure 2.34: Crystal structures of AKT PH in absence (orange) and presence (blue) of IP4 [314]. A. Full PH domain. B. Detail of the membrane interaction surface and IP4 binding region. C. Localisation of Tyr18 and Trp22 (cyan) at the membrane contact interface.

AKT PH domain is specific for PI(3,4)P₂ and PI(3,4,5)P₃, lipids primarily found in late endocytosis as well as some areas of the plasma membrane after activation of PI-3-kinases [315]. AKT is also recruited to EGFR-containing endosomes by Rab5-APPL [316]. As early endosomes consist of a network of tubules and vesicles [317], areas of high curvature are common. AKT PH domain preference might be an additional targeting mechanism to such particular regions on endosomes.

In curvature sensitivity measurements performed using tethered liposomes in SLiC assays, N-BAR as well as F-BAR and I-BAR proteins were found to preferentially bind higher curvatures [98]. The authors explained this preference for smaller liposomes to be driven by amphipathic helices binding into hydrophobic defects, superseding the presence of a BAR domain. However, in my results using NTA as well as the rest of the literature including *in vivo* data, curvature sensing of BAR-domain proteins correlates with the three-dimensional structure of the BAR domain [26, 56, 69]. This discrepancy between both sets of results could be explained by differences in experimental setup. Tethering liposomes to a surface might introduce additional hydrophobic defects, explaining why in SLiC assays only, curvature sensing *via* amphipathic helices dominated, even for BAR domain proteins.

Here I showed that NTA technology could be used as a tool to characterise curvature sensing of protein binding to lipids. NTA reproduced known curvature preferences of BAR domains and allowed identification of a previously non-reported non-BAR domain curvature sensor, the PH domain of AKT. NTA was also shown to be a valuable tool to study membrane remodelling, as exemplified for ENTH domain-mediated vesiculation. This could then be used to characterise newly identified membrane remodelling domains, for example NECAP1 (Adaptin ear-binding coat-associated protein 1) PH-ear domain [318]. Broadening the screen of non-BAR lipid-binding domains should help identify more curvature-sensing domains. This knowledge, combined with study of the relative contributions of Endophilin amphipathic H0 helix *versus* BAR domain in curvature sensing, should expand our understanding of how protein domains sense membrane curvature.

Chapter 3

Endophilin binding motif in Endophilin-mediated endocytosis

3.1 Introduction

Membrane compartmentalisation provides distinct environments to separate biochemical processes within the cell and between the cell and its surroundings. However, this separation introduces the need for transport systems across membranes. Several mechanisms have been described for endocytosis [319, 320]. Endocytosis consists of three main phases: cargo recognition, vesicle formation and membrane scission. Endophilin, a protein formed of an N-BAR (Bin/Amphiphysin/Rvs) domain followed by an SH3 (Src-homology 3) domain, can potentially contribute towards all three steps. Its N-BAR domain can generate curvature and participate in vesicle formation and membrane fission [26], while its SH3 domain binds cargo and cargo adaptors in fast Endophilin-mediated endocytosis (FEME) [120]. However, the basis for this recognition by Endophilin SH3 is not clear.

SH3 domains are 50-70 residues long and consist of a five-stranded β -barrel linked by loops and a short 3_{10} helix (Fig. 3.1A). The canonical binding site on SH3 domains consists of a shallow hydrophobic groove formed by conserved residues (amino acids displayed in sticks in Fig. 3.1A) mostly in $\beta 3$ and $\beta 4$ strands as well as the tip of the asparagine-threonine (RT) loop [321, 322].

SH3 domains generally bind proline-rich sequences folded in a polyproline helix type II (PPII) [324, 325]. PPII helices are all-*trans* left-handed helices with a perfect three-fold

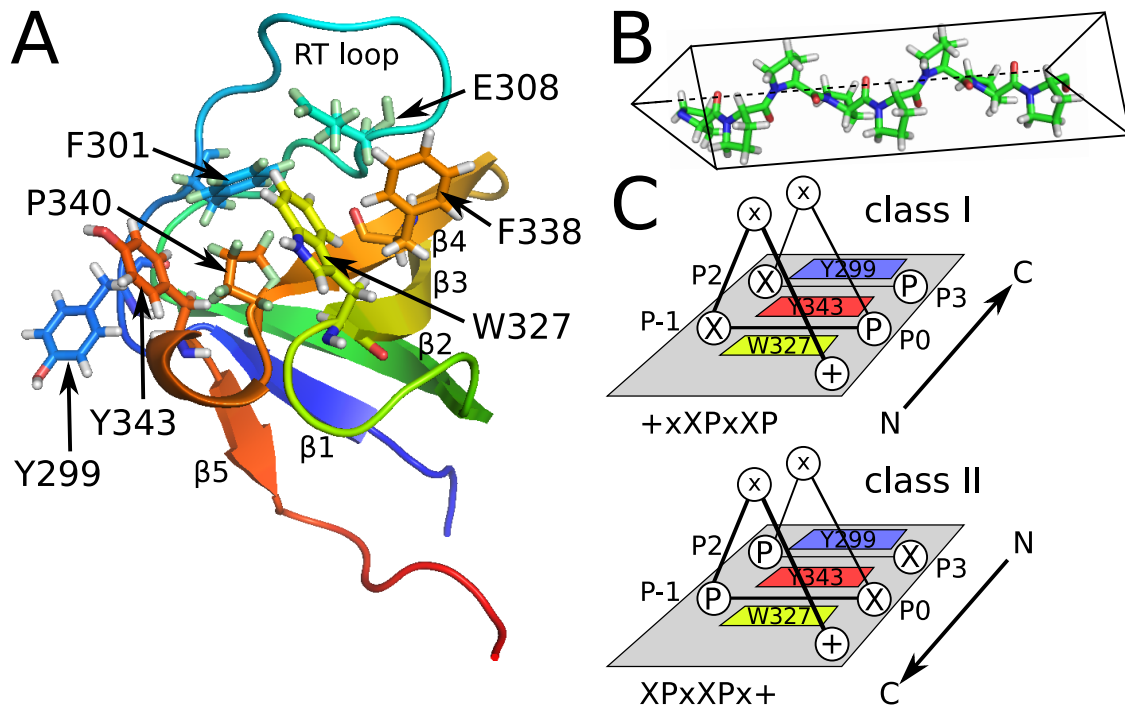


Figure 3.1: SH3 binding to polyproline II helix. A. Endophilin SH3 binding site. Residues lining the binding groove are in sticks (3IQL) [229]. B. Polyproline II helix triangular prism. C. Models of class I and II SH3 binders on Endophilin showing residues contacting SH3 (modified from [323]). SH3 subsites where PPII helix residues contact the SH3 are numbered (P3, P2, P0 and P-1) on the models.

rotational symmetry (Fig. 3.1B). The triangular prism shaped PPII sits on the SH3 on its base, with two residues per helix turn contacting the SH3 surface. The minimal binding motif for SH3 was found to be PxxP (P representing prolines and x any residue) [326, 324]. A PxxP motif can bind to SH3 in two opposite orientations, depending on the position of a positively charged residue on the peptide contacting a negatively charged pocket on the SH3 surface, the specificity/compass pocket (Fig. 3.1C) [323, 327]. This defines two classes of SH3 binders. Class I binders are characterised by a +xXPxXP motif (capitalisation illustrates residues contacting the SH3 surface, + indicate basic residues) and bind C \rightarrow N when facing the SH3 binding groove as in figure 3.1A, whereas class II binders canonically consist of XPxXPx+ and bind N \rightarrow C [326, 324]. Depending on the orientation of the motif, the proline residues of PxxP are in different positions on the SH3. To facilitate comparison between SH3 domains, the subsites where the XP motifs bind are numbered (P3, P2, P0, P-1) (Fig. 3.1C).

Most of the binding energy and therefore specificity is conferred by non-proline residues that contact the SH3, from both XP motifs as well as the positively charged residue in the specificity pocket. Although most SH3s prefer Arg in the specificity pocket, some are

specific for Lys *e.g.* Crk (CT10 Regulator of Kinase) SH3 [328]. Other SH3 domains have different preferences. For example, the specificity pocket of Abl SH3 (Abelson tyrosine-protein kinase 1) lacks conserved negatively charged residues and Abl SH3 accommodates a hydrophobic residue instead of a basic one [326, 329]. Similarly, some SH3 domains like PI3K prefer a basic residue like arginine in the central PxRP motif, with that arginine forming a salt bridge with a glutamate side chain on the RT loop of the SH3 [324]. Other SH3s lacking acidic residues at those positions like Src SH3 prefer a hydrophobic residue like leucine [324]. For some ligands, amino acids outside of the core binding motif contact SH3 residues outside of the peptide binding groove, providing additional specificity [330]. Alternatively, residues next to the core binding motif prevent binding, for example phosphoserine, acidic residues or prolines immediately C-terminal to the core binding motif [331]. For example, autophosphorylation of PAK (p21-activated kinase) prevented binding by Nck (non-catalytic region of tyrosine kinase adaptor protein 1) SH3 [331]. Although most SH3 domains bind canonical proline-rich sequences, some SH3 bind with similar affinities non-consensus peptides. For example, Grb2 C-terminal SH3 (Signal transducing adapter molecule 2) binds PxxxRxxKP with the central RxxK motif forming a 3_{10} helix [332, 333] or SKAP55 (Src kinase associated protein of 55 kDa) recognises a RKxxYxxY motif, lacking any proline [334].

Specificity of Endophilin SH3 has first been studied using phage peptide libraries [335] and P+RPPxpr was identified as the Endophilin binding motif. Further experiments using amino acid point substitutions on two proline-rich motifs of the Synaptojanin proline-rich domain (PRD) lead to xPRRPxPR being recognised as the consensus Endophilin binding motif [335]. In this consensus sequence, the two "x" represent any amino acid apart from acidic ones, the first two proline residues can be replaced by phenylalanine, leucine or isoleucine albeit with reduction of binding, and the last proline can be substituted with any hydrophobic residue (Phe, Tyr, Trp, Leu, Ile, Val). Similarly, the first and third arginine residues can be replaced by lysine. This sequence does not fit perfectly either class I or class II consensus sequence and orientation of the peptide on Endophilin remains unclear, although Cestra *et al.* favoured a class I binding [335].

A recent publication investigated the binding of Itch ubiquitin ligase PRD to several SH3 domains using truncation constructs and mutagenesis in GST pull-downs [336]. The affinity for Endophilin SH3 was measured at $K_D = 33$ nM, a high affinity compared to the common 1-100 μ M affinities for SH3-PRD complexes [337]. Although no crystals were obtained for

Endophilin SH3 – Itch PRD, modelling based on β -PIX – Itch PRD crystal structure and pull-down data identified Itch(249-258) KPSRPPRPSR as the Endophilin binding motif binding in N -> C orientation (class II). Although sharing some similarities, this motif does not conform exactly to the consensus xPRRPxPR identified by Cestra *et al.* [335], leaving the question of an Endophilin SH3 binding motif open.

In addition to proline-rich peptides, some SH3 domains also bind folded protein domains, like ubiquitin [338, 339] or Ubl (ubiquitin-like) domain [229]. An NMR structure of Endophilin SH3 and Parkin Ubl complex shows that Parkin Ubl binds in the canonical, PRD-binding, SH3 groove in a manner reminiscent of SH3-PRD interactions [229]. Although most of the binding is provided by the unstructured C-terminus of Parkin Ubl that folds upon binding, additional contacts are formed between hydrophobic residues on the globular Ubl domain and the peptide binding site of Endophilin SH3.

Experiments based on peptide libraries or modelling identified similar but not identical Endophilin binding motifs, but definitive determinants of Endophilin SH3 specificity are still lacking. Here I have characterised binding of Endophilin SH3 to cell surface receptors and adaptor proteins involved in Endophilin-mediated endocytosis and have derived models of the binding based on NMR data.

3.2 Results

3.2.1 *In vitro* interaction of adrenergic receptors ICL3 and adaptor proteins with Endophilin

Endophilin A (SH3GL1/2/3) consists of a curvature-generating N-BAR domain and a SH3 domain (Src homology 3) mediating protein-protein interactions. Endophilin has recently been described in a clathrin-independent endocytosis pathway responsible for the uptake of bacterial toxins [119] and activated cell-surface receptors [120]. Endophilin SH3 binds some aminergic G-protein coupled receptors (GPCRs) directly in their intracellular loop 3 (ICL3), whereas interaction with receptors tyrosine kinase (RTKs) is mediated by adaptor proteins [120]. Although SH3 domains bind proline-rich domains (PRD), the exact binding site of Endophilin is unknown. Characterising the binding site would allow a database search for a similar motif and help identify other cell-surface receptors potentially

taken up via FEME (fast Endophilin-mediated endocytosis), which would contribute to understanding this clathrin-independent pathway.

In order to identify suitable candidate proteins for characterisation of the Endophilin binding site, I confirmed some of the pull-down experiments from Boucrot *et al.* [120]. For this, I used GST-tagged fragments of adrenergic receptors ICL3 and adaptor proteins PRDs to pull-down Endophilin full-length from bacterial lysate overexpressing Endophilin (Fig. 3.2). Similarly to what Boucrot *et al.* reported [120], α_{2A} (ADRA2A) and β_1 (ADRB1) adrenergic receptors were able to pull-down Endophilin, whereas β_2 adrenergic receptor (ADRB2) could not (Fig. 3.2A). As expected, both constructs of CIN85 (Cbl-interacting protein of 85 kDa) as well as Alix (ALG-2-interacting protein X) PRD could pull-down Endophilin (Fig. 3.2B).

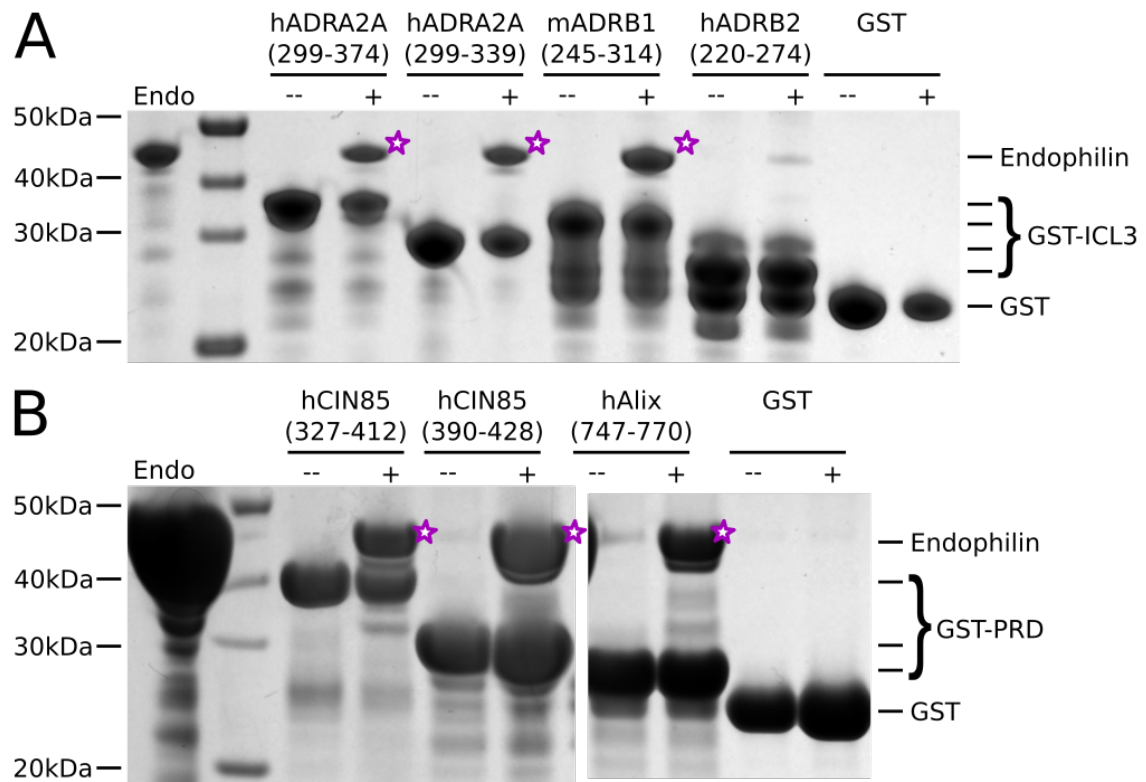


Figure 3.2: Endophilin pull-down by adrenergic GPCRs ICL3 (A) or adaptor proteins PRD (B).

Potential Endophilin binding sites were further characterised by mutating putative recognition site amino acids to alanine. The effect of a mutation was evaluated by pulling down EGFP-tagged ICL3 or PRD fragments from cell lysate using GST-SH3 [120], [HMM unpublished] (Tab. 3.1). Mutation of lysine or arginine to alanine in several, distinct sites of ADRA2A or ADRB1 ICL3 resulted in a decreased pull-down efficiency, suggesting that

Endophilin SH3 binds on multiple sites on these ICL3. In the case of CIN85 and Alix, although the screen was not comprehensive, only one putative binding site was identified (Tab. 3.1).

Table 3.1: Sequences of GPCR ICL3 and adaptor protein PRD tested by mutagenesis experiments.

Colour scheme represents proline residues in blue and residues affecting (red) or not (green) pull-down by Endophilin SH3 when mutated to alanine. Mutation data were taken from [120] or by data from HMM (unpublished).

ADRA2A(299-374)	SDHAERPPGPRRPERGPRGKGKARASQVKPGDSLPRRGPGA TGIGTPAAGPGEERVGA AKASRWRGRQNREKRFTF
ADRA2A(299-339)	SDHAERPPGPRRPERGPRGKGKARASQVKPGDSLPRRGPGA
ADRB1(245-314)	RVFREAQKQVKKIDSCERRFLGGPARPPSPEPS PGGPRPADSLANGRSSKRRPSRLVALREQKALKT
CIN85(327-412)	PPDFEKEGNRPKKPPPSAPVIKQGAGTTERKHEIKKIPPERP EMLPNRTEEKERPEREPKLDLQKPSVPAIPPKKPRPPKTNSLS
CIN85(390-428)	LQKPSVPAIPPKKPRPPKTNSLSRPGALPPRRPERPVGP
Alix(748-770)	PPTKPQPPARPPPPVLPANRAP

Although mutagenesis screen helped pinpoint potential binding site(s), further characterisation was needed, for which two test candidates, one ICL3 and one adaptor protein PRD, were chosen. Among the adrenergic receptor ICL3 fragments tested, ADRA2A(299-339) (called ADRA2A from now on) was the shortest construct that bound tightly to Endophilin (Tab. 3.1) and was more stable than ADRB1 as indicated by the absence of degradation products (Fig. 3.2A). Among the adaptor protein constructs, Alix(748-770) PRD (called Alix from now on) was also a good candidate, as it was the shortest construct tested (Tab. 3.1).

In order to characterise the strength of interaction and evaluate the suitability of those candidates for structure determination, the affinity of interaction was measured by isothermal titration calorimetry (ITC) (Fig. 3.3). Endophilin SH3 affinity for Alix was $1.3 \pm 0.2 \mu\text{M}$ (Fig. 3.3A) and $13 \pm 3 \mu\text{M}$ (Fig. 3.3B) for ADRA2A. In both cases, N was close to 1 (0.89 for Alix and 0.91 for ADRA2A), indicating a 1:1 binding. Interestingly, for both peptides, binding was mostly driven by electrostatics, hydrogen bonds and van der Waals interactions, as $-T\Delta S$ was small and the enthalpy ΔH provided most of the binding energy ΔG (as illustrated in figure 3.3C for Alix). The affinity to Endophilin SH3 was sufficient for both peptides to pursue structural characterisation.

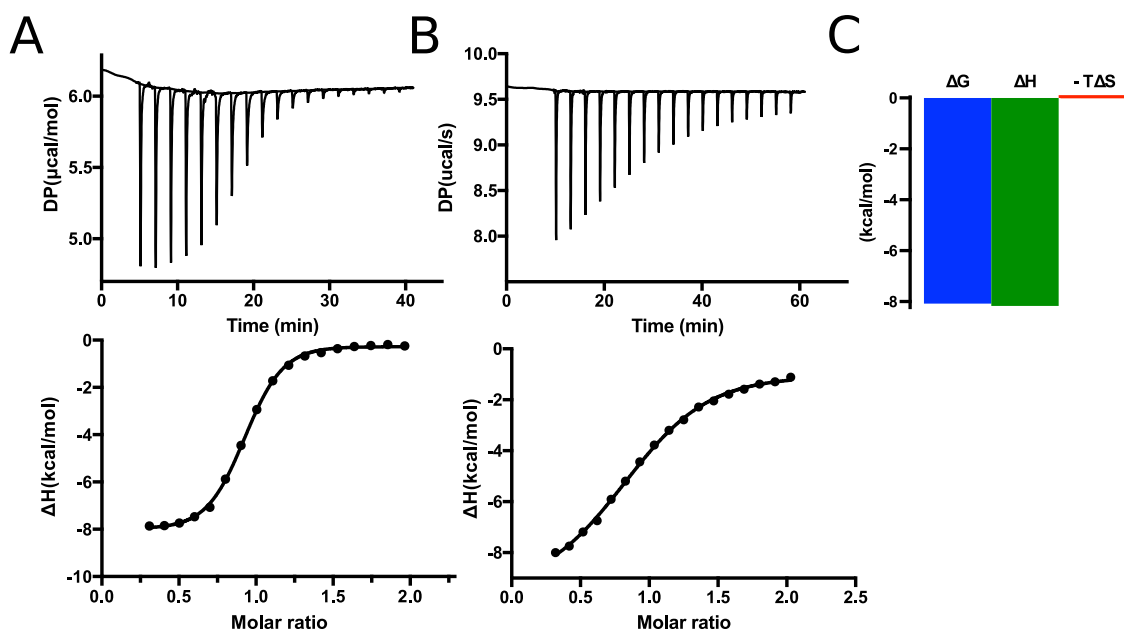


Figure 3.3: ITC measurements of affinity between Endophilin SH3 and Alix PRD (A) or ADRA2A ICL3 (B) fragments. Top: released heat, bottom: binding enthalpy. C. Contributions of ΔH and $-T\Delta S$ to final ΔG

3.2.2 Endophilin A1 SH3 – Alix PRD interaction: NMR model

Chemical shift perturbation analysis

With its low micromolar affinity for SH3, Alix PRD was particularly well suited for structural studies. Co-crystallisation trials of SH3 Alix were conducted but did not produce any reproducible crystals. Crystallisation of an SH3-linker-Alix fusion construct did not lead to any usable crystal for structure determination either. However, as both SH3 (6 kDa) and Alix (2.8 kDa) are small, this constitutes an ideal system for nuclear magnetic resonance spectroscopy (NMR) studies. All NMR experiments were done in collaboration with Trevor Rutherford.

An NMR-active nucleus with a spin $I = 1/2$ exists in two different degenerate states. In a constant magnetic field \mathbf{B}_0 , nuclear spins align with the field or against the field, generating two states with different energies. The energy difference between both states is in the range for photons in the radio frequency (RF) range. Application of RF pulses perturbs the alignment of the spins with \mathbf{B}_0 . The energy difference between both states depends on field strength. The corresponding resonance frequency is most commonly expressed as a frequency ratio, called the "chemical shift", in order to facilitate comparison of data obtained on machines of different magnetic field strengths. Chemical shift for a resonance

is sensitive to its local environment, as the movements of surrounding nuclei and electrons generate a local induced magnetic field. An NMR spectrum is a plot of chemical shifts [340].

Hydrogen (^1H) has a spin of $I = 1/2$, as do ^{13}C and ^{15}N . As ^{13}C and ^{15}N are naturally rare isotopes, protein has to be labelled with these isotopes for resonances to be observed in an NMR spectrum at reasonable protein concentrations. In protein NMR, given the high number of atoms, NMR spectra are generally recorded in more than one dimension. An NMR experiment particularly useful for proteins is a ^1H - ^{15}N HSQC (Heteronuclear Single Quantum Coherence). In this ^1H - ^{15}N two-dimensional correlation spectrum, every spot represents an N-H group, giving information on the magnetic environment of all backbone amide groups (from all amino acids apart from prolines) as well as side chain N-H of Gln, Asn and Trp. Changes in the environment give rise to perturbation of the position of corresponding peaks in the HSQC, which thus provides a sensitive probe for monitoring the formation of protein complexes.

In the first NMR experiment, the stability and folding state of Endophilin SH3 was checked by ^1H - ^{15}N HSQC (Fig. 3.4 red). The ^1H resonances were dispersed indicating a well-folded protein, as in an unfolded region nuclei are in a more similar chemical environment and ^1H resonances tend to cluster [341]. After addition of saturating amounts of Alix (Fig. 3.4, blue), some SH3 peaks were perturbed (examples indicated by arrows), suggesting a change in chemical environment following Alix binding. There were, however, no major conformational changes in the SH3 as most of the chemical shifts remained identical even after addition of Alix.

SH3 state and chemical shift perturbation (CSP) of some, but not all, residues after addition of Alix confirmed suitability of NMR for characterisation of Endophilin binding site. In order to get valuable information on binding site from these spectra, each resonance peak on the spectra needs to be assigned to a specific N-H group in Endophilin SH3. The NMR structure of Endophilin SH3 in complex with Parkin Ubl (ubiquitin-like domain) has been solved and resonance assignments for Endophilin SH3 were obtained [229]. However, despite performing ^1H - ^{15}N HSQC under the same conditions, the overlap between both spectra was not sufficient to use resonance assignments obtained by Trempe *et al.* [229]. Assignment for SH3 resonances would therefore need to be carried out *de novo*.

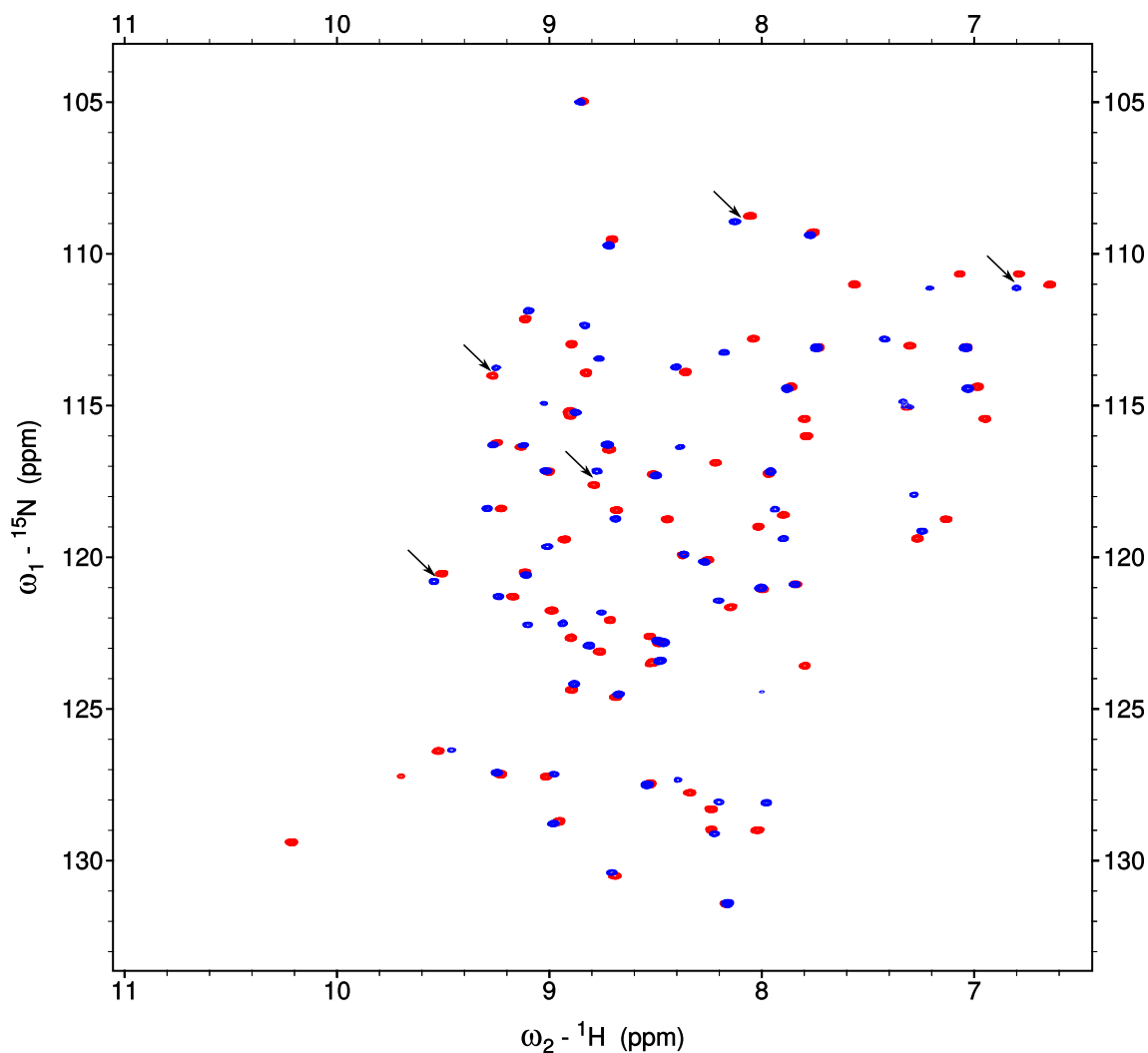


Figure 3.4: ${}^1\text{H}$ - ${}^{15}\text{N}$ HSQC overlay of Endophilin SH3 free (red) or with saturating amounts of Alix (blue). Arrows indicate examples of peaks perturbed upon addition of Alix.

Resonance assignments for proteins is easier with the use of triple-resonance spectra, using ${}^1\text{H}$, ${}^{15}\text{N}$ and ${}^{13}\text{C}$ resonances. In those experiments, magnetisation is not only transferred from amide ${}^1\text{H}$ to ${}^{15}\text{N}$ and back but also to the neighbouring carbon atoms. Using those experiments allows establishing connectivity between the resonances of two adjacent residues in the sequence. For example, CBCA(CO)NH connects an amide group with $\text{C}\alpha$ and $\text{C}\beta$ of the preceding residue (Fig. 3.5A, left) and HNCACB connects an amide group with $\text{C}\alpha$ and $\text{C}\beta$ of both this residue as well as the preceding one [342] (Fig. 3.5A, right). Using these experiments, resonances for ${}^1\text{H}$, ${}^{15}\text{N}$ and ${}^{13}\text{C}$ for the backbone ($\text{C}\alpha$ and amide group) as well as side chain $\text{C}\beta$ can be assigned to a particular protein residue. An example is shown in Figure 3.5B for a short segment of Endophilin SH3. With the presence of signal at the same ${}^{13}\text{C}$ chemical shift in both HNCACB of one residue and CBCA(CO)NH of the preceding residue, a link can be established between the two residues. This information,

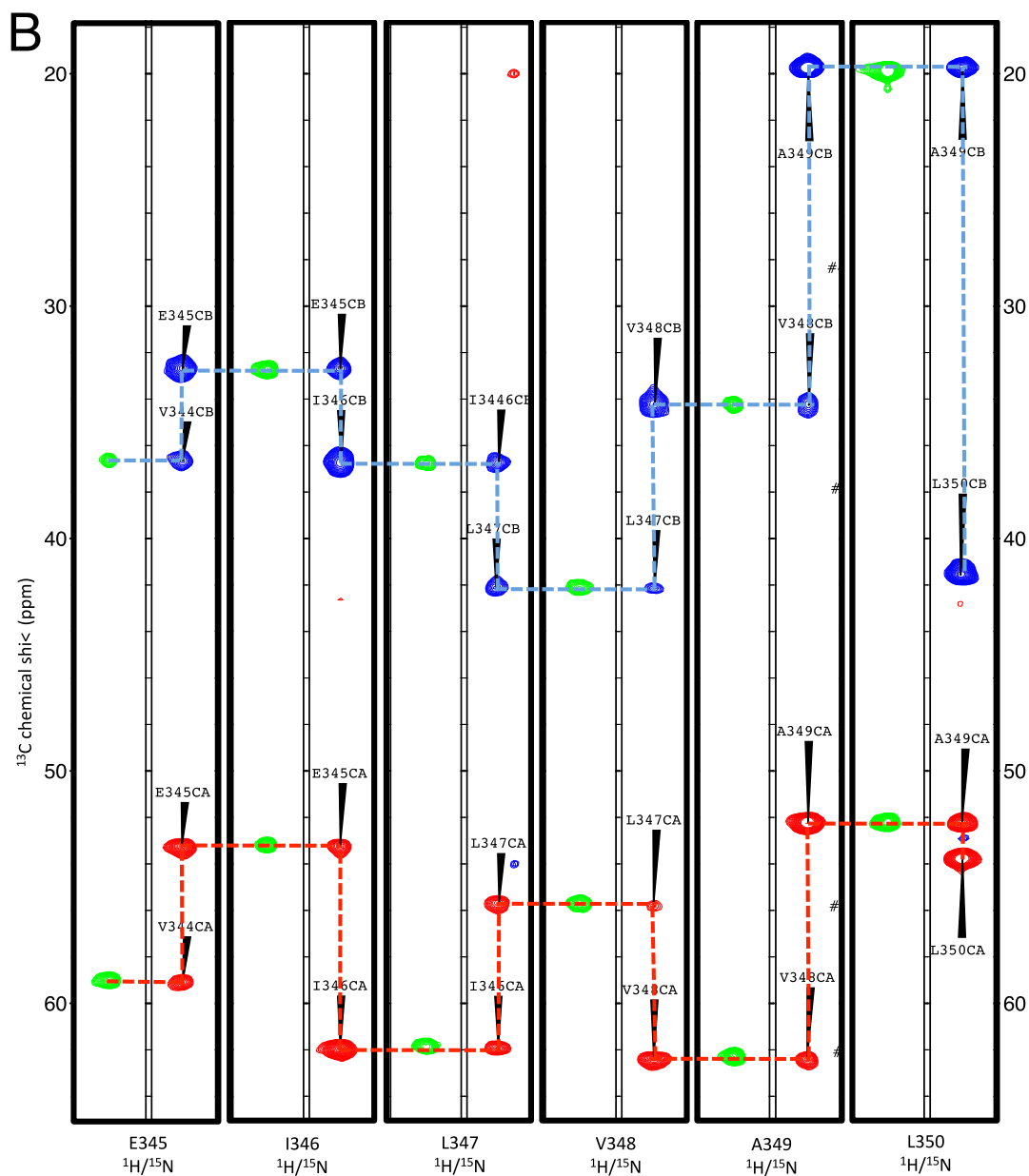
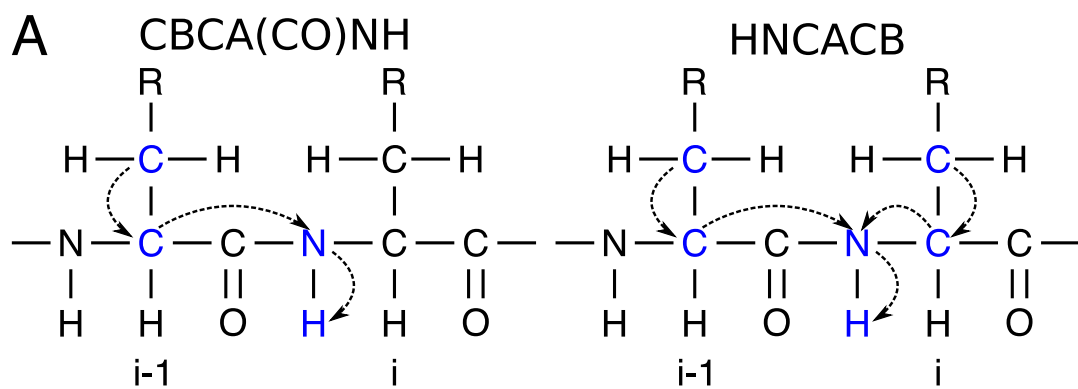


Figure 3.5: A. Magnetisation transfer in CBCA(CO)NH (left) and HNCACB (right) spectra. B. Assignment of a fragment of Endophilin SH3 using CBCA(CO)NH (green) and HNCACB (red for C α and blue for C β)

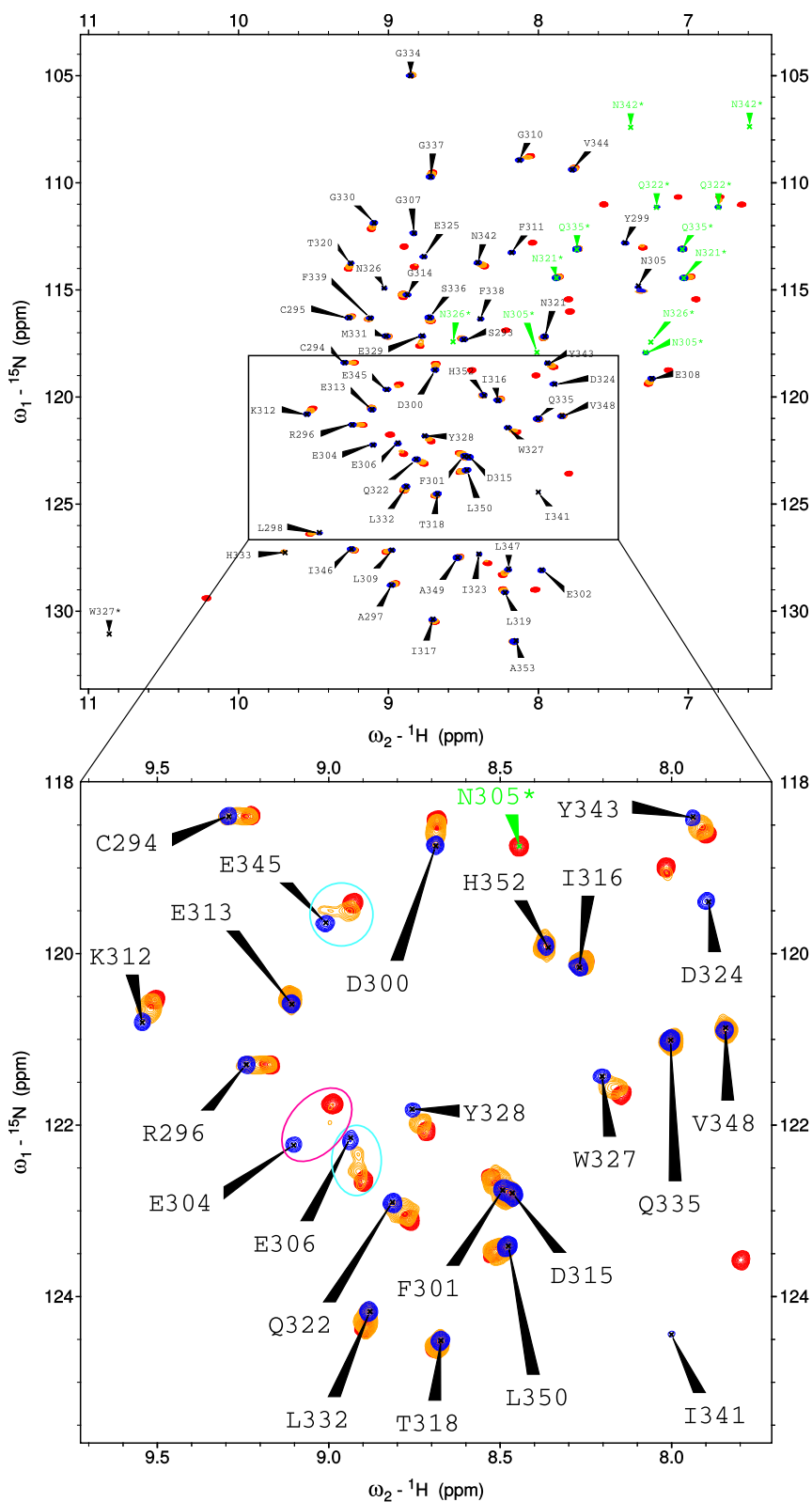


Figure 3.6: Assigned ^1H - ^{15}N HSQC of Endophilin SH3 free (red) or with increasing amounts of Alix (yellow, blue). Blue and pink circles indicate residues with clear intermediate exchange rate.

together with the $C\alpha$ and $C\beta$ chemical shift values characteristic for each amino acid types allows identification of each spot and unambiguous assignment for the backbone resonances of a protein.

After complete assignment of SH3 resonances, CSP data for Endophilin SH3 obtained after addition of increasing amounts of Alix can be quantified and assigned to a particular residue (Fig. 3.6). Assignments are shown in black for backbone N-H and green for Asn and Gln side chain N-H. SH3-Alix shows evidence of intermediate exchange rate on the NMR timescale. This can be seen by the broadening of a single peak at intermediate concentrations (see E304, pink circle in Fig. 3.6) resulting in a reduction of peak intensity, in the case of E304 below the set intensity threshold. Intermediate exchange rate can also be deduced from the presence of two resolved peaks at an intermediate frequency (see E345 or E306, blue circles in Fig. 3.6). This contrasts with slow exchange (tighter binding), where two environments would be seen at the same frequencies of free and bound states or fast exchange (weaker binding), where only one peak at an intermediate frequency weighted according to the relative population of free and bound states would be seen.

The strength of a CSP can be quantified in both ^1H and ^{15}N directions and is then combined into a weighted CSP as described in Material & Methods (chapter 5). The resulting shift map of CSP plotted along the SH3 sequence (Fig. 3.7A) was similar to what was reported for Endophilin SH3 – Synaptojanin PRD or Parkin Ubl complexes [229] and together with the heatmaps of CSP intensities on the structure of Endophilin suggest that Alix binds in the canonical SH3 peptide binding groove (Fig. 3.7B). Repeating the same experiment but using ^1H - ^{13}C HSQC revealed five additional residues with high CSP (L298, D300, P303, N305 and Q322) and confirmed that the canonical SH3 peptide binding groove is the interaction surface with Alix (Fig. 3.7C). No evidence of Alix peptide wrapping around the SH3 and making additional contacts could be seen in either of the spectra as in both, the interaction surface seemed restricted to the canonical one (Fig. 3.7B, C).

The process was then repeated for $^{13}\text{C}/^{15}\text{N}$ -labelled Alix with unlabelled SH3. After assignment of Alix resonances, ^1H - ^{15}N HSQC spectra were recorded in the absence (red) or with saturating concentrations (blue) of Endophilin SH3 (Fig. 3.8A). Chemical shifts for residues R14 and V19 as well as L20, N23 and R24 (blue circles in Fig. 3.8A) were heavily perturbed after addition of SH3. An HSQC recorded for an intermediate concentration of SH3 (not shown) did not show peaks at an intermediate chemical shift but produced severe line broadening. A heatmap of Alix coloured according to the intensity of CSP indicates

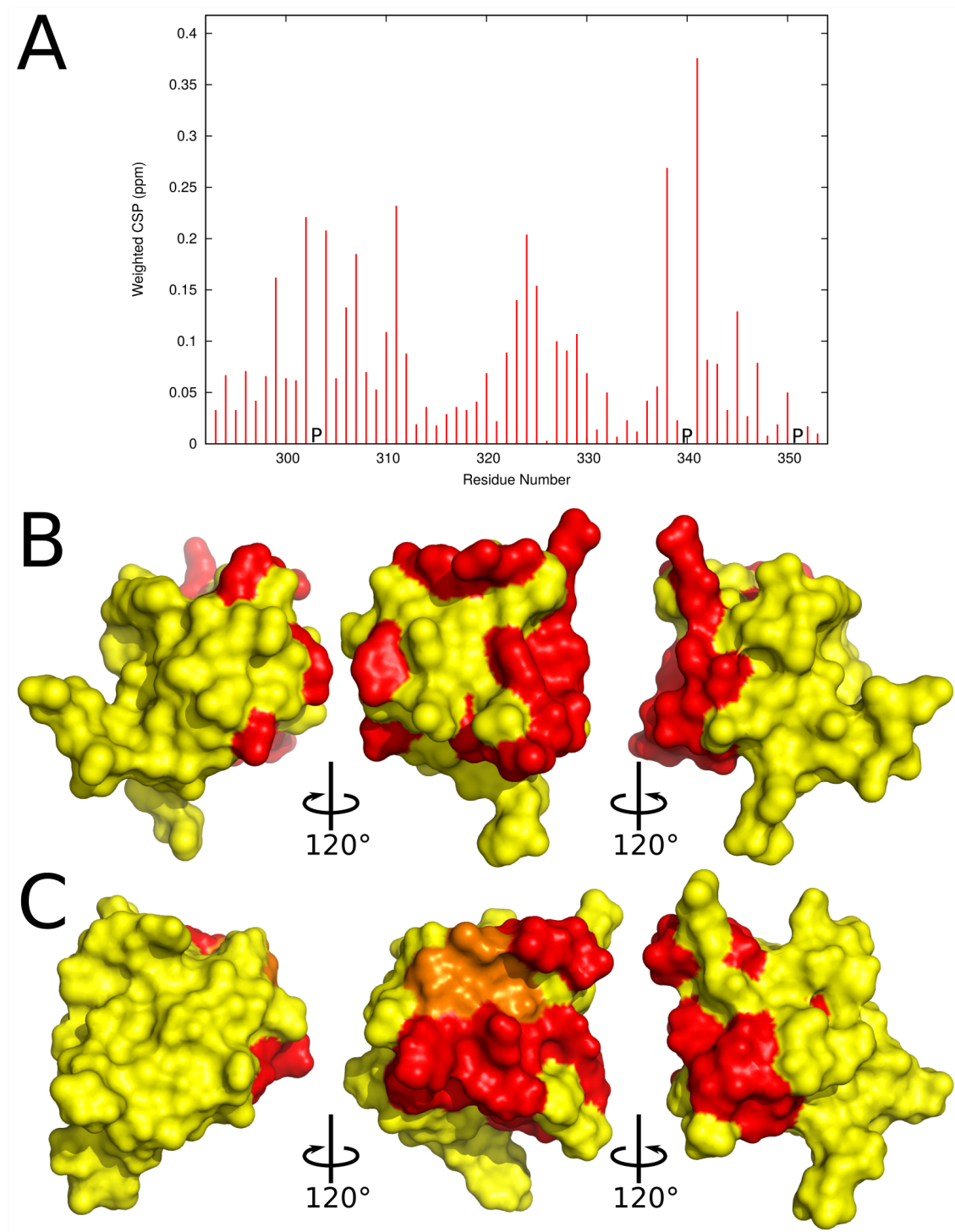


Figure 3.7: Endophilin SH3 CSP upon Alix titration. A. Shift map of CSP derived from ^1H - ^{15}N HSQC. P indicate proline residue for which no information is available. B. Corresponding SH3 heatmap. C. Heatmap of CSP derived from ^1H - ^{13}C HSQC. Yellow is unaffected, red is highly perturbed. The middle figure shows the canonical SH3 binding surface, figures on the left and right are rotated by 120° .

that the binding motif is between residues A13 and A25, as residues outside of this region were barely perturbed upon titration of SH3 (Fig. 3.8B). Interestingly, resonances for some

residues like S3, W4, T7 or K8 as well as side chains amine were split (Fig. 3.8A, pink circles), an effect that was most strongly marked close to P6.

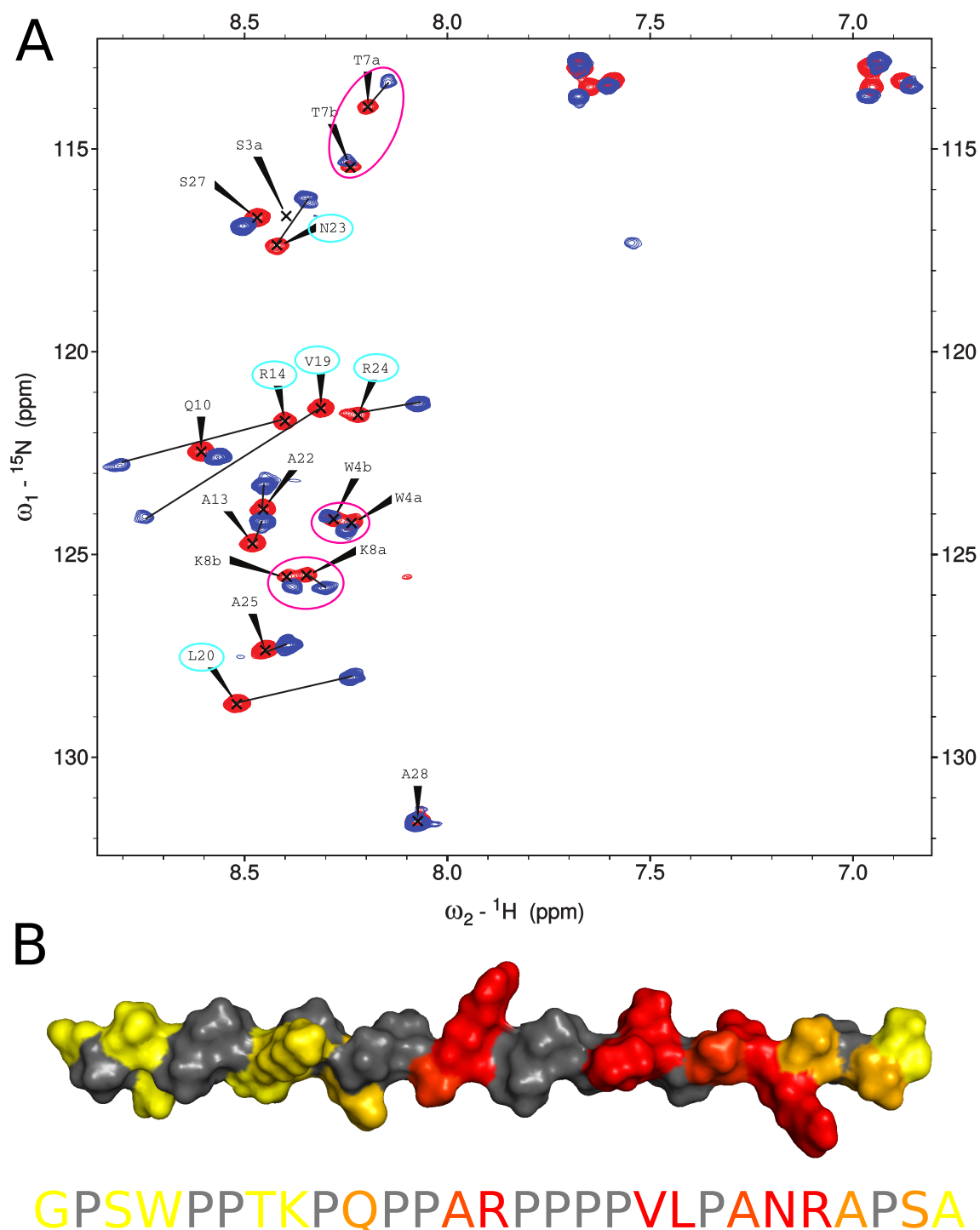


Figure 3.8: Titration of Endophilin SH3 on Alix, effects on ${}^1\text{H}$ - ${}^{15}\text{N}$. A. ${}^1\text{H}$ - ${}^{15}\text{N}$ HSQC of Alix free (red) or with saturating amounts of Endophilin SH3 (blue). B. Heatmap of Alix shown in a PPII helix conformation and coloured according to CSP upon Endophilin SH3 titration and corresponding sequence. Yellow is unaffected, red is highly perturbed, prolines are in grey.

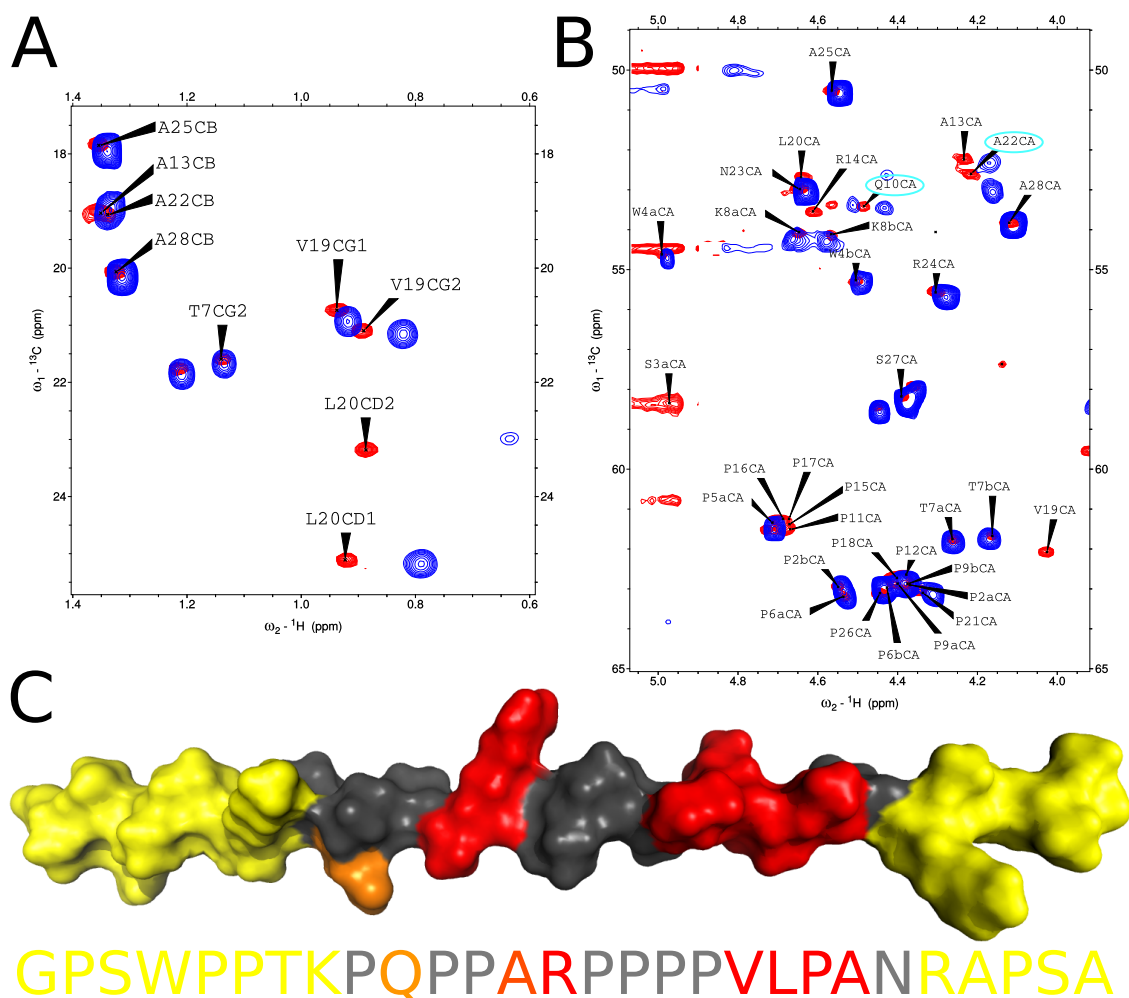


Figure 3.9: Titration of Endophilin SH3 on Alix, effects on ^1H - ^{13}C . A. Methyl group region of ^1H - ^{13}C HSQC of Alix free (red) or with saturating amounts of Endophilin SH3 (blue). B. $\text{C}\alpha/\text{H}\alpha$ region of the same spectra. C. Heatmap of Alix coloured according to CSP of $\text{C}\alpha/\text{H}\alpha$ upon Endophilin SH3 titration and corresponding sequence. Yellow is unaffected, red is highly perturbed, grey indicates residues for which no information was obtained due to peak overlap.

This could be due to a very slow proline *cis-trans* isomerisation, creating different chemical environments for residues ahead of it.

CSP measured in ^1H - ^{15}N HSQC after titration of Endophilin SH3 on Alix gave indications about the putative binding site (Fig. 3.8). However, Alix is composed of a high number of proline residues (12 of the 28 amino acids are proline), for which no information can be obtained in a ^1H - ^{15}N HSQC spectrum due to the absence of backbone N-H in a proline residue (Fig. 3.8B, grey). In order to gain information from prolines as well as side chains, the titration experiment was also assessed by collecting ^1H - ^{13}C HSQC spectra (Fig. 3.9). Two regions of the spectra overlays are shown. In the methyl region (Fig. 3.9A), similarly to what was observed in ^1H - ^{15}N HSQC, both V19 and L20 were highly perturbed. In the

$C\alpha/H\alpha$ region, in addition to residues identified in the 1H - ^{15}N HSQC (Fig. 3.8A), Q10 and A22 also displayed CSP (Fig. 3.9B, blue circles). A heatmap coloured according to the intensity of CSP for $C\alpha/H\alpha$ shows that residues Q10 to A22 are perturbed, in particular R14, V19 and L20 (Fig. 3.9C).

Distance restraints for SH3-Alix complex

Although CSP analysis narrowed down the binding site on Alix, more data were needed to characterise it precisely. 1H - 1H NOESY (Nuclear Overhauser Effect Spectroscopy) spectra provide valuable information for intermolecular interactions. A 1H - 1H NOESY spectrum correlates resonances of protons which are in close distance from each other through space (less than 5 Å), without the need for a covalent link. Using this NMR experiment, close proximity of Alix protons with SH3 protons can be detected. Isotope filtered NOE spectra were acquired to record only NOEs between ^{13}C -labelled SH3 and unlabelled peptide. Unfortunately, no usable NOEs were recorded as is commonly the case for protein complexes stabilised largely by electrostatic interactions. So another strategy to obtain distance restraints was tried. Paramagnetic probes (nitroxide radicals, Mn^{2+} , lanthanides) possess an unpaired electron and can be used to determine long-range distance restraints (up to 20-30 Å). Unpaired electrons in proximity provide additional relaxation mechanisms, resulting in line broadening, called PRE (paramagnetic relaxation enhancement) [340]. As consequence of line broadening, a reduction in peak intensity is observed in the HSQC spectra, indicating proximity to the PRE probe.

To find out the orientation in which Alix binds and differentiate between class I and class II binding as well as obtain some distance restraints, PRE were mapped onto Endophilin SH3 after addition of Alix labelled with 4-maleimido-TEMPO (2,2,6,6-Tetramethyl-1-piperidinyloxy), a PRE probe with a nitroxide radical (Fig. 3.10), at different positions along its sequence. For this, Alix residues T7, P17 and A25 were individually mutated to cysteine and labelled with TEMPO. 1H - ^{15}N HSQC spectra of SH3 were then recorded. Reduction in SH3 peak height (PRE) in the presence of TEMPO-labelled Alix is reported along the SH3 sequence (Fig. 3.11A). Mapping the PRE on the SH3 structure (Fig. 3.11B) indicates that Alix is a class II binder, binding N \rightarrow C when facing the binding pocket. This can be deduced from the fact that with TEMPO labels closer to Alix C-terminus, the right part of the SH3 is more affected by PRE than the left side (when facing the binding pocket) (Fig. 3.11B).

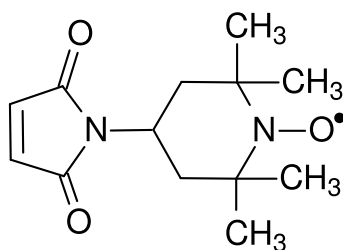


Figure 3.10: Nitroxide radical probe 4-maleimido-TEMPO (2,2,6,6-Tetramethyl-1-piperidinyloxy)

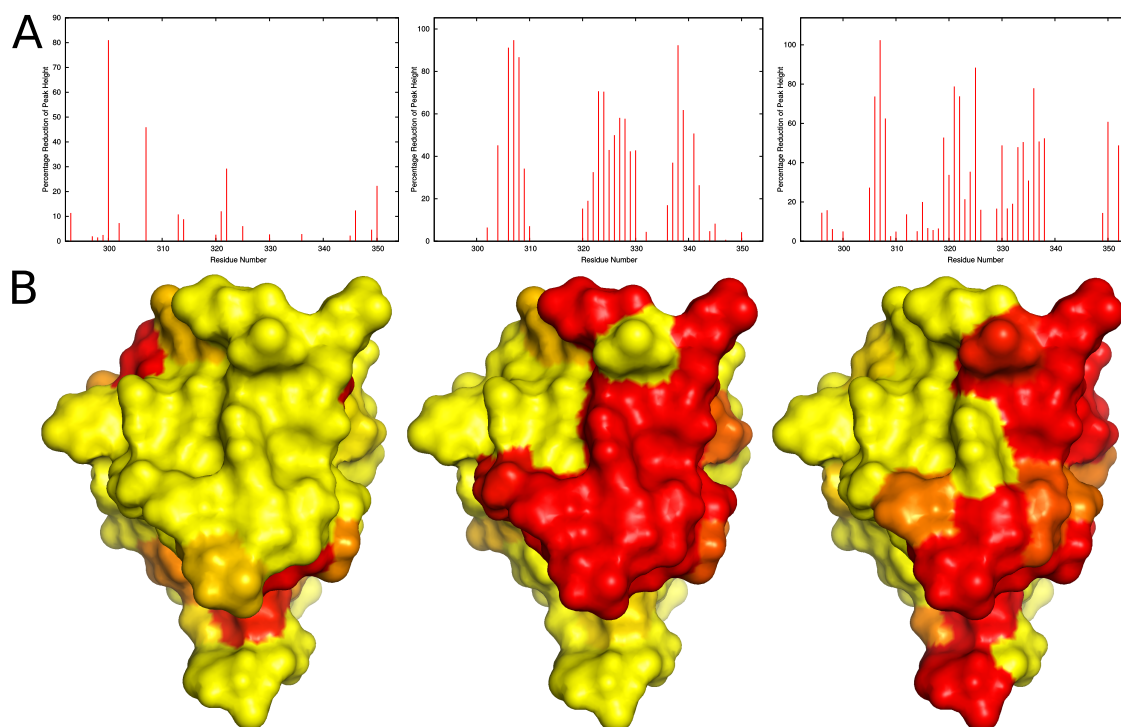


Figure 3.11: Shift maps (A) and heatmaps (B) of Endophilin SH3 PRE induced by TEMPO-labelled Alix at positions T7 (left), P17 (middle) or A25 (right). Yellow is unaffected, red is highly perturbed.

SH3-Alix model

Using CSP and PRE experiments, a binding site of Endophilin on Alix was narrowed down and the orientation of binding determined. While this does not resolve all possible ambiguities of potential binding modes, the information can be used as an input for a docking software that should be able to resolve the energetically most favoured state. HADDOCK (High Ambiguity Driven biomolecular DOCKing) software models the preferred orientation of two molecules relative to each other using ambiguous interaction restraints (AIRs) to drive the docking process [343, 344]. An AIR corresponds to an intermolecular distance shorter than a set threshold between any atom of an active residue of the first protein to

any atom of any residue of the second protein. When using CSP data, a residue is considered active for HADDOCK if it both displays CSP above a certain threshold and has high solvent accessibility at the surface in the free protein. Residues in the core of the protein that display CSP because of a conformational change upon binding will not be used to drive the contact surface. HADDOCK performs rigid body fit between structures of both proteins while the residues at the interface are kept flexible to optimise interface packing. Structures are then ranked by intermolecular energy which comprises electrostatic, van der Waals, solvation and AIR energies [343].

Active residues for SH3 and Alix were defined according to the previously obtained CSP and PRE data (residues 299, 302, 304, 306, 307, 323, 324, 325, 326, 338, 342, 343 for SH3 and 13, 14, 19, 20, 21, 22, 23, 24 for Alix). In the first modelling rounds, an unbiased approach where the structure of Alix was not presupposed, was tried, but no convergence of models was reached. In the next step, modelling with preformed Alix was tried. Alix was either flexible or forming a α -helix, a β -sheet or a polyproline II (PPII) helix. Best models were obtained with Alix in a PPII helix conformation. This is also consistent with the literature, as canonically, SH3 domains bind consensus PxxP peptides in a PPII helix conformation [324, 322]. From then on, all modelling was performed with peptides in a PPII helix conformation. As the initial simulations failed to converge upon a single model with low energy, unambiguous restraints were applied to bias the model in order to evaluate different registers of the peptide within the SH3 binding groove, in both class I and class II binding. All possible permutations of PxxP occupancy were explored for ALIX. The residue in a subsite was restrained to within 7 Å of the following SH3 residues:

P3 site: Y299, D300, Y343

P2 site: Y299, N342, Y343

P0 site: F301, W327, P340, Y343

P-1 site: N326, W327, P340

Models with lowest HADDOCK score (corresponding to $E_{\text{vanderWaals}} + 1/5 E_{\text{electrostatics}} + E_{\text{desolvation}}$) and consistent with PRE data were preferred. However, binding energies calculated by HADDOCK did not identify one binding mode as having a uniquely strong affinity, and several registers of Alix in the SH3 binding groove had similar docking score (Tab. 3.2).

In the best model obtained for Alix (PaRP), Endophilin binding site was identified as KPQPPARPPP (Fig. 3.12, left). PaRP is in the binding pocket (Fig. 3.12A), with R14

Table 3.2: Summary of HADDOCK results for the two best SH3-Alix models

Parameter	PARP	PPPV
HADDOCK Score	-66.9±0.7	-61.3±3.5
Cluster Size (out of 200 calculated structures)	200	200
RMSD from reference structure (Å)	2.1±1.3	2.1±1.3
$E_{\text{VanderWaals}}$ (kcal/mol)	-49.1±2.8	-45.4±5.6
$E_{\text{electrostatics}}$ (kcal/mol)	-145.0±10.8	-79.5±34.8
$E_{\text{desolvation}}$ (kcal/mol)	-2.1±0.9	-3.5±2.6
Buried Surface Area (Å ²)	1205.3±22.1	1240.2±27.4

side chain forming salt bridges with side chains of E304 and E308 (Fig. 3.12B). The compass pocket is occupied by a proline residue (P17) stacking against SH3 W327 (Fig. 3.12B). This model is also consistent with PRE data, placing T7 far on the left of the SH3, P17 close, on the right side of the binding groove and A25 further right (when facing the binding site on the SH3). However, the preferred model cannot on its own explain all of the data collected. In the titration experiment with SH3 on Alix (Fig. 3.8, 3.9), important CSP were observed for R14, V19 and L20. In the current model where PaRP is in the binding site (Fig. 3.12C), high CSP for R14 are easily explained as R14 sits in the binding site in close proximity of the SH3. However, V19 and L20 are further away from the SH3 (Fig. 3.12C) and their chemical environment should not be that heavily perturbed upon addition of SH3. Alix CSP data are more compatible with the second best HADDOCK model, in which RPPPPVLPA sits on the SH3 binding pocket (Fig. 3.12, right).

In this model, PpPV is in the center of the binding site, P15 is situated in a hydrophobic pocket formed by the conserved Y299 and Y343 and the hydrophobic compass pocket formed by W327 and F338 is occupied by P21-A22 (Fig. 3.12E,F). Although this model explains CSP data for Alix well (Fig. 3.12G), it is less compatible with PRE data obtained with TEMPO-labelled Alix at different positions (Fig. 3.11). In particular, P17 labelled with TEMPO gives rise to PRE mostly on the right side of the SH3 (Fig. 3.11B). For a class II binder, this means that P17 is C-terminal of the binding motif. However in rppPpvlp, P17 is N-terminal and part of PpPV.

NMR experiments followed by modelling proposed two models which are each compatible with most but not all data collected. In order to test the importance for SH3-Alix complex formation of some key residues identified, these amino acids from Alix were mutated to alanine. The effect of these mutations was evaluated by pulling down Endophilin full-length or Endophilin SH3 from bacterial lysate overexpressing these constructs with GST-tagged

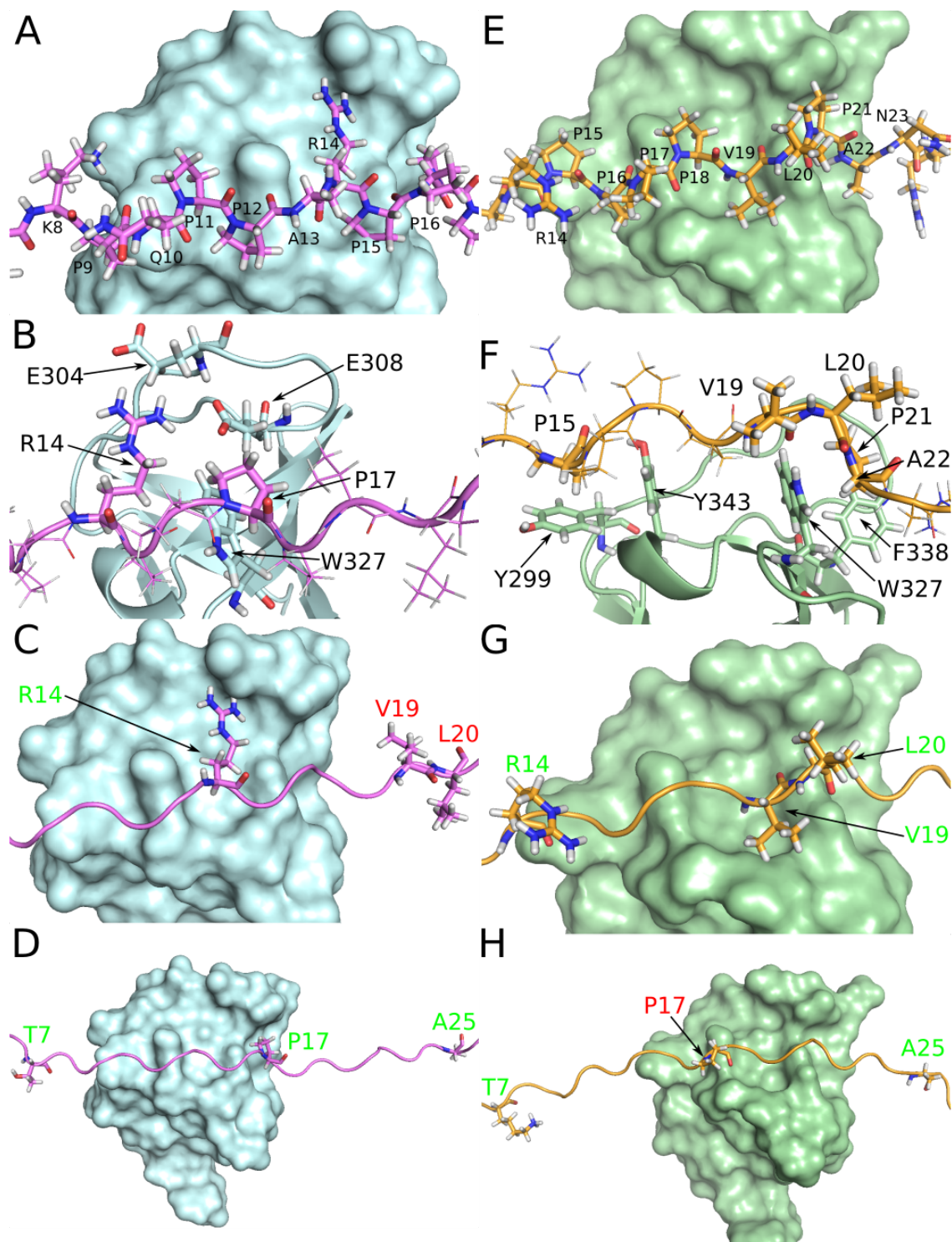
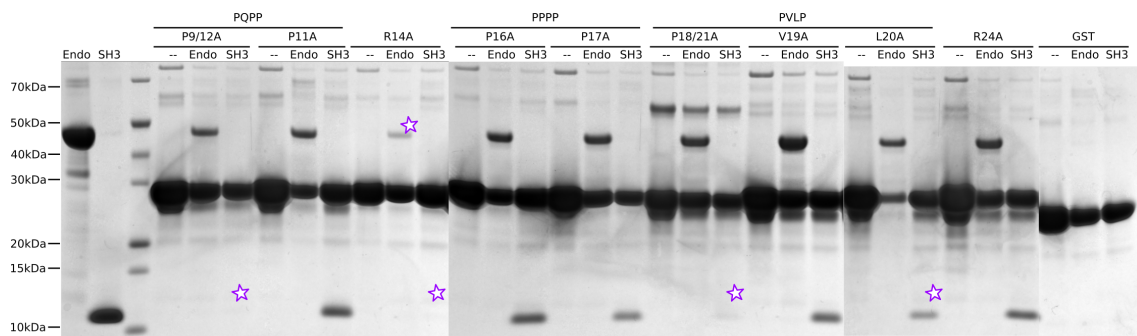


Figure 3.12: Models of SH3-Alix complex with KPQPPARPPP (left) or RPPPPVLPA (right) binding motifs. A, E. Surface representation of SH3 in SH3-Alix complex. B, F. Detail of binding site with residues providing specificity shown in sticks colours. C, G. Overview of CSP fitting (green) the model or not (red). D, H. Overview of PRE fitting (green) the model or not (red).

Alix mutants (Fig. 3.13). R14 and L20 were identified in CSP analysis as being heavily perturbed (Fig. 3.8) and mutation to alanine prevented Endophilin pull-down (Fig. 3.13).

V19 also showed important CSP, however mutating it to alanine did not affect the SH3-Alix complex (Fig. 3.13). This can be explained by the fact that, in the PpPV model (Fig. 3.12E), V19 sits at the top of the prism formed by a PPII helix and its side chain points away from the SH3 or in the PaRP it would be far enough from the SH3. Although chemical shifts for those residues were little affected upon SH3 addition, mutating the pair P9/P12 to alanine prevented pull-down of Endophilin SH3 but not of the full-length protein (Fig. 3.13). Similarly after mutating the pair P18/P21 to alanine, GST-Alix could not pull-down Endophilin SH3 but pull-down of the full-length protein was not affected (Fig. 3.13). This could be due to disruption of the PPII fold upon mutation of these prolines. Pull-down experiments with Alix mutants did not help distinguishing between both proposed models of SH3-Alix complex and further experiments will be needed.



G--P--S--W--P--P--T--K--P--Q--P--P--A--R--P--P--P--V--L--P--A--N--R--A--P--S

Figure 3.13: Pull-down of Endophilin full-length (Endo) or SH3 with GST-Alix mutants. Effect on mutation to alanine is indicated in Alix sequence (red corresponds to no binding, orange to reduced binding and green to unaffected binding).

3.2.3 Endophilin A1 SH3 - ADRA2A ICL3 interaction

SH3-ADRA2A model

Using Alix as a test candidate, its Endophilin binding site could be mapped and a strategy to identify it using NMR was developed. After quantifying ADRA2A fragment affinity for Endophilin SH3 by ITC, structural characterisation of its Endophilin binding site was carried out following the strategy developed for Alix. First ADRA2A was titrated on SH3 to confirm the interaction surface on Endophilin SH3 by measuring CSP (Fig. 3.14). The observed CSP (Fig. 3.14A) plotted onto the SH3 sequence (Fig. 3.14B) were very similar to what was observed for Alix and, together with a heatmap of SH3 coloured according

to CSP, confirmed that binding of ADRA2A by Endophilin SH3 occurred in the canonical SH3 binding pocket (Fig. 3.14C).

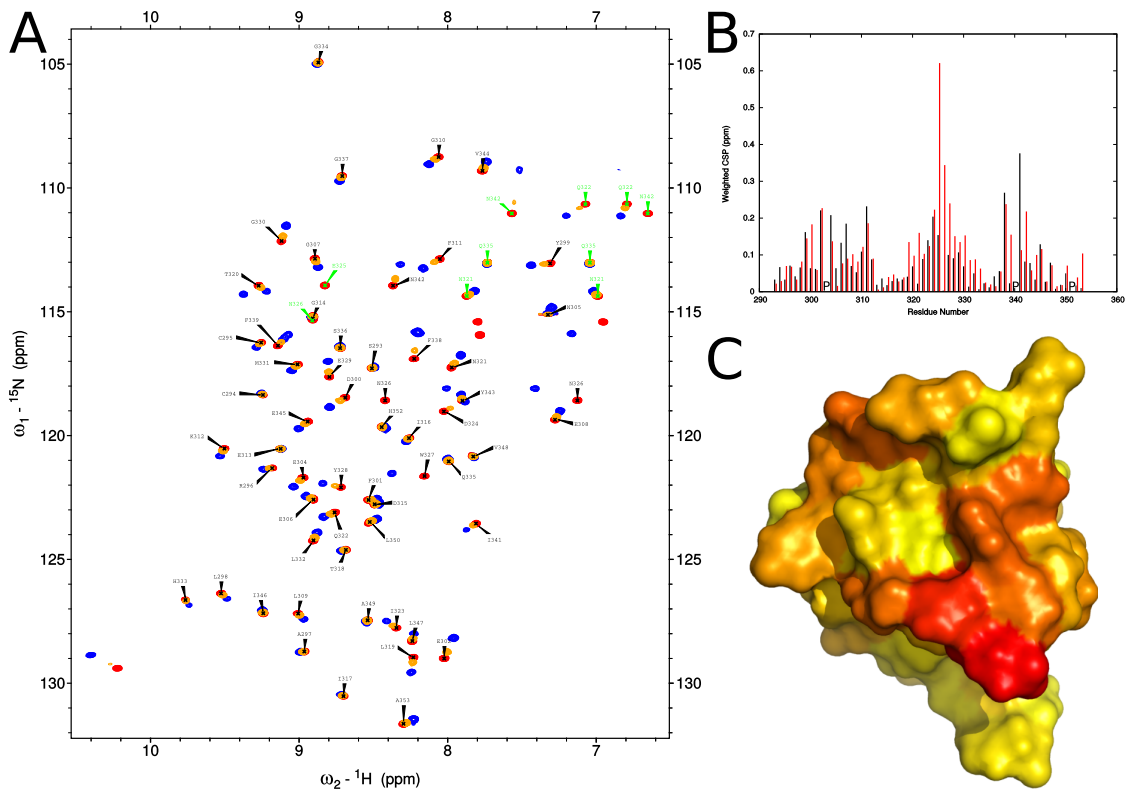


Figure 3.14: Endophilin SH3 CSP upon ADRA2A titration. A. ^1H - ^{15}N HSQC of Endophilin SH3 free (red) or with increasing amounts of ADRA2A (yellow, blue). B. Shift map of CSP derived from ^1H - ^{15}N HSQC for Endophilin SH3 in complex with ADRA2A (red) compared to those obtained with Alix (black), P indicate proline residue for which no information is available. C. Corresponding SH3 heatmap

After assignment of ADRA2A resonances, the binding site on ADRA2A was further delimited by titrating SH3 onto ADRA2A and recording CSP (Fig. 3.15A, resonances shift between free ADRA2A in red, ADRA2A-SH3 complex in blue). In addition, PRE were recorded on ADRA2A after addition of SH3-E304C-TEMPO. E304 residue lies at the top of the RT loop, above the center of the binding site (Fig. 3.16). Weaker peak intensity before (Fig. 3.15B, pink) compared to after TEMPO reduction (Fig. 3.15B, black) indicates NH protons in proximity of SH3 E304 and therefore of the binding site. For example, G19 (circled in pink) both displays CSP as seen by a shift between its free and complex form (Fig. 3.15A) as well as PRE (Fig. 3.15B). This indicates that G19 is in the binding site as it is close to the SH3 and to E304. H13 (circled in blue), on the other hand, is close to the SH3 but away from E304 and therefore away from the binding site, as H13 only shows CSP but no PRE (Fig. 3.15A,B). Combining both CSP and PRE data sets delimits

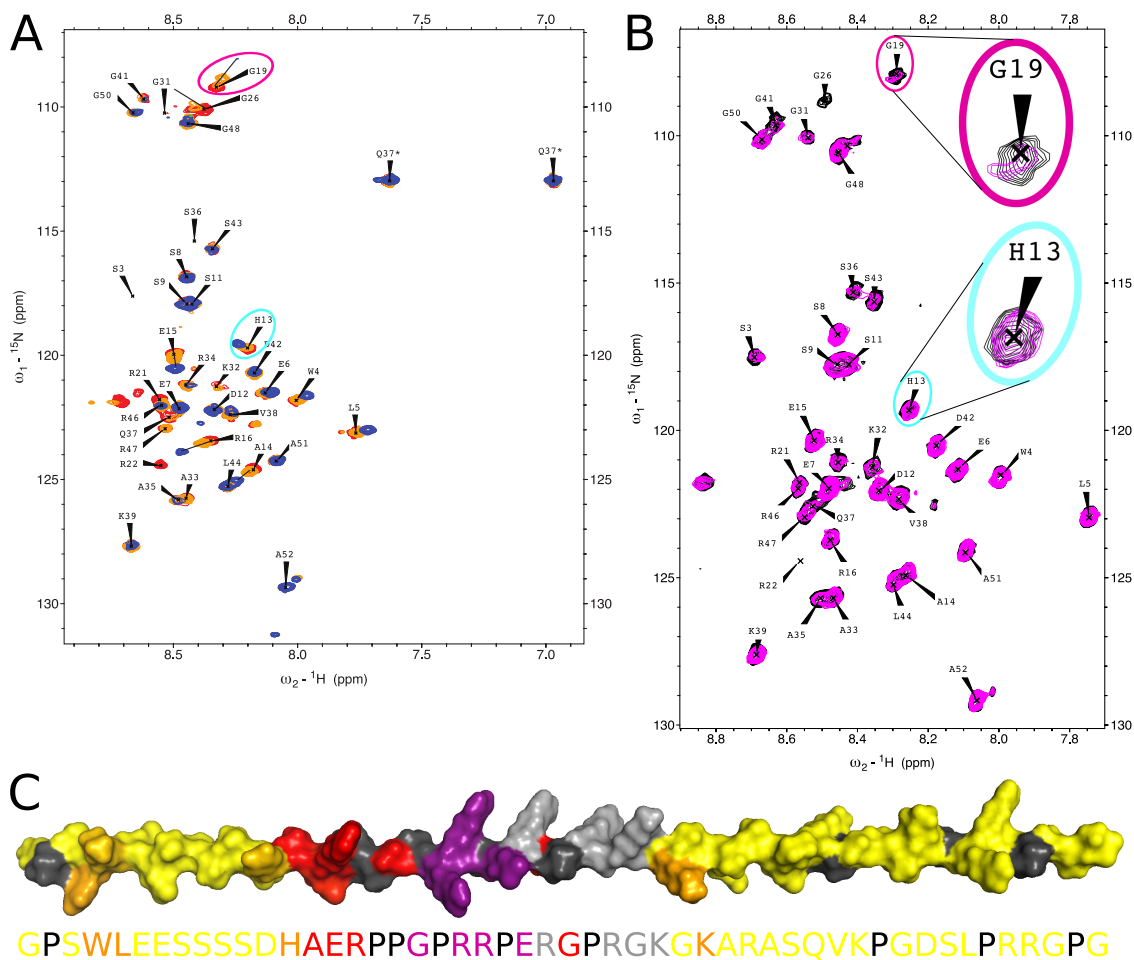


Figure 3.15: CSP and PRE of ADRA2A with Endophilin SH3. A. ^1H - ^{15}N HSQC of ADRA2A free (red) or with increasing amounts of Endophilin SH3 (yellow, blue). B. ^1H - ^{15}N HSQC of PRE on ADRA2A in the presence of SH3-E304C-TEMPO before (pink) and after (black) TEMPO reduction. C. Corresponding heatmap of ADRA2A shown in a PPII helix conformation. CSP are coloured yellow (no perturbation) to red (highly perturbed). Residues in purple show high PRE. Prolines are in dark grey and residues for which no assignment was available are in light grey.

the binding site (Fig. 3.15C) between residues H13 and G26 as residues outside of this sequence remain unaffected by SH3 titration or presence of a paramagnetic probe on top of the binding site.

Similarly to what has been previously done with Alix, ADRA2A was labelled at different sites with TEMPO in order to determine its orientation on SH3. PRE were recorded on SH3 in complex with ADRA2A labelled at D12 or E24 (Fig. 3.17). Labelling ADRA2A N-terminally of the previously identified binding site (D12) mostly affected residues on the left side of the SH3 (Fig. 3.17A), whereas a TEMPO-label on E24, C-terminally of the binding site, induced PRE on the right side of the SH3 (Fig. 3.17B). This data suggest that ADRA2A, like Alix, is a class II binder oriented N \rightarrow C.

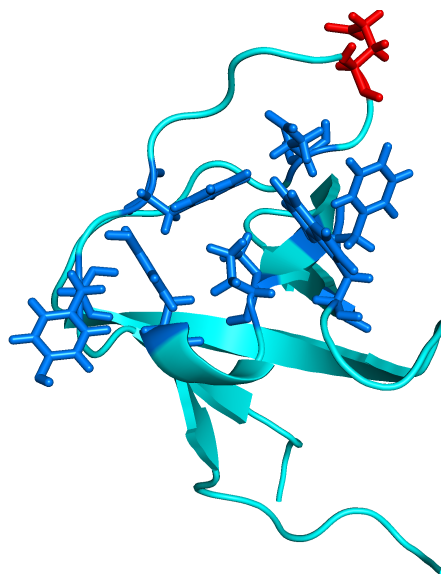


Figure 3.16: Position of E304 on Endophilin SH3 for TEMPO labelling. E304 is in red and residues lining the binding groove in sticks and darker blue.

HADDOCK modelling was then carried out with CSP and PRE similarly to Alix with ADRA2A prefolded in a PPII helix. SH3 residues 299, 326, 327, 338, 342, 348 and ADRA2A residues 13-26 were defined as active. As for Alix, no convergence into a single model was reached in the initial simulations, so unambiguous restraints were applied to evaluate all possible permutations of PxxP occupancy, in both class I and class II binding, for ADRA2A on the SH3. To achieve this, residues were restrained within 2Å of the residues forming each subsite (P3, P2, P1 and P-1) on the SH3. Two models with similar HADDOCK scores were obtained (Tab. 3.2).

Table 3.3: Summary of HADDOCK results for the two best SH3-ADRA2A models

Parameter	PPGP	PRRP
HADDOCK Score	-57.5±2.4	-54.0±1.7
Cluster Size (out of 200 calculated structures)	200	200
RMSD from reference structure (Å)	1.9±2.0	0.8±0.5
$E_{\text{vanderWaals}}$ (kcal/mol)	-42.3±1.3	-43.4±2.1
$E_{\text{electrostatics}}$ (kcal/mol)	-136.1±31.5	-127.9±13.8
$E_{\text{desolvation}}$ (kcal/mol)	4.4±7.5	0.2±0.9
Buried Surface Area (Å ²)	1085.5±68.9	1009.8±31.7

In the best model, HAERPPGPRR was identified as the ADRA2A binding motif on Endophilin SH3 (Fig. 3.18A). PpGP is in the binding pocket and contacts are formed between R16 side chain and D300 main chain carbonyl, R21 and E304 side chains, as well as R22 side chain with both backbone and side chain carbonyl groups of E306 (Fig. 3.18B). An additional contact is formed from R22 backbone amide to the side chain carbonyl of E308

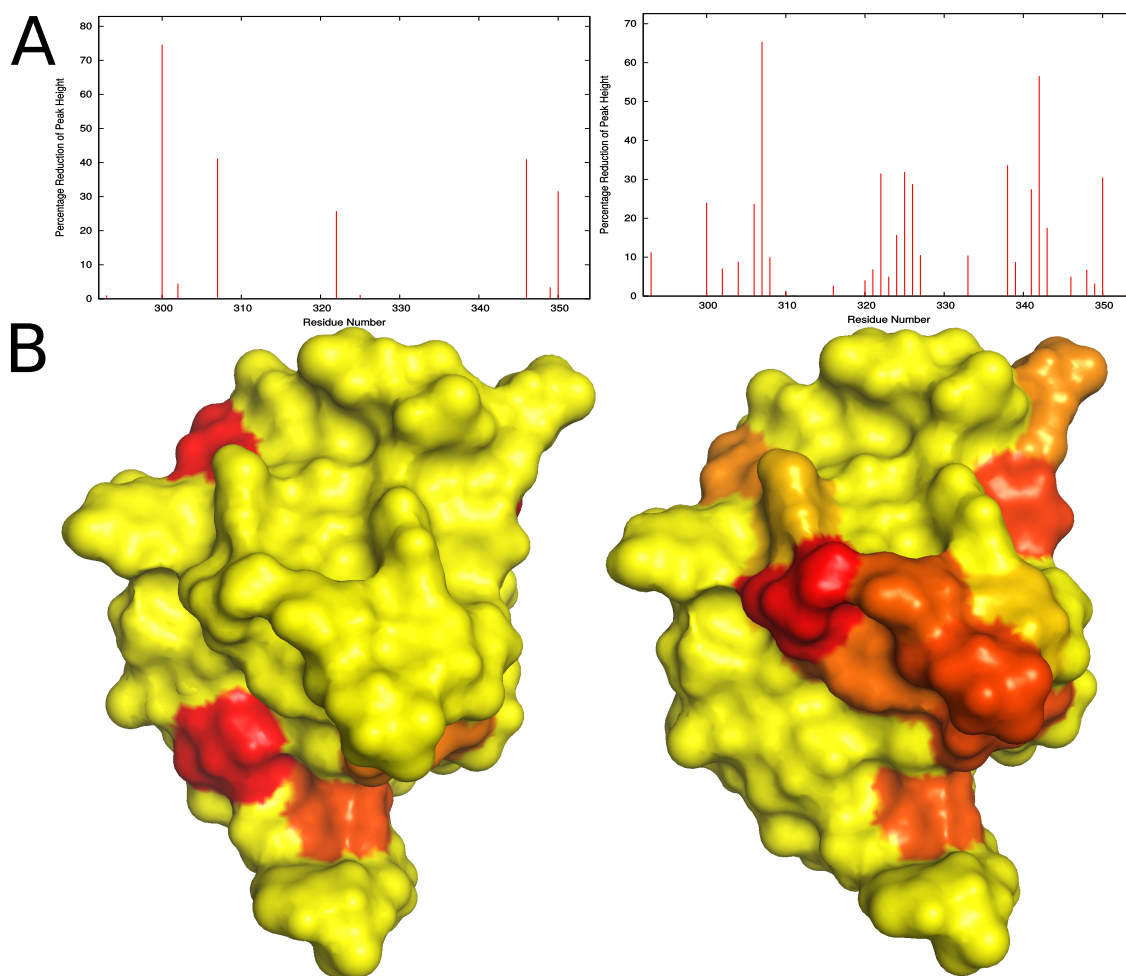


Figure 3.17: Shift maps (A) and heatmaps (B) of Endophilin SH3 PRE induced by TEMPO-labelled ADRA2A at positions D12 (left) or E24 (right). Yellow is unaffected, red is highly perturbed.

(Fig. 3.18B). This model gave slightly higher HADDOCK scores and was better compatible with PRE data, however, a different model could not be excluded. In this alternative model with RPPGPRRPER as ADRA2A binding motif, PrRP was in the binding pocket (Fig. 3.18C), with R22 forming a salt bridge with SH3 E308. R25 is located in the compass pocket and also forms salt bridges with the backbone carbonyl and the side chain of SH3 E306 (Fig. 3.18D).

Phosphoregulation of SH3 – ADRA2A

After short agonist stimulation, ADRA2A is rapidly desensitised by phosphorylation of its ICL3 by GRK3 (G protein-coupled receptor kinase 3) [345, 346, 347]. The phosphorylation site was identified as a stretch of four serines preceded by two glutamates [348]. Following agonist exposure, PKC (protein kinase C) was also shown to phosphorylate

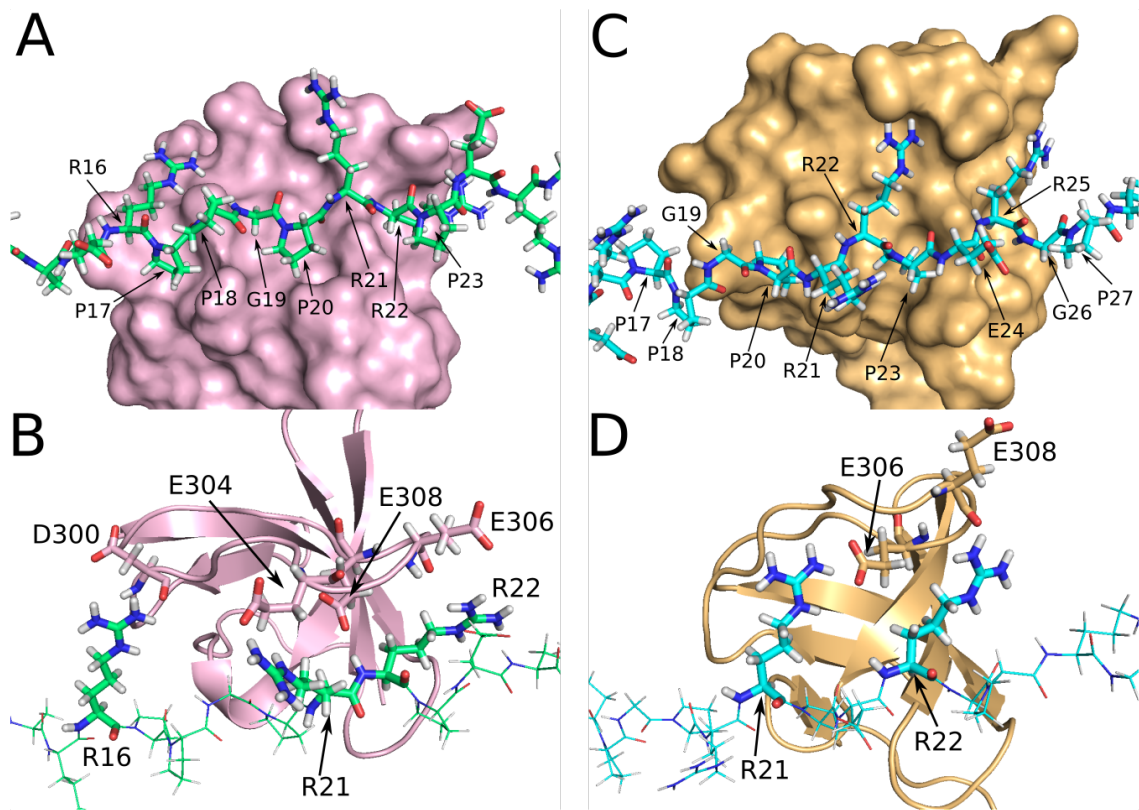


Figure 3.18: Model of SH3-ADRA2A complex with HAERPPGPRR (left) or RPPG-PRRPER (right) binding motif. A,C. Surface representation of SH3. B,D. Detail of binding site with residues providing specificity shown in sticks.

ADRA2A ICL3 at S360 [349], resulting in receptor desensitisation. According to PhosphoSitePlus [www.phosphosite.org], other phosphorylation sites have been identified by mass spectrometry on S324, S331 and T344, for the phosphorylated residues in the ICL3 fragments used here (Fig. 3.19A). To check if phosphorylation could have a role in FEME of ADRA2A, some of those residues were mutated to aspartate or glutamate to imitate a phosphorylated serine. Then binding was assessed by pull-down experiments with GST-SH3 and His-SUMO-tagged peptides after tag cleavage (Fig. 3.19B). Whereas neither S43E nor S72D mutations affected pull-down efficiency of ADRA2A(293-374) by Endophilin SH3, mutation of the four serines SSSS(8-11)DDDD abolished pull-down by Endophilin SH3 in the shorter construct ADRA2A(293-339) only. This was further confirmed by ITC measurements (Fig. 3.19C). Affinity for Endophilin SH3 to ADRA2A ICL3 wild-type was $13\ \mu\text{M}$ (Fig. 3.3B), but was reduced to $63\ \mu\text{M}$ for ADRA2A SSSS(8-11)DDDD mutation, indicating an effect on Endophilin binding. This was surprising as in titration experiments (CSP) of SH3 on ADRA2A, there was no indication that those residues were in proximity of the SH3 (Fig. 3.15). A precise mechanism on the effect of phosphorylation by GRK3

on binding of ADRA2A to Endophilin SH3 is still lacking, although it is likely due to a general electrostatic repulsion.

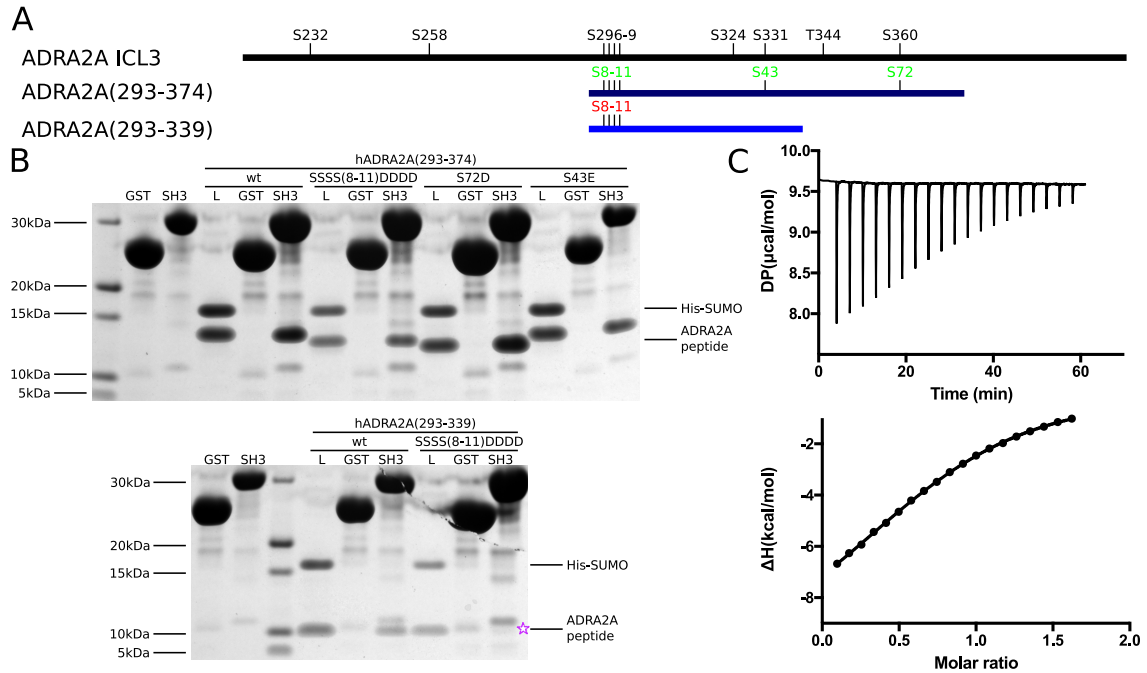


Figure 3.19: Effect of ADRA2A phosphomimetics on Endophilin binding. A. Identified phosphorylation sites in ADRA2A ICL3 (black). Mutations tested here are indicated for the longer (dark blue) and shorter (blue) constructs with numeration according to the NMR construct (blue). Mutations negatively affecting the binding to Endophilin SH3 are indicated in red, mutations with little effect are in green. B. Pull-down by GST-Endophilin SH3 of ADRA2A phosphomimetics mutants on ADRA2A(293-374) (top) or ADRA2A(293-339) (bottom). C. ITC measurement of affinity between Endophilin SH3 and ADRA2A(293-339) SSSS(8-11)DDDD. Top: released heat, bottom: binding enthalpy.

3.3 Discussion

Endocytosis is essential for a cell to take up nutrients, regulate the plasma membrane surface area as well as the concentration of receptors on the cell surface. In addition to its multiple roles in clathrin-mediated endocytosis, Endophilin is also an essential component of a clathrin-independent endocytosis route, FEME (fast Endophilin-mediated endocytosis), in which it binds cargo directly or through adaptor proteins using its SH3 domain [120]. However, despite experiments based on peptide libraries and modelling [335, 336], no consensus sequence for Endophilin SH3 binding was determined. Here, I characterised the binding of Endophilin SH3 to a cargo (ADRA2A) and an adaptor protein (Alix) using pull-downs and measured the affinity of interactions by ITC. We confirmed that both peptides bind Endophilin SH3 in the canonical binding groove. Endophilin binding site

was then mapped on two of these peptides, ADRA2A ICL3 and Alix PRD, by NMR using a strategy combining CSP (chemical shift perturbations), PRE (paramagnetic relaxation enhancement) and modelling.

Endophilin SH3 and Alix PRD fragment offered an ideal system for structure determination by NMR, given their small size and the good spread of resonances for Endophilin SH3 (Fig. 3.4). However, the high number of proline residues in Alix (12 out of 28 amino acids), most of them concentrated around the putative binding site, complicated the process. Several prolines were in a similar chemical environment and therefore showed similar chemical shifts. With overlapping peaks (Fig. 3.9A), these residues could not be distinguished from each other. Critical information was therefore missing or not usable as these residues were in the proximity of the identified binding site.

A powerful NMR experiment for structure determination consists in measuring NOEs (Nuclear Overhauser Effect) between two protons. In our case, intermolecular NOEs between SH3 and Alix protons would be most relevant and provide distance restraints, as presence of an NOE indicates a distance of less than 5Å between the two corresponding atoms. To constrain a structure such as SH3-Alix complex, even fewer than 10-20 NOEs would greatly assist in distinguishing between alternative binding modes. However, no NOEs could be observed experimentally. This has also been reported for other SH3-peptide complexes [350, 351]. The alternative approach we used consisted in collecting PRE data with the nitroxide radical TEMPO. Proximity to the radical, within 20-30Å, results in peak broadening. Labelling Alix or ADRA2A peptides at different positions along their sequence and observing PRE on Endophilin SH3 resonances revealed that these peptides are class II binders, binding N -> C when facing the binding pocket (Fig. 3.11, 3.17).

Although HADDOCK-based modelling of SH3-peptide complexes based on CSP data only has been successful [350, 351], in the case of SH3-Alix, CSP and PRE data were not enough for an unbiased model to converge into one most favoured conformation. However, with the additional information that SH3 generally bind peptides in a polyproline II (PPII) helix conformation, all possible permutations of PxxP on the SH3, in both class I and class II, could be evaluated. For Alix, two putative binding sites were compatible with most but not all CSP and PRE data. The first model with PaRP in the binding site (Fig. 3.12A) is most consistent with PRE data, it however does not explain the high CSP observed for V19 and L20 both for the backbone and the side chains as in this model, these residues would be further away from the SH3 (Fig. 3.12C). In the second model, V19 and L20 are

in the binding site (occupied by PpPV), which explains very well the high CSP observed (Fig. 3.12E). However, PRE data situate T7 N-terminally and P17 and A25 C-terminally of the binding motif, which is incompatible with 15-PPPV-19 in the binding site (Fig. 3.11H).

An attractive hypothesis that could explain why two Endophilin binding sites were identified for Alix is that both coexist and Endophilin SH3 can bind either with similar affinities (explaining why only one transition was observed by ITC). Binding of Alix to Endophilin SH3 occurs in a 1:1 manner as measured by ITC, however, as Endophilin dimerises *via* its BAR domain, close proximity of both SH3 domains in Endophilin full-length might provide avidity and both SH3 might bind, one on the PaRP site and the other on PpPV. Synaptojanin, another Endophilin binding partner [240], also shares similar features where Endophilin binding site is formed of two PxxP motifs separated by two residues. A double PxxP motif might be a common feature for tight Endophilin binders given its dimeric nature. Pull-down of Endophilin full-length or SH3 domain were differently affected by mutations in Alix (Fig. 3.13), also supporting the idea that Endophilin full-length offers additional binding modes compared with SH3 only. Further experiments will be necessary to elucidate mechanistic details of Endophilin – Alix binding and probe the two-binding sites hypothesis.

Titration of SH3 on ADRA2A ICL3 fragment resulted in narrowing the binding site to residues A14-E24 (Fig. 3.15). This explains why mutating R21 and R22 to alanine resulted in a decreased pull-down efficiency (Tab. 3.1) as, according to the model obtained, those residues are located in the middle of the binding pocket (Fig. 3.18). Interestingly, R46 and R47 were also identified as residues contributing to binding to Endophilin as mutating them to alanine also prevented efficient pull-down (Tab. 3.1). There was however no indication of proximity of those residues to Endophilin SH3 as their resonances remained completely unaffected by the presence of SH3 (Fig. 3.15). The effect of the phosphomimetics mutations SSSS(8-11)DDDD resulting in a reduced affinity to Endophilin SH3, as observed both by pull-down and ITC (Fig. 3.19), cannot be explained by the current model, as these residues are positioned further away from the SH3 (Fig. 3.18) and their resonances were not perturbed after addition of SH3 (Fig. 3.15). The importance of these observations should be tested *in vivo*. After confirming that uptake of stimulated ADRA2A is Endophilin-dependent and occurs through the FEME pathway, the importance of the binding site identified here for ADRA2A endocytosis would be confirmed by mutating key residues. The

effect of phosphorylation on ADRA2A uptake could then be probed with phosphomimetics mutants.

Few SH3 – peptide interactions were observed in any of the models. In Alix PaRP as well as ADRA2A PrRP (Fig. 3.12A, 3.18C), an arginine is in the center of the binding pocket and contacts glutamate side chains on the SH3, whereas in Alix PpPV (Fig. 3.12E), a hydrophobic amino acid or, in ADRA2A PpGP, a glycine, is situated there (Fig. 3.18A). The compass pocket is occupied by a hydrophobic amino acid, either a proline stacking against an SH3 tryptophan in the case of Alix PaRP or by an alanine residue for Alix PpPV (Fig. 3.12B, 3.12F), whereas in ADRA2A PrRP, an arginine is situated there and makes additional contacts with backbone and side chain of an SH3 glutamate (Fig. 3.18B) or in PpPG an arginine backbone sits there. In addition, in Alix PpPV model, a hydrophobic pocket on the other side of the binding site is also occupied by a hydrophobic amino acid (Fig. 3.12F). In none of the cases there is indication of the peptide wrapping around or forming any contact outside of the canonical binding groove. This raises the question on the specificity of Endophilin recognition of its targets. PxRP or Px ϕ P (ϕ indicates a hydrophobic residue) followed by either arginine or a hydrophobic residue are very common motifs and might not be enough to explain Endophilin SH3 preference for those sequences over other similar ones.

The identified Alix PaRP and ADRA2A PrRP binding sites show interesting sequence similarities, which are also shared with the PP19 peptide of synaptojanin used to prevent Endophilin – synaptojanin interactions that result in CME defects [240] and a peptide from Itch ubiquitin ligase [336]. An alignment of the sequences (Fig. 3.20) shows a consensus +PxxPxRP (+ indicating a conserved basic residue). Although this consensus does not take into account the other binding site for Alix (PpPV) or ADRA2A (PpPG), search through protein databases was conducted with this consensus sequence and resulted in identification of several cell surface receptors as putative Endophilin targets. It is worth noting though that this sequence is not sufficient to explain all the receptors – SH3 interactions reported by Boucrot *et al.* [120], so this consensus sequence might be too restrictive. Nevertheless, future experiments will be carried out with the receptors identified in the database search, testing for *in vitro* interaction with Endophilin SH3 and so verifying the postulated Endophilin consensus sequence.

Here, we characterised the binding of Endophilin SH3 to two of its targets, a cargo cell surface receptor and a cargo adaptor protein. Using an approach combining NMR chemical

Alix PaRP	KPGPPARP
ADRA2A PrRP	RPPGPRRP
Itch	KPSRPPRP
PP19	RPAPPQRP
	: * * **
Consensus	<u>+PxxPxRP</u>

Figure 3.20: Alignment of Endophilin binding motifs in Alix, ADRA2A, Itch and synaptojanin and resulting consensus sequence.

shift perturbations and paramagnetic relaxation enhancement experiments together with modelling, we identified the Endophilin binding site on ADRA2A and described two putative sites on Alix. I also showed that, in addition to its role in receptor desensitisation, phosphorylation of ADRA2A might also play a role in its Endophilin-mediated uptake. These results confer further insights in the cargo selection step of the FEME pathway and open up the way for identification of additional FEME cargo.

Chapter 4

Final thoughts

In this thesis, I established a new assay, NTA, to study membrane curvature sensitivity of proteins. In a screen of non-BAR lipid-binding domains, I could identify AKT PH domain as a new curvature sensor. During the screen, a key factor was the careful choice of experimental conditions, protein and lipid concentrations and especially lipid composition, in order to observe binding. This reinforces the concept that membrane binding is a complex, fine-tuned process of weak and lipid-specific interactions. It also suggests that there might be non-described lipid-binding domains that bind weakly and cannot be observed with current standard methods and experimental conditions.

Identification of AKT PH domain as a curvature sensor lacking both amphipathic helix and BAR domain raises the question of alternative mechanisms to sense membrane curvature. Although curvature sensing by amphipathic helix insertion or BAR domain scaffolding has been extensively studied, molecular mechanistic details are not completely understood. Similarly, the relationship between curvature sensing and generation is unclear: are they two faces of the same coin or different processes? NTA might help shed light on some of these questions by identifying further curvature sensors or, for example, by helping to understand the contributions to curvature sensing by the BAR domain or the amphipathic H0 helix of Endophilin.

Endophilin is a key effector of FEME pathway, however the molecular basis of cargo selection and how the curvature generation properties of Endophilin contribute to the pathway remain unknown. In this thesis, I investigated Endophilin binding to cargo by modelling the binding of its SH3 domain to two peptides using NMR data. A putative consensus sequence could be identified and will be confirmed. The differences in interactions between

Endophilin SH3 and each of the two peptides suggests that binding is more complex. As new modes of binding SH3 and consensus sequences are published, the view increasingly diverges from the canonical model of SH3 binding to a PxxP motif to a complex collection of several weak interactions.

Endophilin is a particularly interesting protein that encompasses both an N-BAR domain responsible for curvature sensing and generation as well as an SH3 domain binding cargo. This suggests that Endophilin might be responsible for each step of the FEME pathway. It however raises the question of how a small protein can do it all and which are the requirements for molecular arrangements.

In recent years, theoretical and practical technologies have significantly improved. With increasing computer power and algorithms, simulations can be performed on longer time scales or with increasing molecular resolution. Cryo-EM allows structural characterisation of proteins and their relationship with the membrane at atomic resolution. The range of biophysical techniques has expanded, facilitating the study of protein-membrane interactions in multiple ways under different conditions and single-molecule techniques have become more robust and easy to use. The curvature field can benefit from all these developments. Exciting times lie ahead.

Chapter 5

Material and methods

5.1 Reagents

5.1.1 Buffer recipes

Table 5.1: Buffer recipes used in this thesis

Buffer name	Acronym	Buffer composition
<i>Protein purification</i>		
IMAC lysis buffer	IMAC-L	20 mM Tris pH 8.0, 200 mM NaCl, 50 mM imidazole, 0.5 mM TCEP, EDTA-free protease inhibitors
IMAC wash buffer	IMAC-W	20 mM Tris pH 8.0, 200 mM NaCl, 50 mM imidazole, 0.5 mM TCEP
IMAC elution buffer	IMAC-E	20 mM Tris pH 8.0, 200 mM NaCl, 250 mM imidazole, 0.5 mM TCEP
Anion exchange buffer A	IEX-A	20 mM Tris pH 8.0, 0.5 mM TCEP
Anion exchange buffer B	IEX-B	20 mM Tris pH 8.0, 500 mM NaCl, 0.5 mM TCEP

Continued on next page

Table 5.1 – *Continued from previous page*

Buffer name	Acronym	Buffer composition
Cation exchange buffer A	IEX2-A	20 mM HEPES pH 7.4, 0.5 mM TCEP
Cation exchange buffer B	IEX2-B	20 mM HEPES pH 7.4, 500 mM NaCl, 0.5 mM TCEP
Size exclusion buffer	GEF	20 mM HEPES pH 7.4, 150 mM NaCl, 0.5 mM TCEP
<i>Assay buffers</i>		
Pull-down wash buffer	PD	20 mM HEPES pH 7.4, 150 mM NaCl, 1 mM EDTA, 0.1 % Triton X-100
NanoSight buffer	NS	20 mM HEPES pH 7.4, 100 mM NaCl
NMR buffer	NMR	20 mM HEPES pH 7.4, 100 mM NaCl, 0.5 mM TCEP
<i>Bacterial culture</i>		
Transformation buffer	TF	100 mM CaCl ₂
2xTY medium	2xTY	16 g/l Bactotryptone, 10 g/l yeast extract, 5 g/l NaCl
M9- minimal medium	M9-	41 mM Na ₂ HPO ₄ , 22 mM KH ₂ PO ₄ , 8.55 mM NaCl, 2 mM MgS ₄ , 0.1 mM CaCl ₂
100x metal mix	MM	13.4 mM EDTA, 3.1 mM FeCl ₃ , 620 μM ZnCl ₂ , 76 μM CuCl ₂ , 42 μM CoCl ₂ , 162 μM H ₃ BO ₃ , 8.1 μM MnCl ₂

5.1.2 Liposome preparation

Lipid stocks in chloroform were mixed in a glass vial. Lipids used can be found in table 5.2. The solution was evaporated against the walls of the vial using an argon stream. The dried lipid film was then placed for 30 min in a dessicator to completely evaporate remaining organic solvents and water. For long-term storage, the vial was filled with argon gas and stored at -20 °C.

Lipids were resuspended at a concentration of 0.5 mg/ml in NS buffer by rolling for 2 h at room temperature. The solution was vortexed twice for 20 s each during those 2 h. Liposomes were extruded using 800 nm, 200 nm, 100 nm and 50 nm Whatman Nucleopore Polycarbonate filters in an Avanti Mini Extruder. Fresh liposomes were kept at room temperature and used within 24 h.

Table 5.2: Lipids used in this thesis

Lipid	Origin	Acronym	Company
Brain Polar Lipid Extract	Porcine brain	FolchA	Avanti Polar Lipids
Brain Extract, Type I	Bovine brain	FolchS	Sigma-Aldrich
2-Oleoyl-1-palmitoyl- <i>sn</i> -glycero-3-phosphocholine	Synthetic	POPC	Sigma-Aldrich
3- <i>sn</i> -Phosphatidyl-ethanolamine	Bovine brain	PE	Sigma-Aldrich
1,2-Diacyl- <i>sn</i> -glycero-3-phospho-L-serine	Bovine brain	PS	Sigma-Aldrich
Cholesterol	Synthetic	Chol	Sigma-Aldrich
L- α -phosphatidylinositol-4,5-bisphosphate	Porcine brain	PI(4,5)P2	Avanti Polar Lipids
1,2-dioleoyl- <i>sn</i> -glycero-3-phospho-(1'-myo-inositol-3',4',5'-trisphosphate)	Synthetic	PIP3	Avanti Polar Lipids
Phorbol 12-myristate 13-acetate	Synthetic	PMA	Sigma-Aldrich
ATTO647N-1,2-dioleoyl- <i>sn</i> -glycero-3-phosphoethanolamine	Synthetic	DOPE-647N	Atto-Tec

NL liposomes used for measurements of curvature sensitivity of Endophilin contained 38 % POPC, 25 % PE, 20 % PS, 2 % PI(4,5)P2 and 15 % Cholesterol (values given in molar percentages). For PI(4,5)P2 titration experiments, POPC concentration was adjusted accordingly to reach a final 100 % molar content.

For vesiculation with ENTH, liposomes were made of Brain Extract (Sigma) with 2 % PI(4,5)P2.

5.2 Molecular Biology

All the constructs used in this thesis were cloned using Fragment Exchange (FX) cloning [352]. A list of constructs can be found in table 5.3.

Chemocompetent cells were made using calcium chloride and standard protocols [353]. For cloning, MACH1TM T1 competent cells (ThermoFischer Scientific) were used; for protein expression, BL21(DE3) (ThermoFischer Scientific) were used.

For large-scale protein expression, either N-terminal His10-3C (p7xNH3 backbone), N-terminal His10-SUMO (p7xNHS backbone) or N-terminal His10-GST-linker-3C (p7xNHGstG3 backbone) were used. GFP-fusion constructs used in NanoSight experiments were cloned with an N-terminal His10-GFP-linker-3C or a C-terminal 3C-GFP-His10 tag (p7xNHmGfpG3 or p7xC3mGfpH backbones respectively). 3C denotes the Rhinovirus 3C protease cleavage site.

Empty FX vectors were cloned based on p7xNH3 and p7xC3H by inserting SUMO, GST or GFP using inFusion[®] (ClonTech). A schematic of vectors used can be found in Fig. 5.1

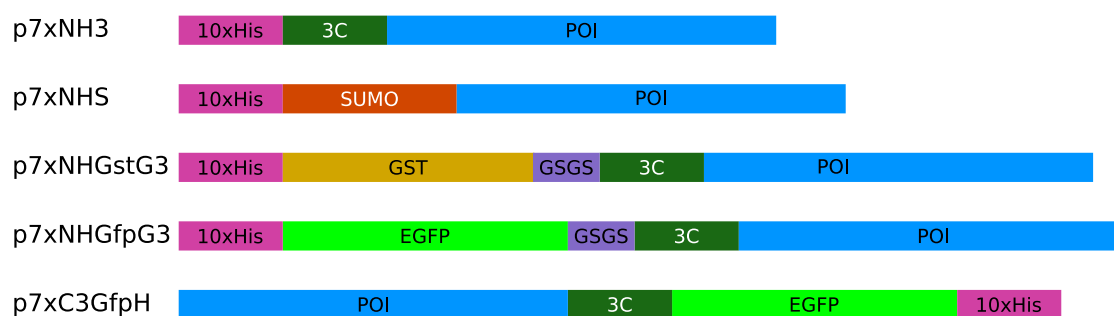


Figure 5.1: Schematic drawing of vector backbones used.

10xHis: His-tag with 10 histidines, 3C: Rhinovirus 3C protease cleavage site, POI: protein of interest, SUMO: Small Ubiquitin-like Modifier tag, GST: glutathione S-transferase, GSGS: Gly-Ser-Gly-Ser linker, EGFP: enhanced Green Fluorescent Protein

Table 5.3: Constructs used in this thesis

ID	Short name	Construct	Tag	Species	Vector
acv385	Endo NBAR-sfGFP	Endophilin A2(1-247)	C-ter 3C-mGFP-His10	rat	p7xC3mGfpH
acv413	FCHo2 BARX-sfGFP	FCHo2(1-327)-Cys	C-ter 3C-mGFP-His10	mouse	p7xC3mGfpH
acv383	IRSp53 BAR-sfGFP	IRSp53(1-250)	C-ter 3C-mGFP-His10	human	p7xC3mGfpH
acv450	Amphiphysin BAR-sfGFP	Amphiphysin1(1-252)	C-ter 3C-mGFP-His10	human	p7xC3mGfpH
acv451	SNX9 PXBAR-sfGFP	SNX9(204-595)	N-ter His10-mGFP-linker-3C	human	p7xNHmGfpG3
acv389	AKT PH-sfGFP	AKT(1-164)	N-ter His10-mGFP-linker-3C	human	p7xNHmGfpG3
acv467	PLCd1 PH-sfGFP	PLCd1(11-140)	C-ter 3C-mGFP-His10	human	p7xC3mGfpH
acv483	CYTH3 PH-sfGFP	CYTH3(257-389)	N-ter His10-mGFP-linker-3C	human	p7xNHmGfpG3
acv473	ING2 PHD-sfGFP	ING2(201-280)	N-ter His10-mGFP-linker-3C	human	p7xNHmGfpG3
acv474	ACF1 PHD-sfGFP	ACF1(1131-1209)	N-ter His10-mGFP-linker-3C	human	p7xNHmGfpG3
acv481	Dab2 PTB-sfGFP	Dab2(33-191)	C-ter 3C-mGFP-His10	human	p7xC3mGfpH
acv482	IRS1 PTB-sfGFP	IRS1(157-267)	C-ter 3C-mGFP-His10	human	p7xC3mGfpH
acv484	NCF4 PX-sfGFP	NCF4(2-149)	C-ter 3C-mGFP-His10	human	p7xC3mGfpH
acv485	SGK3 PX-sfGFP	SGK3(8-126)	C-ter 3C-mGFP-His10	human	p7xC3mGfpH
acv171	PICK1 PDZ-sfGFP	PICK1(11-116)	C-ter 3C-GFP-His10	human	p7xC3GfpH
acv448	PKC δ C1-sfGFP	PKC δ (220-290)	N-ter His10-mGFP-linker-3C	mouse	p7xNHmGfpG3
acv445	PKC β 2 C1B-sfGFP	PKC β 2(91-161)	N-ter His10-mGFP-linker-3C	human	p7xNHmGfpG3
acv446	PKC β 2 C1BC2-sfGFP	PKC β 2(91-289)	N-ter His10-mGFP-linker-3C	human	p7xNHmGfpG3
acv468	PLC δ 1 C2-sfGFP	PLC δ 1(621-756)	N-ter His10-mGFP-linker-3C	human	p7xNHmGfpG3

Continued on next page

Table 5.3 – *Continued from previous page*

ID	Short name	Construct	Tag	Species	Vector
acv469	cPLA2 C2-sfGFP	cPLA2(17-140)C139A	N-ter His10-mGFP-linker-3C	human	p7xNHmGfpG3
acv177	Syt1 C2-sfGFP	Synaptotagmin1(97-422)	C-ter 3C-GFP-His10	mouse	p7xC3GfpH
acv466	PLCb1b C2-Gaq-sfGFP	PLCb1b(677-1173)	N-ter His10-mGFP-linker-3C	human	p7xNHmGfpG3
acv387	HRS FYVE-sfGFP	HRS(149-230)	N-ter His10-mGFP-linker-3C	human	p7xNHmGfpG3
acv471	EEA1 FYVE-sfGFP	EEA1(1325-1411)	N-ter His10-mGFP-linker-3C	human	p7xNHmGfpG3
acv472	WDFY3 FYVE-sfGFP	WDFY3(3451-3516)	N-ter His10-mGFP-linker-3C	human	p7xNHmGfpG3
acv388	FAK1 FERM-sfGFP	FAK1(31-399)	C-ter 3C-mGFP-His10	human	p7xC3mGfpH
acv475	Talin1 FERM-sfGFP	Talin1(1-401)	C-ter 3C-mGFP-His10	human	p7xC3mGfpH
acv476	KRIT1 FERM-sfGFP	KRIT1(259-736)	N-ter His10-mGFP-linker-3C	human	p7xNHmGfpG3
acv452	ANTH-sfGFP	AP180(1-280)	C-ter 3C-mGFP-His10	rat	p7xC3mGfpH
acv418	ENTH-sfGFP	Epsin1(1-164)	C-ter 3C-mGFP-His10	human	p7xC3mGfpH
acv479	MTR2 GRAM-sfGFP	MTMR2(74-200)	C-ter 3C-mGFP-His10	human	p7xC3mGfpH
acv480	OXR1 GRAM-sfGFP	OXR1(175-285)	C-ter 3C-mGFP-His10	human	p7xC3mGfpH
acv477	WIPI1-sfGFP	WIPI1	C-ter 3C-mGFP-His10	human	p7xC3mGfpH
acv478	WDR45B-sfGFP	WDR45B	C-ter 3C-mGFP-His10	human	p7xC3mGfpH
acv453	AnnexinA4-sfGFP	AnnexinA4	N-ter His10-mGFP-linker-3C	human	p7xNHmGfpG3
acv454	AnnexinA7-sfGFP	AnnexinA7	N-ter His10-mGFP-linker-3C	human	p7xNHmGfpG3
acv398	MICALL1(668-863)-sfGFP	MICALL1(668-863)	C-ter 3C-GFP-His10	human	p7xC3GfpH
acv486	MICALL1(676-803)-sfGFP	MICALL1(676-803)	C-ter 3C-mGFP-His10	human	p7xC3mGfpH
acv487	MICALL1(690-803)-sfGFP	MICALL1(690-803)	C-ter 3C-mGFP-His10	human	p7xC3mGfpH

Continued on next page

Table 5.3 – *Continued from previous page*

ID	Short name	Construct	Tag	Species	Vector
acv520	NECAP1 Phear-sfGFP	NECAP1(1-133)	N-ter His10-mGFP-linker-3C	human	p7xNHmGfpG3
acv247	ENTH wt	Epsin1(1-164)	N-His10-SUMO cleaved	human	p7xNHS
acv281	ENTH L6W	Epsin1(1-164)L6W	N-His10-SUMO cleaved	human	p7xNHS
acv293	ADRA2A(299-374)	ADRA2A(299-374)	N-ter His10-GST-linker-3C	human	p7xNHGstG3
acv294	ADRA2A(299-339)	ADRA2A(299-339)-Trp	N-ter His10-GST-linker-3C	human	p7xNHGstG3
acv295	ADRB1(245-314)	ADRB1(245-314)-Trp	N-ter His10-GST-linker-3C	mouse	p7xNHGstG3
acv296	ADRB2(220-274)	ADRB2(220-274)-Trp	N-ter His10-GST-linker-3C	human	p7xNHGstG3
acv318	CIN85(327-412)	CIN85(327-412)-Trp	N-ter His10-GST-linker-3C	human	p7xNHGstG3
acv319	CIN85(390-428)	CIN85(390-428)-Trp	N-ter His10-GST-linker-3C	human	p7xNHGstG3
acv324	Alix	Alix(748-770)-Trp	N-ter His10-GST-linker-3C	human	p7xNHGstG3
acv374	SH3	EndophilinA1(294-352)	N-ter His10-3C	rat	p7xNH3
103-65	Endo	EndophilinA1	N-ter His6-3C	rat	pOPINF
acv400		EndophilinA1(294-352)-3C-Alix(748-770)	N-ter His10-SUMO	rat/human	p7xNHS
acv494	Alix P9/12A	Alix(748-770)P752/5A	N-ter His10-GST-linker-3C	human	p7xNHGstG3
acv495	Alix P11A	Alix(748-770)P754A	N-ter His10-GST-linker-3C	human	p7xNHGstG3
acv493	Alix R14A	Alix(748-770)R757A	N-ter His10-GST-linker-3C	human	p7xNHGstG3
acv506	Alix P16A	Alix(748-770)P759A	N-ter His10-GST-linker-3C	human	p7xNHGstG3
acv505	Alix P17A	Alix(748-770)P760A	N-ter His10-GST-linker-3C	human	p7xNHGstG3
acv489	Alix P18/21A	Alix(748-770)P761/4A	N-ter His10-GST-linker-3C	human	p7xNHGstG3
acv496	Alix V19A	Alix(748-770)V762A	N-ter His10-GST-linker-3C	human	p7xNHGstG3

Continued on next page

Table 5.3 – *Continued from previous page*

ID	Short name	Construct	Tag	Species	Vector
acv490	Alix L20A	Alix(748-770)L763A	N-ter His10-GST-linker-3C	human	p7xNHGstG3
acv491	Alix R24A	Alix(748-770)R767A	N-ter His10-GST-linker-3C	human	p7xNHGstG3
acv516	Alix T7C	Alix(748-770)T750A	N-ter His10-GST-linker-3C	human	p7xNHGstG3
acv502	Alix P17C	Alix(748-770)P759C	N-ter His10-GST-linker-3C	human	p7xNHGstG3
acv499	Alix A25C	Alix(748-770)A768C	N-ter His10-GST-linker-3C	human	p7xNHGstG3
acv416	ADRA2A	ADRA2A(293-339)	N-ter His10-GST-linker-3C	human	p7xNHGstG3
acv527	SH3 E304C	EndophilinA1(294-352)C294/5S-E304C	N-ter His10-SUMO	rat	p7xNHS
acv533	ADRA2A D12C	ADRA2A(293-339)D300C	N-ter His10-GST-linker-3C	human	p7xNHGstG3
acv535	ADRA2A E24C	ADRA2A(293-339)E312C	N-ter His10-GST-linker-3C	human	p7xNHGstG3
95-1		EndophilinA2(309-366)	N-ter GST-3C	human	pGex6P2
acv390	ADRA2A(293-339) wt	ADRA2A(293-339)	N-ter His10-SUMO	human	p7xNHS
acv391	ADRA2A(293-339)SSSS(8-11)DDDD	ADRA2A(293-339)SSSS(296-9)DDDD	N-ter His10-SUMO	human	p7xNHS
acv349	ADRA2A(293-374) wt	ADRA2A(293-374)	N-ter His10-SUMO	human	p7xNHS
acv350	ADRA2A(293-374)SSSS(8-11)DDDD	ADRA2A(293-374)SSSS(296-9)DDDD	N-ter His10-SUMO	human	p7xNHS
acv351	ADRA2A S72D	ADRA2A(293-374)S360D	N-ter His10-SUMO	human	p7xNHS
119-42	ADRA2A S43E	ADRA2A(293-374)S331E	N-ter His10-SUMO	human	p7xNHS

5.2.1 cDNA library generation

For cDNA library generation, RNA was extracted from HEK293T, HeLa and U2OS cell pellets with the RNeasy Mini Kit part 1 (Qiagen) according to the kit instructions. cDNA was synthesised from the extracted RNA with the SuperScript III kit (Invitrogen) using 5 μ g RNA as a template following the manufacturer's protocol. cDNA was synthesised both with oligo-dT and random hexamer primers. To use as a template for PCR, cDNA from all three cell lines and both primer sets were mixed and 1 μ l was used per PCR reaction.

5.2.2 Fragment Exchange (FX) Cloning

Fragment Exchange (FX) Cloning [352] is a restriction-ligation based method which uses the type IIS restriction enzyme SapI that cleaves 3 bp away from its non-palindromic recognition site. The 3 bp overhang were chosen by Geertsma *et al.* to be AGT (coding for serine) at the 5' end of the insert and GCA (coding for alanine) at the 3' end. The overhangs are different on each side of the insert to ensure directionality of the cloning. The small, uncharged amino acids serine and alanine were chosen to limit the impact of added amino acids on protein stability and activity.

During FX cloning, the insert is amplified by PCR. Both the insert and the vector are cut by SapI in the same tube. This excises a cassette containing the negative selection marker *ccdB* from the vector. After ligation and transformation into non-*ccdB* resistant bacterial strain, vectors not containing the insert will cause *ccdB*-mediated bacterial death ensuring close to 100% cloning efficiency.

Transfer from the donor vector into an expression vector happens through SapI digestion and DNA ligation. Both reactions can be carried out simultaneously as in the expression vectors, the SapI recognition sites are located in the excised cassette, so that after ligation of the insert, no SapI sites remain. This ensures directionality of the reaction and increases the yield.

5.2.3 Mutagenesis (HMM and AC)

Mutagenesis primers were designed with 8 bp upstream and 26 downstream of the mutation to be introduced. PCR amplification was done with Phusion[®] High-Fidelity DNA

Polymerase (NEB) using GC buffer and touch-down PCR or with KOD Hot Start DNA Polymerase (Novagen) with addition of betaine (Sigma) and standard protocols.

Template was digested using FastDigest DpnI (ThermoFischer Scientific). PCR products were purified using NucleoSpin[®] Gel and PCR Clean-up (Macherey-Nagel). To increase the efficiency of annealing between both single-stranded ends, inFusion[®] reaction was performed.

5.3 Recombinant protein expression and purification

5.3.1 Recombinant protein expression in *E. coli*

Vectors containing the gene of interest under the control of the T7 promoter were transformed in BL21(DE3) cells (ThermoFischer Scientific) and plated on TYE-agar containing the corresponding antibiotic for selection. The next day, colonies were striked from the plate and inoculated in 50 ml 2xTY. After a few hours, 20 ml preculture was added to 1 l 2xTY and cells were grown until OD₆₀₀ reached 0.8-1. Protein expression was then induced by addition of 160 μ M IPTG overnight at 18 °C. For small-scale protein expression, the protocol was similar except that 1 ml preculture was added to 50 ml 2xTY.

5.3.2 Small-scale protein purification

50 ml cultures were harvested by centrifugation 15 min at 3000 g. Pellets were resuspended in 3 ml IMAC-L containing lysozyme and incubated for 10 min at 4 °C. Cells were lysed by sonication using a Microson Ultrasonic cell disruptor with a micro tip (Misonix incorporate). Unbroken cells and debris were pelleted 5 min at 20000 g. The supernatant was transferred in a fresh tube. After addition of DNaseI 1 mM MgCl₂ and 200 μ l 50% TALON slurry, the cell lysate was incubated at 10 min at 4 °C on a rolling shaker. Beads were washed with 10ml IMAC-L, 1ml IEX-B (high-salt wash), 15ml IMAC-L. Protein was eluted with 1ml IMAC-E.

5.3.3 Large-scale protein purification

Large-scale protein purification was generally realised in three steps, an affinity capture using His-tag, followed by an ion exchange column and finally size exclusion chromatography.

Cultures were harvested by centrifugation 15 min at 4200 g. Pellets were resuspended in IMAC-L containing lysozyme and incubated for 10 min at 4 °C. Cells were lysed by sonication using a Sonics VC 750. After addition of DNaseI and 1 mM MgCl₂, unbroken cells and debris were pelleted 15 min at 40000 g. The supernatant was loaded onto HisTrapTM HP column (GE Healthcare). HisTrap column were washed with IMAC-L and IEX-B, then protein was eluted with IMAC-E.

Depending on the pI of the protein, anion exchange (HisTrapTM Q) or cation exchange (HisTrapTM SP) chromatography was used. Prior to loading on ion exchange column, NaCl and imidazole were diluted out in IEX-A. An NaCl gradient ranging from 100 mM to 500 mM NaCl was run on ÄKTA Purifier 10 system.

For size exclusion chromatography, either SuperdexTM 75 or SuperdexTM 200 column (GE Healthcare) was used depending on the size of the protein. The amount of protein determined which size of column was used: 10/30, HiLoad 16/60 or HiLoad 26/60. Size exclusion chromatography was run in GEF buffer or P-GEF for small peptides. Protein was concentrated using Amicon Ultra centrifugal filter units (Merck Millipore) or, in the case of small peptides in P-GEF buffer, by evaporation in a SpeedVac Vacuum concentrator (Eppendorf). Protein was then aliquoted, flash-frozen in liquid N₂ and stored at -80 °C

5.3.4 Protein labelling

For single-site maleimide labelling of a cysteine, endogeneous cysteines were mutated to alanine or serine and a cysteine residue was mutated in, either at the N-terminus or in a loop. Labelling reactions were set up as in the manufacturer's instruction with 50-100 μM protein and ten-fold excess of Alexa488-maleimide[®] (ThermoFischer Scientific) dissolved in DMSO. TCEP (tris(2-carboxyethyl)phosphine) was added to reduce the cysteines. The labelling reaction was left for a few hours at room temperature or overnight at 4 °C. Excess

of unreacted dye was removed by centrifugation filters. Degree of labelling was determined based on A_{280} for protein concentration and A_{488} for dye concentration.

5.4 Biochemical assays

5.4.1 Liposome flotation

0.1 mM liposomes were incubated with 1 μ M protein in 50 μ l final volume for 5 minutes then mixed 1:1 with 80 % HistodenzTM (Sigma) for a final 40% Histodenz concentration. This was then layered with 50 μ l 30 % Histodenz solution and 30 μ l NS buffer. After centrifugation at 80000 rpm in TLA-100 (250000 g) for 20 minutes, 30 μ l fractions were collected with gel loading pipet tips from the bottom of the tubes.

5.4.2 GST pull-down

Pellets from 10ml cultures of cells expressing GST-fusion proteins were resuspended in 0.75 ml IMAC-L. Cells were lysed by sonication using a Microson Ultrasonic cell disruptor with a micro tip (Misonix incorporate). DNaseI and 1 mM MgCl₂ were added, then unbroken cells and debris were pelleted 5 min at 20000 g. The supernatant was transferred in a fresh tube. This centrifugation step was repeated to ensure clearance of the lysate. After addition of 30 μ l Glutathione Sepharose[®] 4B (GE Healthcare) 50% slurry, the lysate was incubated 30 min at 4 °C on an orbital shaker. Beads were washed six times with 1.4 ml PD buffer by centrifugation.

Lysate of cells expressing prey protein was prepared as above. 150 μ l lysate was incubated with previously prepared beads loaded with GST-bait fusion protein for 10 min at 4 °C on an orbital shaker. The amount of beads used was previously normalised for the amount of protein bound using SDS-PAGE. Beads were washed four times with 1.4 ml PD buffer by centrifugation. Beads were incubated with SB buffer at 95 °C and results analysed on SDS-PAGE.

For pull-down with ADRA2A phosphomimetics mutants, His-SUMO-tagged peptides were first enriched out of lysate from 2 ml *E. coli* cultures overexpressing these constructs. The cell lysate was incubated 5 min with 60 μ l TALON[®] slurry in IMAC-L buffer. The beads were washed with IMAC-L and PD buffer and resuspended in IMAC-L. The peptides were

cleaved off the beads with the SUMO protease His-SENPI and the resulting supernatant was used as prey in pull-down experiments.

5.4.3 Isothermal Titration Calorimetry

ITC experiments were performed on an ITC200 calorimeter (GE-MicroCal) in GEF buffer at 25°C. For Alix-SH3 interaction, 45-80 μM SH3 in the cell and 765 μM Alix peptide in the syringe were used. For measurements with ADRA2A, 1-1.2 mM SH3 in the syringe and 100-150 μM ADRA2A peptide (wild-type and phosphomimetics) were used.

5.5 NanoSight measurements

NanoSight measurements were done on a NanoSight LM10 (Malvern) with a sCMOS camera and a syringe pump. A 488 nm laser together with a 500 nm longpass filter was used for green fluorescence. Fluorescent particles in the far-red range were detected using a 638 nm laser and a 650 nm longpass filter.

To check the calibration, NIST (National Institute of Standards and Technology) traceable calibration beads (3000 Series Nanosphere[®] Size Standards (ThermoFischer Scientific)) were diluted in water. Movies were recorded without pump flow and particles were tracked using the company's software. Results used were FTLA (finite track length adjustment) corrected according to the proprietary algorithm. For comparison with Dynamic Light Scattering, a W130i DLS system (AvidNano) was used.

For measurements of curvature sensitivity, liposome solutions were diluted to reach final $2\text{-}8\cdot 10^8$ particles/ml as recommended by the manufacturer. This corresponded to final concentrations of 1 $\mu\text{g}/\text{ml}$ for unextruded or 800 nm extruded liposomes, 0.5 $\mu\text{g}/\text{ml}$ for 200 nm extruded liposomes and 0.125 $\mu\text{g}/\text{ml}$ for 50 nm extruded liposomes. Fluorescent protein concentration was 1-5 nM to reduce fluorescent background of unbound protein.

Liposomes were diluted in NS buffer, then protein was added. After mixing, the sample was loaded onto the NanoSight. Recordings were made under flow from the syringe pump to reduce bleaching. 120-180 s long movies were recorded using appropriate camera settings to maximise signal/background ratio. Particles were tracked using the company's software. Raw, non-FTLA corrected data was used due to sample heterogeneity.

Single particle tracking and data processing was carried out by the NanoSight NTA software version 3.1 (Malvern). Binned data was analysed using GraphPad Prism version 6.0f for Mac OS X, GraphPad Software, La Jolla California USA, www.graphpad.com. Box plots were created using 25th to 75th percentile, with the middle line representing the median and whiskers 10th to 90th percentiles.

5.6 NMR

5.6.1 Recombinant protein expression

For isotope-labelling for NMR, proteins were expressed in M9- supplemented with 1 g/l $^{15}\text{NH}_4\text{Cl}$ and 4 g/l ^{13}C -glucose. Due to the lower yields in M9-, a protocol based on [354] was used. The preculture was grown in 2xTY and 6 l of 2xTY were inoculated. When OD_{600} reached 0.6-0.8, cells were harvested by centrifugation 15 min at 4200 g, washed twice by resuspension/pelleting in M9- and finally resuspended in 1 l warm M9-. This culture was incubated 40 min at 37°C for the cells to use up the remaining unlabelled nitrogen and carbon sources before heavy isotopes were added. After 30 min incubation during which cells incorporate heavy isotope sources in their metabolism, protein expression was induced by addition of 160 μM IPTG overnight at 18 °C.

5.6.2 Protein labelling for Paramagnetic Relaxation Enhancement PRE

For 4-maleimido-TEMPO (2,2,6,6-tetramethyl-1-piperidinyloxy) (Sigma) labelling, constructs were designed to contain only one cysteine at a chosen position. Proteins were kept reduced by a five-fold excess of TCEP. Labelling reactions were conducted with a ten-fold excess of TEMPO for 4 hours at room temperature. Unreacted TEMPO was quenched by an addition of a two-fold excess (over TEMPO) of DTT (dithiothreitol) for 30 min at room temperature. Free TEMPO was removed by dialysis against NMR buffer overnight at 4 °C. After NMR spectra recording, TEMPO radical was quenched by incubation with a five-fold excess of sodium ascorbate and NMR spectre were recorded again as a control.

5.6.3 Data collection (TR) and analysis (TR and AC)

Spectra were collected on 600 and 800 MHz Bruker Advance III (Bruker) spectrometers equipped with a triple-resonance inverse cryogenic probe head at 10 °C sample temperature. Backbone resonance assignments were performed using standard triple-resonance experiments (HNCACB, CBCA(CO)NH, HNC(O) and HN(CA)CO), acquired using unmodified Bruker pulse programs. Chemical shift perturbations were recorded by comparing fast HSQC spectra [355] obtained with typically 1024 and 256 data points in t_2 and t_1 , covering spectral widths of 14.0 and 40 ppm, respectively. The digital resolution of processed data was 1.5 and 4.3 Hz/point in f_2 and f_1 . Spectra were processed with TopSpin version 3 (Bruker) and analysed with Sparky version 3.115 [Goddard T. D. & Kneller D. G., SPARKY 3, University of California, San Francisco].

For titration experiments, occupancy on the isotopically labelled binding partner was calculated using an in-house spreadsheet for solving saturation binding equations. Concentrations were chosen so that in the fully saturated complex, occupancy of the labelled material was >95%. For the intermediate concentration point, concentrations were chosen to reach an occupancy of 25%.

CSP were quantified as $CSP = |\Delta\delta^1H| + 1/5 |\Delta\delta^{15N}|$, where $|\Delta\delta|$ is the absolute change in chemical shift. Solvent accessibility of residues in Endophilin SH3 structure (pdb 2KNB) was calculated using NACCESS [S. Hubbard and J. Thornton 1992-6]. Modelling was performed using HADDOCK [343, 344]. A threshold of >40% relative solvent accessibility was used to define active interaction restraints (AIR) in HADDOCK modelling. Passive residues (residues which have lower CSP and/or are in proximity of active residues) were assigned automatically.

Docking calculations were performed by submission to the HADDOCK2.2 web server [344]. The docking simulations were performed with default server parameters throughout, except that non-polar hydrogen atoms were not removed and the peptides were defined to be fully flexible along the entire length. The default option to randomly exclude a proportion of active restraints was disabled. The starting model for Endophilin SH3 was taken from Protein Data Bank submission 2KNB [229], with the Ubl domain removed. Starting models for Alix and ADRA2A peptides were constructed with PyMol software [PyMol Molecular Graphics System, version 1.8.4, Schrödinger, LLC.], setting all backbone torsion angles initially set to conform to elements of regular secondary structure ($\phi, \psi = -78^\circ, 149^\circ$

for polyproline-II helix, -57° , -47° for α -helix; -139° , -135° for β -strand). Models were subjected to docking, semi-flexible refinement followed by refinement with explicit water solvation, with convergence statistics generated for 200 individual models.

Chapter 6

Bibliography

- [1] Fawcett DW. *The Cell*. W. B. Saunders Company, Philadelphia, 2nd edition (1981).
- [2] Shibata Y, Hu J, Kozlov MM & Rapoport TA. Mechanisms Shaping the Membranes of Cellular Organelles. *Annual Review of Cell and Developmental Biology*, 25:329–354 (2009).
- [3] Griparic L & van der Blik AM. The Many Shapes of Mitochondrial Membranes. *Traffic*, 2:235–244 (2001).
- [4] McMahon HT & Gallop JL. Membrane curvature and mechanisms of dynamic cell membrane remodelling. *Nature*, 438(7068):590–6 (2005).
- [5] Kozlov MM, Campelo F, Liska N, Chernomordik LV, Marrink SJ *et al.* Mechanisms shaping cell membranes. *Current opinion in cell biology*, 29C:53–60 (2014).
- [6] McMahon HT & Boucrot E. Membrane curvature at a glance. *Journal of Cell Science*, 128(6):1065–1070 (2015).
- [7] Jarsch IK, Daste F & Gallop JL. Membrane curvature in cell biology : An integration of molecular mechanisms. *Journal of Cell Biology*, 214(4):375–387 (2016).
- [8] Farge E, Ojcius DM, Subtil A & Dautry-Varsat A. Enhancement of endocytosis due to aminophospholipid transport across the plasma membrane of living cells. *American Journal of Physiology*, 276:725–733 (1999).
- [9] Hua Z & Graham TR. Requirement for Neo1p in Retrograde Transport from the Golgi Complex to the Endoplasmic Reticulum. *Molecular biology of the cell*, 14(December):4971–4983 (2003).

- [10] Laan EVDBvD, Killian JA & Kruijff BD. Nonbilayer lipids affect peripheral and integral membrane proteins via changes in the lateral pressure profile. *Biochimica et biophysica acta*, 1666:275–288 (2004).
- [11] Hammond K, Reboiras MD, Lyle IG & Jones MN. Characterisation of phosphatidylcholine/phosphatidylinositol sonicated vesicles. Effects of phospholipid composition on vesicle size. *Biochimica et biophysica acta*, 774(1):19–25 (1984).
- [12] Kooijman EE, Carter KM, van Laar EG, Chupin V, Burger KNJ *et al.* What makes the bioactive lipids phosphatidic acid and lysophosphatidic acid so special? *Biochemistry*, 44(51):17007–15 (2005).
- [13] Brown WJ, Chambers K & Doody A. Phospholipase A2 (PLA2) enzymes in membrane trafficking: mediators of membrane shape and function. *Traffic (Copenhagen, Denmark)*, 4(4):214–21 (2003).
- [14] Shemesh T, Luini A, Malhotra V, Burger KNJ & Kozlov MM. Prefission constriction of Golgi tubular carriers driven by local lipid metabolism: a theoretical model. *Biophysical journal*, 85(6):3813–27 (2003).
- [15] Unwin N. Refined structure of the nicotinic acetylcholine receptor at 4Å resolution. *Journal of molecular biology*, 346(4):967–89 (2005).
- [16] Lee Sa, Eyeson R, Cheever ML, Geng J, Verkhusha VV *et al.* Targeting of the FYVE domain to endosomal membranes is regulated by a histidine switch. *Proceedings of the National Academy of Sciences of the United States of America*, 102(37):13052–7 (2005).
- [17] Fertuck HC & Salpeter MM. Localization of Acetylcholine Receptor by 125I-Labeled alpha-Bungarotoxin Binding at Mouse Motor Endplates. *Proceedings of the National Academy of Sciences*, 71(4):1376–1378 (1974).
- [18] Aimon S, Callan-jones A, Berthaud A, Pinot M, Toombes GES *et al.* Membrane Shape Modulates Transmembrane Protein Distribution. *Developmental Cell*, 28(2):212–218 (2014).
- [19] Parton RG & Simons K. The multiple faces of caveolae. *Nature Reviews Molecular Cell Biology*, 8:185–194 (2007).

- [20] Boudin H, Doan A, Xia J, Shigemoto R, Haganir RL *et al.* Presynaptic Clustering of mGluR7a Requires the PICK1 PDZ Domain Binding Site. *Neuron*, 28:485–497 (2000).
- [21] Eckler SA, Kuehn R & Gautam M. Deletion of N-terminal Rapsyn domains disrupts clustering and has dominant negative effects on clustering of full-length Rapsyn. *Neuroscience*, 131:661–670 (2005).
- [22] Campelo F, McMahon HT & Kozlov MM. The hydrophobic insertion mechanism of membrane curvature generation by proteins. *Biophysical journal*, 95(5):2325–39 (2008).
- [23] Braun AR, Sevcik E, Chin P, Rhoades E, Tristram-Nagle S *et al.* α -Synuclein induces both positive mean curvature and negative Gaussian curvature in membranes. *Journal of the American Chemical Society*, 134(5):2613–20 (2012).
- [24] Ford MGJ, Mills IG, Peter BJ, Vallis Y, Praefcke GJK *et al.* Curvature of clathrin-coated pits driven by epsin. *Nature*, 419(6905):361–366 (2002).
- [25] Brooks A, Shoup D, Kustigian L, Puchalla J, Carr CM *et al.* Single Particle Fluorescence Burst Analysis of Epsin Induced Membrane Fission. *Plos One*, 10(3):e0119563 (2015).
- [26] Gallop JL, Jao CC, Kent HM, Butler PJG, Evans PR *et al.* Mechanism of endophilin N-BAR domain-mediated membrane curvature. *The EMBO journal*, 25(12):2898–910 (2006).
- [27] Ambroso MR, Hegde BG & Langen R. Endophilin A1 induces different membrane shapes using a conformational switch that is regulated by phosphorylation. *Proceedings of the National Academy of Sciences of the United States of America*, 111(19):6982–7 (2014).
- [28] Martens S, Kozlov MM & McMahon HT. How synaptotagmin promotes membrane fusion. *Science (New York, N. Y.)*, 316(5828):1205–8 (2007).
- [29] Herrick DZ, Sterbling S, Rasch KA, Hinderliter A & Cafiso DS. Position of Synaptotagmin I at the Membrane Interface : Cooperative Interactions of Tandem C2 Domains. *Biochemistry*, 45:9668–9674 (2006).

- [30] Voeltz GK, Prinz Wa, Shibata Y, Rist JM & Rapoport Ta. A class of membrane proteins shaping the tubular endoplasmic reticulum. *Cell*, 124(3):573–86 (2006).
- [31] Stachowiak JC, Schmid EM, Ryan CJ, Ann HS, Sasaki DY *et al.* Membrane bending by protein-protein crowding. *Nature cell biology*, 14(9):944–9 (2012).
- [32] Busch DJ, Houser JR, Hayden CC, Sherman MB, Lafer EM *et al.* Intrinsically disordered proteins drive membrane curvature. *Nature Communications*, 6:7875 (2015).
- [33] Matsudaira P. Actin crosslinking proteins at the leading edge. *Seminars in Cell & Developmental Biology*, 5:165–174 (1994).
- [34] Condeelis J, Hall A, Bresnick A, Warren V, Hock R *et al.* Actin Polymerization and Pseudopod Extension During Amoeboid Chemotaxis. *Cell Motility and the Cytoskeleton*, 10:77–90 (1988).
- [35] Swanson Ja, Johnson MT, Beningo K, Post P, Mooseker M *et al.* A contractile activity that closes phagosomes in macrophages. *Journal of cell science*, 112 (Pt 3:307–316 (1999).
- [36] Forscher P & Smith SJ. Actions of Cytochalasins on the Organization of Actin Filaments and Microtubules in a Neuronal Growth Cone. *Journal of Cell Biology*, 107:1505–1516 (1988).
- [37] Glotzer M. The mechanism and control of cytokinesis. *Curr Opin Cell Biol*, 9:815–823 (1997).
- [38] Hirokawa N & Noda Y. Intracellular Transport and Kinesin Superfamily Proteins, KIFs: Structure, Function, and Dynamics. *Physiological reviews*, 88:1089–1118 (2008).
- [39] Dabora SL & Sheetz MP. The microtubule-dependent formation of a tubulovesicular network with characteristics of the ER from cultured cell extracts. *Cell*, 54(1):27–35 (1988).
- [40] Vale RD & Hotani H. Formation of membrane networks in vitro by kinesin-driven microtubule movement. *The Journal of cell biology*, 107(6 Pt 1):2233–41 (1988).
- [41] Hinshaw JE & Schmid SL. Dynamin self-assembles into rings suggesting a mechanism for coated vesicle budding. *Nature*, 374:190–192 (1995).

- [42] Marks B, Stowell MH, Vallis Y, Mills IG, Gibson a *et al.* GTPase activity of dynamin and resulting conformation change are essential for endocytosis. *Nature*, 410(6825):231–5 (2001).
- [43] Praefcke GJK & McMahon HT. The Dynamin Superfamily : Universal Membrane Tubulation And Fission Molecules ? *Nature Reviews Molecular Cell Biology*, 5:133–47 (2004).
- [44] Alonso Y Adell M & Teis D. Assembly and disassembly of the ESCRT-III membrane scission complex. *FEBS Letters*, 585(20):3191–3196 (2011).
- [45] Gruenberg J & Stenmark H. The biogenesis of multivesicular endosomes. *Nature Reviews Molecular Cell Biology*, 5:317–23 (2004).
- [46] Hurley JH. ESCRT complexes and the biogenesis of multivesicular bodies. *Curr Opin Cell Biol*, 20:4–11 (2008).
- [47] Piper RC & Katzmann DJ. Biogenesis and Function of Multivesicular Bodies. *Annual Review of Cell and Developmental Biology*, 23(1):519–547 (2007).
- [48] Bieniasz PD. Late budding domains and host proteins in enveloped virus release. *Journal of virology*, 344:55–63 (2006).
- [49] Fujii K, Hurley JH & Freed EO. Beyond Tsg101 : the role of Alix in "ESCRTing" HIV-1. *Nature Reviews Microbiology*, 5:912–6 (2007).
- [50] Morita E & Sundquist WI. Retrovirus budding. *Annual Review of Cell and Developmental Biology*, 20:395–425 (2004).
- [51] Carlton JG & Cullen PJ. Coincidence detection in phosphoinositide signaling. *Trends in Cell Biology*, 15(10):540–547 (2007).
- [52] Lindås Ac, Karlsson EA, Lindgren MT, Ettema TJG & Bernander R. A unique cell division machinery in the Archaea. *Proceedings of the National Academy of Sciences*, 105:18942–18946 (2008).
- [53] Morita E, Sandrin V, Chung HY, Morham SG, Gygi SP *et al.* Human ESCRT and ALIX proteins interact with proteins of the midbody and function in cytokinesis. *EMBO Journal*, 26:4215–4227 (2007).
- [54] Frost A, Unger VM & De Camilli P. The BAR Domain Superfamily: Membrane-Molding Macromolecules. *Cell*, 137(2):191–196 (2009).

- [55] Tarricone C, Xiao B, Justin N, Walker PA & Rittinger K. The structural basis of Arfaptn- mediated cross-talk between Rac and Arf signalling pathways. *Nature*, 411(May):215–219 (2001).
- [56] Henne WM, Kent HM, Ford MGJ, Hegde BG, Daumke O *et al.* Structure and analysis of FCHo2 F-BAR domain: a dimerizing and membrane recruitment module that effects membrane curvature. *Structure (London, England : 1993)*, 15(7):839–52 (2007).
- [57] Millard TH, Bompard G, Heung MY, Dafforn TR, Scott DJ *et al.* Structural basis of filopodia formation induced by the IRSp53/MIM homology domain of human IRSp53. *The EMBO journal*, 24(2):240–50 (2005).
- [58] Peter BJ, Kent HM, Mills IG, Vallis Y, Butler PJG *et al.* BAR domains as sensors of membrane curvature: the amphiphysin BAR structure. *Science (New York, N.Y.)*, 303(5657):495–9 (2004).
- [59] Mattila PK, Pykäläinen A, Saarikangas J, Paavilainen VO, Vihinen H *et al.* Missing-in-metastasis and IRSp53 deform PI(4,5)P2-rich membranes by an inverse BAR domain-like mechanism. *The Journal of cell biology*, 176(7):953–64 (2007).
- [60] Saarikangas J, Zhao H, Pyka A, Mattila PK & Kinnunen PKJ. Molecular Mechanisms of Membrane Deformation by I-BAR Domain Proteins. *Current Biology*, 19:95–107 (2009).
- [61] Antonny B, Gounon P, Schekman R & Orci L. Self-assembly of minimal COPII cages. *EMBO reports*, 4(4):419–424 (2003).
- [62] Nossal R. Energetics of Clathrin Basket Assembly. *Traffic*, 2:138–147 (2001).
- [63] Fernandes F, Loura LM, Chichón FJ, Carrascosa JL, Fedorov A *et al.* Role of Helix 0 of the N-BAR Domain in Membrane Curvature Generation. *Biophysical Journal*, 94(April):3065–3073 (2008).
- [64] Chen Z, Zhu C, Kuo CJ, Robustelli J & Baumgart T. The N-terminal amphipathic helix of Endophilin does not contribute to its molecular curvature generation capacity. *Journal of the American Chemical Society*, p. jacs.6b06820 (2016).

- [65] Farsad K, Ringstad N, Takei K, Floyd SR, Rose K *et al.* Generation of high curvature membranes mediated by direct endophilin bilayer interactions. *Journal of Cell Biology*, 155(2):193–200 (2001).
- [66] Antony B. Mechanisms of membrane curvature sensing. *Annual review of biochemistry*, 80:101–23 (2011).
- [67] Drin G & Antony B. Amphipathic helices and membrane curvature. *FEBS letters*, 584(9):1840–1847 (2010).
- [68] Bhatia VK, Hatzakis NS & Stamou D. A unifying mechanism accounts for sensing of membrane curvature by BAR domains, amphipathic helices and membrane-anchored proteins. *Seminars in cell & developmental biology*, 21(4):381–90 (2010).
- [69] Barooji YF, Rørvig-lund A, Semsey S, Reihani SNS & Bendix PM. Dynamics of membrane nanotubes coated with I-BAR. *Scientific Reports*, 6:1–12 (2016).
- [70] Roux A, Koster G, Lenz M, Sorre B, Manneville JB *et al.* Membrane curvature controls dynamin polymerization. *Proceedings of the National Academy of Sciences of the United States of America*, 107(9):4141–6 (2010).
- [71] Merrifield CJ, Feldman ME, Wan L & Almers W. Imaging actin and dynamin recruitment during invagination of single clathrin-coated pits. *Nature cell biology*, 4:691–99 (2002).
- [72] Lenarcic R, Halbedel S, Visser L, Shaw M, Wu LJ *et al.* Localisation of DivIVA by targeting to negatively curved membranes. *The EMBO Journal*, 28(15):2272–2282 (2009).
- [73] Ramamurthi KS & Losick R. Negative membrane curvature as a cue for subcellular localization of a bacterial protein. *Proceedings of the National Academy of Sciences*, 106(32):13541–13545 (2009).
- [74] Eswaramoorthy P, Winter PW, Wawrzusin P, York AG, Shroff H *et al.* Asymmetric Division and Differential Gene Expression during a Bacterial Developmental Program Requires DivIVA. *PLoS Genetics*, 10(8) (2014).
- [75] Janmey PA & Kinnunen PKJ. Biophysical properties of lipids and dynamic membranes. *Trends in Cell Biology*, 16(10):538–546 (2006).

- [76] Vamparys L, Gautier R, Vanni S, Bennett WFD, Tieleman DP *et al.* Conical Lipids in Flat Bilayers Induce Packing Defects Similar to that Induced by Positive Curvature. *Biophysj*, 104(3):585–593 (2013).
- [77] Bigay J, Casella JF, Drin G, Mesmin B & Antony B. ArfGAP1 responds to membrane curvature through the folding of a lipid packing sensor motif. *The EMBO journal*, 24(13):2244–53 (2005).
- [78] White SH & Wimley WC. Hydrophobic interactions of peptides with membrane interfaces. *Biochimica et Biophysica Acta - Reviews on Biomembranes*, 1376(3):339–352 (1998).
- [79] Hristova K, Wimley WC, Mishra VK, Anantharamiah GM, Segrest JP *et al.* An amphipathic alpha-helix at a membrane interface: A structural study using a novel X-ray diffraction method. *Journal of Molecular Biology*, 290(1):99–117 (1999).
- [80] Jao CC, Hegde BG, Chen J, Haworth IS & Langen R. Structure of membrane-bound alpha-synuclein from site-directed spin labeling and computational refinement. *Proceedings of the National Academy of Sciences of the United States of America*, 105(50):19666–19671 (2008).
- [81] Drin G, Casella JF, Gautier R, Boehmer T, Schwartz TU *et al.* A general amphipathic alpha-helical motif for sensing membrane curvature. *Nature structural & molecular biology*, 14(2):138–46 (2007).
- [82] Bigay J, Gounon P, Robineau S & Antony B. Lipid packing sensed by Arf-GAP1 couples COPI coat disassembly to membrane bilayer curvature. *Nature*, 426(December):563–566 (2003).
- [83] Tanigawa G, Orci L, Amherdt M, Ravazzola M, Helms JB *et al.* Hydrolysis of Bound GTP by ARF Protein Triggers Uncoating of Golgi-derived COP-coated Vesicles. *Journal of Cell Biology*, 123(6):1365–1371 (1993).
- [84] Cukierman E, Huber I, Rotman M & Cassel D. The ARF1 GTPase-Activating Protein: Zinc Finger Motif and Golgi Complex Localization. *Science*, 270(1995):1999–2002 (1995).
- [85] Reinhard C, Schweikert M, Wieland FT & Nickel W. Functional reconstitution of COPI coat assembly and disassembly using chemically defined components. *Proceedings of the National Academy of Sciences*, 100:8253–8257 (2003).

- [86] Ambroggio E, Sorre B, Bassereau P, Goud B, Manneville JB *et al.* ArfGAP1 generates an Arf1 gradient on continuous lipid membranes displaying flat and curved regions. *The EMBO journal*, 29(2):292–303 (2010).
- [87] Mesmin B, Drin G, Levi S, Rawet M, Cassel D *et al.* Two lipid-packing sensor motifs contribute to the sensitivity of ArfGAP1 to membrane curvature. *Biochemistry*, 46(7):1779–90 (2007).
- [88] Doucet CM, Esmery N, De Saint-Jean M & Antonny B. Membrane curvature sensing by amphipathic helices is modulated by the surrounding protein backbone. *PLoS ONE*, 10(9):1–23 (2015).
- [89] Cornell RB & Taneva SG. Amphipathic Helices as Mediators of the Membrane Interaction of Amphitropic Proteins, and as Modulators of Bilayer Physical Properties. *Current protein & peptide science*, 6:539–552 (2006).
- [90] Johnson JE, Xie M, Singh LMR, Edge R & Cornell RB. Both acidic and basic amino acids in an amphitropic enzyme, CTP:phosphocholine cytidyltransferase, dictate its selectivity for anionic membranes. *Journal of Biological Chemistry*, 278(1):514–522 (2003).
- [91] Ramamurthi KS, Lecuyer S, Stone Ha & Losick R. Geometric cue for protein localization in a bacterium. *Science (New York, N. Y.)*, 323(5919):1354–7 (2009).
- [92] Jensen MB, Bhatia VK, Jao CC, Rasmussen JE, Pedersen SL *et al.* Membrane curvature sensing by amphipathic helices: a single liposome study using α -synuclein and annexin B12. *The Journal of biological chemistry*, 286(49):42603–14 (2011).
- [93] Saludes JP, Morton La, Ghosh N, Beninson La, Chapman ER *et al.* Detection of highly curved membrane surfaces using a cyclic peptide derived from synaptotagmin-I. *ACS chemical biology*, 7(10):1629–35 (2012).
- [94] Hatzakis NS, Bhatia VK, Larsen J, Madsen KL, Bolinger PY *et al.* How curved membranes recruit amphipathic helices and protein anchoring motifs. *Nature chemical biology*, 5(11):835–41 (2009).
- [95] Taylor KMP & Roseman MA. Effect of Cholesterol , Fatty Acyl Chain Composition , and Bilayer Curvature on the Interaction of Cytochrome b 5 with Liposomes of Phosphatidylcholines +. *Biochemistry*, 34:3841–50 (1995).

- [96] Roshholm KR, Leijnse N, Mantsiou A, Tkach V, Pedersen SL *et al.* Membrane curvature regulates ligand-specific membrane sorting of GPCRs in living cells. *Nature chemical biology*, 13:724–9 (2017).
- [97] Pylypenko O, Lundmark R, Rasmuson E, Carlsson SR & Rak A. The PX-BAR membrane-remodeling unit of sorting nexin 9. *The EMBO journal*, 26(22):4788–800 (2007).
- [98] Bhatia VK, Madsen KL, Bolinger PY, Kunding A, Hedegård P *et al.* Amphipathic motifs in BAR domains are essential for membrane curvature sensing. *The EMBO journal*, 28(21):3303–14 (2009).
- [99] Rostislavleva K, Soler N, Ohashi Y, Zhang L, Pardon E *et al.* Structure and flexibility of the endosomal Vps34 complex reveals the basis of its function on membranes. *Science*, 350(6257):aac7365–aac7365 (2015).
- [100] Prévost C, Zhao H, Manzi J, Lemichez E, Lappalainen P *et al.* IRSp53 senses negative membrane curvature and phase separates along membrane tubules. *Nature Communications*, 6:8529 (2015).
- [101] Pucadyil TJ & Schmid SL. Conserved Functions of Membrane Active GTPases in Coated Vesicle Formation. *Science*, 325:1217–1221 (2009).
- [102] Takei K, Slepnev VI, Haucke V & Camilli PD. Functional partnership between amphiphysin and dynamin in clathrin-mediated endocytosis. *Nature cell biology*, 180:33–39 (1999).
- [103] Capraro BR, Shi Z, Wu T, Chen Z, Dunn JM *et al.* Kinetics of endophilin N-BAR domain dimerization and membrane interactions. *The Journal of biological chemistry*, 288(18):12533–43 (2013).
- [104] Masuda M, Takeda S, Sone M, Ohki T, Mori H *et al.* Endophilin BAR domain drives membrane curvature by two newly identified structure-based mechanisms. *The EMBO journal*, 25(12):2889–2897 (2006).
- [105] Richnau N, Fransson A, Farsad K & Aspenström P. RICH-1 has a BIN/Amphiphysin/Rvsp domain responsible for binding to membrane lipids and tubulation of liposomes. *Biochemical and Biophysical Research Communications*, 320:1034–1042 (2004).

- [106] Boucrot E, Pick A, Çamdere G, Liska N, Evergren E *et al.* Membrane fission is promoted by insertion of amphipathic helices and is restricted by crescent BAR domains. *Cell*, 149(1):124–136 (2012).
- [107] Henne WM, Boucrot E, Meinecke M, Evergren E, Vallis Y *et al.* FCHO proteins are nucleators of clathrin-mediated endocytosis. *Science (New York, N.Y.)*, 328(5983):1281–4 (2010).
- [108] Frost A, Perera R, Roux A, Spasov K, Destaing O *et al.* Structural Basis of Membrane Invagination by F-BAR Domains. *Cell*, 132:807–817 (2008).
- [109] Wang T, Li H, Lin G, Tang C, Li D *et al.* Structural insights on the Mycobacterium tuberculosis proteasomal ATPase Mpa. *Structure (London, England : 1993)*, 17(10):1377–85 (2009).
- [110] Shimada A, Niwa H, Tsujita K, Suetsugu S, Nitta K *et al.* Curved EFC / F-BAR-Domain Dimers Are Joined End to End into a Filament for Membrane Invagination in Endocytosis. *Cell*, 129:761–772 (2007).
- [111] Suetsugu S, Murayama K, Sakamoto A, Hanawa-suetsugu K, Seto A *et al.* The RAC Binding Domain / IRSp53-MIM Homology Domain of IRSp53 Induces RAC-dependent Membrane Deformation *. *Journal of Biological Chemistry*, 281(46):35347–35358 (2006).
- [112] Carlton J, Bujny M, Peter BJ, Oorschot VMJ, Rutherford A *et al.* Sorting nexin-1 mediates tubular endosome-to-TGN transport through coincidence sensing of high-curvature membranes and 3-phosphoinositides. *Current biology : CB*, 14(20):1791–800 (2004).
- [113] Li Y, Augustine GJ & Wenginger K. Kinetics of complexin binding to the SNARE complex: correcting single molecule FRET measurements for hidden events. *Biophysical journal*, 93(6):2178–87 (2007).
- [114] Chial HJ, Wu R, Ustach CV, Mcphail LC, Mobley WC *et al.* Membrane Targeting by APPL1 and APPL2 : Dynamic Scaffolds that Oligomerize and Bind Phosphoinositides. *Traffic*, 9:215–229 (2008).
- [115] Umasankar PK, Sanker S, Thieman JR, Chakraborty S, Wendland B *et al.* Distinct and separable activities of the endocytic clathrin-coat components Fcho1 / 2 and AP-2 in developmental patterning. *Nature cell biology*, 14:488–501 (2012).

- [116] Meinecke M, Boucrot E, Camdere G, Hon WC, Mittal R *et al.* Cooperative recruitment of dynamin and BIN/amphiphysin/Rvs (BAR) domain-containing proteins leads to GTP-dependent membrane scission. *The Journal of biological chemistry*, 288(9):6651–61 (2013).
- [117] Neumann S & Schmid SL. Dual role of BAR domain-containing proteins in regulating vesicle release catalyzed by the GTPase, dynamin-2. *Journal of Biological Chemistry*, 288(35):25119–25128 (2013).
- [118] Lundmark R, Doherty G, Vallis Y, Peter B & McMahon H. Arf family GTP loading is activated by, and generates, positive membrane curvature. *Biochemical Journal*, 414(2):189–194 (2008).
- [119] Renard HF, Simunovic M, Lemièrre J, Boucrot E, Garcia-Castillo MD *et al.* Endophilin-A2 functions in membrane scission in clathrin-independent endocytosis. *Nature* (2014).
- [120] Boucrot E, Ferreira APa, Almeida-Souza L, Debard S, Vallis Y *et al.* Endophilin marks and controls a clathrin-independent endocytic pathway. *Nature* (2014).
- [121] Hong T & Shaw RM. Cardiac T-tubule Microanatomy and Function. *Physiological reviews*, 97:227–252 (2017).
- [122] Razzaq A, Robinson IM, McMahon HT, Skepper JN, Su Y *et al.* Amphiphysin is necessary for organization of the excitation – contraction coupling machinery of muscles, but not for synaptic vesicle endocytosis in *Drosophila*. *Genes & Development*, 15:2967–2979 (2001).
- [123] Nicot As, Toussaint A, Tosch V, Kretz C, Wallgren-Pettersson C *et al.* Mutations in amphiphysin 2 (BIN1) disrupt interaction with dynamin 2 and cause autosomal recessive centronuclear myopathy. *Nature genetics*, 39(9):1134–1139 (2007).
- [124] Saarikangas J, Kourdougli N, Senju Y, Chazal G, Segerstrale M *et al.* MIM-Induced Membrane Bending Promotes Dendritic Spine Initiation. *Developmental Cell*, 33:644–659 (2015).
- [125] Carlson BR, Lloyd KE, Kruszewski A, Kim Ih, Rodriguiz RM *et al.* WRP / srGAP3 Facilitates the Initiation of Spine Development by an Inverse F-BAR Domain, and Its Loss Impairs Long- Term Memory. *Journal of Neuroscience*, 31(7):2447–2460 (2011).

- [126] van Meer G, Voelker DR & Feigenson GW. Membrane lipids: where they are and how they behave. *Nature Reviews Molecular Cell Biology*, 9(2):112–124 (2008).
- [127] Behnia R & Munro S. Organelle identity and the signposts for membrane traffic. *Nature*, 438(7068):597–604 (2005).
- [128] Harlan JE, Hajduk PJ, Yoon HS & Fesik SW. Pleckstrin homology domains bind to phosphatidylinositol-4,5-bisphosphate. *Nature*, 371(6493):168–170 (1994).
- [129] Lemmon MA & Ferguson KM. Signal-dependent membrane targeting by pleckstrin homology (PH) domains. *Biochemical Journal*, 18:1–18 (2000).
- [130] Forman-kay JD & Pawson T. Diversity in protein recognition by PTB domains. *Current Opinion in Structural Biology*, 9:690–695 (1999).
- [131] Yan KS, Kuti M & Zhou MM. PTB or not PTB - that is the question. *FEBS Letters*, 513:67–70 (2002).
- [132] Berger P, Schaffitzel C, Berger I, Ban N & Suter U. Membrane association of myotubularin-related protein 2 is mediated by a pleckstrin homology- GRAM domain and a coiled-coil dimerization module. *Proceedings of the National Academy of Sciences*, 100(21):12177–12182 (2003).
- [133] Pearson MA, Reczek D, Bretscher A & Karplus PA. Structure of the ERM protein moesin reveals the FERM domain fold masked by an extended actin binding tail domain. *Cell*, 101(3):259–270 (2000).
- [134] Mangeat P, Roy C & Martin M. ERM proteins in cell adhesion and membrane dynamics. *Trends in cell biology*, 9(5):187–92 (1999).
- [135] Ellson CD, Gobert-Gosse S, Anderson KE, Davidson K, Erdjument-Bromage H *et al.* PtdIns(3)P regulates the neutrophil oxidase complex by binding to the PX domain of p40(phox). *Nature cell biology*, 3(July):679–682 (2001).
- [136] Cheever ML, Sato TK, de Beer T, Kutateladze TG, Emr SD *et al.* Phox domain interaction with PtdIns(3)P targets the Vam7 t-SNARE to vacuole membranes. *Nature cell biology*, 3(7):613–618 (2001).
- [137] Kanai F, Liu H, Field SJ, Akbary H, Matsuo T *et al.* The PX domains of p47phox and p40phox bind to lipid products of PI(3)K. *Nature cell biology*, 3(7):675–8 (2001).

- [138] Hiroaki H, Ago T, Ito T, Sumimoto H & Kohda D. Solution structure of the PX domain, a target of the SH3 domain. *Nature structural biology*, 8(6):526–530 (2001).
- [139] Gaullier JM, Simonsen A, D’Arrigo A, Bremnes B, Stenmark H *et al.* FYVE fingers bind PtdIns(3)P. *Nature*, 394(6692):432–3 (1998).
- [140] Misra S & Hurley JH. Crystal Structure of a Phosphatidylinositol the FYVE Domain of Vps27p. *Cell*, 97:657–666 (1999).
- [141] Kutateladze TG, Ogburn KD, Watson WT, Beer TD, Emr SD *et al.* Phosphatidylinositol 3-Phosphate Recognition by the FYVE Domain. *Molecular cell*, 3:805–811 (1999).
- [142] Gozani O, Karuman P, Jones DR, Ivanov D, Cha J *et al.* The PHD finger of the chromatin-associated protein ING2 functions as a nuclear phosphoinositide receptor. *Cell*, 114(1):99–111 (2003).
- [143] Kaadige MR & Ayer DE. The Polybasic Region That Follows the Plant Homeodomain Zinc Finger 1 of Pf1 Is Necessary and Sufficient for Specific Phosphoinositide Binding *. *Journal of Biological Chemistry*, 281(39):28831–28836 (2006).
- [144] Dove SK, Piper RC, McEwen RK, Yu JW, King MC *et al.* Svp1p defines a family of phosphatidylinositol 3,5-bisphosphate effectors. *The EMBO Journal*, 23(9):1922–1933 (2004).
- [145] Nourry C, Grant SGN & Borg JP. PDZ Domain Proteins: Plug and Play! *Science Signaling*, 2003(179):re7–re7 (2003).
- [146] Legendre-Guillemin V. ENTH/ANTH proteins and clathrin-mediated membrane budding. *Journal of Cell Science*, 117(1):9–18 (2004).
- [147] Mao Y, Chen J, Maynard JA, Zhang B & Quioco FA. A novel all helix fold of the AP180 amino-terminal domain for phosphoinositide binding and clathrin assembly in synaptic vesicle endocytosis. *Cell*, 104(3):433–440 (2001).
- [148] Ford MG, Pearse BM, Higgins MK, Vallis Y, Owen DJ *et al.* Simultaneous binding of PtdIns(4,5)P₂ and clathrin by AP180 in the nucleation of clathrin lattices on membranes. *Science (New York, N. Y.)*, 291(5506):1051–5 (2001).

- [149] Colón-gonzález F & Kazanietz MG. C1 domains exposed : From diacylglycerol binding to protein – protein interactions. *Biochimica et biophysica acta*, 1761:827–837 (2006).
- [150] Cho W & Stahelin RV. Membrane binding and subcellular targeting of C2 domains. *Biochimica et biophysica acta*, 1761(8):838–49 (2006).
- [151] Gerke V, Creutz CE & Moss SE. Annexins: linking Ca²⁺ signalling to membrane dynamics. *Nature Reviews Molecular Cell Biology*, 6(6):449–461 (2005).
- [152] Huang M, Rigby AC, Morelli X, Grant MA, Huang G *et al.* Structural basis of membrane binding by Gla domains of vitamin K – dependent proteins. *Nature Structural & Molecular Biology*, 10(9):751–756 (2003).
- [153] Macedo-ribeiro S, Bode W, Huber R, Quinn-allen MA, Kim SW *et al.* Crystal structures of the membrane-binding C2 domain of human coagulation factor V. *Nature*, 402(November):434–9 (1999).
- [154] Ferguson KM, Lemmon MA, Schlessinger J & Sigler PB. Structure of the High Affinity Complex of Inositol Trisphosphate with a Phospholipase C Pleckstrin Homology. *Cell*, 83:1037–1046 (1995).
- [155] Isakoff SJ, Cardozo T, Andreev J, Li Z, Ferguson KM *et al.* Identification and analysis of PH domain-containing targets of phosphatidylinositol 3-kinase using a novel in vivo assay in yeast. *EMBO Journal*, 17(18):5374–5387 (1998).
- [156] Fukuda M & Mikoshiba K. Structure-Function Relationships of the Mouse Gap1 m. *Journal of Biological Chemistry*, 271(31):18838–18842 (1996).
- [157] Salim K, Bottomley MJ, Querfurth E, Zvelebil MJ, Gout I *et al.* Distinct specificity in the recognition of phosphoinositides by the pleckstrin homology domains of dynamin and Bruton’s tyrosine kinase. *The EMBO journal*, 15(22):6241–6250 (1996).
- [158] Klarlund JK, Guilherme A, Holik JJ, Virbasius JV, Chawla A *et al.* Signaling by phosphoinositide-3,4,5-trisphosphate through proteins containing pleckstrin and Sec7 homology domains. *Science (New York, N. Y.)*, 275(5308):1927–1930 (1997).
- [159] Lemmon Ma. Membrane recognition by phospholipid-binding domains. *Nature reviews. Molecular cell biology*, 9(2):99–111 (2008).

- [160] Cantley LC. The Phosphoinositide 3-Kinase Pathway. *Science*, 296(May):1655–1657 (2002).
- [161] Stephens L, Mc Gregor A & Hawkins P. Phosphoinositide3-kinases, regulation by cell surface receptors and function of 3-phosphorylated phospholipids. In Cockcroft S (Editor), *Biology of Phosphoinositides*, pp. 32–108. Oxford University Press, Oxford (2000).
- [162] Yu JW, Mendrola JM, Audhya A, Singh S, Keleti D *et al.* Genome-wide analysis of membrane targeting by *S. cerevisiae* pleckstrin homology domains. *Molecular Cell*, 13(5):677–688 (2004).
- [163] Stolt PC, Jeon H, Song HK, Herz J, Eck MJ *et al.* Origins of peptide selectivity and phosphoinositide binding revealed by structures of Disabled-1 PTB domain complexes. *Structure*, 11(5):569–579 (2003).
- [164] Yun M, Keshvara L, Park CG, Zhang YM, Bradley Dickerson J *et al.* Crystal structures of the Dab homology domains of mouse disabled 1 and 2. *Journal of Biological Chemistry*, 278(38):36572–36581 (2003).
- [165] Mishra SK, Keyel PA, Hawryluk MJ, Agostinelli NR, Watkins SC *et al.* Disabled-2 exhibits the properties of a cargo-selective endocytic clathrin adaptor. *The EMBO Journal*, 21(18):4915–4926 (2002).
- [166] Begley MJ, Taylor GS, Kim SA, Veine DM, Dixon JE *et al.* Crystal Structure of a Phosphoinositide Phosphatase, MTMR2: Insights into Myotubular Myopathy and Charcot-Marie-Tooth Syndrome. *Molecular Cell*, 12(6):1391–1402 (2003).
- [167] Hamada K, Shimizu T, Matsui T, Tsukita S, Tsukita S *et al.* Structural basis of the membrane-targeting and unmasking mechanisms of the radixin FERM domain. *EMBO Journal*, 19(17) (2000).
- [168] Cooper LA, Shen Tl & Guan JI. Regulation of Focal Adhesion Kinase by Its Amino-Terminal Domain through an Autoinhibitory Interaction. *Molecular and cellular biology*, 23(22):8030–8041 (2003).
- [169] Jácamo RO & Rozengurt E. A truncated FAK lacking the FERM domain displays high catalytic activity but retains responsiveness to adhesion-mediated signals. *Biochemical and Biophysical Research Communications*, 334(4):1299–1304 (2005).

- [170] Cai X, Lietha D, Ceccarelli DF, Karginov AV, Rajfur Z *et al.* Spatial and Temporal Regulation of Focal Adhesion Kinase Activity in Living Cells. *Molecular and Cellular Biology*, 28(1):201–214 (2008).
- [171] Begley MJ, Taylor GS, Brock MA, Ghosh P, Woods VL *et al.* Molecular basis for substrate recognition by MTMR2, a myotubularin family phosphoinositide phosphatase. *Proceedings of the National Academy of Sciences*, 103(4):927–932 (2006).
- [172] Bravo J, Karathanassis D, Pacold CM, Pacold ME, Ellson CD *et al.* The crystal structure of the PX domain from p40phox bound to phosphatidylinositol 3-phosphate. *Molecular Cell*, 8(4):829–839 (2001).
- [173] Dumas JJ, Merithew E, Sudharshan E, Rajamani D, Hayes S *et al.* Multivalent endosome targeting by homodimeric EEA1. *Molecular Cell*, 8(5):947–958 (2001).
- [174] Pena PV, Davrazou F, Shi X, Walter KL, Verkhusha VV *et al.* Molecular mechanism of histone H3K4me3 recognition by plant homeodomain of ING2. *Nature*, 442(7098):100–103 (2006).
- [175] Krick R, Busse RA, Scacioc A, Stephan M, Janshoff A *et al.* Structural and functional characterization of the two phosphoinositide binding sites of PROPPINs, a β -propeller protein family. *Proceedings of the National Academy of Sciences of the United States of America*, 109(30):E2042–9 (2012).
- [176] Pan L, Wu H, Shen C, Shi Y, Jin W *et al.* Clustering and synaptic targeting of PICK1 requires direct interaction between the PDZ domain and lipid membranes. *The EMBO journal*, 26(21):4576–4587 (2007).
- [177] Zhang G, Kazanietz MG, Blumberg PM & Hurley JH. Crystal Structure of the Cys2 Activator-Binding Domain of Protein Kinase Cd in Complex with Phorbol Ester. *Cell*, 81:917–924 (1995).
- [178] Verdaguer N, Corbalan-Garcia S, Ochoa WF, Fita I & Gomez-Fernandez JC. Calcium Bridges the C2 Membrane-Binding Domain of Protein Kinase C-alpha Directly to Phosphatidylserine. *Embo J.*, 18(22):6329–6338 (1999).
- [179] Swairjo Ma, Concha NO, Kaetzel Ma, Dedman JR & Seaton Ba. Ca(2+)-bridging mechanism and phospholipid head group recognition in the membrane-binding protein annexin V. *Nature structural biology*, 2(11):968–974 (1995).

- [180] Ponting CP. Novel domains in NADPH oxidase subunits, sorting nexins, and PtdIns 3-kinases: binding partners of SH3 domains? *Protein science*, 5(11):2353–7 (1996).
- [181] Yu JW & Lemmon MA. All Phox Homology (PX) Domains from *Saccharomyces cerevisiae* Specifically Recognize Phosphatidylinositol 3-Phosphate. *Journal of Biological Chemistry*, 276(47):44179–44184 (2001).
- [182] Karathanassis D, Stahelin RV, Bravo J, Perisic O, Pacold CM *et al.* Binding of the PX domain of p47 phox to and phosphatidic acid is masked by an intramolecular interaction. *EMBO Journal*, 21(19):5057–5068 (2002).
- [183] Xing Y, Liu D, Zhang R, Joachimiak A, Songyang Z *et al.* Structural basis of membrane targeting by the phox homology domain of cytokine-independent survival kinase (CISK-PX). *Journal of Biological Chemistry*, 279(29):30662–30669 (2004).
- [184] Song X, Xu W, Zhang A, Huang G, Liang X *et al.* Phox Homology Domains Specifically Bind Phosphatidylinositol Phosphates. *Biochemistry*, 40:8940–8944 (2001).
- [185] Kutateladze TG. Phosphatidylinositol 3-phosphate recognition and membrane docking by the FYVE domain (2006).
- [186] Lawe DC, Patki V, Heller-harrison R, Lambright D & Corvera S. The FYVE Domain of Early Endosome Antigen 1 Is Required for Both Phosphatidylinositol 3-Phosphate and Rab5 Binding. *Journal of Biological Chemistry*, 275(5):3699–3705 (2000).
- [187] Baskaran S, Ragusa MJ, Boura E & Hurley JH. Two-Site Recognition of Phosphatidylinositol 3-Phosphate by PROPPINs in Autophagy. *Molecular Cell*, 47(3):339–348 (2012).
- [188] Watanabe Y, Kobayashi T, Yamamoto H, Hoshida H & Akada R. Structure-based Analyses Reveal Distinct Binding Sites for Atg2 and Phosphoinositides in Atg18. *Journal of Biological Chemistry*, 287(38):31681–31690 (2012).
- [189] Strømhaug PE, Reggiori F, Guan J, Wang Cw & Klionsky DJ. Atg21 Is a Phosphoinositide Binding Protein Required for Efficient Lipidation and Localization of Atg8 during Uptake of Aminopeptidase I by Selective Autophagy. *Molecular biology of the cell*, 15:3553–3566 (2004).

- [190] Busse RA, Scacioc A, Krick R, Pérez-Lara A, Thumm M *et al.* Characterization of PROPPIN-Phosphoinositide Binding and Role of Loop 6CD in PROPPIN-Membrane Binding. *Biophysical journal*, 108(May):2223–2234 (2015).
- [191] Tamura N, Oku M, Ito M, Noda NN, Inagaki F *et al.* Atg18 phosphoregulation controls organellar dynamics by modulating its phosphoinositide-binding activity. *Journal of Cell Biology*, 202(4):685–698 (2013).
- [192] Cowburn D. Peptide recognition by PTB and PDZ domains (1997).
- [193] Wu H, Feng W, Chen J, Chan LN, Huang S *et al.* PDZ Domains of Par-3 as Potential Phosphoinositide Signaling Integrators. *Molecular Cell*, 28(5):886–898 (2007).
- [194] Collins BM, Mccoy AJ, Kent HM, Evans PR & Owen DJ. Molecular Architecture and Functional Model of the Endocytic AP2 Complex. *Cell*, 109:523–535 (2002).
- [195] Mills IG, Praefcke GJK, Vallis Y, Peter BJ, Olesen LE *et al.* EpsinR: An AP1/clathrin interacting protein involved in vesicle trafficking. *Journal of Cell Biology*, 160(2):213–222 (2003).
- [196] Hirst J, Motley A, Harasaki K, Chew SYP & Robinson MS. EpsinR : an ENTH Domain-containing Protein that Interacts with AP-1. *Molecular biology of the cell*, 14:625–641 (2003).
- [197] Xu RX, Pawelczyk T, Xia Th & Brown SC. NMR Structure of a Protein Kinase C γ Phorbol-Binding Domain and Study of Protein - Lipid Micelle Interactions. *Biochemistry*, 2960(97):10709–10717 (1997).
- [198] Medkova M. Interplay of C1 and C2 Domains of Protein Kinase C-alpha in Its Membrane Binding and Activation. *Journal of Biological Chemistry*, 274(28):19852–19861 (1999).
- [199] Bittova L, Stahelin RV & Cho W. Roles of Ionic Residues of the C1 Domain in Protein Kinase C-a Activation and the Origin of Phosphatidylserine Specificity. *Journal of Biological Chemistry*, 276(6):4218–4226 (2001).
- [200] Corbalan-Garcia S & Gómez-Fernández JC. Signaling through C2 domains: More than one lipid target. *Biochimica et Biophysica Acta - Biomembranes*, 1838(6):1536–1547 (2014).

- [201] Shao X, Li C, Fernandez I, Zhang X, Südhof TC *et al.* Synaptotagmin–Syntaxin Interaction: The C2 Domain as a Ca²⁺-Dependent Electrostatic Switch. *Neuron*, 18(1):133–142 (1997).
- [202] Murray D & Honig B. Electrostatic control of the membrane targeting of C2 domains. *Molecular Cell*, 9(1):145–154 (2002).
- [203] Perisic O, Fong S, Lynch DE, Bycroft M & Williams RL. Crystal structure of a calcium-phospholipid binding domain from cytosolic phospholipase A2. *The Journal of biological chemistry*, 273(3):1596–1604 (1998).
- [204] Nalefski EA, McDonagh T, Somers W, Seehra J, Joseph JJ *et al.* Independent Folding and Ligand Specificity of the C2 Calcium-dependent Lipid Binding Domain of Cytosolic Phospholipase A2. *Journal of Biological Chemistry*, 273(3):1365–1372 (1998).
- [205] Johnson JE, Giorgione J & Newton AC. The C1 and C2 Domains of Protein Kinase C Are Independent Membrane Targeting Modules, with Specificity for Phosphatidylserine Conferred by the C1 Domain †. *Biochemistry*, 39(37):11360–11369 (2000).
- [206] Nalefski EA & Newton AC. Membrane Binding Kinetics of Protein Kinase C β Mediated by the C2 Domain. *Biochemistry*, 40(44):13216–13229 (2001).
- [207] Giorgione JR, Lin JH, McCammon JA & Newton AC. Increased membrane affinity of the C1 domain of protein kinase C δ compensates for the lack of involvement of its C2 domain in membrane recruitment. *The Journal of biological chemistry*, 281(3):1660–9 (2006).
- [208] Lizarbe MA, Barrasa JI, Olmo N, Gavilanes F & Turnay J. Annexin-phospholipid interactions. Functional implications. *International Journal of Molecular Sciences*, 14:2652–2683 (2013).
- [209] Zwaal RF, Comfurius P & Bevers EM. Lipid–protein interactions in blood coagulation. *Biochimica et Biophysica Acta (BBA) - Reviews on Biomembranes*, 1376(3):433–453 (1998).
- [210] Hurley JH. Membrane binding domains. *Biochimica et biophysica acta*, 1761(8):805–11 (2006).

- [211] Stahelin RV. Lipid binding domains : more than simple lipid effectors. *Journal of lipid research*, 50:S299–S304 (2009).
- [212] Fan W, Nassiri A & Zhong Q. Autophagosome targeting and membrane curvature sensing by Barkor/Atg14(L). *Proceedings of the National Academy of Sciences of the United States of America*, 108(19):7769–74 (2011).
- [213] Cocucci E, Aguet F, Boulant S & Kirchhausen T. The first five seconds in the life of a clathrin-coated pit. *Cell*, 150(3):495–507 (2012).
- [214] Stimpson HE, Toret CP, Cheng AT, Pauly BS & Drubin DG. Early-Arriving Syp1p and Ede1p Function in Endocytic Site Placement and Formation in Budding Yeast. *Molecular biology of the cell*, 20:4640–51 (2009).
- [215] Taylor MJ, Perrais D & Merrifield CJ. A high precision survey of the molecular dynamics of mammalian clathrin-mediated endocytosis. *PLoS Biology*, 9(3) (2011).
- [216] Ferguson SM, Brasnjo G, Hayashi M, Wolfel M, Collesi C *et al.* A Selective Activity-Dependent Requirement for Dynamin 1 in Synaptic Vesicle Endocytosis. *Science*, 316(5824):570–574 (2007).
- [217] Schlossman DM, Schmid SL, Braell WA & Rothman JE. An enzyme that removes clathrin coats: Purification of an uncoating ATPase. *Journal of Cell Biology*, 99(2):723–733 (1984).
- [218] Cremona O, Di Paolo G, Wenk MR, Lüthi A, Kim WT *et al.* Essential role of phosphoinositide metabolism in synaptic vesicle recycling. *Cell*, 99(2):179–188 (1999).
- [219] Hayashi, Raimondi, O’Toole, Paradise, Collesi *et al.* Cell- and stimulus-dependent heterogeneity of synaptic vesicle endocytic recycling mechanisms revealed by studies of dynamin 1-null neurons. *Proceedings of the National Academy of Sciences of the United States of America*, 105(6):2175–2180 (2008).
- [220] Perry MM & Gilbert AB. Yolk transport in the ovarian follicle of the hen (*Gallus domesticus*): lipoprotein-like particles at the periphery of the oocyte in the rapid growth phase. *Journal of cell science*, 39:257–72 (1979).
- [221] Gnad F, Ren S, Cox J, Olsen JV, Macek B *et al.* PHOSIDA (phosphorylation site database): management, structural and evolutionary investigation, and prediction of phosphosites. *Genome Biology*, 8(11):R250 (2007).

- [222] Zhai B, Villén J, Beausoleil SA, Mintseris J & Gygi SP. Phosphoproteome analysis of *Drosophila melanogaster* embryos - SUPP. *Journal of proteome research*, 7(4):1675–1682 (2008).
- [223] Kjaerulff O, Brodin L & Jung A. The Structure and Function of Endophilin Proteins. *Cell Biochemistry and Biophysics*, 60(3):137–154 (2011).
- [224] Li F, Tiwari N, Rothman JE & Pincet F. Kinetic barriers to SNAREpin assembly in the regulation of membrane docking/priming and fusion. *Proceedings of the National Academy of Sciences*, p. 201604000 (2016).
- [225] Wang L, Johnson A, Hanna M & Audhya A. Eps15 membrane binding and bending activity acts redundantly with Fcho1 during clathrin-mediated endocytosis. *Molecular Biology of the Cell*, 1 (2016).
- [226] Modregger J, Schmidt AA, Ritter B, Huttner WB & Plomann M. Characterization of endophilin B1b, a brain-specific membrane-associated lysophosphatidic acid acyl transferase with properties distinct from endophilin A1. *Journal of Biological Chemistry*, 278(6):4160–4167 (2003).
- [227] Pierrat B, Simonen M, Cueto M, Mestan J, Ferrigno P *et al.* SH3GLB, a New Endophilin-Related Protein Family Featuring an SH3 Domain. *Genomics*, 71(2):222–234 (2001).
- [228] Ringstad N, Nemoto Y & De Camilli P. The SH3p4/Sh3p8/SH3p13 protein family: Binding partners for synaptojanin and dynamin via a Grb2-like Src homology 3 domain. *Cell Biology*, 94(August):8569–8574 (1997).
- [229] Trempe JF, Chen CXQ, Grenier K, Camacho EM, Kozlov G *et al.* SH3 Domains from a Subset of BAR Proteins Define a Ubl-Binding Domain and Implicate Parkin in Synaptic Ubiquitination. *Molecular Cell*, 36(6):1034–1047 (2009).
- [230] Heuser JE & Reese TS. Evidence for recycling of synaptic vesicle membrane during transmitter release at the frog neuromuscular junction. *Journal of Cell Biology*, 57(2):315–344 (1973).
- [231] Guichet A, Wucherpfennig T, Dudu V, Etter S, Wilsch-Br??uniger M *et al.* Essential role of endophilin A in synaptic vesicle budding at the *Drosophila* neuromuscular junction. *EMBO Journal*, 21(7):1661–1672 (2002).

- [232] Verstreken P, Kjaerulff O, Lloyd TE, Atkinson R, Zhou Y *et al.* Endophilin mutations block clathrin-mediated endocytosis but not neurotransmitter release. *Cell*, 109(1):101–112 (2002).
- [233] De Gois S, Jeanclos E, Morris M, Grewal S, Varoqui H *et al.* Identification of endophilins 1 and 3 as selective binding partners for VGLUT1 and their co-localization in neocortical glutamatergic synapses: Implications for vesicular glutamate transporter trafficking and excitatory vesicle formation. *Cellular and Molecular Neurobiology*, 26(4-6):679–693 (2006).
- [234] Schuske KR, Richmond JE, Matthies DS, Davis WS, Runz S *et al.* Endophilin is required for synaptic vesicle endocytosis by localizing synaptojanin. *Neuron*, 40(4):749–762 (2003).
- [235] Vinatier J, Herzog E, Plamont MA, Wojcik SM, Schmidt A *et al.* Interaction between the vesicular glutamate transporter type 1 and endophilin A1, a protein essential for endocytosis. *Journal of Neurochemistry*, 97(4):1111–1125 (2006).
- [236] Andersson F, Löw P & Brodin L. Selective perturbation of the BAR domain of endophilin impairs synaptic vesicle endocytosis. *Synapse*, 64(7):556–560 (2010).
- [237] Dickman DK, Horne JA, Meinertzhagen IA & Schwarz TL. A slowed classical pathway rather than kiss-and-run mediates endocytosis at synapses lacking synaptojanin and endophilin. *Cell*, 123(3):521–533 (2005).
- [238] Verstreken P, Koh TW, Schulze KL, Zhai RG, Hiesinger PR *et al.* Synaptojanin is recruited by endophilin to promote synaptic vesicle uncoating. *Neuron*, 40(4):733–748 (2003).
- [239] Sundborger A, Soderblom C, Vorontsova O, Evergren E, Hinshaw JE *et al.* An endophilin – dynamin complex promotes budding of clathrin-coated vesicles during synaptic vesicle recycling. *Journal of Cell Science*, 124(1) (2011).
- [240] Ringstad N, Gad H, Lo P, Paolo GD, Brodin L *et al.* Endophilin / SH3p4 Is Required for the Transition from Early to Late Stages in Clathrin-Mediated Synaptic Vesicle Endocytosis. *Transition*, 24:143–154 (1999).
- [241] Gad H, Ringstad N, Löw P, Kjaerulff O, Gustafsson J *et al.* Fission and Uncoating of Synaptic Clathrin-Coated Vesicles Are Perturbed by Disruption of Interactions with the SH3 Domain of Endophilin. *Neuron*, 27(2):301–312 (2000).

- [242] Perera RM, Zoncu R, Lucast L, De Camilli P & Toomre D. Two synaptojanin 1 isoforms are recruited to clathrin-coated pits at different stages. *Proceedings of the National Academy of Sciences*, 103(51):19332–19337 (2006).
- [243] Milosevic I, Giovedi S, Lou X, Raimondi A, Collesi C *et al.* Recruitment of endophilin to clathrin-coated pit necks is required for efficient vesicle uncoating after fission. *Neuron*, 72(4):587–601 (2011).
- [244] Beutner D, Voets T, Neher E & Moser T. Calcium dependence of exocytosis and endocytosis at the cochlear inner hair cell afferent synapse. *Neuron*, 29(3):681–690 (2001).
- [245] Sun JY, Wu XS & Wu LG. Single and multiple vesicle fusion induce different rates of endocytosis at a central synapse. *Nature*, 417:555–9 (2002).
- [246] Klingauf J, Kavalali ET & Tsien RW. Kinetics and regulation of fast endocytosis at hippocampal synapses. *Nature*, 394(August):581–585 (1998).
- [247] Pyle JL, Kavalali ET, Piedras-Rentería ES & Tsien RW. Rapid reuse of readily releasable pool vesicles at hippocampal synapses. *Neuron*, 28(1):221–31 (2000).
- [248] Jockusch WJ, Praefcke GJ, McMahon HT & Lagnado L. Clathrin-dependent and clathrin-independent retrieval of synaptic vesicles in retinal bipolar cells. *Neuron*, 46(6):869–878 (2005).
- [249] Neves G & Lagnado L. The kinetics of exocytosis and endocytosis in the synaptic terminal of goldfish retinal bipolar cells. *Journal of Physiology*, 515:181–202 (1999).
- [250] Llobet A, Gallop JL, Burden JJE, Camdere G, Chandra P *et al.* Endophilin Drives the Fast Mode of Vesicle Retrieval in a Ribbon Synapse. *Journal of Neuroscience*, 31(23):8512–8519 (2011).
- [251] Kononenko NL, Puchkov D, Classen Ga, Walter AM, Pechstein A *et al.* Clathrin/AP-2 mediate synaptic vesicle reformation from endosome-like vacuoles but are not essential for membrane retrieval at central synapses. *Neuron*, 82(5):981–988 (2014).
- [252] Levkowitz G, Waterman H, Etenberg SA, Katz M, Tsygankov AY *et al.* Ubiquitin Ligase Activity and Tyrosine Phosphorylation Underlie Suppression of Growth Factor Signaling by c-Cbl/Sli-1. *Molecular Cell*, 4(6):1029–1040 (1999).

- [253] Take H, Watanabe S, Takeda K, Yu ZX, Iwata N *et al.* Cloning and Characterization of a Novel Adaptor Protein, CIN85, That Interacts with c-Cbl. *Biochemical and Biophysical Research Communications*, 268(2):321–328 (2000).
- [254] Soubeyran P, Kowanetz K, Szymkiewicz I, Langdon WY & Dikic I. Cbl–CIN85–endophilin complex mediates ligand-induced downregulation of EGF receptors. *Nature*, 416(6877):183–187 (2002).
- [255] Ahmad G, Mohapatra BC, Schulte NA, Nadeau SA, Luan H *et al.* Cbl-family ubiquitin ligases and their recruitment of CIN85 are largely dispensable for epidermal growth factor receptor endocytosis. *The international journal of biochemistry & cell biology*, 57:123–34 (2014).
- [256] Petrelli A, Gilestro GF, Lanzardo S, Comoglio PM, Migone N *et al.* The endophilin–CIN85–Cbl complex mediates ligand-dependent downregulation of c-Met. *Nature*, 416(6877):187–190 (2002).
- [257] Mercier V, Laporte MH, Destaing O, Blot B, Blouin CM *et al.* ALG-2 interacting protein-X (Alix) is essential for clathrin-independent endocytosis and signaling. *Science Reports*, 6(February):8–11 (2016).
- [258] Moore CA, Milano SK & Benovic JL. Regulation of Receptor Trafficking by GRKs and Arrestins. *Annual Review of Physiology*, 69(1):451–482 (2007).
- [259] Tang Y, Hu La, Miller WE, Ringstad N, Hall Ra *et al.* Identification of the endophilins (SH3p4/p8/p13) as novel binding partners for the beta1-adrenergic receptor. *Proceedings of the National Academy of Sciences of the United States of America*, 96(22):12559–12564 (1999).
- [260] Simunovic M, Manneville JB, Renard HF, Evergren E, Raghunathan K *et al.* Friction Mediates Scission of Tubular Membranes Scaffolded by BAR Proteins. *Cell*, 170:172–184 (2017).
- [261] Römer W, Berland L, Chambon V, Gaus K, Windschiegl B *et al.* Shiga toxin induces tubular membrane invaginations for its uptake into cells. *Nature*, 450(7170):670–675 (2007).
- [262] Nozumi M, Nakatsu F, Katoh K & Igarashi M. Coordinated Movement of Vesicles and Actin Bundles during Nerve Growth Revealed by Superresolution Microscopy. *Cell Reports*, 18(9):2203–2216 (2017).

- [263] Serfass JM, Takahashi Y, Zhou Z, Imamura Kawasawa Y, Liu Y *et al.* Endophilin B2 facilitates endosome maturation in response to growth factor stimulation, autophagy induction, and influenza A virus infection. *Journal of Biological Chemistry*, 292:jbc.M117.792747 (2017).
- [264] Cuddeback SM, Yamaguchi H, Komatsu K, Miyashita T, Yamada M *et al.* Molecular cloning and characterization of Bif-1. A novel Src homology 3 domain-containing protein that associates with Bax. *Journal of Biological Chemistry*, 276(23):20559–20565 (2001).
- [265] Takahashi Y, Karbowski M, Yamaguchi H, Kazi A, Wu J *et al.* Loss of Bif-1 Suppresses Bax / Bak Conformational Change and Mitochondrial Apoptosis. *Molecular and Cellular Biology*, 25(21):9369–9382 (2005).
- [266] Kumarswamy R & Chandna S. Putative partners in Bax mediated cytochrome-c release: ANT, CypD, VDAC or none of them? *Mitochondrion*, 9(1):1–8 (2009).
- [267] Karbowski M, Jeong SY & Youle RJ. Endophilin B1 is required for the maintenance of mitochondrial morphology. *Journal of Cell Biology*, 166(7):1027–1039 (2004).
- [268] Takahashi Y, Coppola D, Matsushita N, Cualing HD, Sun M *et al.* Bif-1 interacts with Beclin 1 through UVRAG and regulates autophagy and tumorigenesis. *Nature Cell Biology*, 9(10):1142–1151 (2007).
- [269] Matta S, Van Kolen K, da Cunha R, van den Bogaart G, Mandemakers W *et al.* LRRK2 Controls an EndoA Phosphorylation Cycle in Synaptic Endocytosis. *Neuron*, 75(6):1008–1021 (2012).
- [270] Soukup Sf & Verstreken P. EndoA / Endophilin-A creates docking stations for autophagic proteins at synapses. *Autophagy*, 13(5):1–2 (2017).
- [271] Soukup SF, Kuenen S, Vanhauwaert R, Manetsberger J, Hernandez-Diaz S *et al.* A LRRK2-Dependent EndophilinA Phosphoswitch Is Critical for Macroautophagy at Presynaptic Terminals. *Neuron*, 92(4):829–844 (2016).
- [272] Ichimura Y, Kirisako T, Takao T, Satomi Y, Shimonishi Y *et al.* A ubiquitin-like system mediates protein lipidation. *Nature*, 408(6811):488–492 (2000).
- [273] Murdoch JD, Rostosky CM, Gowrisankaran S, Arora AS, Soukup SF *et al.* Endophilin-A Deficiency Induces the Foxo3a-Fbxo32 Network in the Brain and

- Causes Dysregulation of Autophagy and the Ubiquitin-Proteasome System. *Cell Reports*, 17(4):1071–1086 (2016).
- [274] Sorre B, Callan-Jones A, Manzi J, Goud B, Prost J *et al.* Nature of curvature coupling of amphiphysin with membranes depends on its bound density. *Proceedings of the National Academy of Sciences of the United States of America*, 109(1):173–8 (2012).
- [275] Parthasarathy R, Yu Ch & Groves JT. Curvature-Modulated Phase Separation in Lipid Bilayer Membranes. *Langmuir*, 22(11):5095–5099 (2006).
- [276] MacDonald RC, MacDonald RI, Menco BP, Takeshita K, Subbarao NK *et al.* Small-volume extrusion apparatus for preparation of large, unilamellar vesicles. *Biochimica et biophysica acta*, 1061(2):297–303 (1991).
- [277] Morton La, Yang H, Saludes JP, Fiorini Z, Beninson L *et al.* MARCKS-ED peptide as a curvature and lipid sensor. *ACS chemical biology*, 8(1):218–25 (2013).
- [278] Zhao W, Hanson L, Lou HY, Akamatsu M, Chowdary PD *et al.* Nanoscale manipulation of membrane curvature for probing endocytosis in live cells. *Nature Nanotechnology*, Advance On:1–9 (2017).
- [279] Keire DA, Mannon P, Kobayashi M, Walsh JH, Solomon TE *et al.* Primary structures of PYY, [Pro(34)]PYY, and PYY-(3-36) confer different conformations and receptor selectivity. *American journal of physiology. Gastrointestinal and liver physiology*, 279(1):G126–31 (2000).
- [280] Kunding AH, Mortensen MW, Christensen SM & Stamou D. A fluorescence-based technique to construct size distributions from single-object measurements: application to the extrusion of lipid vesicles. *Biophysical journal*, 95(3):1176–88 (2008).
- [281] Sorre B, Callan-Jones A, Manneville JB, Nassoy P, Joanny JF *et al.* Curvature-driven lipid sorting needs proximity to a demixing point and is aided by proteins. *Proceedings of the National Academy of Sciences of the United States of America*, 106(14):5622–6 (2009).
- [282] Tian A, Capraro BR, Esposito C & Baumgart T. Bending stiffness depends on curvature of ternary lipid mixture tubular membranes. *Biophysical Journal*, 97(6):1636–1646 (2009).

- [283] Reddy AS, Warshaviak DT & Chachisvilis M. Effect of membrane tension on the physical properties of DOPC lipid bilayer membrane. *Biochimica et Biophysica Acta - Biomembranes*, 1818(9):2271–2281 (2012).
- [284] NanoSight L. *NanoSight NTA 2.1 Analytical Software*. NanoSight Ltd., Amesbury, v1.0 edition (2010).
- [285] Saveyn H, De Baets B, Thas O, Hole P, Smith J *et al.* Accurate particle size distribution determination by nanoparticle tracking analysis based on 2-D Brownian dynamics simulation. *Journal of Colloid and Interface Science*, 352(2):593–600 (2010).
- [286] Carr B & Wright M. *Nanoparticle Tracking Analysis - A Review of Applications and Usage 2010-2012*. NanoSight Ltd. (2012).
- [287] Sakamuro D, Elliott KJ, Wechsler-Reya R & Prendergast GC. BIN1 is a novel MYC-interacting protein with features of a tumour suppressor. *Nature genetics*, 14(1):69–77 (1996).
- [288] Weissenhorn W. Crystal structure of the endophilin-A1 BAR domain. *Journal of Molecular Biology*, 351(3):653–661 (2005).
- [289] Mim C, Cui H, Gawronski-Salerno JA, Frost A, Lyman E *et al.* Structural basis of membrane bending by the N-BAR protein endophilin. *Cell*, 149(1):137–145 (2012).
- [290] Simunovic M, Evergren E, Golushko I, Prévost C, Renard HF *et al.* How curvature-generating proteins build scaffolds on membrane nanotubes. *Proceedings of the National Academy of Sciences*, p. 201606943 (2016).
- [291] Pédelacq JD, Cabantous S, Tran T, Terwilliger TC & Waldo GS. Engineering and characterization of a superfolder green fluorescent protein. *Nature biotechnology*, 24(1):79–88 (2006).
- [292] Busse RA, Scacioc A, Schalk AM, Krick R, Thumm M *et al.* Analyzing Protein–Phosphoinositide Interactions with Liposome Flotation Assays. *Methods in Molecular Biology*, 1376(1):155–162 (2016).
- [293] Chang-Ileto B, Frere SG, Chan RB, Voronov SV, Roux A *et al.* Synaptojanin 1-Mediated PI(4,5)P₂ Hydrolysis Is Modulated by Membrane Curvature and Facilitates Membrane Fission. *Developmental Cell*, 20(2):206–218 (2011).

- [294] Yamagishi A, Masuda M, Ohki T, Onishi H & Mochizuki N. A Novel Actin Bundling/Filopodium-forming Domain Conserved in Insulin Receptor Tyrosine Kinase Substrate p53 and Missing in Metastasis Protein. *Journal of Biological Chemistry*, 279(15):14929–14936 (2004).
- [295] Gallop JL, Butler PJG & McMahon HT. Endophilin and CtBP/BARS are not acyl transferases in endocytosis or Golgi fission. *Nature*, 438(7068):675–8 (2005).
- [296] Xue J, Kalafatis M & Mann KG. Determination of the Disulfide Bridges in Factor Va Light Chain1-. *Biochemistry*, 32:5917–23 (1993).
- [297] Price PA, Urist MR & Otawara Y. Matrix Gla protein, a new ??-carboxyglutamic acid-containing protein which is associated with the organic matrix of bone. *Biochemical and Biophysical Research Communications*, 117(3):765–771 (1983).
- [298] Bondos SE & Bicknell A. Detection and prevention of protein aggregation before, during, and after purification. *Analytical Biochemistry*, 316(2):223–231 (2003).
- [299] Ingolia T & Koshland D. The role of calcium in fusion of artificial vesicles. *Journal of Biological Chemistry*, 253:3821—29 (1978).
- [300] Sharkey NA, Leach KL & Blumberg PM. Competitive inhibition by diacylglycerol of specific phorbol ester binding. *Proceedings of the National Academy of Sciences of the United States of America*, 81(2):607–10 (1984).
- [301] Clark JD, Milona N & Knopf JL. Purification of a 110-kilodalton cytosolic phospholipase A2 from the human monocytic cell line U937. *Proceedings of the National Academy of Sciences of the United States of America*, 87(19):7708–12 (1990).
- [302] Perin MS, Fried VA, Mignery GA, Jahn R & Sudhof TC. Phospholipid binding by a synaptic vesicle protein homologous to the regulatory region of protein kinase C. *Nature (London)*, 345:260–263 (1990).
- [303] Downward J. A target for PI(3) kinase. *Nature*, 376:553–4 (1995).
- [304] Franke TF, Kaplan DR, Cantley LC & Toker A. Direct Regulation of the Akt Proto-Oncogene Product by Phosphatidylinositol-3,4-bisphosphate. *Science*, 275:665–668 (1997).

- [305] Lietzke SE, Bose S, Cronin T, Klarlund J, Chawla A *et al.* Structural Basis of 3-Phosphoinositide Recognition by Pleckstrin Homology Domains. *Molecular Cell*, 6(2):385–394 (2000).
- [306] Takeuchi H, Matsuda M, Yamamoto T, Kanematsu T, Kikkawa U *et al.* PTB domain of insulin receptor substrate-1 binds inositol compounds. *The Biochemical journal*, 334 (Pt 1:211–8 (1998).
- [307] Ramamurthi KS. Protein localization by recognition of membrane curvature. *Current opinion in microbiology*, 13(6):753–7 (2010).
- [308] Strahl H, Ronneau S, González BS, Klutsch D, Schaffner-Barbero C *et al.* Transmembrane protein sorting driven by membrane curvature. *Nature Communications*, 6:8728 (2015).
- [309] Zanetti-domingues LC, Tynan CJ, Rolfe DJ, Clarke DT & Martin M. Hydrophobic Fluorescent Probes Introduce Artifacts into Single Molecule Tracking Experiments Due to Non- Specific Binding. *Plos One*, 8(9) (2013).
- [310] Hughes LD, Rawle RJ, Boxer SG, Alexa C, Alexa C *et al.* Choose Your Label Wisely : Water-Soluble Fluorophores Often Interact with Lipid Bilayers. *Plos One*, 9(2) (2014).
- [311] Vonkova I, Saliba AE, Deghou S, Anand K, Ceschia S *et al.* Lipid Cooperativity as a General Membrane- Recruitment Principle for PH Domains. *CellReports*, 12(9):1519–1530 (2015).
- [312] Gillooly DJ, Morrow IC, Lindsay M, Gould R, Bryant NJ *et al.* Localization of phosphatidylinositol 3-phosphate in yeast and mammalian cells. *The EMBO Journal*, 19(17):4577–4588 (2000).
- [313] Datta K, Franke TF, Chan TO, Makris A, Yang Si *et al.* AH / PH Domain-Mediated Interaction between Akt Molecules and Its Potential Role in Akt Regulation. *Molecular and cellular biology*, 15(4):2304–2310 (1995).
- [314] Milburn CC, Deak M, Kelly SM, Price NC, Alessi DR *et al.* Binding of phosphatidylinositol 3 , 4 , 5-trisphosphate to the pleckstrin homology domain of protein kinase B induces a conformational change. *Biochemical Journal*, 375:531–538 (2003).

- [315] Di Paolo G & De Camilli P. Phosphoinositides in cell regulation and membrane dynamics. *Nature*, 443(7112):651–657 (2006).
- [316] Schenck A, Goto-Silva L, Collinet C, Rhinn M, Giner A *et al.* The Endosomal Protein Appl1 Mediates Akt Substrate Specificity and Cell Survival in Vertebrate Development. *Cell*, 133:486–497 (2008).
- [317] Gruenberg J. The endocytic pathway: a mosaic of domains. *Nature Reviews Molecular Cell Biology*, 2(10):721–730 (2001).
- [318] Martinović V. Protein Complex Formation and Membrane Remodelling in Clathrin-Mediated Endocytosis. Ph.D. thesis, University of Cambridge (2015).
- [319] Doherty GJ & McMahon HT. Mechanisms of endocytosis. *Annual review of biochemistry*, 78:857–902 (2009).
- [320] Elkin SR, Lakoduk AM & Schmid SL. Endocytic Pathways and Endosomal Trafficking: A Primer. *Wien Med Wochenschr*, 166:196–204 (2016).
- [321] Musacchio A. How SH3 domains recognize proline. *Advances in Protein Chemistry*, 61:211–268 (2002).
- [322] Saksela K & Permi P. SH3 domain ligand binding: What’s the consensus and where’s the specificity? *FEBS Letters*, 586(17):2609–2614 (2012).
- [323] Feng S, Chen JK, Yu H, Simon JA & Schreiber SL. Two binding orientations for peptides to the Src SH3 domain: development of a general model for SH3-ligand interactions. *Science*, 266(5188):1241–1247 (1994).
- [324] Yu H, Chen JK, Feng S, Dalgarno DC, Brauer AW *et al.* Structural basis for the binding of proline-rich peptides to SH3 domains. *Cell*, 76(5):933–945 (1994).
- [325] Musacchio A, Wilmanns M & Saraste M. Structure and Function of the SH3 Domain. *Progress in Biophysics and Molecular Biology*, 61:283–297 (1994).
- [326] Ren R, Mayer BJ, Cicchetti P & Baltimore D. Identification of a ten-amino acid proline-rich SH3 binding site. *Science*, 259(February):1157–1161 (1993).
- [327] Lim WA, Richards FM & Rox RO. Structural determinants of peptide-binding orientation and of sequence specificity in SH3 domains. *Nature*, 372:375–9 (1994).

- [328] Wu X, Knudsen B, Feller SM, Zheng J, Sali A *et al.* Structural basis for the specific interaction of lysine-containing proline-rich peptides with the N-terminal SH3 domain of c-Crk. *Structure*, 3(2):215–226 (1995).
- [329] Weng Z, Rickles RJ, Feng S, Richard S, Shaw AS *et al.* Structure-function analysis of SH3 domains: SH3 binding specificity altered by single amino acid substitutions. *Molecular and cellular biology*, 15(10):5627–34 (1995).
- [330] Feng S, Kasahara C, Rickles RJ, Schreiber SL, Feng, S, Kasahara, C, Rickles RJ SS *et al.* Specific interactions outside the proline-rich core of two classes of Src homology 3 ligands. *Proceedings of the National Academy of Sciences of the United States of America*, 92(26):12408–15 (1995).
- [331] Zhao ZS, Manser E & Lim L. Interaction between PAK and nck: a template for Nck targets and role of PAK autophosphorylation. *Molecular and cellular biology*, 20(11):3906–17 (2000).
- [332] Lewitzky M, Kardinal C, Gehring NH, Schmidt EK, Konkol B *et al.* The C-terminal SH3 domain of the adapter protein Grb2 binds with high affinity to sequences in Gab1 and SLP-76 which lack the SH3-typical P-x-x-P core motif. *Oncogene*, 20(9):1052–1062 (2001).
- [333] Liu Q, Berry D, Nash P, Pawson T, McGlade CJ *et al.* Structural basis for specific binding of the gads SH3 domain to an RxxK motif-containing SLP-76 peptide: A novel mode of peptide recognition. *Molecular Cell*, 11(2):471–481 (2003).
- [334] Kang H, Freund C, Duke-Cohan JS, Musacchio A, Wagner G *et al.* SH3 domain recognition of a proline-independent tyrosine-based RKxxYxxY motif in immune cell adaptor SKAP55. *EMBO Journal*, 19(12):2889–2899 (2000).
- [335] Cestra G, Castagnoli L, Dente L, Minenkova O, Petrelli A *et al.* The SH3 domains of endophilin and amphiphysin bind to the proline-rich region of synaptojanin 1 at distinct sites that display an unconventional binding specificity. *Journal of Biological Chemistry*, 274(45):32001–32007 (1999).
- [336] Desrochers G, Cappadocia L, Lussier-price M, Ton At & Ayoubi R. Molecular basis of interactions between SH3 domain- containing proteins and the proline-rich region of the ubiquitin ligase Itch Edited by Thomas Söllner. *Journal of Biological Chemistry*, 292(15):6325–6338 (2017).

- [337] Li SSC. Specificity and versatility of SH3 and other proline-recognition domains: structural basis and implications for cellular signal transduction. *The Biochemical journal*, 390(Pt 3):641–53 (2005).
- [338] He Y, Hicke L & Radhakrishnan I. Structural Basis for Ubiquitin Recognition by SH3 Domains. *Journal of Molecular Biology*, 373(1):190–196 (2007).
- [339] Stamenova SD, French ME, He Y, Francis SA, Kramer ZB *et al.* Ubiquitin Binds to and Regulates a Subset of SH3 Domains. *Molecular Cell*, 25(2):273–284 (2007).
- [340] Marion D. An Introduction to Biological NMR Spectroscopy. *Molecular and Cellular Proteomics*, 12:3006–3025 (2013).
- [341] Marion D, Tabouriech N, Ruigrok RW, Burmeister WP & Blanchard L. Assignment of ^1H , ^{15}N and ^{13}C resonances of the carbohydrate recognition domain of human galectin-3. *Journal of Biomolecular NMR*, 21:75–6 (2001).
- [342] Grzesiek S & Bax A. An efficient experiment for sequential backbone assignment of medium-sized isotopically enriched proteins. *Journal of Magnetic Resonance (1969)*, 99(1):201–207 (1992).
- [343] Dominguez C, Boelens R & Bonvin A. HADDOCK: a protein– protein docking approach based on biochemical or biophysical Information. *Journal of the American Chemical Society*, 125:1731–1737 (2003).
- [344] Van Zundert GCP, Rodrigues JPGLM, Trellet M, Schmitz C, Kastiris PL *et al.* The HADDOCK2.2 Web Server: User-Friendly Integrative Modeling of Biomolecular Complexes. *Journal of Molecular Biology*, 428(4):720–725 (2016).
- [345] Benovic JL, Regan JW, Matsui H, Mayor F, Cotecchia S *et al.* Agonist-dependent phosphorylation of the alpha 2-adrenergic receptor by the beta-adrenergic receptor kinase. *The Journal of biological chemistry*, 262(36):17251–17253 (1987).
- [346] Liggett SB, Ostrowski J, Chesnut C, Kurose H, Raymond JR *et al.* Sites in the Third Intracellular Loop of the alpha2A-Adrenergic Receptor Confer Short Term Agonist-promoted Desensitization. *Journal of Biological Chemistry*, 267(7):4740–4746 (1992).
- [347] Kurose H & Lefkowitz RJ. Differential desensitization and phosphorylation of three cloned and transfected $\alpha 2$ -adrenergic receptor subtypes. *Journal of Biological Chemistry*, 269(13):10093–10099 (1994).

- [348] Eason MG, Moreira SP & Liggett SB. Four consecutive serines in the third intracellular loop are the sites for β -adrenergic receptor kinase-mediated phosphorylation and desensitization of the α_2A -adrenergic receptor. *Journal of Biological Chemistry*, 270:4681–4688 (1995).
- [349] Liang M, Eason MG, Theiss CT & Liggett SB. Phosphorylation of Ser360 in the third intracellular loop of the α_2A -adrenoceptor during protein kinase C-mediated desensitization. *European Journal of Pharmacology*, 437:41–46 (2002).
- [350] Musi V, Birdsall B, Fernandez-Ballester G, Guerrini R, Salvatori S *et al.* New approaches to high-throughput structure characterization of SH3 complexes: the example of Myosin-3 and Myosin-5 SH3 domains from *S. cerevisiae*. *Protein science : a publication of the Protein Society*, 15(4):795–807 (2006).
- [351] Luo L, Xue J, Kwan A, Gamsjaeger R, Wielens J *et al.* The binding of syndapin SH3 domain to Dynamin proline-rich domain involves short and long distance elements. *Journal of Biological Chemistry*, 291(18):9411–9424 (2016).
- [352] Geertsma ER & Dutzler R. A versatile and efficient high-throughput cloning tool for structural biology. *Biochemistry*, 50(15):3272–8 (2011).
- [353] Dagert M & Ehrlich SD. Prolonged incubation in calcium chloride improves the competence of *Escherichia coli* cells. *Gene*, 6(1):23–38 (1979).
- [354] Marley J, Lu M & Bracken C. A method for efficient isotopic labeling of recombinant proteins. *J Biomol NMR*, 20:71–75 (2001).
- [355] Mori S, Abeygunawardana C, Johnson MO & van Zijl PC. Improved Sensitivity of HSQC Spectra of Exchanging Protons at Short Interscan Delays Using a New Fast HSQC (FHSQC) Detection Scheme That Avoids Water Saturation. *Journal of Magnetic Resonance, Series B*, 108:94–98 (1995).